KU LEUVEN

ARENBERG DOCTORAL SCHOOL
Faculty of Engineering Science

Large-eddy simulation of wind farms in conventionally neutral and stable atmospheric boundary layers

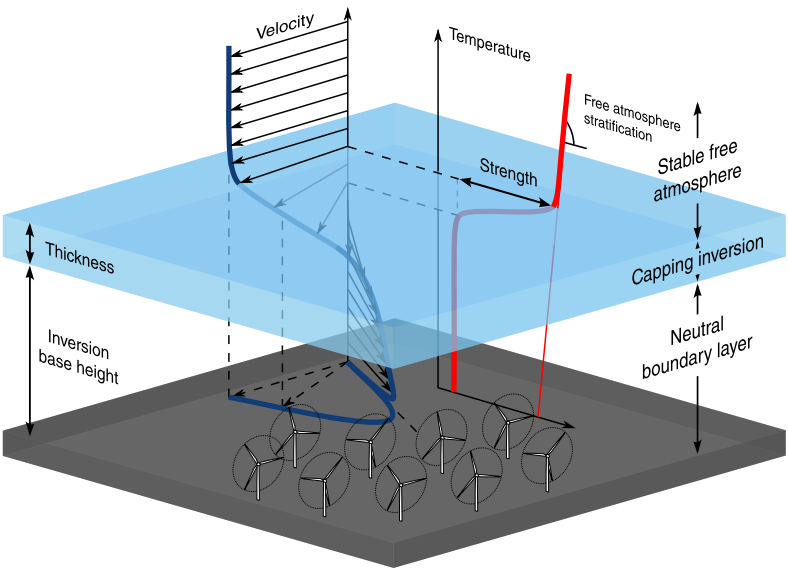

Dries Allaerts

Supervisor:
Prof. dr. ir. J. Meyers

Dissertation presented in partial fulfillment of the requirements for the degree of Doctor of Engineering Science (PhD): Mechanical Engineering

November 2016

Large-eddy simulation of wind farms in conventionally neutral and stable atmospheric boundary layers

Dries ALLAERTS

Examination committee:
Prof. dr. ir. O. Van der Biest, chair
Prof. dr. ir. J. Meyers, supervisor
Prof. dr. ir. J. Driesen, co-supervisor
Prof. dr. N. van Lipzig
Prof. dr. ir. S. Vandewalle
dr. S. R. de Roode
(Delft University of Technology)
Prof. dr. J. N. Sørensen
(Technical University of Denmark)

Dissertation presented in partial fulfillment of the requirements for the degree of Doctor of Engineering Science (PhD): Mechanical Engineering

November 2016

Voor Fran

Preface

People often hear but almost never pay attention to the phrase, “Please keep your seat belt fastened throughout the flight, as turbulence might occur unexpectedly.” After four years of PhD research, I believe I finally understand and appreciate the full meaning of that sentence. First, it reminds me of my “job interview” before the start of this PhD. The only thing I understood from that meeting was that the research project concerned large wind farms and involved something called parallel computing, and I accepted the position because the project sounded exciting. With my general background on energy sciences and a master thesis in nuclear fusion, I had no idea what I signed up for, and turbulence did occur unexpectedly. Throughout my PhD, I further discovered the underlying message in that phrase, and, if I could go back in time, I would give it as an advice to myself before starting this PhD: Prepare yourself, because this journey is certainly not without ups and downs. Luckily, I was surrounded by many people who helped me in achieving this PhD, and I want to express my sincere gratitude to all of them.

First and foremost, I am very grateful to my supervisor, Prof. Johan Meyers, for guiding me in this PhD project. I really appreciate the fact that he was always available to discuss new results or to help break an impasse, even when his own agenda was overloaded or when he was actually on babysitting duty. Moreover, he was not only managing the research group, but also actively contributed to the research through our discussions and brainstorm sessions, as he was always fully up-to-date on the scientific content of the research. Further, I would like to thank Johan for his important contribution in developing my scientific writing and presentation skills. Although I never enjoyed rewriting entire sections or remaking a presentation from scratch, in the end, I truly benefited from his high standards. Overall, I believe I could not have had a better supervisor, and this PhD would not have been possible without his guidance and expertise.

I would like to extend my gratitude to all members of my examination committee for critically reviewing the dissertation and for making valuable suggestions to

improve the overall quality of the final text. I would also like to thank each jury member, especially those coming from abroad, for their effort to attend both the preliminary and public defence, and for initiating interesting discussions during these meetings.

I would like to thank all current and former colleagues at the TME division for creating a warm, friendly and often amusing working environment. Special thanks are due to my fellow colleagues of the TFSO group, who have shared the inevitable joy and pain of computational fluid dynamics and high-performance computing. I am especially grateful to a number of colleagues who had a profound influence on my scientific and personal development. First, I have benefited significantly from several of Wim's implementations in the research code, and for that I am greatly indebted to him. Although his renewed parallelisation probably increased the credit use of our group with several orders of magnitude, without it I would not have been able to taste the pure excitement that accompanies simulations on more than ten thousand processors. Second, I wish to thank Ruben for his support and guidance throughout the first years of my PhD. It was he who introduced me to the wonderful world of Inkscape and taught me how to create and appreciate the aesthetics in figures, posters and presentations. Further, I would like to thank Tijs for his never ending questions of what is the true relevance of my research, and of when will I finally propose to my girlfriend. I am convinced that his perseverance made me a more critical, and a married, researcher. Finally, I am very grateful for Lieven's advice in the final years of my PhD, and for learning me how to put (PhD) life in perspective.

Further, it is only fair to say that this research "lives by the grace of the super-computing center" (J. Meyers). Therefore, I am most grateful for the training events, the lunch-box meetings and the user-support organised by the HPC team. I also thank the secretary of TME for their administrative support, and for the personal notifications in case of leftovers.

Tot slot wil ik graag mijn vrienden, familie en schoonfamilie bedanken voor hun onvoorwaardelijke steun. Welke hulp ik ook nodig had — een luisterend oor, een controle op dt-fouten, een stoofvlees-bevoorrading, afleiding in de aanloop naar en vlak na een deadline — ik kon steeds op jullie rekenen. In het bijzonder wil ik Fran bedanken voor het begrip en geduld dat ze al die jaren heeft moeten opbrengen. Zeker de laatste maanden van mijn doctoraat, toevallig ook de eerste maanden van ons huwelijk, waren voor mij een ware uitputtingsslag. Zonder jouw steun had ik hier niet gestaan, en daarvoor kan ik je maar niet genoeg bedanken.

Dries Allaerts
Leuven, November 2016

Abstract

The accumulated effect of energy extraction by wind turbines in a wind farm leads to a collective interaction between the farm and the atmospheric boundary layer (ABL). To date, many aspects of wind-farm–ABL interaction are still not entirely understood, and wind-farm boundary layers remain an active field of research. In addition to measurement campaigns and wind-tunnel experiments, numerical simulations provide an indispensable tool to study the complex flow phenomena in and around large wind farms in an idealised and controlled environment. The general purpose of the present dissertation is to improve the current understanding of the flow through large wind farms and the interaction with the atmospheric boundary layer. The main focus thereby lies on the influence of atmospheric stability, inversion layers and Coriolis effects on wind-energy extraction in large wind farms.

In the current thesis, the wind flow through large wind farms is analysed by means of large-eddy simulations. For this purpose, the SP-Wind code developed at KU Leuven is extended to allow simulations of various ABL types. Two particular boundary layers are investigated in detail: the conventionally neutral and the stable atmospheric boundary layer. Moreover, two wind-farm regimes are considered, i.e., one regime in which the boundary layer is fully adapted to the presence of the wind farm, and a second regime in which the boundary-layer transition towards equilibrium is included.

In a first step, wind farms under conventionally neutral conditions in a fully developed regime are studied. The main focus is on the role of the overlying inversion layer and the influence of its strength and height on the boundary-layer flow and wind-farm power output. It is found that the energy extraction in large wind farms is controlled by the amount of work done by the large-scale pressure gradient, which depends on the boundary-layer height and the geostrophic wind angle. The inversion layer thereby influences the wind-farm energy extraction by effectively controlling the height of the boundary layer.

In a next step, wind farms in a developing boundary layer under conventionally neutral conditions are investigated, and the importance of the inflow boundary-layer height is assessed. It is shown that the flow deceleration induced by the wind turbines causes a displacement of the boundary-layer top, which in turn excites gravity waves in the inversion layer and the free atmosphere. These waves induce significant pressure gradients in the farm and affect the local energy balance. A detailed energy budget analysis reveals that all energy available at turbine level comes from upstream kinetic energy in the boundary layer, while the work done by the large-scale pressure gradient is only of minor importance in the developing flow regime. Even though an extensive wind farm with 180 turbines over a fetch of 15 km is considered, the fully developed regime is not yet reached.

A final study concerns wind-farm behaviour during the evening transition from an equilibrium conventionally neutral boundary layer towards a nocturnal stable atmospheric boundary layer. Various processes are shown to affect the wind-farm power output. The decreasing wind velocity near the surface is the main effect in the beginning, but soon after that the turning of the wind starts to modify the effective wind-farm layout. Some hours after the onset of surface cooling, the formation of a low-level jet and the associated high wind speeds become dominant in the turbine region.

Beknopte samenvatting

Het gecombineerde effect van energie-extractie door verschillende windturbines in een windturbinepark leidt tot een collectieve interactie tussen het park en de atmosferische grenslaag. Hoe deze interactie juist in zijn werk gaat, is tot op de dag van vandaag niet volledig bekend, en de grenslaagstroming in windturbineparken vormt daarom een actief onderzoeksdomein. Numerieke simulaties vormen, naast meetcampagnes en windtunnelexperimenten, een onmisbaar instrument om de complexe stroming in en rond grote windturbineparken te bestuderen, en dit in een geïdealiseerde en gecontroleerde omgeving. Dit proefschrift heeft als doel de huidige kennis van de stroming in windturbineparken en de interactie met de atmosferische grenslaag te verbeteren. De nadruk ligt daarbij op de invloed van thermische stabiliteit, inversielagen en het corioliseffect op de energie-extractie in grote parken.

De stroming van wind door grote windturbineparken wordt in dit proefschrift bestudeerd aan de hand van large-eddy simulations (*NL: simulaties van grote wervelingen*). Hiervoor wordt de SP-Wind code, ontwikkeld aan de KU Leuven, uitgebreid voor simulaties van verscheidene atmosferische grenslaagtypes. Twee grenslaagtypes worden in detail bestudeerd: de conventioneel neutrale en de stabiele atmosferische grenslaag. Verder worden twee stromingsregimes in windturbineparken onderzocht. In het eerste regime is de grenslaag volledig aangepast aan het windturbinepark, terwijl het tweede regime de transitie van vrije stroming naar stroming in een windturbinepark omvat.

Het eerste deel van dit proefschrift handelt over windturbineparken met volledig ontwikkelde stroming in conventioneel neutrale grenslagen, en onderzoekt de rol van de inversielaag en de invloed van die zijn hoogte en sterkte op de grenslaagstroming en het geproduceerde vermogen van het windturbinepark. Er wordt aangetoond dat de energie-extractie in grote parken gecorreleerd is met de hoeveelheid energie geleverd door de geostrofe drukgradiënt, en deze hoeveelheid hangt af van de grenslaaghoogte en de geostrofe windrichting. De inversielaag beïnvloedt het vermogen door de hoogte van de grenslaag te controleren.

In een tweede stap worden windturbineparken in een ontwikkelende, conventioneel neutrale stroming bestudeerd, en het belang van de grenslaaghoogte stroomopwaarts van het park wordt geëvalueerd. Onder voornoemde omstandigheden zorgt de vertraging van de wind door de windturbines voor een opwaartse verplaatsing van de top van de grenslaag, wat op zijn beurt atmosferische zwaartekrachtsgolven in de inversielaag en in de vrije atmosfeer exciteert. Deze golven induceren drukgradiënten in het park en beïnvloeden zo de lokale energiebalans. Een gedetailleerde analyse van de kinetische energiebalans toont aan dat alle energie op turbinehoogte afkomstig is van kinetische energie stroomopwaarts in de grenslaag, terwijl de energie geleverd door de geostrofe drukgradiënt slechts een kleine rol speelt in ontwikkelende stromingen. Hoewel het bestudeerde windturbinepark 180 turbines bevat en uitstrekt over een lengte van 15 km, slaagt de stroming er niet in om zich volledig te ontwikkelen.

Het laatste deel van dit werk gaat over windturbineparken tijdens het vallen van de avond en de nacht, wanneer de conventioneel neutrale grenslaag overgaat in een stabiele grenslaag. Tijdens deze transitie wordt het geproduceerde vermogen van een windturbinepark beïnvloed door verschillende processen. De afname in windsnelheid dichtbij het aardoppervlak is dominant in het begin, maar kort daarna draait de wind waardoor de stroming een ander geometrisch patroon van wind turbines ervaart. Enkele uren na de start van de oppervlaktekoeling vormt er zich een low-level jet (*NL: laag hangende straalstroming*) waarvan de hoge snelheden de vermogenproductie beïnvloeden.

Nomenclature

Acronyms

ABL	Atmospheric Boundary Layer
ADM	Actuator Disk Model
CBL	Convective Boundary Layer
CFL	Courant–Friedrichs–Lewy number
CNBL	Conventionally Neutral Boundary Layer
DNS	Direct Numerical Simulation
GABLS	GEWEX Atmospheric Boundary Layer Study
GEWEX	Global Energy and Water Cycle Experiment
IBL	Internal Boundary Layer
LES	Large-Eddy Simulation
LLJ	Low-Level Jet
NBL	Neutral Boundary Layer
PBL	Pressure-driven Boundary Layer
RANS	Reynolds-Averaged Navier–Stokes equations
SBL	Stable Boundary Layer
SGS	Subgrid Scale
TKE	Turbulent Kinetic Energy

Greek symbols

α	Angle between the geostrophic velocity vector and the x-axis
Δ	Local grid size, $\Delta = (\Delta x \Delta y \Delta z)^{1/3}$
η	Boundary-layer displacement
γ	Free atmosphere lapse rate
κ	von Kármán constant, $\kappa = 0.4$
Λ	Local Obukhov length, see eq. (2.14)
λ_{max}^{fr}	Fringe region damping coefficient
λ_{max}^{ra}	Rayleigh damping coefficient
ν	Kinematic viscosity
ρ_0	Density of the background adiabatic base state
$\Delta\theta$	Temperature difference over the capping inversion
θ	Potential temperature, see eq. (2.1)
θ_0	Potential temperature of the background adiabatic base state
θ_*	Surface-layer temperature scale or friction temperature, $\theta_* = -q_w/u_*$
θ_m	Potential temperature of the well-mixed layer
τ_{ij}^R	Residual-stress tensor, $\tau_{ij}^R = \widetilde{u_i u_j} - \tilde{u}_i \tilde{u}_j$
τ_{ij}^{sgs}	Subgrid-scale stress tensor, i.e., the anisotropic part of τ_{ij}^R
τ_w	Wall stress
τ_{xz}, τ_{yz}	Total (resolved plus subgrid) shear stress
ϕ	Horizontal wind direction
ϕ_h	Dimensionless temperature gradient, see eq. (3.22)
ϕ_m	Dimensionless velocity shear, see eq. (3.21)
Ψ_h	Stability correction function for heat in Monin–Obukhov theory
Ψ_m	Stability correction function for momentum in Monin–Obukhov theory

Roman symbols

C_g	Geostrophic drag, $C_g = u_{*hi}/G$
c_p	Specific heat per unit mass at constant pressure
C'_T	Disk-based turbine thrust coefficient
c'_{ft}	Wind-farm friction coefficient based on the horizontal surface, $c'_{ft} = \pi C'_T/(4 s_x s_y)$
D	Turbine rotor diameter
$\mathscr{E}$	Dissipation, see eq. (4.13)
E_k	Total kinetic energy, $E_k = u_i u_i/2$
f_c	Coriolis parameter, $f_c = 2\Omega \sin\phi$ with Ω the earth's rotation and ϕ the latitude
f_i	Body forces exerted by the wind turbines on the flow
f_s	Grid stretching factor
F_t	Turbine thrust force, see eq. (3.18)
G	Geostrophic wind speed
g	Gravitational acceleration, $g = 9.81$ m/s^2
h	Boundary-layer height
h_0	Inversion base height
h_1	Inversion centre height
h_2	Inversion top height
h_{IBL}	Internal boundary layer height
Δh	Inversion thickness
k	Resolved turbulent kinetic energy
k_{sgs}	Subgrid-scale turbulent kinetic energy
K	Eddy viscosity
K_{sgs}	Subgrid-scale eddy viscosity
L	Obukhov length, see eq. (2.13)

L^{fr}	Fringe region width
L^{ra}	Rayleigh damping layer width
L_x, L_y, L_z	Numerical domain size in x, y and z direction, respectively
N	Brunt–Väisälä frequency, see eq. (2.5)
$\mathscr{P}_\infty$	Power related to the background pressure gradient, see eq. (4.13)
$\mathscr{P}_\theta$	Production of potential energy, see eq. (4.13)
$\mathscr{P}_F$	Wind-farm power extraction, see eq. (4.13)
p	Pressure
p_∞	Mean background pressure
$p^\star$	Modified pressure
Pr	Prandtl number
Pr_{sgs}	Subgrid-scale Prandtl number
q_j^{sgs}	Subgrid-scale heat flux
q_w	Surface heat flux
q_z	Total (resolved plus subgrid) vertical heat flux
Ri	Gradient Richardson number, $Ri = N^2/S^2$
Re	Reynolds number
Ro_h	Rossby number based on the turbine hub height, $Ro_h = G/f_c z_h$
R_d	Gas constant for dry air, $R_d = 287\ \mathrm{m^2/s^2K}$
S	Characteristic filtered rate of strain, $S = (2S_{ij}S_{ij})^{1/2}$
S_{ij}	Filtered rate of strain, $S_{ij} = 0.5\,(\partial\tilde{u}_i/\partial x_j + \partial\tilde{u}_j/\partial x_i)$
s_x	Relative streamwise turbine spacing
s_y	Relative spanwise turbine spacing
TI	Turbulent intensity
T	Temperature
$\langle\bar{u}_\perp^T\rangle_d$	Local disk-averaged and time-filtered velocity perpendicular to the turbine disk

u_*	Friction velocity, $u_* = (\tau_w/\rho_0)^{1/2}$
u_1, u_2, u_3	Components of the three-dimensional velocity field, also noted as (u, v, w)
x_1, x_2, x_3	Streamwise, spanwise and vertical coordinate direction, also noted as (x, y, z)
z_0	Surface roughness length
z_h	Wind-turbine hub height

Miscellaneous symbols

a_{hi}	Quantity characteristic for the log law above the wind-turbine region
a_{lo}	Quantity characteristic for the log law below the wind-turbine region
$\bar{a}$	Time-averaged quantity
$\langle a \rangle$	Quantity averaged over the horizontal, homogeneous direction(s)
$\tilde{a}$	LES filtered quantity
a'	Fluctuation in time, $a' = a - \bar{a}$
a''	Fluctuation in space, $a'' = a - \langle a \rangle$

Contents

List of Figures

List of Tables

Chapter 1

Introduction

The commercial deployment of wind turbines for wind-energy harvesting began in the 1970s, partly driven by the oil crises. The rapid expansion of the wind-energy market, however, did not start until the 21st century. Near the end of 2015, the global capacity of wind power reached 433 GW, making it the world's second largest renewable-energy market after hydro power (Ren21 2016). In the European Union, more wind-power capacity was installed in 2015 than any other form of power generation, causing wind power to replace hydro power as the third largest power source (GWEC 2015) (see figure 1.1). Nowadays, it is customary to assemble large amounts of wind turbines together in a wind farm to reduce investment costs related to grid infrastructure (transformers, high-voltage transmission lines, etc.) as well as operation and maintenance costs. Although the first wind farms were exclusively built over land, the offshore wind industry is rapidly growing, and the majority of future wind energy projects is expected to go offshore as well. To date, the European Union holds the world's largest offshore wind industry, which, by the end of 2015, consisted of 80 wind farms with a total of 3230 wind turbines fully connected to the electricity grid (see table 1.1) (EWEA 2016*a*). Furthermore, the average size of new wind farms has increased considerably over the past few years, and wind farms are expected to become even more extended and to cover even larger surface areas in the future (see, e.g., the average size of installed and planned EU offshore wind projects in figure 1.2).

Despite the impressive growth of the wind industry over the past decades, the International Energy Agency reports that the annual installed wind capacity has to increase even more to arrive at the targets set in the technology roadmap for wind energy (IEA 2013), i.e., 15–18 % share of global electricity production

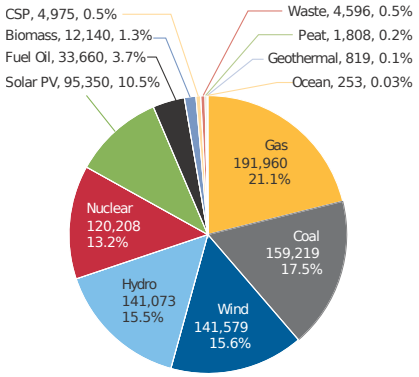

Figure 1.1: Installed capacity [MW] per energy technology in the European Union in 2015. Reproduced from EWEA, Wind in power – 2015 European statistics.

Table 1.1: Statistics of offshore wind industry per country in the European Union, including number of wind farms with grid-connected turbines, no. of turbines connected and no. of MW fully connected to the grid at the end of 2015. Note that the offshore industry in Spain, Norway and Portugal consists of only one wind turbine which is technically not a farm. Reproduced from EWEA, The European offshore wind industry – key trends and statistics 2015.

Country	BE	DE	DK	ES	FI	IE	NL	NO	PT	SE	UK	Total
No. of farms	5	18	13	1	2	1	6	1	1	5	27	80
No. of turbines	182	792	513	1	9	7	184	1	1	86	1,454	3,230
Capacity installed (MW)	712	3,295	1,271	5	26	25	427	2	2	202	5,061	11,027

from wind energy by 2050. Reducing the levelised cost of wind energy by means of technological development is an essential instrument in achieving this goal. In this regard, assessment of wind characteristics is identified as an important research track that can help to achieve better performance and reliability of wind turbines and can reduce uncertainties in power production forecasts (IEA 2013).

For a long time, both design standards and operational strategies of wind farms presumed that the wind characteristics are a fixed boundary condition imposed by the project site. However, for the limit of very large wind farms, already in 1992, Frandsen (1992) hypothesised that the energy extraction itself

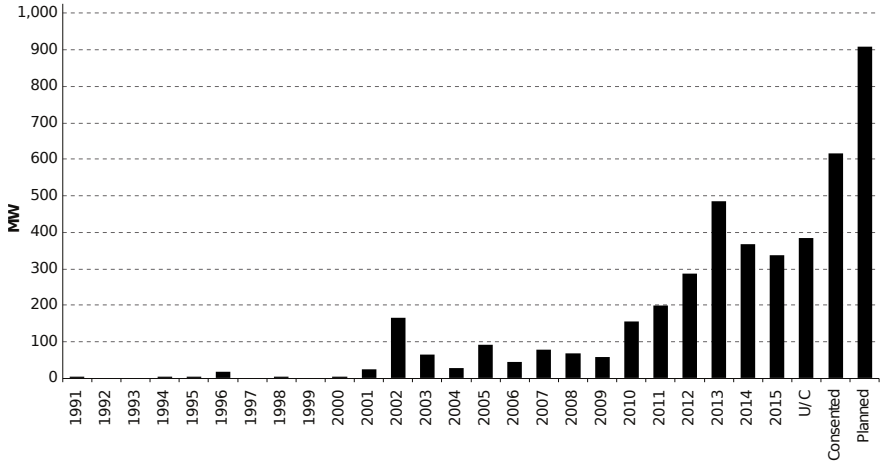

Figure 1.2: Average size of offshore wind-farm projects in the European Union. Reproduced from EWEA, The European offshore wind industry – key trends and statistics 2015.

causes the atmospheric boundary layer (ABL) to slow down as a whole, thereby reducing the available wind energy at the turbine level. More recently, Calaf *et al.* (2010) performed large-eddy simulations (LES) of wind farms in the ABL and corroborated Frandsen's result. Meyers & Meneveau (2012) further showed that the interaction with the ABL is not just an academic curiosity in the limit of infinite wind farms, but that it already affects the power output of existing wind farms at Horns Rev I and Nysted with moderate fetches of 5 to 6 km. Given the trend towards larger wind farms, the influence of the ABL is expected to become even more important in future.

Although the physics of the ABL have been under investigation for a very long time, the combination with wind-energy research is a relatively new field of study. Measurement campaigns form a crucial ingredient for this new research field as they increase the knowledge of wind characteristics and pose benchmark cases for engineering models. However, measurements in operational wind farms are also very challenging given the large size and the fact that atmospheric conditions are continuously changing in time and influenced by a variety of phenomena such as, e.g., complex terrain, land–sea transition, etc. Numerical simulations therefore provide essential support to the field by allowing systematic studies in an idealised environment with full control of the topographic and atmospheric conditions.

To date, many aspects of the wind-farm–ABL interaction are still not entirely understood. Therefore, the general purpose of the present dissertation is to improve the current understanding of the flow through large wind farms and the interaction with the atmospheric boundary layer. This objective is pursued by performing high-fidelity numerical simulations of the wind-farm–ABL interaction using large-eddy simulation models, which form an established numerical technique in the atmospheric boundary-layer community and have also been applied in the wind-farm community in recent years.

In the current chapter, the broader context of this thesis is introduced and the main objectives are formulated. Section 1.1 describes the intrinsic difference between wind turbines operating in isolated conditions and in a wind farm, and introduces the concept of wind-farm–ABL interaction. Next, section 1.2 focuses on the state-of-the-art in numerical modelling of flow through wind farms and the challenges in this field. Finally, the aims and objectives of this thesis are summarised in section 1.3 and an outline of the remainder of the thesis is provided in section 1.4.

1.1 Wind-farm–ABL interaction

A wind turbine extracting energy from the flow gives rise to a region of reduced wind speed and increased turbulence with respect to the free stream. This region behind the wind turbine is called the wind-turbine wake. The wake structure behind a one-bladed rotor is shown in figure 1.3, visualised by dye in a water channel experiment (Leweke *et al.* 2014). The figure illustrates the organised helical vortex structure close to the turbine and the breakdown into turbulence. The momentum deficit in the wake is largest near the turbine and is gradually replenished downstream as turbulence transfers energy from the free stream into the wake region (see, e.g., given reviews by Crespo *et al.* 1999*b*). Although turbine-wake recovery is generally assumed to extend about ten times the rotor diameter D downstream (Ammara *et al.* 2002), Mehta *et al.* (2014) mentioned measurements of increased turbulent intensity as far as $15D$ downstream. Moreover, recent experimental (Chamorro & Porté-Agel 2010) and numerical (Wu & Porté-Agel 2011) studies found wake effects until distances of $20D$. A considerable amount of literature has been published on wakes from individual wind turbines, and reviews are given by, e.g., Crespo *et al.* (1999*b*), Vermeer *et al.* (2003), Sanderse *et al.* (2011) and Sørensen (2011).

Despite the significant influence of a wind turbine on the flow downstream, the impact of a lone-standing wind turbine on the ABL is negligible from a larger point of view. In wind farms, however, the flow behaviour becomes more

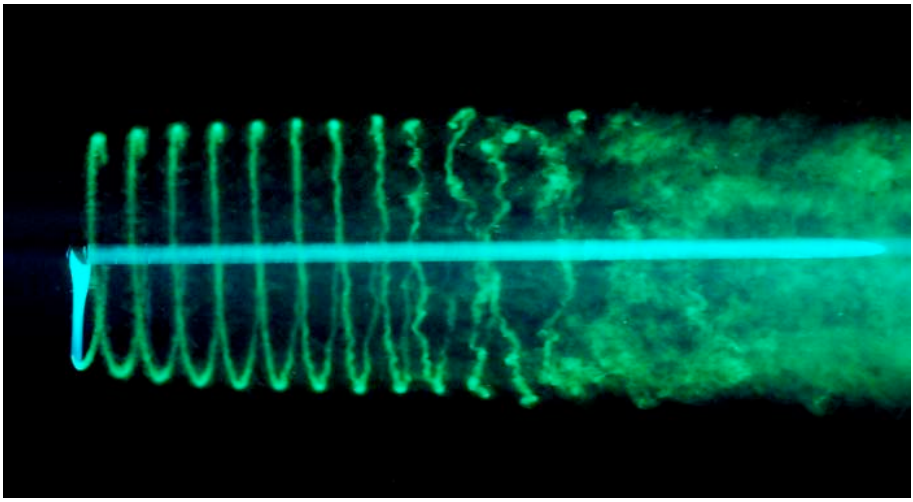

Figure 1.3: Example of a wake behind a one-bladed rotor, showing the breakdown of helical vortices and the development of turbulence (dye visualisation in water). Reproduced from T. Leweke et al. Long- and short-wave instabilities in helical vortices, J. Phys.: Conf. Ser. 524 (2014), 012154. This figure is licensed under a Creative Commons Attribution 3.0 License.

complex as it comprises several wind-turbine wakes instead of only one. This situation is illustrated in figure 1.4, showing a picture of the Horns Rev II wind farm where the wind-turbine wakes are visualised by low hanging fog that is mixed into the wake region. When the spacing between the turbines along the mean flow direction is too low, turbulence may fail to replenish the momentum deficit of the wake region in time before reaching the next turbine. As a result, wind turbines located inside the farm may be positioned entirely or partially in the wake of an upstream turbine (see figure 1.4). These downstream turbines will experience higher turbulence levels than in stand-alone operation, leading to higher mechanical loading (see, e.g. Thomsen & Sørensen 1999). Furthermore, the inflow velocities at these turbines will be lower, which reduces the turbine energy extraction. Power deficits in downstream rows have been reported as high as 60 %, depending on turbine size, spacing and layout (see, e.g., Barthelmie *et al.* 2007*b*). The associated underperformance of wind farms is a well-known phenomenon and has been observed in many operational installations. For example, Crespo *et al.* (1999*b*) and Frandsen *et al.* (2006) showed figures of velocity deficits (calculated from the wind-turbine power signals) for the Zeebrugge and Nørregærd Enge II wind farms, respectively. Other studies have reported reduced power production in Middelgrunden (Barthelmie *et al.* 2007*a*),

Figure 1.4: Aerial picture of the Horns Rev II wind farm, in which the wind-turbine wakes are visualised by low hanging fog that is mixed into the wake region. Photo by: Bel Air Aviation Denmark – Helicopter Services. January 26th, 2016. Used with permission.

Horns Rev I (Barthelmie *et al.* 2007*b*, 2009, 2010), Nysted (Barthelmie & Jensen 2010; Barthelmie *et al.* 2010; Nygaard 2014) and Lillgrund (Dahlberg *et al.* 2009). In addition, Nygaard (2014) also discussed power losses for three of the largest offshore wind farms built to date: Walney, Anholt and London Array.

The flow through large wind farms is even further complicated as turbine wakes impact with the surface and merge in streamwise and spanwise directions, eventually filling up the entire wind-farm region and resulting in a wind-farm wake. In this context, the term *wind-farm–ABL interaction* is sometimes used, referring to the two-way coupling between the wind-energy extraction and the atmospheric boundary layer. On the one hand, wind-turbine wake size, magnitude and recovery rate largely depend on atmospheric conditions such as wind speed and direction, vertical shear and wind veer, and turbulence intensity. These flow aspects are often related to the atmospheric stability, and its effect on

wind turbines and wind farms is discussed in § 1.1.1. On the other hand, large wind farms increase the effective surface roughness (Frandsen 1992), causing the ABL to slow down as a whole and reducing the available wind energy at the turbine level. Both experimental (Cal *et al.* 2010) and numerical (Calaf *et al.* 2010) studies further illustrated that for large wind farms, the energy extracted by the turbines is transported into the wind-turbine region by vertical turbulent fluxes. These findings imply that the aggregated wind-turbine energy extraction plays an important role in the total energy household of the ABL and changes the equilibrium state of the boundary layer. Very large wind farms may even induce effects on a regional scale beyond their own boundaries and impact local weather and climate. Observational and numerical evidence of these effects are reviewed in § 1.1.2.

1.1.1 Effect of stability on wind turbines and wind farms

Regarding the impact of atmospheric conditions on wind-turbine wakes, thermal stability plays an important role for two reasons, i.e., it directly affects the mechanical turbulence in the wake region, but it also strongly determines the ambient turbulent intensity. Magnusson & Smedman (1994, 1999) investigated wind-turbine wakes in the Alsvik wind farm and showed that the velocity deficit in the wake is higher under stable atmospheric conditions. Since then, many studies have investigated the effect of atmospheric stability on wind-turbine performance and wake structure using numerical simulations (Churchfield *et al.* 2012*a*; Abkar & Porté-Agel 2015), wind-tunnel experiments (Chamorro & Porté-Agel 2010; Zhang *et al.* 2013*b*; Hancock & Pascheke 2014) and field measurements (Iungo & Porté-Agel 2014). The main conclusion in all these studies is that wake recovery is most efficient under unstable conditions, while stable conditions yield very long wakes with large velocity deficits.

In large wind farms, the dependence of the turbine wakes on atmospheric stability will greatly influence power deficits in downstream turbines. Barthelmie & Jensen (2010) reported lower wind-farm efficiencies for the Lillgrund wind farm when the atmosphere was stably stratified, while unstable conditions yielded only marginally higher efficiencies compared with neutral conditions. Hansen *et al.* (2012) and Vanderwende & Lundquist (2012) reached similar conclusions based on measurement of the Horns Rev I wind farm and of a wind farm in central North America (exact location undisclosed).

Further, atmospheric stability also affects the vertical wind shear and the variation of turbulent intensity with height across the turbine rotor disk (Wharton & Lundquist 2012*a*). Wharton & Lundquist (2012*b*) showed that these characteristics influence individual turbine performance, and found differences

in power output up to 15 % between stability classes but for equal hub-height wind speed.

1.1.2 Effect of wind farms on ABL flow

The impact of wind farms on local meteorology has been studied by many authors, mainly using field observations and numerical weather-prediction models. Christiansen & Hasager (2005) identified regions of reduced wind speed and high turbulence intensity behind the Horns Rev I and Nysted offshore wind farms based on satellite images. These wind-farm wakes were observed to extend 5 to 20 km downstream of the farm depending on atmospheric conditions. Using the Weather Research and Forecasting model (WRF), Fitch *et al.* (2012) found similar wind-speed deficits behind an idealised wind farm. Such wakes can have a detrimental effect on the efficiency of neighbouring wind farms. For instance, Nygaard (2014) compared power measurements of the Nysted wind farm before and after the installation of the Rødsand II wind farm. The results showed a significant drop in the efficiency of the Nysted turbines when Rødsand II was operational and located upstream. Van der Laan *et al.* (2015) performed RANS (Reynolds-Averaged Navier–Stokes equations) simulations of the same wind farms and found losses of 10 to 15 % in Rødsand II when operating in the wake of Nysted.

Van der Laan *et al.* (2015) also showed that wind-farm wakes can be deflected due to the Coriolis effect, indicating that outer-layer effects play a role in large wind farms. However, there is no consensus on the turning direction of wind-farm wakes in literature, i.e., some authors predicted a deflection towards the pressure gradient related to the reduced wind speed (Dörenkämper *et al.* 2015), while others found a deflection towards the Coriolis force due to the increased turbulent mixing (Fitch *et al.* 2012; Van der Laan *et al.* 2015). Moreover, Volker *et al.* (2015) demonstrated that opposite directions could be obtained when using various wind farm parametrisation in WRF.

Large wind farms also affect other flow characteristics, such as the local temperature and fluxes of heat and moisture. For example, Rajewski *et al.* (2013) found evidence of turbines modifying fluxes of heat and carbon dioxide during the Crop Wind Experiment (CWEX). Furthermore, modified surface air temperatures were observed by Baidya Roy & Traiteur (2010) for the San Gorgonio wind farm and by Zhou *et al.* (2012) for four wind farms in west–central Texas. These observation have been confirmed by numerical simulations, showing that the changes in surface air are related to the enhanced vertical mixing of momentum and heat (Baidya Roy *et al.* 2004; Baidya Roy & Traiteur 2010; Baidya Roy 2011; Fiedler & Bukovsky 2011; Fitch *et al.* 2013). These

studies also reported local changes in surface humidity, sensible and latent heat fluxes and precipitation. Using wind-tunnel experiments of scaled-down wind farms, Zhang *et al.* (2013*a*) further showed that the spatial distribution of the surface heat flux is highly heterogeneous and depends on the wind-farm layout. The impact of wind farms on the global climate has also been investigated by some authors, but the reported effects were minimal (see, e.g., Fitch 2015, and references therein).

1.2 State-of-the-art in wind-farm modelling

Insight into the complex wind-farm–ABL system forms a key instrument in improving wind-farm operation and design. Field measurements and wind-tunnel studies help to achieve this objective by providing data for understanding the fundamental aspects of wind-farm dynamics. These techniques are assisted by numerical simulations, which allow systematic studies in idealised environments. State-of-the-art wind-farm modelling therefore relies on the large-eddy simulations (LES) technique.

Over the past three decades, LES has been the preferred tool for modelling atmospheric turbulence because of its detailed spatial and temporal resolution (see, e.g., Moeng 1984; Mason 1989; Mason & Derbyshire 1990; Porté-Agel *et al.* 2000). Moreover, LES has also been used in several studies on wind-turbine wakes (see, e.g., Jimenez *et al.* 2007, 2008; Wu & Porté-Agel 2011). The idea to simulate an entire wind farm with LES was launched by the two pioneering studies of Calaf *et al.* (2010) and Ivanell (2009). Calaf *et al.* (2010) were the first to perform a systematic study of the asymptotic limit of "infinite" wind farms by means of large-eddy simulations on a fully periodic domain. This situation represents *fully developed* wind farms, i.e., wind farms whose length exceeds the ABL height by an order of magnitude so that the turbulent boundary layer may approach a fully developed regime. Ivanell (2009), on the other hand, simulated two of the ten columns of the Horns Rev I wind farm and used a power law profile with Mann turbulence to represent neutral atmospheric inflow conditions (Mann 1994). Ivanell's simulation therefore corresponds to a *developing* wind farm because it includes entrance effects and streamwise flow development.

The two studies mentioned above, as well as almost all numerical studies on wind farms since then have focused on neutral pressure-driven boundary layers (PBLs), in which rotation and stratification effects are absent. Examples are studies by Meyers & Meneveau (2010); Calaf *et al.* (2011); Yang *et al.* (2012); Meyers & Meneveau (2013); VerHulst & Meneveau (2014); Yang *et al.* (2014*a*,*b*); Goit & Meyers (2015) for fully developed wind farms, and by Porté-Agel *et al.*

(2011, 2013); Wu & Porté-Agel (2013, 2015); Stevens *et al.* (2014*a*,*b*, 2015*b*); Nilsson *et al.* (2015); Goit *et al.* (2016); Munters *et al.* (2016) for wind farms with entrance effects and a developing boundary layer. A fairly recent review of LES investigations into wind farm aerodynamics can be found in the paper of Mehta *et al.* (2014). The main working assumption in these studies is that the wind turbines are located in the inner region of the ABL (i.e., the lower 10%–15% of the ABL height), so that outer-layer effects such as Coriolis forces and the boundary-layer height do not directly influence the farm. However, this assumption breaks down for shallow boundary layers in which case the wind turbines reach into the outer layer and external effects start to influence the wind-farm flow behaviour (Goit & Meyers 2013). Furthermore, as shown in the previous section, observations in operational wind farms indicate that wind-farm efficiency is very sensitive to the atmospheric stability and the associated variations in turbulent intensity, vertical shear and wind veer.

Despite the obvious limitations of the PBL approach, only a few studies have included more details of the ABL in their wind farm simulations. The interaction between a large wind farm and the fully developed boundary layer with Coriolis effects was studied by Johnstone & Coleman (2012), using direct numerical simulations (DNS) with an artificially low Reynolds number. They showed that the work by the driving pressure gradient can vary in two ways to balance the sum of turbulent energy dissipation and wind-farm energy extraction: through a thickening of the boundary layer or by rotating the wind towards the pressure gradient. Both of these possibilities are impossible in the PBL approach, in which the boundary-layer height is fixed and the mean velocity is unidirectional. Similarly, Goit & Meyers (2013) performed LES of fully developed wind farms with rotation effects, and they determined the Rossby number at which outer-layer effects start influencing the wind farm.

The effects of atmospheric stability on wind-farm performance were first simulated by Lu & Porté-Agel (2011) for the stably stratified boundary layer. However, their numerical domain only contained one wind turbine, and wind-farm conditions were approximated by using periodic boundary conditions. More realistic simulations containing several wind turbines were later performed for the unstable ABL by Lu & Porté-Agel (2015). Further, Abkar & Porté-Agel (2013, 2014) investigated the influence of the free atmosphere stratification on wind-farm power extraction and found a decrease in performance for increasing stability aloft.

Simulations of entrance effects and developing boundary layers over wind farms have been performed by Churchfield *et al.* (2012*b*) and Archer *et al.* (2013) for the Lillgrund wind farm under conventionally neutral conditions (i.e., in a neutral ABL developing against a stable background). These studies used the OpenFOAM based LES solver SOWFA (Simulator for Offshore/Onshore Wind

Farm Applications) developed at the National Renewable Energy Laboratory (NREL). Keck *et al.* (2014) used the same LES code to simulate part of the OWEZ (Offshore Wind farm Egmond aan Zee) and North Hoyle wind farms under conventionally neutral and unstable conditions. However, due to the finite volume approach of OpenFOAM, wind-farm simulations with SOWFA are extremely expensive, and to date, only allow modest domain sizes and limited time horizons of about ten minutes. Moreover, only one ABL case is considered in these studies.

Witha *et al.* (2014) simulated two small German offshore wind farms, i.e., alpha ventus and EnBW Baltic 1, with the LES model PALM for various atmospheric stabilities ranging from slightly stable to unstable. The impact of stable stratification on EnBW Baltic 1 was further elaborated by Dörenkämper *et al.* (2015). Finally, Abkar *et al.* (2016) recently simulated a generic wind farm consisting of 36 wind turbines during a full diurnal cycle using the WiRE LES code, which is developed at the École Polytechnique Fédérale de Lausanne and in an early version at Johns Hopkins University. As expected, these studies found higher wind-farm power deficits under stable atmospheric conditions compared to neutral or unstable conditions due to the lower turbulent intensities and therefore slower wake recovery.

1.3 Aims and objectives

This dissertation aims at improving the current understanding of turbulent flow through wind farms and the interaction with the atmospheric boundary layer. The main goal is to explore the effects of atmospheric stability on boundary-layer flow and power output in large wind farms by means of detailed numerical simulations. To date, only a limited amount of studies have considered the effect of atmospheric stability on wind farms, and most of these studies were restricted to relatively small wind farms and very short time periods. Moreover, these studies leave some fundamental research questions related to the importance of the boundary-layer height and the role of overlying inversion layers unanswered. In addition, although many studies have used the neutral pressure-driven approach to locate the point where the wind-farm boundary layer becomes fully developed, these results have never been verified in the presence of thermal stability.

For the current dissertation, the SP-Wind code developed at KU Leuven for wind-energy research is available. This in-house code is a fast and efficiently parallellised LES code, allowing the simulation of very large wind farms with fine resolutions at an affordable computational cost. However, extensions to

the research code are necessary as the effect of gravity – the fundamental driver of atmospheric stability – was not yet included.

Given the wide variety of atmospheric boundary-layer types, two particular stability conditions are considered in this thesis, i.e., the conventionally neutral and the stable atmospheric boundary layer. These cases are considered the most interesting as they will have a larger influence on wind-farm flow behaviour and power performance than the highly turbulent, unstable atmospheric boundary layer.

Three objectives are formulated for the current dissertation:

1. Extend the research code to allow simulation of turbulent boundary-layer flows including effects of thermal stability. This requires the implementation of an additional transport equation for potential temperature and the addition of buoyancy forces to the momentum equation. Moreover, new subgrid-scale models, accounting for stability effects on the subgrid-scale motions, are needed. The extensions to the existing code need to be verified and validated thoroughly with data from literature.

2. Study the influence of inversion layers in the conventionally neutral atmospheric boundary layer on the wind-farm flow behaviour and the power performance in both fully developed and developing boundary-layer flows. Further, as will be shown in the dissertation, simulations should include the free atmosphere in the numerical domain, and care should be taken to prevent non-physical reflection of vertically propagating atmospheric gravity waves at the domain boundaries. Additionally, careful initialisation of both velocity and potential temperature profiles is necessary to maintain control over the boundary-layer structure.

3. Study wind-farm performance in stable atmospheric boundary layers. This is the most challenging ABL regime as it requires very fine grid resolutions and as it is more demanding for the subgrid-scale model. Again, initialisation should be done rigorously, and reflection of gravity waves should be minimised.

1.4 Outline

This dissertation is organised as follows. First, before diving into numerical aspects and wind-farm–ABL interactions, chapter 2 provides a general background on the atmospheric boundary layer and its various aspects.

The important concept of thermal stability and the definition of potential temperature are introduced in section 2.1. Next, frequently used approximations to the more general compressible Navier–Stokes equations are discussed, and an adequate numerical framework for studying the wind-farm–ABL interaction is chosen in section 2.2. The traditional atmospheric stability classification into neutral, unstable and stable atmospheric boundary layers is described in section 2.3, and the two ABL types of particular interest to this thesis are elaborated more thoroughly in § 2.3.1 and § 2.3.2. In section 2.4, two ABL aspects relevant for wind-farm flows are discussed, i.e., internal boundary layer development and atmospheric gravity waves. The main findings are summarised in section 2.5.

In chapter 3, the numerical methods for large-eddy simulations are reviewed, and the basic extensions to the SP-Wind code for simulating atmospheric stability effects are described and validated (objective 1). Section 3.1 introduces the governing equations, which now include a transport equation for the potential temperature in addition to the usual equations of continuity and momentum. Next, sections 3.2 and 3.3 describe the wall model and subgrid-scale model, respectively. Extension of the wall model is simply achieved by applying correction functions. The subgrid-scale model is more delicate and two models available in literature are implemented. The representation of wind turbines by the actuator disk method is briefly mentioned in section 3.4. Subsequently, section 3.5 documents the verification and validation process of the extended LES code. To this extent, three case studies are simulated and discussed, including stratified turbulent channel flow and atmospheric boundary layers under conventionally neutral and stable conditions. Conclusions related to the first objective are summarised in section 3.6.

Chapter 4 presents the first wind-farm study of this dissertation, which focuses on wind farms in fully developed, conventionally neutral atmospheric boundary layers (objective 2). In particular, the role of the overlying inversion layer and the influence of its strength and height on the boundary layer and the wind farm are assessed with a suite of LES simulations with varying inversion characteristics. The parameters are thereby chosen to cover a range of offshore wind conditions. Section 4.1 first introduces some additional numerical aspects, among which the development of a wind-angle controller and an innovative procedure for initialising velocity and temperature profiles. The general characteristics of conventionally neutral wind farms are described in section 4.2, which is continued by a discussion on the effects of varying inversion layer parameters in section 4.3. A simple, analytical model is developed in section 4.4 for estimating the wind-farm power output in quasi-steady conditions, and conclusions of this case study are given in section 4.5.

A second wind-farm study under conventionally neutral conditions is described

in chapter 5, now focusing on the streamwise development of boundary-layer flow and energy extraction (objective 2). As before, the atmospheric conditions are set to represent a typical offshore location. Three LES simulations with varying inflow boundary-layer heights are performed to investigate the effect of inflow conditions on boundary-layer development and wind-farm performance. In order to simulate this kind of wind farms with SP-Wind, special treatment of the boundary conditions is needed. This is discussed in section 5.1, along with the numerical set-up and the wind-farm characteristics. Initialisation of the boundary-layer flow is achieved in two phases, which are described in section 5.2. The general behaviour of developing wind farms under conventionally neutral conditions is first discussed in section 5.3, after which section 5.4 compares different cases with varying inflow conditions. Section 5.5 summarises the conclusions of this case study.

Chapter 6 presents the last case study of this dissertation concerning wind farms in stable atmospheric boundary layers (objective 3). In particular, the temporal development of this boundary layer starting from a conventionally neutral boundary layer is studied. This situation occurs almost daily in onshore wind farms during the evening transition. Three cases with varying surface cooling are compared, corresponding to neutral, weakly stable and moderately stable conditions. First, the set-up of the numerical domain and the wind farm is summarised in section 6.1. Next, section 6.2 describes the initialisation and development of the boundary-layer flow in absence of wind turbines. The wind-farm simulations are discussed in section 6.3, and conclusion are given in section 6.4.

Finally, chapter 7 summarises the conclusions of this dissertation and gives suggestions for future research.

Chapter 2

The atmospheric boundary layer

Boundary layers develop when a flow experiences a drag force by a bounding surface. In the atmosphere, the surface of the earth or the sea forms a solid boundary for the wind flow and gives rise to the atmospheric boundary layer (ABL). In *An Introduction to Boundary layer Meteorology* (1988, p. 2), Stull defines the atmospheric boundary layer as

> "... that part of the troposphere that is directly influenced by the presence of the earth's surface, and responds to surface forcings with a timescale of about an hour or less."

Perhaps the most important feature of the ABL is its complex, three-dimensional, turbulent nature, as opposed to the steady, mainly horizontal flow in the free atmosphere above. The turbulence in the atmosphere is generated to a large extent by wind shear, but it is also affected considerably by buoyancy, which can either produce or destroy turbulent energy. The structure and depth of the ABL are therefore closely related to the static, thermal stability of the atmosphere.

The ABL is generally deeper than standard turbine heights, which means that wind turbines are almost always located inside the turbulent boundary layer. Consequently, detailed insight into wind turbine and wind farm operation can only be gained by taking the structure and stability of the ABL into account. The current chapter therefore provides an overview of the atmospheric boundary layer and its various aspects. First, the concept of thermal stability

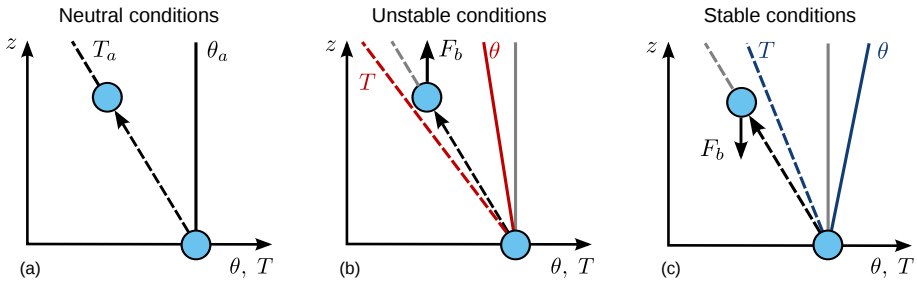

Figure 2.1: Vertical profiles of temperature (dashed lines) and potential temperature (solid lines) for various stability regimes, illustrating the effect of buoyancy on an air parcel (blue circle) that is moving upwards. (a) Neutral conditions: No buoyancy force and the motion is not affected; (b) Unstable conditions: Buoyancy force F_b in the direction of the motion, so the parcel is accelerated; (c) Stable conditions: Buoyancy force F_b opposite to the direction of motion, so the movement is counteracted.

in the atmosphere is defined in section 2.1, and the anelastic and Boussinesq approximations for atmospheric flow are explained in section 2.2. The typical atmospheric stability classes are introduced in section 2.3, and two regimes of particular interest to this thesis are discussed in more detail: the conventionally neutral boundary layer (§ 2.3.1) and the stable boundary layer (§ 2.3.2). Two aspects of ABL flow that resemble the flow modification in a wind farm are elaborated in section 2.4: the development of an internal boundary layer after a surface roughness transition (§ 2.4.1), and the generation of atmospheric gravity waves due to flow displacement under stable stratification (§ 2.4.2). The main findings of this chapter are summarised in section 2.5.

2.1 Thermal stability

Buoyancy plays an important role in the ABL as it can either accelerate or counteract vertical motions, thereby leading to generation or destruction of turbulence. The sign of the buoyancy force depends on the magnitude of the background temperature lapse rate relative to the adiabatic lapse rate. Three different situations can occur, i.e., neutral, unstable or stable stability, as indicated in figure 2.1. To understand the behaviour of an air parcel in these three situations, imagine the vertical displacement of a parcel without exchanging heat with the surrounding. This parcel will experience a compression or expansion, accompanied by a change in temperature and density according

to the universal gas law (see the decrease in temperature when the air parcel (blue circle) moves upwards in figure 2.1). The atmosphere is called neutral (figure 2.1(a)) if the change in temperature of an air parcel moving up or down (dashed line) exactly matches the variation in background temperature and density. As a result, the air parcel does not experience any buoyancy force as its density is always equal to that of the background. Neutral atmospheric stability occurs when the decrease in background temperature with height is equal to the adiabatic lapse rate $g/c_p = 9.8$ K/km, with g the gravitational acceleration and c_p the specific heat of dry air at constant pressure. In unstable conditions, the temperature decreases more than adiabatically, as shown by the red dashed line in figure 2.1(b). In this case, an air parcel will be warmer than its surroundings after an upward displacement, causing it to rise even further. The opposite happens under stable conditions, when the temperature decreases less than adiabatically (see blue dashed line in figure 2.1(c)). An air parcel is now colder than the surrounding after an upward displacement, and the parcel will experience a downward buoyancy force.

In this context, it is convenient to introduce the potential temperature θ, defined as "the temperature that would result if a parcel of air were brought adiabatically to a standard or reference pressure" (Garratt 1992, p. 22):

$$\theta = T \left[\frac{p}{p_{ref}} \right]^{-R_d/c_p}, \tag{2.1}$$

where R_d is the gas constant for dry air. The potential temperature is a popular variable for studying the ABL as it removes temperature variations caused by changes in pressure altitude. In this way, the potential temperature simplifies the interpretation of various stability regimes considerably, i.e., neutral, unstable or stable conditions are characterised by a potential temperature gradient being zero, negative or positive, respectively (see potential temperature profiles in figure 2.1). Although effects of moisture can easily be included in this framework by using the virtual potential temperature (Stull 1988, p. 7), the current thesis will always assume dry atmospheric conditions. This simplifies the study of wind-farm–ABL interactions and avoids more complex phenomena such as cloud formation and phase transitions, which are beyond the scope of this work. Throughout this manuscript, the modifier *potential* is sometimes neglected for brevity, but in general *temperature* is to be interpreted as *potential temperature*.

2.2 Anelastic and Boussinesq approximations

In its most general form, the flow in the atmosphere is described by the compressible Navier–Stokes equations (see, e.g., Stull 1988; Wyngaard 2010).

This set of equations covers the wide range of characteristic time and length scales present in atmospheric flows, i.e., from the largest planetary scales ($\sim 10^8$ m) through the synoptic and meso scales down to the dissipative scales of atmospheric turbulence ($\sim 10^{-3}$ m) (Klein 2010). Moreover, a variety of flow phenomena is supported in this set of equations, including three-dimensional turbulent motions, atmospheric gravity waves, Rossby waves, acoustic waves, etc. In the current work, meso-scale variability is disregarded and only effects with length scales smaller than meso scale ($\sim 10^4$ m) are taken into account. Furthermore, acoustic waves are physically insignificant as the energy density of these waves is very small. Numerically, it is desirable to eliminate sound-wave solutions from the system of equations as these waves impose a severe restriction on the maximum step for time integration. The classic, incompressible Navier–Stokes equations are a typical set of equations that does not allow the propagation of sound waves, and they are extensively used to describe engineering flows. However, these equations do not account for buoyancy effects and need to be generalised in order to study ABL dynamics. As discussed by Klein (2010), multiple reduced sets of equations have been derived to model various atmospheric flow phenomena, each one applicable to a specific range of characteristic length and time scales (see figure 2.2).

A first model that provides a suitable framework for studying wind-farm–ABL interaction is the anelastic model. This model was first proposed by Ogura & Phillips (1962) and was modified later on by several authors (see, e.g., Bannon 1996; Durran 1989; Dutton & Fichtl 1969; Lipps & Hemler 1982). The anelastic equations can be derived from the general set of equations based on three conditions (Bannon 1996). First, it is assumed that buoyancy is a dominant term in the vertical momentum equation, which simply states that stratification effects are important. Second, the characteristic vertical displacement η of an air parcel is of the same order of magnitude as or lower than the density scale height

$$H_\rho = \left(\frac{-1}{\rho} \frac{\mathrm{d}\rho}{\mathrm{d}z} \right)^{-1} = \frac{\kappa R_d T}{g}, \tag{2.2}$$

with κ representing the isentropic exponent, which is 1.4 for dry air. In the lower atmosphere, the density scale height is typically on the order of 10 km (Klein 2010; Wyngaard 2010, p. 177). The third condition states that the horizontal variations of density, temperature and pressure are small compared to their respective mean values at that height. The resulting set of equations is very similar to the general set of equations, except for the fact that the compressible continuity equation is replaced by the pseudo-incompressible equation

$$\boldsymbol{\nabla} \cdot (\rho_s \boldsymbol{u}) = 0, \tag{2.3}$$

where ρ_s is the density of a motionless, adiabatic base state that only depends on the height z. This equation eliminates acoustic waves while taking into

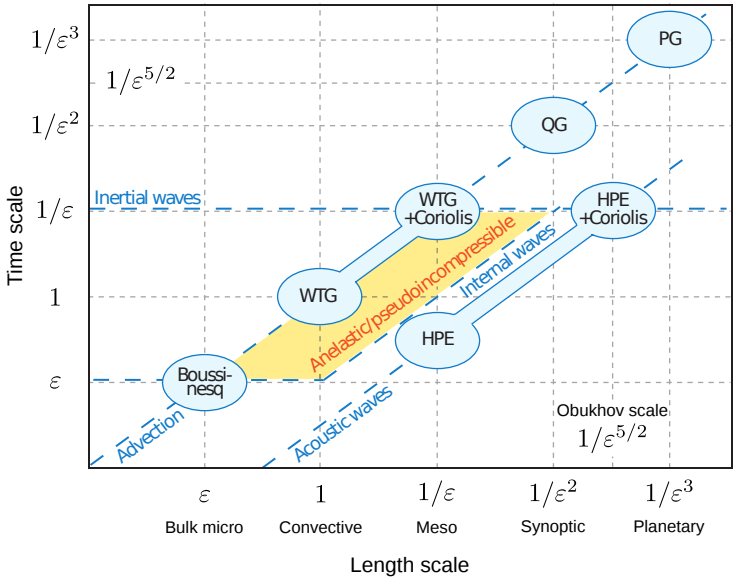

Figure 2.2: Scale-dependent models for atmospheric flow phenomena. WTG, weak-temperature-gradient; HPE, hydrostatic primitive equation; PG, planetary geostrophic; QG, quasi-geostrophic. Reprinted from R. Klein, Scale-dependent models for atmospheric flows, Annu. Rev. Fluid Mech. 42 (2010), p. 249. Copyright © 2010, Annual Reviews.

account the background density variation with height. For a detailed derivation and a thorough discussion of the anelastic model see, e.g., Bannon (1996).

For the present purpose, the anelastic approximation is in fact too general, i.e., vertical displacements on the order of 10 km only occur in deep convective or meso-scale atmospheric dynamics. The vertical scale of the ABL types considered here is considerably less than the density scale height, which means that the Boussinesq approximation (Spiegel & Veronis 1960) can be applied. This model is a simplification of the anelastic approximation for flows for which $\eta \ll H_\rho$, and it is the standard model used in ABL studies. Under the Boussinesq approximation, the background adiabatic base state is assumed to be independent of height, i.e., the base state is characterised by constant density ρ_0, temperature T_0 and potential temperature θ_0. Further, an important consequence of the Boussinesq approximation is that all density variations are neglected except when multiplied with the gravitational acceleration in the buoyancy term. This also implies that the continuity equation reduces to the requirement of a non-divergent flow, which states that volume rather than mass

is a conserved quantity (Lilly 1996). Finally, the equation of state is linearised to

$$\frac{\rho'}{\rho_0} = -\frac{T'}{T_0} = -\frac{\theta'}{\theta_0} \tag{2.4}$$

where the primes indicate variations with respect to the base state. Equation (2.4) gives a linear relation between ρ' and θ' and therefore allows either one of them to be used as independent variable. ABL studies typically look at θ', whereas some more fundamental studies of stably stratified turbulence use ρ'. For the remainder of this work, the Boussinesq approximation is used.

2.3 Atmospheric stability types

In the absence of radiation and latent heat release, the main driver for thermal stability effects is surface heating or cooling. Hence, ABLs are historically divided into three stability classes, based on the surface heating: neutral boundary layers (NBL), unstable or convective boundary layers (CBL) and stable boundary layers (SBL).

In a neutral boundary layer, there is no heat flux at the surface and the potential temperature is constant with height. Consequently, vertical motions are neither enhanced nor suppressed and buoyancy forces are completely absent. For this reason, the NBL is the simplest case of ABL flow and has been studied extensively in the past. A comprehensive overview of NBL modelling and a comparison between several models and observations have been provided by Hess & Garratt (2002*a*,*b*). Numerical simulations of the NBL have been performed by several authors, using both DNS (Coleman *et al.* 1990; Coleman 1999; Shingai & Kawamura 2004; Deusebio *et al.* 2014) and LES (Mason & Thomson 1987; Andren & Moeng 1993; Andren *et al.* 1994; Kosović 1997; Momen & Bou-Zeid 2016). The NBL is sometimes called the Ekman boundary layer, referring to the work of Ekman (1905) on the importance of Coriolis effects on boundary-layer flow in the ocean. Over land, NBLs are only found during a short transition period after sunset or in overcast conditions with very strong winds (see, e.g., Garratt 1992, p. 2; Stull 1988, p. 171). By contrast, offshore NBLs occur more often as the surface heat flux tends to be smaller at sea (Businger & Charnock 1983).

Convective boundary layers are caused by a positive heat flux at the ground or, in the presence of heat radiation and clouds, due to radiative cooling from the top. In both cases, less-dense air underlies more-dense air, thereby creating a statically unstable condition which gives rise to convective circulations and high turbulent intensities. The CBL is a typical stability regime found over land

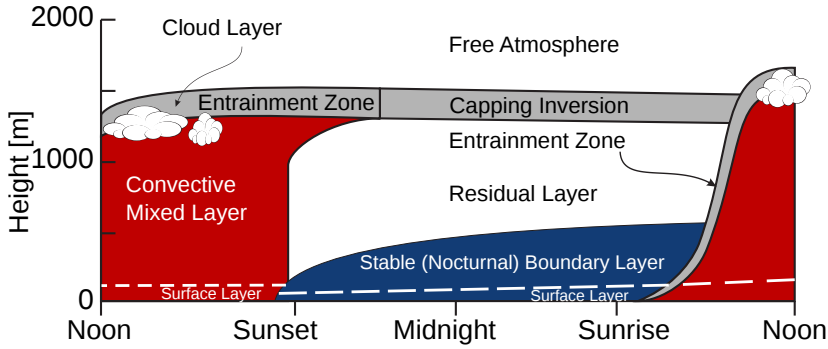

Figure 2.3: Boundary-layer structure during a diurnal cycle in a high pressure region over land. Adapted with permission of Springer, from "An introduction to Boundary Layer Meteorology", R. B. Stull (1988). © 1988, Kluwer Academic Publishers.

during daytime (as part of the diurnal cycle in high pressure regions), when the sun heats the surface (see figure 2.3). Over sea, the diurnal cycle is less pronounced and CBLs occur less frequent. LES of the convective boundary layer have been performed by, e.g., Moeng (1984); Moeng & Wyngaard (1988); Mason (1989); Nieuwstadt *et al.* (1993); Moeng & Sullivan (1994); Sullivan *et al.* (1994); Kim *et al.* (2003).

Stable boundary layers, by contrast, are formed by a negative surface heat flux. Here, the air near the surface is cooled, thereby generating a statically stable condition that tends to suppress vertical turbulent motions. Over land, SBLs start to grow after sunset when the surface is no longer heated by the sun (see figure 2.3), in which case they are called nocturnal boundary layers. SBLs can also occur in other circumstances, as long as the underlying surface is colder than the air, e.g., warm air advected over a cold body of water. SBLs are typically much thinner than neutral or convective cases, and the turbulent eddies are much smaller and weaker (i.e., lower turbulent intensities). Furthermore, SBLs have a high mean velocity shear and wind veer due to the low mixing in the boundary layer.

Below, two types of atmospheric boundary layers of particular interest to the current work are further elaborated, i.e., the conventionally neutral boundary layer (CNBL) and the stable boundary layer (SBL). Convective boundary layers will not be considered in depth in this work. The main reason is that wind farm underperformance is less likely to be an issue in the CBL due to the large boundary-layer height and high turbulent mixing. Instead, the focus will lie on shallow boundary layers, mostly associated with CNBLs and SBLs.

2.3.1 Conventionally neutral atmospheric boundary layer

The traditional classification into unstable, neutral or stable ABLs is purely based on the heat flux at the earth's surface. However, it was already found in the 1970s that the Brunt–Väisälä frequency, defined as

$$N = \sqrt{\frac{g}{H_\rho}} = \sqrt{\frac{g}{\theta_0}\frac{\partial\theta}{\partial z}} \tag{2.5}$$

and characteristic for the free-atmosphere stratification, appeared as a scaling parameter in expressions for the ABL height (Phillips 1977; Pollard *et al.* 1972; Thompson 1973). For this reason, an extended classification accounting for the effect of N was proposed for both neutral (Zilitinkevich & Esau 2002) and stable boundary layers (Zilitinkevich 2002; Zilitinkevich & Calanca 2000). For NBLs, the terms *truly neutral* and *conventionally neutral* were introduced for flows developing against a neutrally or stably stratified fluid, respectively (Zilitinkevich & Esau 2002).

Observation and simulation

Based on atmospheric data covering a period of more than 85 yr, Hess (2004) found that the truly neutral ABL forms an idealised case which "does not seem to exist in the atmosphere, or is so rare that it has not been well observed." In other words, neutral atmospheric boundary layers are almost always of the conventionally neutral type. As mentioned before, neutral boundary layers occur mostly offshore, and are only found over land during short transition periods or on very windy and cloudy days. Under certain conditions, CNBLs can form above large lakes or semi-enclosed seas (e.g., the Baltic Sea) due to boundary-layer air advected from land. Especially during daytime, when the land is heated by the sun, and in early spring, when the water temperature is still relatively low, the air will warm up over land and flow out over the colder water. The change in surface roughness and heat flux will result in the growth of a stable internal boundary layer, which eventually develops into a neutral boundary layer capped by an inversion layer. This flow regime has been observed and analysed in several studies (Csanady 1974; Garratt 1987; Garratt & Ryan 1989; Lange *et al.* 2004; Melas 1989; Smedman *et al.* 1997; Tjernström & Smedman 1993).

The first LES with conventionally neutral conditions actually considered oceanic bottom boundary layers (McWilliams *et al.* 1993) or limiting cases in the comparison between shear- and buoyancy-driven ABL flows (Moeng & Sullivan 1994; Sullivan *et al.* 1994). Later, Lin *et al.* (1996) also included capping

inversions when studying coherent structures and dynamics in the neutral boundary layer. However, the actual importance of the capping inversion and the free atmosphere stratification was only realised when Zilitinkevich & Esau (2002) discovered that the free stream Brunt–Väisälä frequency N forms a key scaling parameter for the ABL. Since then, a number of authors have studied the conventionally neutral boundary layer. For instance, following the suggestion of Zilitinkevich & Esau (2002), Hess (2004) presented a comparative study with several models of various degrees of sophistication, similar to previous work (Hess & Garratt 2002*a*,*b*) but now for conventionally neutral conditions. Zilitinkevich & Esau (2003, 2005) and Zilitinkevich *et al.* (2007*b*), on the other hand, continued to improve equilibrium height formulations and similarity theory predictions for the CNBL, and Esau (2004*a*,*b*) showed the importance of the inversion-layer height for flow properties such as turbulent kinetic energy and surface drag. Further, Taylor & Sarkar (2007, 2008*a*,*b*) investigated stratification effects in the bottom Ekman layer of the ocean, and Pedersen *et al.* (2014) recently examined the dynamic evolution of the CNBL towards a statistically steady-state, fully turbulent boundary layer.

Vertical structure

A schematic representation of the vertical structure of the CNBL is shown in figure 2.4. Above the CNBL lies the stably-stratified free atmosphere, where the flow is non-turbulent and the potential-temperature gradient is constant (typically ranging between 1 and 10 K/km (Sorbjan 1996)). In this region, the wind speed G results from the balance between the horizontal pressure gradient and the Coriolis force (Tennekes & Lumley 1972, p. 166):

$$\frac{1}{\rho_0}\frac{\partial p_\infty}{\partial x} = f_c G \sin\alpha, \qquad \frac{1}{\rho_0}\frac{\partial p_\infty}{\partial y} = -f_c G \cos\alpha \tag{2.6}$$

with α the angle between the geostrophic velocity vector and the x-axis, and $f_c = 2\Omega \sin\phi$ the Coriolis parameter (given the earth's rotation Ω and the latitude ϕ). Thus, the direction of the flow in the free atmosphere is perpendicular to the pressure gradient (see figure 2.4(b)). Near the surface lies the neutral, turbulent boundary layer. Here, the wind speed decreases towards the ground, and, as a result, rotates towards the pressure gradient due to the decreasing Coriolis force.

At the interface between the free atmosphere and the boundary layer, a thin layer with a strong increase in potential temperature can often be found, as indicated in figure 2.4(a). This so-called inversion layer or capping inversion has a large influence on the flow behaviour below, and effectively controls the boundary-layer height by limiting the penetration of turbulent gusts into the free

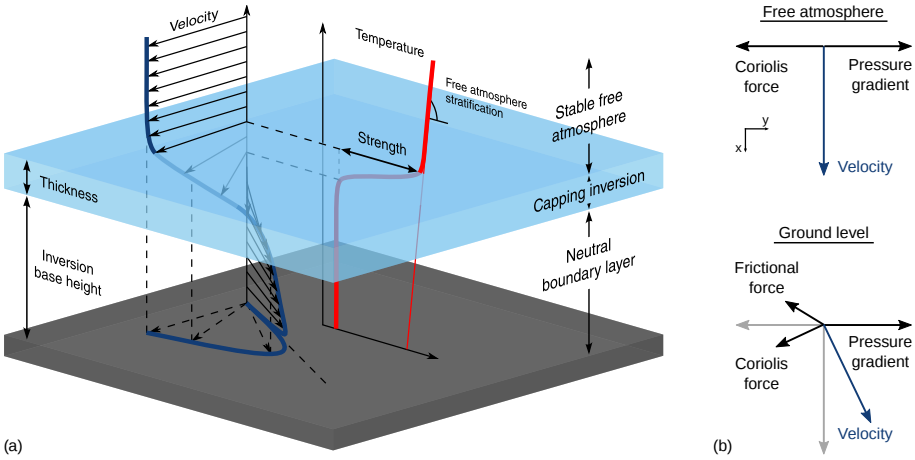

Figure 2.4: (a) Schematic representation of the conventionally neutral atmospheric boundary layer, showing a three-dimensional view of the profiles of potential temperature and velocity as a function of height, indicating the temperature jump in the capping inversion and the typical Ekman spiral in the boundary layer. Reprinted from D. Allaerts and J. Meyers, Large eddy simulation of a large wind-turbine array in a conventionally neutral atmospheric boundary layer, Phys. Fluids **27**, 065108 (2015) with the permission of AIP Publishing. (b) Plane view of the horizontal force balance in the free atmosphere and at ground level.

atmosphere. Moreover, the angle between the surface stress and the geostrophic wind velocity is larger than in the classical, unstratified Ekman layer (Kraus 1968; Weatherly & Martin 1978). However, most of the wind direction change occurs in the inversion layer, and the mean wind speed in the boundary layer is almost unidirectional.

In literature, basically two types of models are used to parametrise the potential temperature structure in inversion layers (see figure 2.5(a) and (b)). A first type are the zeroth-order jump models, which assume a piecewise linear temperature profile with the inversion layer represented as a discontinuity, i.e., with zero thickness (see, e.g., Lilly 1968; Betts 1973; Tennekes 1973). On the other hand, first-order jump model avoid the discontinuity by assuming a finite inversion thickness (Betts 1974; Deardorff 1979; VanZanten *et al.* 1999). However, both theoretical models are difficult to compare with field observations or numerical simulations and yield unsatisfactory results when used to estimate boundary-layer height, inversion strength, etc. For this reason, Rampanelli & Zardi (2004) introduced a smooth analytical curve for representing the vertical temperature

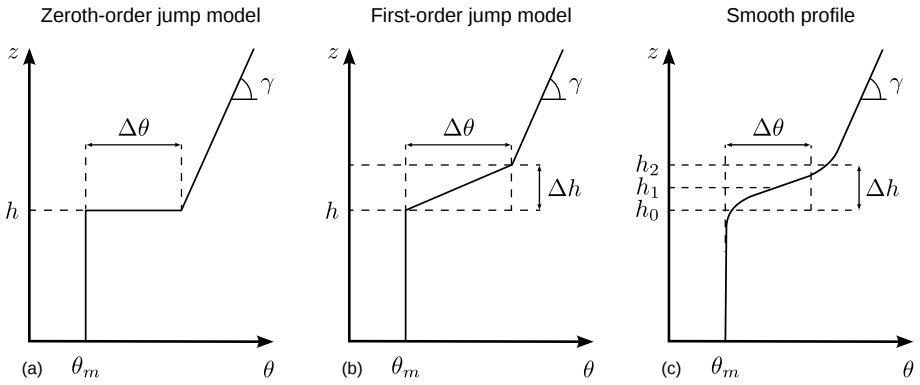

Figure 2.5: Vertical structure of the capping inversion, as parametrised by (a) zeroth-order jump models, (b) first-order jump models and (c) the smooth, analytical approach of Rampanelli & Zardi (2004).

structure, which is shown in figure 2.5(c) and defined as

$$\theta(z) = \theta_m + a\frac{\tanh(\zeta)+1}{2} + b\frac{\ln[2\cosh(\zeta)]+\zeta}{2}, \tag{2.7}$$

where ζ is a dimensionless height and a and b are fitting parameters. Rampanelli & Zardi specifically designed this function so that the parameters are directly related to the physical variables defining the inversion layer structure, such as the strength $\Delta\theta$, the thickness Δh and the height of the inversion base h_0, centre h_1 and top h_2 (see figure 2.5(c)). Also indicated are the temperature of the mixed layer θ_m and the lapse rate γ of the free atmosphere above the inversion.

Importance of the capping inversion

The influence of the capping inversion on the boundary-layer flow is to a large extent determined by two parameters, i.e., the height of the inversion base and the inversion strength. For instance, the effect of the capping inversion is negligible when it is situated above the equilibrium height of the truly neutral boundary layer. This idea was translated by Arya (1975, 1978) into the similarity parameter $h_* = |f_c|h/u_*$, which relates the actual height of the ABL with the Rossby–Montgomery scale $u_*/|f_c|$ (with u_* the friction velocity). Later, Hess (2004) found that the effect of the capping inversion becomes insignificant for $h_* > 0.15$.

The importance of the inversion strength for lower inversion heights was first predicted by Lilly (1968), stating that the rate of rise of the inversion base is inversely proportional to the inversion strength. Furthermore, Csanady (1974) predicted the existence of "an asymptotic depth h, at which no further entrainment takes place", and this height is determined by the strength of the capping inversion. He proposed an empirical formula that estimates this height as

$$h = A\frac{\theta_0}{g\Delta\theta}u_*^2 \tag{2.8}$$

with $A \approx 500$ an empirical parameter. This estimation was later confirmed by Tjernström & Smedman (1993) using airborne measurement data over the Baltic Sea.

Finally, Tennekes (1973) concluded that the potential-temperature gradient above the ABL plays no role when the initial inversion height or strength is very high. Similarly, when discussing the inversion strength, Hess (2004) mentioned that "the value of this jump may be more important than the precise value of N." Nevertheless, most formulations of the boundary-layer height only use the free-atmosphere Brunt–Väisälä frequency N as scaling parameter (Steeneveld *et al.* 2007; Zilitinkevich *et al.* 2007*b*) and completely ignore the effect of capping inversions.

2.3.2 Stable atmospheric boundary layer

The stable boundary layer is by far the most challenging and therefore the least understood element of the atmospheric boundary layer. Although the basic principles are well described in many standard textbooks on boundary layer meteorology (see, e.g., Stull 1988; Garratt 1992; Wyngaard 2010), many features of SBLs are still not fully understood, especially in the very stable regime (see, e.g., Fernando & Weil (2010) and Mahrt (2014) for a survey of remaining research questions). The fundamental difficulty of stable boundary layers and stably stratified turbulence arises from the buoyancy effect on the turbulent kinetic energy budget, i.e., while buoyancy creates turbulent energy under convective conditions, it destroys energy under stable conditions. This means that the turbulence shear production should now compensate for the energy loss due to both viscous dissipation and buoyant destruction in order to maintain turbulence. There is, however, an important difference in the nature of viscosity and buoyancy that considerably complicates the dynamic balance of turbulent kinetic energy in the stable boundary layer (Wyngaard 2010, p. 268). Viscous forces directly impact on the smallest eddies, enabling an equilibrium between viscous dissipation and the turbulent energy cascade. This equilibrium is stable in the sense that it quickly restores itself after a perturbation, e.g., too

much viscous dissipation would decrease the kinetic energy of the dissipative eddies, decreasing the dissipation rate and thereby restoring the energy balance. Buoyancy, on the other hand, selectively damps out the largest eddies. As a result, excessive stability extinguishes the large energy-containing scales and shuts down the energy cascade, which results in the total decay of turbulence.

Stably stratified turbulence

Stably stratified turbulence is highly anisotropic due to the limitation of vertical length scales. As a result, stratified flow is organised in thin layers with quasi-horizontal velocities and strong vertical shear (Riley & Lelong 2000). In order to characterise stratified turbulence, two important length scales are often used. First, the Ozmidov length scale is defined as (Lumley 1964; Ozmidov 1965)

$$L_O = 2\pi(\epsilon/N^3)^{1/2}, \tag{2.9}$$

with ϵ the dissipation rate and N the Brunt–Väisälä frequency (see equation (2.5)). The Ozmidov scale corresponds to the smallest eddies for which buoyancy effects are important, and divides the inertial subrange into an anisotropic part (from the large scales down to the Ozmidov scale) and an isotropic part (for smaller scales down to the Kolmogorov scale) (Khani & Waite 2014). Second, the buoyancy length scale is given by

$$L_b = 2\pi u_{rms}/N, \tag{2.10}$$

and represents the thickness of the shear layers in stratified turbulence (Waite & Bartello 2004; Lindborg 2006). These two length scales are important when designing numerical simulations of stably stratified turbulence. For instance, direct numerical simulation requires resolution of the Kolmogorov scale and therefore resolves the Ozmidov scale, while large-eddy simulations might use grid sizes large than this scale. However, several studies showed that, even in LES, the buoyancy length scale should be resolved in order to capture the stratified turbulent energy cascade (Waite & Bartello 2004; Lindborg 2006; Brethouwer *et al.* 2007; Waite 2011; Khani & Waite 2014).

The stability strength of stratified turbulence can be measured in a variety of ways. The flux Richardson number R_f measures the relative importance of buoyant destruction in the turbulent kinetic energy budget and is given by (Stull 1988, p. 175)

$$R_f = \frac{\text{buoyant destruction rate}}{\text{shear production rate}} = \frac{\dfrac{g}{\theta_0}\overline{w'\theta'}}{\overline{u_i'u_j'}\dfrac{\partial \bar{u}_i}{\partial x_j}}, \tag{2.11}$$

where $\bar{u}_i$ is the mean velocity and (u_i', θ') indicate turbulent fluctuations. Although the flux Richardson number is useful to determine whether turbulent flow will become laminar, it is undefined for laminar flows due to the dependence on turbulent correlations $\overline{u_i' u_j'}$. An alternative stability measure is found in the gradient Richardson number Ri, defined as

$$Ri = \frac{\dfrac{g}{\theta_0}\dfrac{\partial \bar{\theta}}{\partial z}}{\left(\dfrac{\partial \bar{u}}{\partial z}\right)^2 + \left(\dfrac{\partial \bar{v}}{\partial z}\right)^2}. \tag{2.12}$$

It is easy to show using dimensional analyses that the gradient Richardson number expresses the ratio of buoyancy forces to inertial forces (Wyngaard 2010, p. 224). Moreover, gradient transport theory allows to relate the two Richardson numbers using turbulent eddy diffusivities. Traditionally, it is understood that turbulence decays when Ri exceeds some critical value Ri_c, estimated to be about 0.20 to 0.25 (see, e.g., Stull 1988; Wyngaard 2010). However, the existence of a cut-off Richardson number is much debated in literature as numerous experiments, large-eddy simulations and direct numerical simulations demonstrate that turbulence is continuously maintained by the velocity shear even in very stable conditions (Zilitinkevich *et al.* 2007*a*, 2013).

Boundary-layer structure

While both flux and gradient Richardson numbers evaluate the local flow stability, stable boundary layers are usually classified based on the stability parameter z/L in the surface layer. The Obukhov length L is thereby defined as

$$L = -\frac{\theta_0 u_*^3}{\kappa g q_w} \tag{2.13}$$

with $\kappa = 0.4$ the von Kármán constant and q_w the surface heat flux. Note that the surface heat flux is used in kinematic form, i.e., with dimensions [Km/s] (Stull 1988, p. 48). The actual heat flux in energy per unit area per unit time is given by $\rho_0 c_p q_w$. Physically, L relates to the height above the surface at which buoyancy effects become dynamically important (Wyngaard 2010, p. 223).

Mahrt (1998, 1999) clarified the vertical structure of stable boundary layers for varying stability z/L with a schematic representation (see figure 2.6). Above the roughness sublayer, four different scaling regimes are identified. A first regime is found in the surface layer, where Monin–Obukhov similarity theory can be applied and the dimensionless turbulent fluxes depend only on z/L (see appendix A for an overview of the similarity theory by Monin & Obukhov

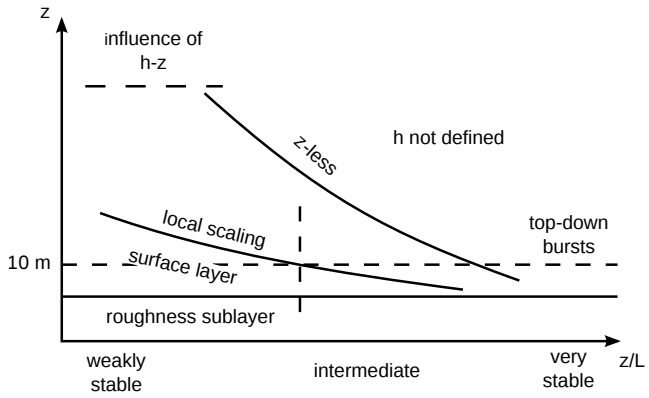

Figure 2.6: Idealised, stable boundary-layer flow regimes as a function of height and stability. The vertical dashed line indicates the value of z/L corresponding to the maximum downward heat flux. Reproduced from Springer Boundary-Layer Meteorology, Stratified atmospheric boundary layers, 90 (1999), p. 375, L. Mahrt. Copyright © 1999, Kluwer Academic Publishers. With permission of Springer.

(1954)). A second regime is found above the surface layer where the so-called local scaling of stable turbulence holds (Nieuwstadt 1984), i.e., the dimensionless quantities are described by a single parameter z/Λ, where Λ is an Obukhov length based on the local fluxes, i.e.,

$$\Lambda = -\frac{\theta_0 \tau^{3/2}}{\kappa g q_z}, \tag{2.14}$$

where q_z is the total vertical heat flux and $\tau = (\tau_{xz}^2 + \tau_{yz}^2)^{0.5}$ is the total vertical momentum flux. As a third regime, Nieuwstadt showed that the boundary layer structure does not depend explicitly on the height z in the limit of $z/\Lambda \to \infty$. This scaling regime is called z-less stratification (Wyngaard 1973), and arises when the vertical size of turbulent eddies is restricted so much that turbulence can not feel the presence of the surface. A fourth regime is sometimes found near the top of the boundary layer where the distance from the top $h - z$ becomes a relevant length scale (Holtslag & Nieuwstadt 1986). Note that not all scaling regimes are always present in the SBL, and that the thickness of these layers is expected to decrease with increasing stability as shown in figure 2.6 (Holtslag & Nieuwstadt 1986).

Mahrt (1998, 1999) further introduced two prototype stable boundary layers to examine the complexities of SBLs, though he stressed explicitly that "any attempt to divide the stable boundary layer into a few classes or states is an

oversimplification." The weakly stable boundary layer occurs in windy conditions when the effect of surface cooling is relatively low. In this case, turbulence is expected to be continuous (at least near the surface) and similarity theory is likely to hold in both the surface layer and the outer layer. Further, the downward heat flux decreases with decreasing stability in this regime due to the reduced temperature fluctuations. The very stable boundary layer, on the other hand, is characterised by weak winds and strong surface cooling. Turbulence is now weak and globally intermittent, i.e., the boundary layer is characterised by alternating periods of turbulent bursts and nearly-laminar flow. Moreover, the top of the boundary layer may not be definable due to strong turbulence at elevated heights. In this regime, the heat flux decreases with increasing stability due the limitation of vertical fluctuations. It follows that the downward heat flux must reach a maximum value somewhere between the weakly stable and very stable regime (see vertical dashed line in figure 2.6), and Malhi (1995) finds this maximum to occur at $z/L = 0.2$. This further implies that a given surface heat flux can occur at two different turbulent intensities, i.e., due to a weakly or a strongly stable case. This is called the dual nature of heat flux in stable conditions, and has been recognised in meteorology for some time (Taylor 1971; de Bruin 1994; Malhi 1995; van de Wiel *et al.* 2007; Basu *et al.* 2008).

The study of stable boundary layers is complicated even more by a multitude of physical aspects (Mahrt 1998), such as the increased influence of surface heterogeneity and terrain slopes, the possible importance of radiative flux divergence and the excitation of atmospheric gravity waves (see § 2.4.2 for a discussion on gravity waves). Further, SBLs frequently develop a low-level jet (LLJ), which is a thin stream of fast moving air relatively close to the ground. The velocity inside the jet is often supergeostrophic and leads to an elevated source of turbulence due to increased vertical shear. Low-level jets can have many possible causes, e.g., baroclinity associated with sloping terrain, coastal effects, frontal dynamics, etc. (Stull 1988, p. 521). Of particular interest to this work are LLJs formed by inertial oscillations, as these can occur in even the most simplified case without surface heterogeneity, topographical effects or baroclinity. This type of low-level jet is triggered by the collapse of the daytime boundary-layer turbulence due to the onset of surface cooling. As a result, the flow becomes decoupled from the surface and performs an inertial oscillations with period equal to $2\pi/f_c \approx 17.5$ h (see, e.g., Blackadar 1957; Shapiro & Fedorovich 2010; van de Wiel *et al.* 2010). Low-level jets have implications in numerous research fields and could also play an important role for wind-farm dynamics in the stable boundary layer.

Numerical simulation

The characteristic length scales in stratified turbulence are smaller than their neutral or convective counterparts, which makes numerical simulation of the SBL very challenging. Mason & Derbyshire (1990) were the first to use LES to simulate a stably stratified boundary layer, and they were followed by many others (see, e.g., Brown *et al.* 1994; Andren 1995; Kosović & Curry 2000; Saiki *et al.* 2000; Basu & Porté-Agel 2006; Zhou & Chow 2012; Sullivan *et al.* 2016). As the subgrid-scale model plays a very important role in the delicate energy balance of the SBL, many of these studies introduced new subgrid-scale models or modifications to existing models to better capture the physics of the SBL.

A leading initiative on atmospheric boundary layer research with particular focus on stable boundary layers is the GEWEX (Global Energy and Water Cycle Experiment) Atmospheric Boundary Layer Study (GABLS), established in 2001 (Holtslag 2006; Holtslag *et al.* 2012, 2013). The general objective of this programme is to improve the understanding and representation of the atmospheric boundary layer by means of model intercomparison studies. In the first GABLS intercomparison study, an idealised, moderately stable case was selected to assess the state-of-the-art of numerical models. Beare *et al.* (2006) presented the results of a large number of LES models for the GABLS1 case, which has become the standard benchmark case for moderately stable boundary layers. Since then, intercomparison studies GABLS2 and GABLS3 have followed, moving to more realistic cases including diurnal cycles, large-scale forcing, baroclinity and interactions with the surface. LES results of the GABLS2 and GABLS3 case are reported by Kumar *et al.* (2010) and Basu *et al.* (2012), respectively. Currently, GABLS4 is being conducted, focusing on extremely stable boundary layers on the Antarctic plateau (see, e.g., Bazile *et al.* 2016).

2.4 ABL aspects relevant for wind-farm flow

Wind-farm flow behaviour forms a fairly recent field of research, and not many studies looked at the large-scale response of the ABL. However, there are some similarities between wind-farm flows and other atmospheric phenomena that have been investigated thoroughly in the past. The current section introduces two aspects of the ABL that are relevant for wind-farm studies. First, the development of an internal boundary layer is discussed in § 2.4.1. Second, the concept of atmospheric gravity waves is introduced in § 2.4.2.

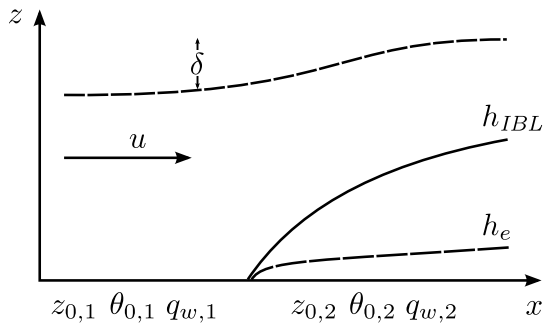

Figure 2.7: Schematic representation of the internal boundary layer (h_{IBL}) and the inner equilibrium layer (h_e) downstream of a step change in roughness (z_0), temperature (θ_0) and heat or moisture flux (q_w). Streamline displacement (δ) is also shown. Reproduced from Springer Boundary-Layer Meteorology, The internal boundary layer – A review, 50 (1990), p. 171, J. R. Garratt. Copyright © 1990, Kluwer Academic Publishers. With permission of Springer.

2.4.1 Internal boundary layer development

A fully developed turbulent boundary layer encountering a discontinuity in surface parameters such as, e.g., surface roughness, surface temperature or surface heat flux, does not adjust immediately at all heights. On the contrary, the adjustment takes place gradually, and the portion of the boundary layer influenced by the new surface condition increases with downstream distance. In this context, the internal boundary layer (IBL) is often defined as the layer within which the velocity and the turbulent stress are significantly affected by the changes in surface conditions. In the atmosphere, IBLs are often observed near land–sea transitions or over large lakes (see, e.g., Csanady 1974; Melas 1989; Smedman *et al.* 1997). Furthermore, plant canopies and urban terrain are also known to trigger IBL development (Belcher *et al.* 2003).

The flow behaviour after a surface discontinuity is represented schematically in figure 2.7. The internal boundary layer height h_{IBL} separates the free stream from the region influenced by the surface. This IBL height can be determined from numerical or observational data in various ways, based on either velocity or stress criteria. The simplest approach is to define h_{IBL} as the lowest level where the velocity reaches a given percentage of the upstream velocity at the same level (see, e.g., Garratt 1990, and references therein). This definition corresponds roughly to the point where the velocity is equally controlled by the incoming flow and the new surface conditions. Similarly, h_{IBL} can be defined based on a threshold value for the stress, identifying the height where the stress

rather than the velocity is considerably affected by the surface conditions. The latter height is typically higher than the estimate based on the velocity as velocity profiles adapt more slowly than stress. Bou-Zeid *et al.* (2004) provide additional methods based on the vertical gradients changing sign, which rather look for the point where the velocity or stress is insensitive to the underlying surface. Further, an inner equilibrium layer with height h_e is sometimes defined in addition to the IBL, marking the region where the flow is fully governed by the local boundary conditions. The flow above the IBL remains unchanged, except for a displacement δ of the streamlines due to the conservation of mass (Garratt 1990).

The IBL growth with streamwise distance resembles the turbulent boundary-layer growth over a smooth plate, for which Schlichting (1979, p. 638) showed that $h_{IBL} \sim x^{4/5}$ on the assumption of a 1/7-th-power law for the velocity profile, with x the downwind distance. Elliott (1958) was the first to study flow adjustment in a surface roughness transition close to the ground, using a logarithmic velocity profile. Although his formal solution of the IBL height is "extremely clumsy", Elliott found that the IBL growth follows a 0.8 power law for $x > 10^3 z_0$. Since then, a considerable amount of literature has been published on this flow transition (see, e.g., Garratt 1990, 1992, for a review). Several of these papers proposed new formulas for the IBL evolution, often predicting a growth rate slower than that found by Elliott (Blom & Wartena 1969; Walmsley 1989). A number of other authors have extended the traditional surface-layer approach to meso-scale flows, i.e., including Coriolis effects and the full depth of the ABL, and considered larger downwind fetches (Hunt *et al.* 2004; Jensen 1978; Taylor 1969; Wright *et al.* 1998). These studies predicted that the change in surface stress is accompanied by a change in surface wind direction. For example, it is well-known that the wind changes direction when it flows from the sea to the coast (Orr *et al.* 2005). Taylor (1969) further found that the length scales related to the adaptation of the wind direction and the turbulent stress are very different, i.e., the turbulent stress adapts rapidly to the new roughness and spreads up from the surface, whereas the changes in wind direction occur more uniformly across the boundary layer and take place at larger downstream fetches. Moreover, Hunt *et al.* (2004) showed that variations in surface roughness also affect the inversion height and the pressure field.

The reason why IBL growth is of importance to wind farms is the fact that, in large wind farms, the adjustment of the ABL to the increased drag by the wind turbines shows similarities with a surface roughness transition (Crespo *et al.* 1999*a*; Frandsen *et al.* 2006). In fact, Elliott's 0.8 power law is still commonly used in the wind energy community (see, e.g., Meneveau 2012). In a wind farm, the internal boundary layer is the region where the flow is controlled by both the incoming flow and the wind turbines (Chamorro & Porté-Agel 2011).

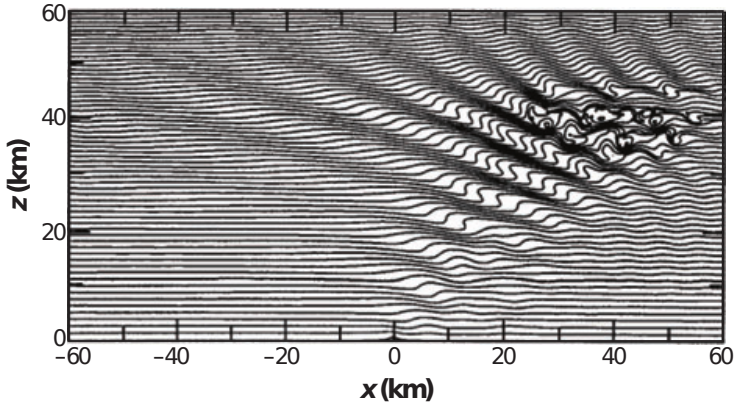

Figure 2.8: Vertically propagating gravity waves triggered by the flow over a two-dimensional ridge, visualised by contours of potential temperature. At high altitudes, non-linear effects occur and result in gravity wave breakdown. Adapted from P. K. Smolarkiewicz and L. G. Margolin, Atmos.-Ocean 35 (1997), p. 127 (their figure 4b). Copyright © 1997, Taylor & Francis.

The equilibrium layer, on the other hand, corresponds to the fully developed wind-farm flow and is sometimes viewed as the wind-farm wake.

2.4.2 Atmospheric gravity waves

A stably stratified fluid supports the formation and propagation of wave motions, with buoyancy acting as the restoring force. In the atmosphere, these waves are known as atmospheric or internal gravity waves. Excitation of gravity waves occurs when a stably stratified flow is displaced vertically, which can be caused by a variety of phenomena such as, e.g., flow over topography (mountains, ridges, hills, etc.), frontal passage, thunder storms or even turbulence. Figure 2.8 illustrates the concept of gravity waves triggered by topographical effects, visualised by contours of potential temperature. These waves are triggered by the flow over a two-dimensional ridge and cause a local disturbance of the flow field. The waves propagate upwards and are advected downstream by the mean background flow, although some perturbations are visible upstream of the ridge. At high altitudes, non-linear effects start to play a role and wave breakdown occurs due to local overturning.

Gravity waves form an important process for the dynamics of the atmosphere as they can transport momentum and energy over large distances. The eventual

breakdown of gravity waves can result in regions of clear-air turbulence, which may pose a hazard to aviation. Furthermore, pressure gradients induced by the gravity waves can cause severe wind storms along the lee side of large mountain ranges. Much research has focused on gravity waves triggered by mountains and ridges. For instance, Queney (1948) presented solutions for flow over bell-shaped ridges, and Smith (1980) considered the flow past an isolated mountain. Extended reviews of theoretical and numerical studies on mountain waves are given by (Gill 1982; Durran 1990; Teixeira 2014).

Smith (2010) postulated that gravity waves can also be triggered by very large wind farms. This findings follows from the previous section as well: combining the idea of a wind-farm induced IBL with the vertical flow displacement above the IBL mentioned by Garratt (1990), one arrives at the concept of wind-farm induced gravity waves. Stated differently, wind farms acts as *semi-permeable* mountains that redirect part of the flow upwards, thereby generating gravity waves similar to real *solid* mountains, but with a smaller amplitude. As the wave energy scales with the square of the flow displacement, the impact of these wind-farm induced gravity waves on meso-scale dynamics is expected to be rather small (compared to mountain waves), and their eventual breakdown is unlikely to cause problems for aviation. However, the induced pressure perturbations may play an important role on a regional scale and may considerably influence the boundary-layer flow inside and around the wind farm.

In the remainder of this section, the fundamental aspects of gravity waves are reviewed to facilitate a more thorough physical understanding of the waves excited by large wind farms. Most properties of gravity waves can be explained using linear theory, i.e., by linearising the Navier–Stokes equations for small perturbations. Several standard textbooks (see, e.g., Gill 1982; Nappo 2002; Holton 2004; Lynch & Cassano 2006) and reviews (Durran 1990; Teixeira 2014) cover linear theory of gravity waves, and the main ideas are summarised below.

Linear theory for gravity waves

For simplicity, it is assumed that the velocity (u_0, v_0) and the Brunt–Väisälä frequency N of the equilibrium state are independent of height, and that the Boussinesq approximation can be made. In the absence of rotation and friction, the governing equations for *small* perturbations (u_1, v_1, w_1) in velocity, p_1 in

pressure and θ_1 in potential temperature are

$$\frac{\mathrm{D}u_1}{\mathrm{D}t} + \frac{1}{\rho_0}\frac{\partial p_1}{\partial x} = 0, \tag{2.15a}$$

$$\frac{\mathrm{D}v_1}{\mathrm{D}t} + \frac{1}{\rho_0}\frac{\partial p_1}{\partial y} = 0, \tag{2.15b}$$

$$\frac{\mathrm{D}w_1}{\mathrm{D}t} + \frac{1}{\rho_0}\frac{\partial p_1}{\partial z} - \frac{\theta_1}{\theta_0}g = 0, \tag{2.15c}$$

$$\frac{\mathrm{D}\theta_1}{\mathrm{D}t} + w_1\frac{\mathrm{d}\theta_0}{\mathrm{d}z} = 0, \tag{2.15d}$$

$$\frac{\partial u_1}{\partial x} + \frac{\partial v_1}{\partial y} + \frac{\partial w_1}{\partial z} = 0, \tag{2.15e}$$

with the material derivative $\frac{\mathrm{D}}{\mathrm{D}t} = \left(\frac{\partial}{\partial t} + \boldsymbol{u}_0 \cdot \boldsymbol{\nabla}\right)$. These equations are sometimes called the polarisation equations as they give the relative phases and amplitudes of the various perturbation quantities. Equation (2.15) can be reduced to a single equation in w_1: taking the material derivative of equation (2.15c) allows the substitution of equation (2.15d), and the pressure is found by taking the divergence of the momentum equations (2.15a)–(2.15c) and applying the continuity equation. The result is

$$\left(\frac{\mathrm{D}}{\mathrm{D}t}\right)^2 \nabla^2 w_1 + N^2 \nabla_H^2 w_1 = 0, \tag{2.16}$$

with the horizontal Laplacian operator defined as $\nabla_H^2 = \frac{\partial^2}{\partial x^2} + \frac{\partial^2}{\partial y^2}$. Equation (2.16) is a simplified form of the more general Taylor–Goldstein equation for wave motions in a stably stratified shear flow (see, e.g., Nappo 2002, p. 26). Assuming a wave-like solution of the form $w_1 = \hat{w}(z)\exp[i(kx+ly-\omega t)]$, equation (2.16) can be written as

$$\frac{\partial^2 \hat{w}}{\partial z^2} + m^2 \hat{w} = 0 \tag{2.17}$$

where the vertical wavenumber m is given by

$$m^2 = (k^2 + l^2)\left(\frac{N^2}{\Omega^2} - 1\right). \tag{2.18}$$

The intrinsic frequency Ω is defined as the frequency of a wave relative to the flow, i.e., in a coordinate frame moving with velocity (u_0, v_0). The apparent frequency ω, observed in a fixed coordinate system, is related to the intrinsic

frequency as $\omega = \Omega + \boldsymbol{u}_0 \cdot \boldsymbol{k}$, with $\boldsymbol{k} = (k, l, m)$ the wave vector (i.e., the direction of phase propagation). Rewriting equation (2.18) in terms of Ω yields the dispersion relation

$$\Omega = \frac{N\kappa_H}{\|\boldsymbol{k}\|} = N\cos\varphi \tag{2.19}$$

with $\|\boldsymbol{k}\| = (k^2 + l^2 + m^2)^{0.5}$ and $\kappa_H = (k^2 + l^2)^{0.5}$, taking $\Omega > 0$ by convention. The dispersion relation is a very important equation as it contains several physical properties of gravity waves. First, it is observed that the Brunt–Väisälä frequency (or buoyancy frequency) is a fundamental parameter for gravity waves, being the frequency with which an air parcel would oscillate along a vertical axis. Second, equation (2.19) shows that the frequency of gravity waves is determined by the angle φ between the wave vector and the horizontal, independent of the wavenumber magnitude (contrary to wave types such as surface water waves or acoustic waves). Hence, the maximum frequency of gravity waves is the buoyancy frequency, attained by horizontally propagating waves, and the frequency decreases as the direction of phase propagation steepens. The dependence on the angle also has an intuitive explanation. For a vertically propagating wave, the parcels oscillate along a slanted path (perpendicular to the direction of phase propagation), and the factor $\cos\varphi$ arises due to the projection of gravity in the direction of motion and the reduction in apparent stratification (see Gill 1982, p. 132).

The dispersion relation directly specifies the group velocity of gravity waves, which is defined as $\boldsymbol{c}_g = (\partial\omega/\partial k, \partial\omega/\partial l, \partial\omega/\partial m)$. For now, consider a coordinate frame moving with the background velocity. In this frame, it can be shown that the group velocity is perpendicular to the wave vector, and that the vertical component of these two vectors point in the opposite direction (Gill 1982, p. 134). In other words, for a wave with an upward group velocity, the wave fronts are in fact moving downwards. This remarkable property of gravity waves makes numerical simulation, and specification of numerical boundary conditions in particular, a challenging task. For instance, Klemp & Durran (1983) argued that wave-advection radiation conditions, commonly used in lateral directions, cannot be used at the upper boundary of the domain. They showed that, as the wave fronts of an upward travelling wave move downwards, the wave-advection condition would require disturbances to be appropriately advected into the domain, which would result in unstable numerical algorithms.

The instantaneous distribution of velocity, pressure and potential temperature perturbations in a gravity wave field is clarified in figure 2.9, for a two-dimensional case with $k < 0$ and $m < 0$. The solid lines indicate the wave fronts where the velocity perturbations reach an extremum, and the direction is shown by the white arrows. According to the polarisation equations (2.15a) and (2.15e), the pressure perturbation reach an extremum on the same line, as indicated in

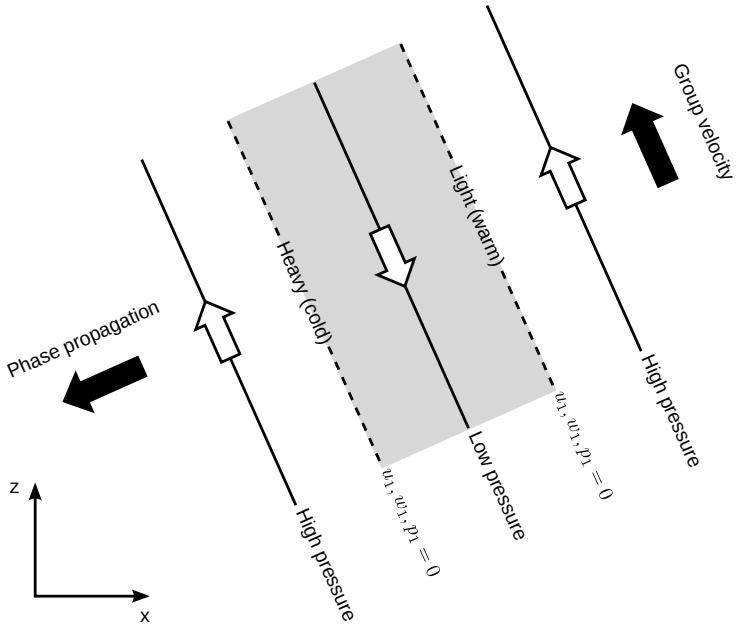

Figure 2.9: Schematic representation of an atmospheric gravity wave field in an x–z plane, indicating the instantaneous distribution of perturbations in velocity (u_1, w_1), pressure p_1 and potential temperature θ_1. Wave fronts (i.e., lines of constant phase) where u_1, w_1, p_1 reach an extremum and $\theta_1 = 0$ are shown as solid lines, and wave fronts where θ_1 reaches an extremum and $u_1, w_1, p_1 = 0$ are shown as dashed lines. The white arrows indicate the direction of the perturbation velocity, which is always parallel to the wave fronts. The black arrows indicate the direction of phase propagation and group velocity. This figure is based on similar representations in Durran (1990), Gill (1982, p. 133), Lynch & Cassano (2006, p. 216) and Holton (2004, p. 200).

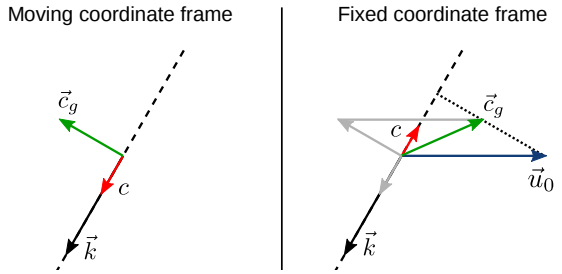

Figure 2.10: Vector diagram in a coordinate frame moving with the background flow and in a fixed coordinate frame, indicating the direction of the wave vector (solid arrow), the group velocity (green arrow) and the phase velocity (red arrow).

figure 2.9. Along the dashed lines, velocity and pressure perturbations are zero, and, according to equation (2.15d), the potential temperature perturbation has an extremum. Figure 2.9 only shows the instantaneous distribution. The evolution in time can be deduced as follows (Durran 1990). According to equation (2.15d), potential temperature perturbations arise when vertical velocity perturbations act against the background stratification. Since $w_1 < 0$ everywhere within the shaded region in figure 2.9, the temperature increases and the line of maximum temperature (indicated as warm) moves into the shaded region. Similar arguments hold for the other perturbation quantities, so the wave fronts all move in the direction of phase propagation as indicated by the black arrow. Note also that the air parcels oscillates perpendicular to the wave fronts, which means that gravity waves are transversal waves. Finally, the direction of the group velocity, i.e., the direction in which energy is transported, can be deduced from figure 2.9 using the fact that the energy flux vector is equal to $p_1 \boldsymbol{u}_1$ (Durran 1990). The correlation between p_1 and $\boldsymbol{u}_1$ indicates that energy is transported parallel to the wave fronts and upwards, as indicated by a black arrow. Hence, as discussed before, this wave field with downward travelling wave fronts transports energy upwards.

In a fixed coordinate frame with a constant background velocity, the phase velocity, i.e., the velocity of the wave fronts in the direction of the wave vector, and the group velocity are modified, as shown in figure 2.10. As the group velocity is a vector, its modification due to a background velocity is given by $\boldsymbol{c}_g + \boldsymbol{u}_0$. As a result, the group velocity is no longer perpendicular to the wave vector. The phase velocity, on the other hand, is not a vector quantity, and changes in a different way. The wave fronts continue to move along the wave vector, but the phase velocity is now the sum of the intrinsic phase velocity

$\Omega/\|\boldsymbol{k}\|$ and the projection of the background velocity on the wave vector (see figure 2.10):

$$c = \frac{\omega}{\|\boldsymbol{k}\|} = \frac{\Omega}{\|\boldsymbol{k}\|} + \boldsymbol{u}_0 \cdot \frac{\boldsymbol{k}}{\|\boldsymbol{k}\|} \tag{2.20}$$

Application to mountain waves

The linear theory elaborated above can be used to describe mountain waves. In the limit of small-amplitude waves, the mountain can be approximated by a horizontal surface imposing a boundary condition for the vertical velocity, i.e.,

$$w_1(x, y, 0, t) = \frac{\mathrm{D}h}{\mathrm{D}t} = \frac{\partial h}{\partial t} + \boldsymbol{u}_0 \cdot \boldsymbol{\nabla} h, \tag{2.21}$$

where h describes the shape of the mountain. In steady state conditions, this boundary condition is independent of time, which implies that the solution w_1 is also independent of time. Therefore, mountain waves are stationary waves with apparent frequency $\omega = 0$. Consequently, the phase velocity c as observed in a fixed coordinate is zero (see equation (2.20)). Further, the definition of the intrinsic frequency states that $\Omega = -\boldsymbol{u}_0 \cdot \boldsymbol{k}$.

For an infinite surface corrugation with a single wavenumber ($h = h_0 \cos k_0 x$), only one wave with wavenumber k_0 and intrinsic frequency $-u_0 k_0$ is excited. The maximum frequency is given by N, which means that two regimes are distinguished. If $|u_0 k_0| < N$, gravity waves propagate upwards without loss of amplitude. However, when $|u_0 k_0| > N$, no oscillatory solutions are possible and so-called evanescent mountain waves occur, the amplitude of which decays exponentially with height. An isolated two-dimensional ridge can now be viewed as the superposition of many (infinite) surface corrugations (this is equivalent to taking the Fourier transform), and the flow over a ridge excites a spectrum of wavenumbers instead of only one. The behaviour of the gravity waves now depends on the characteristic length scale of the ridge (e.g., the width L), and several flow regimes are identified depending on the relative size of L and u_0/N. For example, when $L \leq u_0/N$, the waves will be mostly evanescent, and energy is transported vertical and downwind. This situation corresponds to narrow ridges, weak stratification and strong winds. For typical atmospheric conditions of $u_0 = 10$ m/s and $N = 0.01$ s^{-1}, this behaviour occurs for characteristic length scales on the order of 1 km. On the other hand, when $L \geq u_0/N$ (i.e., a wide ridge with $L \sim 10$ km, or due to strong stratification and weak winds), the waves are aligned above the ridge and energy is transported purely vertical. For very large widths ($L \sim 100$ km), Coriolis effects will become important and affect the local wind direction. A detailed description of mountain waves and the different flow regimes can be found in Gill (1982, p. 274) and Nappo (2002, p. 59).

These different flow regimes will also occur for wind-farm generated gravity waves, depending on the width of the boundary-layer displacement. Hence, the impact of gravity waves on the boundary-layer flow and the power output in wind farms will depend on the wind-farm length and the flow blockage due to wind-turbine trust forces.

2.5 Summary

This chapter provided a brief introduction to boundary-layer meteorology and gave an overview of existing literature on various ABL types and flow aspects. It was found that the conventionally neutral boundary layer has not received much attention as the importance of overlying inversion layers and free atmosphere stratification has long been neglected. However, inversion layers may influence the boundary-layer flow significantly by controlling the boundary-layer height. Considerably more studies investigated the stable boundary layer, but numerical simulation of this ABL type remains very challenging. Finally, it was shown that a modification of the surface characteristics leads to the development of an internal boundary layer. The associated flow displacement above the IBL can excite gravity waves on the inversion layer and in the free atmosphere, which may disturb the boundary-layer flow.

Chapter 3

Simulation methodology

In this chapter, the numerical methods necessary to model atmospheric flows are reviewed. The Reynolds numbers encountered in such flows are typically very large, i.e., $Re \sim 10^7$ in the surface layer and even higher in the well-mixed layer (Stull 1988, p. 93). Direct numerical simulation (DNS) without any explicit modelling would need very fine grid resolutions to resolve the dissipative scales, which are on the order of 10^{-3} m for the Reynolds numbers encountered in the atmosphere (Wyngaard 2010, p. 17). Simulation of atmospheric turbulence in an entire wind farm on such fine grids is therefore still about 10^{12} times more expensive than what is currently possible with the state-of-the-art in high-performance computing. In large-eddy simulations (LES), the large, energy-containing scales are resolved, and the smaller dissipative scales are modelled, allowing for a coarser resolution than in DNS studies. For this reason, LES has been the preferred tool for modelling atmospheric turbulence, offering a reasonable trade-off between computational cost and spatial and temporal resolution.

The numerical simulations in this work are performed by the SP-Wind solver. This in-house research code was developed in a series of studies by Meyers & Sagaut (2007); Delport *et al.* (2009); Meyers & Meneveau (2010); Munters *et al.* (2016). In SP-Wind, time integration is performed using a classic four-stage fourth-order Runge–Kutta scheme and a Courant–Friedrichs–Lewy (CFL) number of 0.4. Further, SP-Wind uses pseudo-spectral discretisation schemes and periodic boundary conditions in the lateral directions (Canuto *et al.* 1988), and a fourth-order energy-conservative finite difference scheme for the vertical direction (Verstappen & Veldman 2003).

In the aforementioned studies with SP-Wind, the solver did not include buoyancy

effects, and was therefore restricted to neutral, pressure-driven boundary layers. The current chapter describes how the SP-Wind code is extended to allow simulations of various ABL types. Moreover, a verification and validation study of the extended research code is performed. To this extent, three case studies are considered, i.e., DNS of stratified turbulent channel flow and LES of atmospheric boundary layers under conventionally neutral and stable conditions.

This chapter is further organised as follows. The governing equations for large-eddy simulations including buoyancy effects are reviewed in section 3.1. Further, sections 3.2, 3.3 and 3.4 describe the wall model, the subgrid-scale model and the wind-turbine model implemented in SP-Wind, respectively. The verification and validation of the extended version of SP-Wind is documented in section 3.5, and a summary is provided in section 3.6.

3.1 Governing flow equations

In large-eddy simulations, the governing equations are filtered in order to obtain a separation between the large, energy-containing eddies and the small, dissipative eddies. The large scales are resolved on a numerical grid, whereas the impact of the small scales on the large-scale motions is modelled by a subgrid-scale model. Under the Boussinesq approximation, the filtered continuity, momentum and potential-temperature equations are given by

$$\frac{\partial \tilde{u}_i}{\partial x_i} = 0, \tag{3.1}$$

$$\frac{\partial \tilde{u}_i}{\partial t} + \tilde{u}_j \frac{\partial \tilde{u}_i}{\partial x_j} = \delta_{i3} g \frac{\tilde{\theta} - \theta_0}{\theta_0} + 2\epsilon_{ijk}\tilde{u}_j\Omega_k - \frac{1}{\rho_0}\frac{\partial \tilde{p}^\star}{\partial x_i} - \frac{1}{\rho_0}\frac{\partial p_\infty}{\partial x_i} - \frac{\partial \tau_{ij}^{sgs}}{\partial x_j} + f_i, \tag{3.2}$$

$$\frac{\partial \tilde{\theta}}{\partial t} + \tilde{u}_j \frac{\partial \tilde{\theta}}{\partial x_j} = -\frac{\partial q_j^{sgs}}{\partial x_j}, \tag{3.3}$$

where horizontal and vertical directions are indicated by $i = 1, 2$ and $i = 3$, respectively. Further, u_i represents the components of the three-dimensional velocity field and θ is the potential temperature, and the tilde represents the LES filtering operation. Throughout this work, the notations for coordinate directions (x_1, x_2, x_3) and (x, y, z) and velocity components (u_1, u_2, u_3) and (u, v, w) are used interchangeably. Furthermore, the LES filtering tilde is often omitted in the following chapters to simplify the notation.

The first term on the right-hand side of equation (3.2) represents the effect of gravity, i.e., the buoyancy force, and couples the momentum equation with the potential-temperature equation. The second term describes the influence of

the earth's rotation (Coriolis effects). In a coordinate frame with the positive x and y directions pointing east and north, respectively, the components of the angular velocity vector Ω_k are $[0, \Omega\cos\phi, \Omega\sin\phi]$, with ϕ the latitude and Ω the angular velocity of the earth. Using scale analysis, it can be readily shown that the terms involving Ω_2 are small compared to the other terms in the momentum equation (see, e.g., Gill 1982, p. 204; Wyngaard 2010, p. 209). It is therefore common practice to neglect these terms and to write the Coriolis forces as $f_c\epsilon_{ij3}\tilde{u}_j$ using the Coriolis parameter $f_c = 2\Omega\sin\phi$.

The filtered modified pressure is defined as $\tilde{p}^\star = \tilde{p} - p_\infty + \rho_0\tau_{kk}^R/3$, with p_∞ the mean background pressure and $\tau_{kk}^R/3$ the trace of the residual-stress tensor $\tau_{ij}^R = \widetilde{u_i u_j} - \tilde{u}_i\tilde{u}_j$. The gradient of the mean background pressure is related to the geostrophic wind speed G by the geostrophic balance, eq. (2.6). Further, the anisotropic part of the residual-stress tensor $\tau_{ij}^{sgs} = \tau_{ij}^R - \delta_{ij}\tau_{kk}^R/3$ and the residual heat flux $q_j^{sgs} = \widetilde{u_j\theta} - \tilde{u}_j\tilde{\theta}$ are modelled by a subgrid-scale model (see § 3.3). Finally, f_i represents the force exerted by the wind turbines on the flow (see § 3.4).

In equation (3.3), external heat sources due to radiation or latent heat release are set to zero as these are beyond the scope of this work. Furthermore, in view of the large Reynolds number of atmospheric flows, contributions due to viscous stress and heat flux are neglected. However, when using SP-Wind to perform DNS (see, e.g., § 3.5.1), the viscous terms $\nu\partial^2 u_i/\partial x_j^2$ and $\nu Pr^{-1}\partial^2\theta/\partial x_j^2$ are added to equations (3.2) and (3.3), respectively, and the subgrid terms are set to zero.

3.2 Wall stress and heat flux model

In turbulent wall-bounded flows, the length scale of the energy-containing eddies decreases near the wall. Therefore, a very fine grid is required near the wall in order to sufficiently resolve the near-wall motions. For the large Reynolds numbers encountered in atmospheric flows, resolving near-wall motions is too expensive, and the effect of the wall on the flow is modelled instead (see, e.g., Moeng 1984).

Provided that the first grid point lies within the surface layer, the wall stress $\tau_w = \rho_0 u_*^2$ and heat flux $q_w = -\theta_* u_*$ can be estimated from the velocity and potential temperature values using the Monin–Obukhov similarity theory (see appendix A):

$$u_* = \frac{\kappa M_1}{\ln(z_1/z_0) - \Psi_m(\zeta_1)}, \tag{3.4}$$

$$\theta_* = \frac{\kappa\,(\theta_1 - \theta_s)}{\ln(z_1/z_0) - \Psi_h(\zeta_1)}, \tag{3.5}$$

with θ_* the surface-layer temperature scale and M_1, θ_1 and z_1 the velocity, temperature and height of the first grid point, respectively. Further, z_0 is a surface roughness length and θ_s is the surface temperature. Stability effects are accounted for by the correction functions Ψ_m and Ψ_h, which depend on the Obukhov length (see eq. 2.13) through the stability parameter $\zeta_1 = z_1/L$. Equations (3.4) and (3.5) are implicit expressions for u_* and θ_* due to the dependence of the stability correction functions on ζ_1. Appendix A describes how to solve this set of equations depending on the applied boundary condition.

Finally, the estimates of the wall stress and heat flux are added as a body force in the first grid cell adjacent to the wall, thereby assuming that the stress is aligned with the velocity vector:

$$\tau_{w1} = -\rho_0 u_*^2 \frac{\hat{\tilde{u}}_1}{|\hat{\tilde{u}}|}, \qquad \tau_{w2} = -\rho_0 u_*^2 \frac{\hat{\tilde{u}}_2}{|\hat{\tilde{u}}|}, \tag{3.6}$$

with the horizontal velocity magnitude $|\hat{\tilde{u}}| = \left(\hat{\tilde{u}}_1^2 + \hat{\tilde{u}}_2^2\right)^{0.5}$. Locally averaged horizontal velocities, denoted with a hat, are used to match the average wall stress with the classic log law (Bou-Zeid *et al.* 2005). A filter width of 4Δ is used. Note that equations (3.4–3.5) and the Obukhov length L are also evaluated using locally averaged values, i.e., $M_1 = |\hat{\tilde{u}}|\,(z_1)$ and $\theta_1 = \hat{\tilde{\theta}}\,(z_1)$.

3.3 Subgrid-scale model

The subgrid-scale (SGS) model is an essential part of the LES strategy and is responsible for providing correct turbulent dissipation characteristics. In literature, numerous SGS models are available (see, e.g., Meneveau & Katz 2000, for a review) many of which rely on an eddy-viscosity model to calculate the residual stress from the resolved velocity, i.e.,

$$\tau_{ij}^{sgs} = -2K_{sgs}S_{ij}, \tag{3.7}$$

with $S_{ij} = 0.5\,(\partial\tilde{u}_i/\partial x_j + \partial\tilde{u}_j/\partial x_i)$ the filtered rate of strain and K_{sgs} the subgrid-scale eddy viscosity. The SGS heat flux is calculated in a similar manner from the resolved potential temperature profile using an eddy-diffusivity model

$$q_j^{sgs} = -K_{sgs}Pr_{sgs}^{-1}\frac{\partial\tilde{\theta}}{\partial x_j}, \tag{3.8}$$

with Pr_{sgs} the subgrid-scale Prandtl number. The popular Smagorinsky model (Smagorinsky 1963) combines equation (3.7) with a mixing-length approximation

for the eddy viscosity, i.e., $K_{sgs} = (c_s\Delta)^2 S$ with $S = (2S_{ij}S_{ij})^{1/2}$ the characteristic filtered rate of strain, $\Delta = (\Delta x \Delta y \Delta z)^{1/3}$ the local grid size and c_s the Smagorinsky constant.

The main difficulty of the Smagorinsky model is the specification of the model coefficients c_s and Pr_{sgs}. For isotropic turbulence with a spherical sharp cut-off filter in the inertial subrange, theoretical values for the model coefficients can be derived assuming that the energy spectrum follows the Kolmogorov $-5/3$ law, yielding $c_s \approx 0.17$ (Lilly 1967) and $Pr_{sgs} \approx 0.5$ (for a passive scalar) (Antonopoulos-Domis 1981). However, the isotropic values are not optimal when the flow becomes anisotropic due to, e.g., mean shear or stability effects. For high-Reynolds number wall-bounded flows, the length scale l is often damped using a wall damping function to obtain a log-law behaviour near the wall (Mason & Thomson 1992), i.e.,

$$l^{-n} = [c_s\Delta]^{-n} + [\kappa\,(z + z_0)]^{-n}\,. \tag{3.9}$$

Close to the wall, equation (3.9) causes a transition from an LES approach to an ensemble-averaged approach, while far from the wall the isotropic solution $l = c_s\Delta$ is retained. Meyers (2011) found optimal values of $c_s = 0.14$ and $n = 1$ for a neutral atmospheric boundary layer. However, the optimal combination appears to dependent on the grid cell aspect ratio. Furthermore, prescribing a constant Pr_{sgs} in conventionally neutral or stable conditions gave unsatisfactory results, and a more complex SGS model is needed to model these cases.

One possibility is to adopt a (scale-dependent) dynamic Smagorinsky model, in which the model coefficients c_s and Pr_{sgs} are calculated based on information from the resolved field (see, e.g., Meneveau *et al.* 1996; Porté-Agel *et al.* 2000; Bou-Zeid *et al.* 2005). This procedure is tuning-free and has been shown to give good dissipation characteristics, but the numerical implementation is rather complicated. Furthermore, the dynamic procedure does not change the eddy-viscosity character of the SGS model, which means that it is still implicitly assumed that the SGS stress tensor is aligned with the strain rate tensor. Gradient models overcome this shortcoming of the eddy-viscosity closure by using a Taylor expansion of the SGS stresses. In a series of papers, Lu & Porté-Agel (2010, 2013, 2014) developed a modulated gradient model for LES of atmospheric flows. Although their model showed promising results, it has not yet been used by other authors. Moreover, I was not able to reproduce their results, suggesting that the model performance depends to some extent on the discretisation.

For the different reasons given above, only eddy-viscosity models that do not require additional filtering operations are used. Below, two different methods are discussed.

3.3.1 Turbulent kinetic energy model

The first SGS model is the turbulent kinetic energy (TKE) model developed by Deardorff (1980), which defines the eddy viscosity as

$$K_{sgs} = c_m l \sqrt{k_{sgs}}, \tag{3.10}$$

where the SGS turbulent kinetic energy $k_{sgs} \equiv \frac{1}{2}\tau_{ii}^R$ follows from the additional transport equation

$$\frac{\partial k_{sgs}}{\partial t} + \tilde{u}_j \frac{\partial k_{sgs}}{\partial x_j} = K_{sgs} S^2 - K_{sgs} Pr_{sgs}^{-1} N^2 + \frac{\partial}{\partial x_j}\left(2K_{sgs}\frac{\partial k_{sgs}}{\partial x_j}\right) - c_\epsilon \frac{k_{sgs}^{3/2}}{l}. \tag{3.11}$$

The characteristic length scale l is given by

$$l = \min(\Delta, l_s), \tag{3.12}$$

with $l_s = c_l \sqrt{k_{sgs}} N^{-1}$ a stability related length scale. Finally, the subgrid-scale Prandtl number and the model coefficient c_ϵ depend on the length scale, i.e.,

$$Pr_{sgs}^{-1} = 1 + \frac{2l}{\Delta} \quad \text{and} \quad c_\epsilon = c_{\epsilon 1} + \frac{c_{\epsilon 2} l}{\Delta}. \tag{3.13}$$

For the model coefficients $(c_{\epsilon 1}, c_{\epsilon 2}, c_l)$ the values proposed by Stevens *et al.* (2000) are used: $(0.225, 0.705, 0.82)$.

The Smagorinsky model can be derived from the TKE model by setting $l = \Delta$ and assuming that the production term $K_{sgs}S^2$ and dissipation term $c_\epsilon k_{sgs}^{3/2}/l$ balance locally in equation (3.11). In that case, the Smagorinsky coefficient is given by

$$c_s = \left(\frac{c_m^3}{c_\epsilon}\right)^{1/4}. \tag{3.14}$$

In literature, c_m is often set to 0.1 (Deardorff 1980; Stevens *et al.* 2000). However, with $(c_{\epsilon 1}, c_{\epsilon 2})$ as specified above, equation (3.14) yields $c_s = 0.18$. In order to comply with the optimal value $c_s = 0.14$ found by Meyers (2011), c_m is set equal to 0.071.

3.3.2 Stability-dependent Smagorinsky model

As a second SGS model, the $\mathcal{S}_\sigma$ model proposed by Stevens *et al.* (2000) is adopted. This model is an extension of the classic Smagorinsky model that includes stability dependence without having to solve the TKE equation explicitly. The derivation starts from equation (3.11) and is very similar to that

of the standard Smagorinsky model, but now a balance is assumed between the production term, the dissipation term and the buoyancy term $-K_{sgs}Pr_{sgs}^{-1}N^2$. The SGS kinetic energy is then given by

$$k_{sgs} = \frac{c_m}{c_\epsilon}(lS)^2\left(1 - RiPr_{sgs}^{-1}\right), \tag{3.15}$$

with $Ri = N^2/S^2$ the gradient Richardson number. From equation (3.15) and the definition of the eddy viscosity, eq. (3.10), it follows that

$$K_{sgs} = (c_s l)^2 S\sqrt{1 - RiPr_{sgs}^{-1}}. \tag{3.16}$$

In this model, the minimum function in equation (3.12) for the characteristic length scale is replaced by the smoother geometric mean. Moreover, a classic wall damping of the length scale near the bottom surface similar to equation (3.9) is also included. Thus, the length scale is given by

$$l^{-n} = \Delta^{-n} + l_s^{-n} + \left[\kappa(z + z_0)\right]^{-n}, \tag{3.17}$$

where $n = 2$ is used in the current thesis. Further, $c_m = 0.1$, Pr_{sgs} and c_ϵ are defined by equation (3.13) and the values for $(c_{\epsilon 1}, c_{\epsilon 2}, c_l)$ of the TKE model are reused here.

3.4 Actuator disk model

Given the large domain sizes required to model entire wind farms, full resolution of the boundary layer around the turbine blades is infeasible. Instead, the effect of the turbines on the flow is computed using an actuator disk model (ADM). This model represents the wind turbines as porous disks and has been used in many LES studies (Jimenez *et al.* 2007, 2008; Meyers & Meneveau 2010; Calaf *et al.* 2010; Meyers & Meneveau 2013; Goit & Meyers 2015). In the current work, a non-rotating actuator disk method is applied, in which tangential forces are neglected. The performance of ADM has been investigated by Wu & Porté-Agel (2011) and later by Meyers & Meneveau (2013), and it is generally accepted that ADM provides an accurate representation of the turbulent mixing in the far wake behind a wind turbine ($x/D > 3$).

The total thrust force exerted by a turbine on the flow is modelled as (Calaf *et al.* 2010)

$$F_t = -\rho_0 \frac{1}{2} C_T' \langle \bar{u}_\perp^T \rangle_d^2 \frac{\pi}{4} D^2, \tag{3.18}$$

where D is the rotor diameter and $\langle \bar{u}_\perp^T \rangle_d$ is the local disk-averaged and time-filtered velocity perpendicular to the turbine disk, using a one-sided exponential

time filter. Equation (3.18) differs from classic actuator disk theory (Burton *et al.* 2001) in that it uses the axial wind speed at the rotor disk as velocity scale instead of an upstream undisturbed reference velocity. In wind farms with considerable interaction among turbine wakes, however, the definition of an upstream undisturbed velocity is ambiguous, and a disk-based approach is more appropriate. The disk-based thrust coefficient C_T' represents the overall effect of blade lift and drag forces on the air flow at the rotor disk, non-dimensionalised with the axial velocity at the rotor disk. Using one-dimensional momentum theory (Burton *et al.* 2001), the disk-based coefficient can be related to the classic thrust coefficient C_T:

$$C_T = \frac{16C_T'}{(C_T' + 4)^2}. \tag{3.19}$$

The thrust force, eq. (3.18), is first distributed constant over the disk area in a coordinate system in the turbine rotor plane. Subsequently, the wind-turbine forces f_i are obtained by filtering the distributed thrust force onto the LES grid by means of a Gaussian convolution filter. Details can be found in the studies of Calaf *et al.* (2010) and Meyers & Meneveau (2010).

The current dissertation only considers wind turbines operating in region II, i.e., below rated wind speed, when severe wind-farm underperformance occurs. In this region, conventional controllers vary the generator torque to maintain an optimal tip-speed ratio, which corresponds to using a constant disk-based thrust coefficient in ADM. The optimal value for a lone-standing wind turbine corresponds to the Betz limit (Burton *et al.* 2001), i.e., $C_T = 8/9$, and $C_T' = 2$. Following Meyers & Meneveau (2010), a typical value of $C_T' = 4/3$ is used throughout this thesis, which is equivalent to $C_T = 0.75$. For comparison, Nilsson *et al.* (2015) used $C_T = 0.812$ ($C_T' = 1.58$) to represent the turbines of the Lillgrund wind farm, and several studies of Horns Rev I used $C_T = 0.78$ ($C_T' = 1.45$) (see, e.g. Stevens *et al.* 2015*a*; Munters *et al.* 2016).

3.5 Verification and validation

The extensions to SP-Wind need to be verified and validated before reliable results of the wind-farm–ABL interaction can be obtained. The performance of the extended version is assessed using three benchmark cases. First, a stratified turbulent channel flow is simulated to verify the new implementation (§ 3.5.1). After that, SP-Wind simulations of the two ABL types that are considered in the current dissertation, i.e., a conventionally neutral case and a moderately stable case, are validated in subsections § 3.5.2 and § 3.5.3, respectively. For an

Table 3.1: Case set-up for the verification using stably stratified turbulent channel flow.

Domain size	$L_x \times L_y \times L_z = 4\pi h \times 2\pi h \times 2h$
Numerical grid	$N_x \times N_y \times N_z = 256 \times 256 \times 128$
Grid resolution	$\Delta x \times \Delta y \times \Delta z \approx 0.05h \times 0.025h \times 0.016h$
Friction Reynolds number	$Re_\tau = 180$
Friction Richardson number	$Ri_\tau = 0, 18, 60, 120$

extensive verification of the SP-Wind code and the actuator disk model, see Calaf *et al.* (2010).

3.5.1 Verification using stratified turbulent channel flow

The implementation of the additional equation for the potential temperature (eq. 3.3) and the coupling with the momentum equation is verified based on a study of stably stratified turbulent channel flows. Numerical simulation of this flow type is fairly straightforward, and many studies therefore rely on this prototypical case to investigate fundamental aspects of stratified wall-bounded flows, such as flow modification and relaminarisation (see, e.g., Garg *et al.* 2000; Armenio & Sarkar 2002; García-Villalba & del Álamo 2011). Furthermore, from a verification point of view, this simple case study proves to be very useful as it omits some of the more challenging aspects of ABL flows like capping inversions or Coriolis effects. Further, by performing DNS, the validation of the subgrid-scale model can be postponed to a later step.

García-Villalba & del Álamo (2011) present DNS of stably stratified channel flow at low and moderate Reynolds numbers for a wide range of Richardson numbers, and their results are used here as a reference. For the strongly stratified cases, they needed large computational boxes to sustain turbulence and to avoid artificial oscillations due to flow relaminarisation. In the current verification step, computational costs are kept low by only considering weak stratification with a low friction Reynolds number $Re_\tau = u_* h/\nu = 180$, where h is the channel half-width and ν is the kinematic viscosity. Table 3.1 summarises the set-up of the various DNS simulations. Four cases are simulated at friction Richardson number $Ri_\tau = \Delta\theta g h/\theta_0 u_*^2 = 0, 18, 60$ and 120, with $\Delta\theta$ the temperature difference between both walls and θ_0 a reference temperature. These simulations are set up to match cases A1, A2, A3 and A4a of García-Villalba & del Álamo (2011). The Prandtl number is $Pr = 0.71$ and corresponds to thermally stratified

air. The domain size is $4\pi h \times 2\pi h \times 2h$ with a numerical grid of $256 \times 256 \times 128$ grid points. In the wall-normal direction, a non-uniform grid with a tangens-hyperbolic distribution is used. All simulations are initialised with a parabolic velocity profile and a linear temperature profile. Random perturbations are added to the velocity profile to trigger turbulence. The simulations are run for 60 non-dimensional time units tu_*/h to reach a statistical steady state, after which statistics are collected over a period of 30 time units (60 for $Ri_\tau = 120$).

Figure 3.1 shows vertical profiles of velocity and temperature statistics, averaged in time and over horizontal planes (denoted by bars and angular brackets, respectively). The statistics in figure 3.1(a–d) are scaled by the friction velocity and the friction temperature, computed as

$$u_* = \left[\nu \left(\frac{\partial \langle \bar{u} \rangle}{\partial z}\right)_w\right]^{1/2} \quad \text{and} \quad \theta_* = -\frac{q_w}{u_*} = \frac{1}{u_*}\frac{\nu}{Pr}\left(\frac{\partial \langle \bar{\theta} \rangle}{\partial z}\right)_w . \tag{3.20}$$

The root-mean-square quantities in figure 3.1(e–f) are computed as $u_{rms} = \langle \overline{u'u'} \rangle^{1/2}$ and $\theta_{rms} = \langle \overline{\theta'\theta'} \rangle^{1/2}$, where the primes denote fluctuations in time, i.e., $u' = u - \bar{u}$ and $\theta' = \theta - \bar{\theta}$. The root-mean-square velocity and temperature are scaled by the bulk velocity u_b and the temperature difference $\Delta\theta$ across the channel, respectively.

Consistent trends of laminarisation are observed in all vertical profiles in figure 3.1 for increasing stratification. The mean velocity has a typical blunt shape in the passive scalar case ($Ri_\tau = 0$) and evolves towards a parabolic shape for increasing Richardson number. The mean velocity gradient near the wall, however, stays the same for all cases as the driving pressure gradient and thus the viscous wall stress are held constant. Further, the turbulent shear stress and velocity fluctuations are observed to decrease with increasing stratification. The buoyancy flux is almost unity except in the inner layer of the channel ($z/h < 0.1$) for $Ri_\tau = 0$. Increasing the stratification results in a strong decrease of the buoyancy flux in the core of the channel. Finally, temperature fluctuations decrease monotonically in the log-zone but increase in the core region for increasing Ri_τ.

García-Villalba & del Álamo compare their results at $Re_\tau = 180$ with the studies of Kim & Moin (1987) and Armenio & Sarkar (2002). For the sake of brevity, the results obtained with SP-Wind are only compared with data from García-Villalba & del Álamo. For $Ri_\tau = 0$ and 18, good agreement is found for all statistics throughout the channel. The case with stronger stability ($Ri_\tau = 120$) shows some small differences in the core region, especially in the profiles of heat flux (about 5 %) and root-mean-square temperature (about 7 %), which are attributed to the size of the numerical domain. García-Villalba & del Álamo hypothesise that relaminarisation of the flow occurs when the numerical

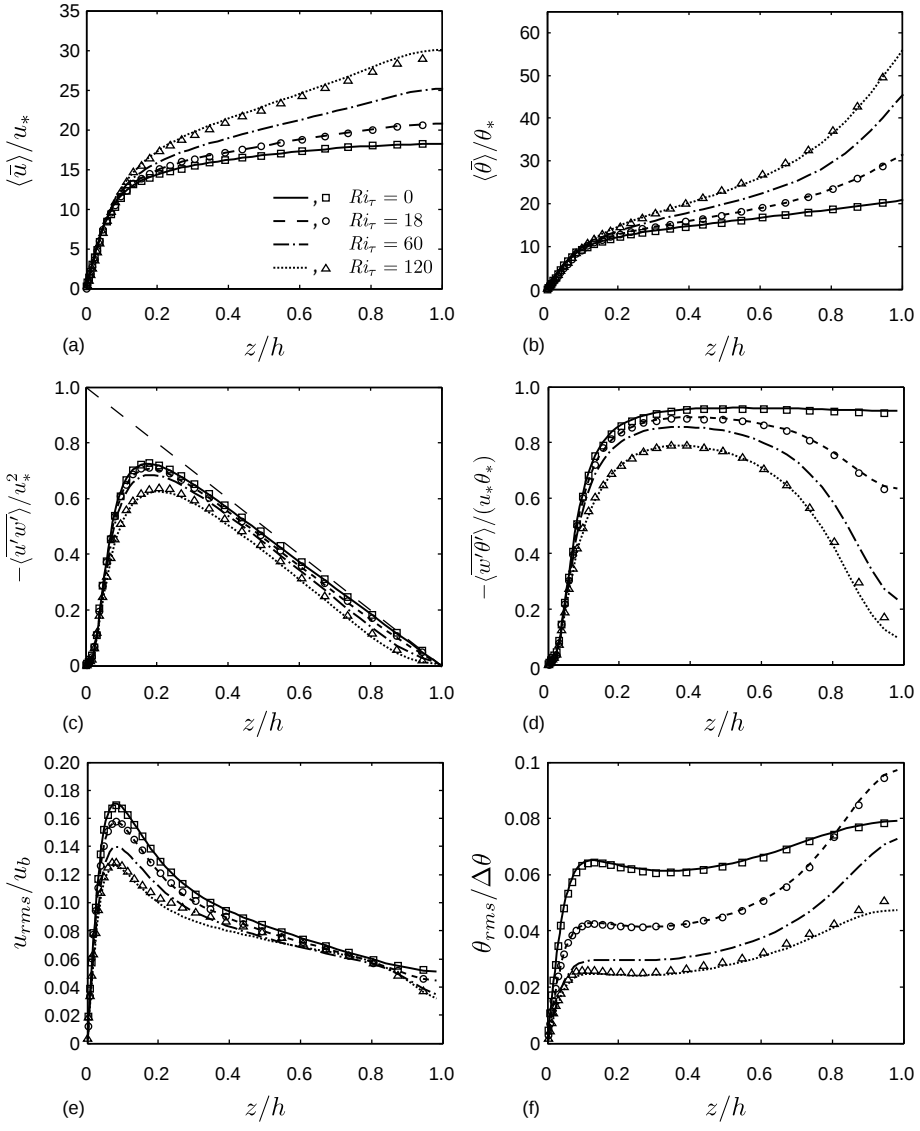

Figure 3.1: Vertical profiles of (a) mean velocity, (b) mean temperature, (c) vertical shear stress, (d) vertical heat flux, (e) root-mean-square velocity and (f) root-mean-square temperature, averaged in time and over horizontal planes. Results obtained from SP-Wind (plotted using lines) are compared with data from García-Villalba & del Álamo (2011) (plotted with symbols), for $Ri_\tau = 0, 18, 60$ and 120.

Table 3.2: Case set-up for the validation of conventionally neutral boundary-layer simulations.

Domain size	$L_x \times L_y \times L_z = 3 \text{ km} \times 3 \text{ km} \times 2 \text{ km}$
Numerical grid	$N_x \times N_y \times N_z = 256 \times 256 \times 256$
Grid resolution	$\Delta x \times \Delta y \times \Delta z \approx 11.7 \text{ m} \times 11.7 \text{ m} \times 7.8 \text{ m}$
Geostrophic wind speed	$G = 10 \text{ m/s}$
Coriolis parameter	$f_c = 10^{-4} \text{ s}^{-1}$
Surface roughness	$z_0 = 0.01 \text{ m}$
Free atmosphere lapse rate	$\gamma = 1$ and 10 K/km
Reference temperature	$\theta_0 = 290 \text{ K}$

domain is not able "to contain the minimal flow unit that is able to sustain itself as stratification increases." As a result, the channel flow alternates between laminar and turbulent flow regimes, resulting in low-frequency oscillations in the time evolution of global quantities. Such oscillations are also observed in the simulations performed with SP-Wind, making the time-averaged profiles very sensitive to the initial conditions and the averaging time. Better agreement could be obtained for $Ri_\tau = 120$ by using a large numerical domain according to case A4b of García-Villalba & del Álamo. For the present purpose, however, the agreement between both data sets is sufficient.

3.5.2 Validation of CNBL simulations

The ability of SP-Wind to perform large-eddy simulations of the conventionally neutral boundary layer is validated in this subsection. Contrary to the previous subsection, Coriolis forces, wall modelling and subgrid-scale modelling now need to be included. For the current case study, the simple stability-dependent Smagorinsky model (see § 3.3.2) is used.

Two simulations of neutral atmospheric boundary layers developing against a stable background with a lapse rate γ of 1 K/km and 10 K/km are performed. The results are compared with the simulations of Abkar & Porté-Agel (2013) and Pedersen *et al.* (2014). The numerical set-up is identical to cases n_{01} and n_{04} of Pedersen *et al.* and is summarised in table 3.2. In these cases, the geostrophic wind speed is $G = 10$ m/s, the Coriolis parameter is $f_c = 10^{-4} \text{ s}^{-1}$, the surface roughness is $z_0 = 0.01$ m and the reference temperature is equal to $\theta_0 = 290$ K. The numerical domain size is 3 km × 3 km × 2 km with 256^3 grid points, corresponding to a grid resolution of approximately 11.7 m × 11.7 m × 7.8 m.

Table 3.3: Parameters of the quasi-steady CNBL, including free atmosphere stratification γ (imposed), boundary-layer height h, friction velocity u_*, boundary-layer growth $\mathrm{d}h/\mathrm{d}t$ and minimal heat flux $q_{z,min}$, as computed by the SP-Wind code, the NCAR LES code (Pedersen *et al.* 2014) and the WiRE LES code (Abkar & Porté-Agel 2013). Boundary-layer height and friction velocity were not mentioned explicitly by Abkar & Porté-Agel and have been estimated from their figures 2 and 3.

	γ [K/km]	h [m]	$\mathrm{d}h/\mathrm{d}t$ [mm/s]	u_* [m/s]	$q_{z,min}$ [10^{-4} K m/s]
SP-Wind	1	690	2.0	0.34	−4.2
NCAR LES	1	708	2.1	0.37	−5.8
WiRE LES	1	671	–	0.36	–
SP-Wind	10	353	1.4	0.34	−13.8
NCAR LES	10	397	1.3	0.37	−25.5
WiRE LES	10	378	–	0.35	–

Velocity and temperature fields are initialised with a constant or linear profile equal to the geostrophic velocity and the background stratification. Furthermore, random perturbations with an amplitude of $0.1G$ are added to the velocity profile below 100 m to trigger turbulence. The simulations are advanced in time for 24 h, and statistics are collected over the last hour. Cases A2 and A4 of Abkar & Porté-Agel (2013) are almost the same, except for a coarser grid resolution (≈ 31 m $\times$ 18.6 m $\times$ 13 m) and possible differences in reference temperature and simulation time (both not mentioned explicitly). In SP-Wind, a Rayleigh damping layer is used to avoid reflection of gravity waves (Klemp & Lilly 1978), with a thickness of $L^{ra} = 500$ m and a Rayleigh damping coefficient of $\lambda^{ra}_{max} = 0.016\ \mathrm{s}^{-1}$.

Some parameters of the quasi-steady CNBL are given in table 3.3, including the boundary-layer height, the friction velocity, the boundary-layer growth and the minimal heat flux. In SP-Wind, the boundary-layer height is taken as the centre of the inversion layer h_1 and is determined through a best-fit analysis of the steady-state vertical temperature profile with the smooth test function in equation 2.7. Abkar & Porté-Agel calculate h as the height where the total momentum flux reaches 5 % of the surface value. Unfortunately, Pedersen *et al.* do not mention how they estimate the height. Nevertheless, the estimates of both height and growth of the quasi-steady CNBL obtained from SP-Wind agree very good with the values found in literature. Furthermore, friction

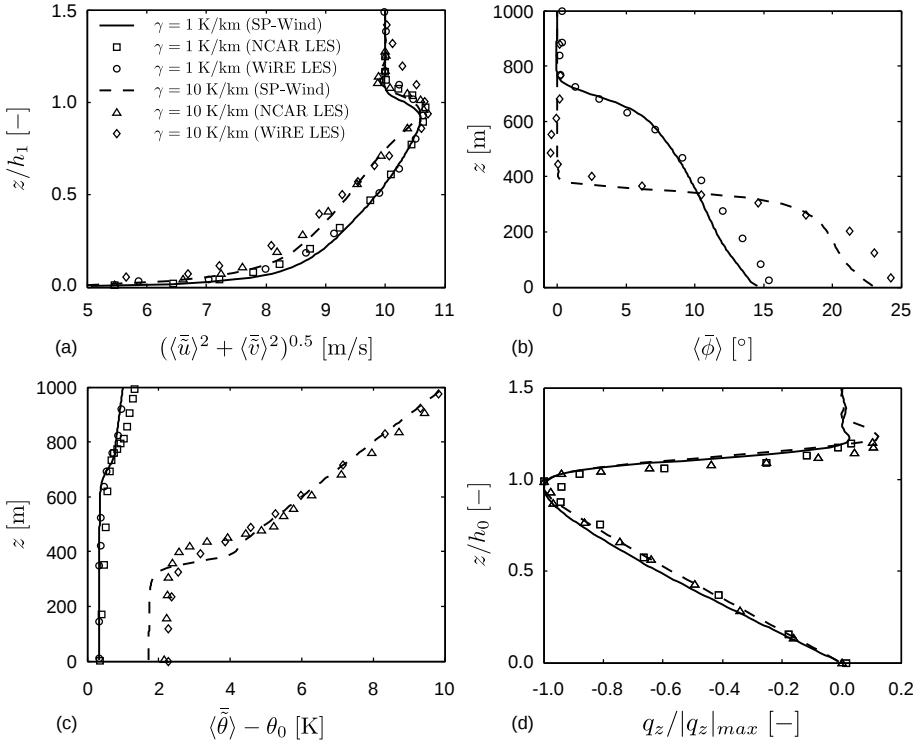

Figure 3.2: Vertical profiles, averaged over the horizontal directions and over the last simulation hour, of (a) horizontal velocity magnitude, (b) horizontal wind direction, (c) potential temperature and (d) kinematic heat flux. Results obtained from SP-Wind are compared with data from the NCAR LES code (Pedersen *et al.* 2014) and the WiRE LES code (Abkar & Porté-Agel 2013), for $\gamma = 1$ K/km and 10 K/km.

velocities are found to be nearly independent of free stream stratification and correspond reasonably well with the reference values. However, the minimal heat flux is underestimated by SP-Wind compared to the results of Pedersen *et al.*, indicating that current simulations predict less mixing of potential temperature.

Figure 3.2 compares vertical profiles of various flow variables obtained from SP-Wind with the profiles reported by Pedersen *et al.* and Abkar & Porté-Agel. In figure 3.2(a), good agreement is found for the horizontal velocity magnitude. Near the top of the boundary layer, the maximum wind speed in the distinct supergeostrophic jet matches very well. In the lower half of the boundary layer, SP-Wind predicts slightly higher velocities than the other LES codes,

but the bias is never higher than 5 % with respect to the values of Pedersen *et al.*. The mean wind direction is compared in figure 3.2(b). The geostrophic wind angle and the strong directional change in the inversion layer correspond reasonably well with the reference data, although the wind direction in lower half of the boundary layer is slightly lower than what is found in literature. The vertical profiles of potential temperature, shown in figure 3.2(c), indicate that temperature mixing is lower in SP-Wind, as noted before. This results in lower inversion layers and lower temperature of the mixing layer below. Finally, figure 3.2(d) shows the kinematic heat flux scaled by the maximum value. Good results are obtained when scaling z with the height of the inversion base h_0 (not with the inversion centre h_1), despite the difference in absolute values of the kinematic heat flux (see table 3.3).

Overall, very good agreement if found between the result obtained with SP-Wind and literature, especially considering the differences in discretisation schemes and subgrid-scale models. Therefore, it is concluded that SP-Wind can be used to provide reliable simulations of the CNBL.

3.5.3 Validation of SBL simulations

In addition to CNBLs, SP-Wind is used to simulate stable atmospheric boundary layers (see chapter 6). Therefore, a second validation study is performed using the SBL benchmark introduced in the first GABLS intercomparison study (Beare *et al.* 2006). As mentioned in § 2.3.2, stably stratified turbulence is difficult to simulate due to the reduced vertical length scales and the destruction of turbulence due to buoyancy. Although it is true that the inversion layer in the CNBL contains stratified turbulence as well, the SBL is found to be considerably more challenging. The reason is that, while in the SBL shear production is the only mechanism to sustain turbulence, TKE production in the inversion layer is aided by turbulent transport from below (Wyngaard 2010, p. 268).

To illustrate the increased complexity of SBLs compared to inversion layers, figure 3.3 shows the total fluxes of momentum and heat and the contributions due to resolved and subgrid-scale motions for the GABSL1 benchmark case (see below for a complete case set-up). These results have been obtained using the simple SGS model discussed in § 3.3.2 and used in the previous validation step. Further, a grid resolution of 12.5 m $\times$ 12.5 m $\times$ 5.0 m was chosen, which is very close to that used for the validation of CNBL simulations. Moreover, the stratification in the inversion layer in the CNBL benchmark cases is considerably stronger than anywhere in the GABLS1 case (compare, e.g., fig. 3.2(c) and fig. 3.5(b)). Nevertheless, figure 3.3 clearly shows that there is hardly any

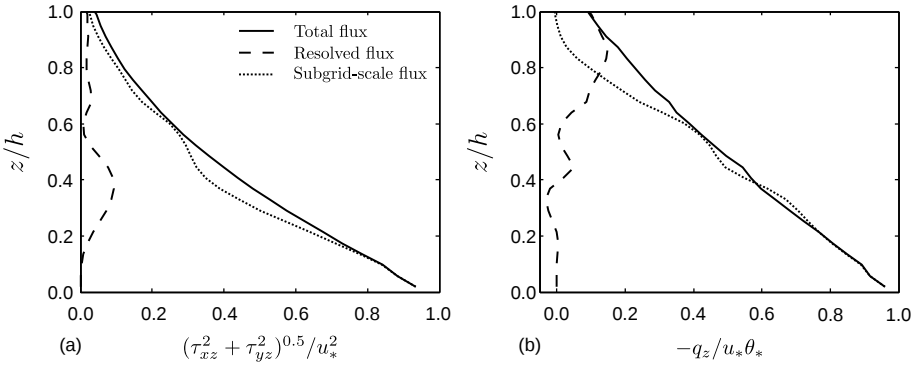

Figure 3.3: Vertical profiles of (a) momentum flux and (b) heat flux for the GABLS1 benchmark case, averaged over horizontal planes and over one simulation hour, using the simple stability-dependent Smagorinsky model and a grid resolution of 12.5 m × 12.5 m × 5.0 m. Results include total fluxes, resolved fluxes, and subgrid-scale fluxes.

resolved turbulence in the boundary layer, and that almost all momentum flux is due to the subgrid-scale stress. Furthermore, the simulated SBL was characterised by too low surface heat flux and friction velocity, poor mixing throughout the boundary layer and too low boundary-layer height (not shown here). Despite several attempts to tune the parameters c_m and n of the stability-dependent Smagorinsky model, I was not able to simulate a proper SBL with resolved turbulence using this model. However, using the SGS model with a prognostic TKE equation did produce successful results, and this approach is further analysed below.

Grid sensitivity study

The GABLS1 intercomparison study (Beare *et al.* 2006) simulates a moderately stable atmospheric boundary layer with a prescribed surface cooling. Table 3.4 summarises the case set-up of the GABLS1 benchmark simulation. The surface cooling rate is 0.25 K/h and a geostrophic wind speed of 8 m/s is imposed. Further, the Coriolis parameter is $f_c = 1.39 \times 10^{-4}$ s^{-1}, the surface roughness is $z_0 = 0.1$ m and the reference temperature is equal to $\theta_0 = 263.5$ K. Following Stoll & Porté-Agel (2008), the horizontal domain size is doubled compared to that used in the original GABLS1 benchmark to allow larger length scales in the domain, so $L_x = L_y = 800$ m. The domain height is set to $L_z = 500$ m, of which 200 m is occupied by a Rayleigh damping layer with a damping coefficient

Table 3.4: Case set-up for the GABLS1 benchmark simulation.

Domain size	$L_x \times L_y \times L_z = 800\ \text{m} \times 800\ \text{m} \times 500\ \text{m}$
Geostrophic wind speed	$G = 8\ \text{m/s}$
Coriolis parameter	$f_c = 1.39 \times 10^{-4}\ \text{s}^{-1}$
Surface roughness	$z_0 = 0.1\ \text{m}$
Free atmosphere lapse rate	$\gamma = 10\ \text{K/km}$
Reference temperature	$\theta_0 = 263.5\ \text{K}$
Surface cooling rate	$\text{d}\theta_s/\text{d}t = 0.25\ \text{K/h}$

Table 3.5: Set of simulations with varying amount of grid points and grid resolution used for studying grid resolution of the GABLS1 benchmark case.

	$N_x \times N_y \times N_z$	$\Delta x \times \Delta y \times \Delta z$ [m]
SBL1	$32 \times 32 \times 40$	$25.0 \times 25.0 \times 12.5$
SBL2	$32 \times 32 \times 80$	$25.0 \times 25.0 \times 6.25$
SBL3	$32 \times 64 \times 160$	$25.0 \times 12.5 \times 3.125$
SBL4	$64 \times 64 \times 40$	$12.5 \times 12.5 \times 12.5$
SBL5	$64 \times 64 \times 60$	$12.5 \times 12.5 \times 8.33$
SBL6	$64 \times 64 \times 80$	$12.5 \times 12.5 \times 6.25$
SBL7	$64 \times 64 \times 100$	$12.5 \times 12.5 \times 5.0$
SBL8	$64 \times 64 \times 160$	$12.5 \times 12.5 \times 3.125$
SBL9	$128 \times 128 \times 80$	$6.25 \times 6.25 \times 6.25$
SBL10	$128 \times 128 \times 160$	$6.25 \times 6.25 \times 3.125$

of $\lambda_{max}^{ra} = 0.016\ \text{s}^{-1}$. The initial temperature profile is constant ($\theta_m = 265\ \text{K}$) up to 100 m and then increases with 10 K/km. Initialising the velocity profile with a constant value like in Beare *et al.* yielded poor results, so instead a more realistic boundary-layer profile was used (the exact method is described in detail in § 4.1.3). The simulation is advanced for 9 h and statistics are collected over the last hour.

The GABLS1 study presents results using an isotropic grid with grid lengths of 12.5 m, 6.25 m, 3.125 m, 2 m and 1 m. Keeping in mind that this thesis aims at the simulation of entire wind farms, the question is how fine the grid must be to resolve turbulence and to produce realistic results. Therefore, a grid sensitivity study is performed using the set of simulations described in table 3.5.

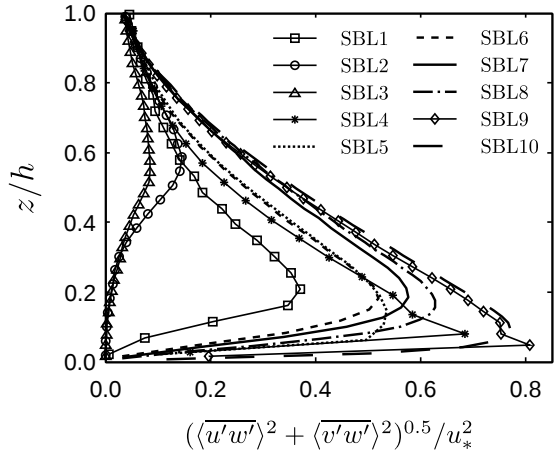

Figure 3.4: Vertical profiles of resolved momentum flux for the GABLS1 benchmark case, averaged over horizontal planes and over one simulation hour. An overview of the simulations is given in table 3.5.

A first selection of acceptable grid sizes is made based on the ability to resolve the momentum flux, as shown in figure 3.4. Two conclusions can be drawn from this figure, i.e.,

- Cases SBL2 and SBL3 clearly fail to resolve turbulence. Case SBL1 does seem to resolve some turbulence despite the fact that its vertical grid resolution is lower than that of case SBL2. However, the resolved part is still low compared to the other cases, so it is concluded that *horizontal grid sizes should be at least 12.5 m in order to sufficiently resolve turbulence.*
- Although many SBL studies use isotropic grid resolutions (Beare *et al.* 2006), the results in figure 3.4 show that isotropic grid sizes (i.e., cases SBL4 and SBL9) lead to sharp peaks in the resolved momentum flux near the wall. I suspect that this non-smooth behaviour points to resolution issues near the wall. Reducing the grid resolution in the vertical direction with respect to that in the horizontal direction solves this issue (compare, e.g., SBL9 with SBL6), which is probably due to the difference in horizontal and vertical discretisation schemes used in SP-Wind. Therefore, in order to avoid this issue, *numerical grids should have a finer resolution in the vertical than in the horizontal.*

Based on these rules, simulations SBL1-4 and SBL9 (i.e, all simulations marked by symbols) are dropped. Next, figure 3.5 shows vertical profiles of horizontal

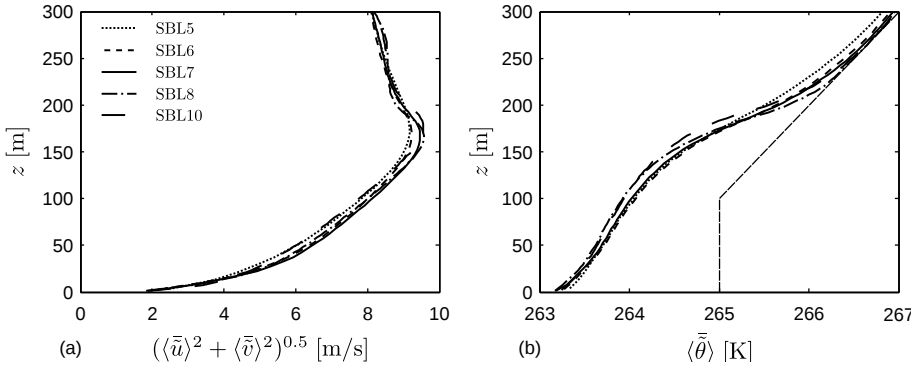

Figure 3.5: Vertical profiles of (a) horizontal velocity magnitude and (b) potential temperature for the GABLS1 benchmark case, averaged over horizontal planes and over one simulation hour, for cases SBL5-8 and SBL10 (see table 3.5 for the corresponding grid resolutions). The piecewise linear line in (b) indicates the initial temperature profile.

velocity and potential temperature for the remaining simulations, i.e., SBL5-8 and SBL10. The grid sensitivity of the mean velocity and temperature profiles is relatively low. It is observed that higher resolutions yield higher boundary-layer heights and stronger low-level jets, but the differences are small. In the remainder of this thesis, a grid resolution of 12.5 m $\times$ 12.5 m $\times$ 5.0 m, i.e., case SBL7, is chosen as a trade-off between accurate results and affordable computational costs. Note that this is the same resolution as was used for figure 3.3, which illustrates the gain of using the TKE model over the simpler, stability-dependent Smagorinsky model.

Validation with GABLS1

In a final step, the results of case SBL7 are validated with data from literature, including numerical simulations, empirical correlations, experimental observations and theoretical predictions. Vertical profiles of first and second-order statistics are shown in figures 3.6 and 3.7. Results of SP-Wind have been averaged over horizontal planes and over the last simulation hour. Further, the output of eleven LES models is reported in the intercomparison study of Beare *et al.* (2006) for grid resolutions between 2 m and 6.25 m. From this large data set, the profiles at a resolution of 2 m are used here for reference, for which the range of solutions is indicated in the figures below.

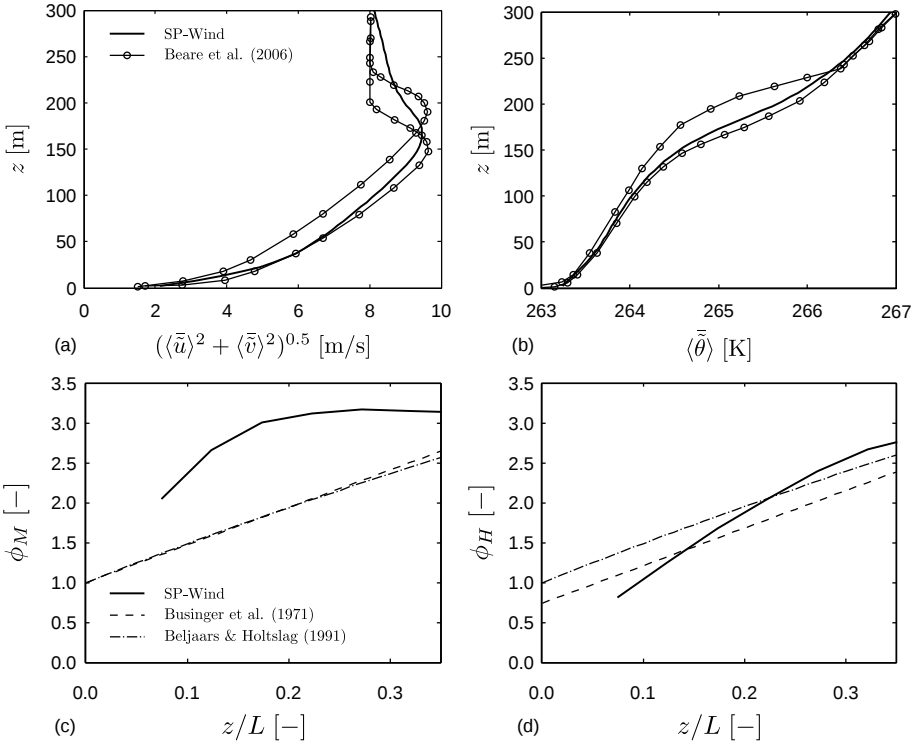

Figure 3.6: Vertical profiles of first-order statistics for the GABLS1 benchmark case, averaged over horizontal planes and over one simulation hour. (a) Horizontal velocity magnitude, (b) potential temperature, (c) non-dimensional shear and (d) non-dimensional temperature gradient. Results obtained from SP-Wind are compared with LES data from Beare *et al.* (2006), i.e., their range of 2 m resolution simulations, and with empirical correlations obtained by Businger *et al.* (1971) (see eq. (3.23)) and Beljaars & Holtslag (1991) (see eq. (3.25)).

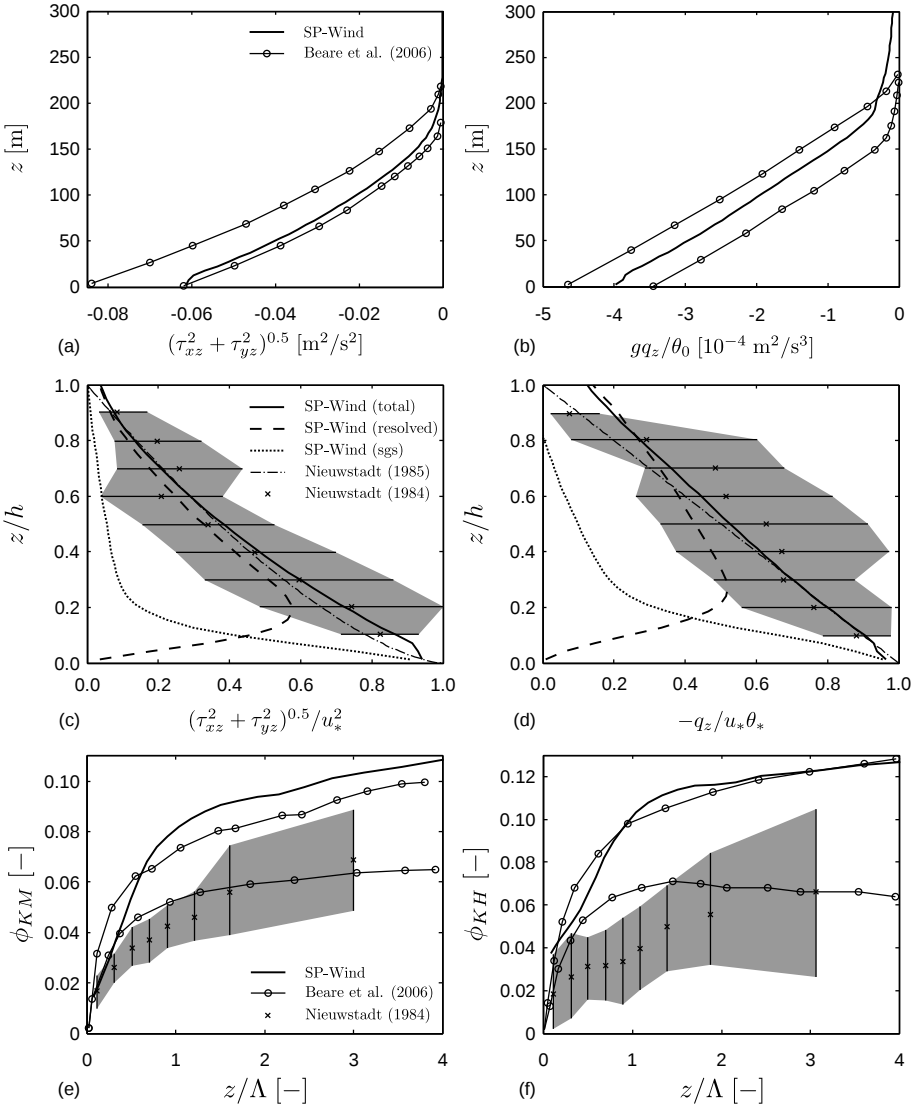

Figure 3.7: Vertical profiles of second-order statistics for the GABLS1 benchmark case, averaged over horizontal planes and over one simulation hour. (a) Dimensional momentum flux, (b) dimensional buoyancy flux, (c) non-dimensional momentum flux, (d) non-dimensional heat flux, (e) effective eddy viscosity (local scaling) and (f) effective eddy diffusivity (local scaling). Results obtained from SP-Wind are compared with LES data from Beare *et al.* (2006), i.e., their range of 2 m resolution simulations, with the theoretical model of Nieuwstadt (1985) and with experimental data from Nieuwstadt (1984) (grey area indicates standard deviation).

In figures 3.6(a–b), the horizontal velocity magnitude and potential temperature are compared with the range of LES data reported by Beare *et al.* (2006) (shown by the two lines with circles). Within the boundary layer, the results of SP-Wind fall perfectly within the range of data, even though a coarser grid was used. Above the low-level jet, the velocity decreases slower than what is found in literature. This was also observed in Beare *et al.* (2006) for lower grid resolutions.

The non-dimensional gradients of velocity and temperature profiles are key parameters in the surface layer and are therefore used in some studies to assess the performance of the SGS model (see, e.g., Basu & Porté-Agel 2006; Stoll & Porté-Agel 2008). The non-dimensional shear and temperature gradient are defined as

$$\phi_m = \frac{\kappa z}{u_*}\left[\left(\frac{\partial\langle\bar{\tilde{u}}\rangle}{\partial z}\right)^2 + \left(\frac{\partial\langle\bar{\tilde{v}}\rangle}{\partial z}\right)^2\right]^{0.5}, \tag{3.21}$$

$$\phi_h = \frac{\kappa z}{\theta_*}\frac{\partial\langle\bar{\tilde{\theta}}\rangle}{\partial z}. \tag{3.22}$$

Following Stoll & Porté-Agel (2008), these gradients are compared in figure 3.6(c–d) with the empirical correlation found by Businger *et al.* (1971), i.e.,

$$\phi_m = 1 + 4.7\frac{z}{L}, \tag{3.23}$$

$$\phi_h = 0.74 + 4.7\frac{z}{L}, \tag{3.24}$$

and with the alternative formulation of Beljaars & Holtslag (1991), i.e.,

$$\phi_m = 1 + \frac{z}{L}\left[1 + \frac{2}{3}e^{-0.35z/L}\left(6 - 0.35\frac{z}{L}\right)\right], \tag{3.25}$$

$$\phi_h = 1 + \frac{z}{L}\left[\left(1 + \frac{2}{3}\frac{z}{L}\right)^{0.5} + \frac{2}{3}e^{-0.35z/L}\left(6 - 0.35\frac{z}{L}\right)\right]. \tag{3.26}$$

The non-dimensional shear does not correspond well with the empirical relations, and suggest that SP-Wind overpredicts the velocity gradient in the surface layer. The magnitude of the non-dimensional temperature gradient, on the other hand, lies within the range of the empirical correlations. The issue of the velocity shear is related to the log-layer mismatch often found in LES simulations. As mentioned before, Meyers (2011) calibrated the Smagorinsky model for neutral atmospheric boundary layers to avoid this effect. However, the newly implemented TKE model is not yet optimally tuned. In fact, when

simulating a neutral ABL with the TKE model, the same problems near the wall were experienced as with a sub-optimal Smagorinsky model (not shown here). Better performance of the SGS model may therefore be obtained by tuning the model coefficients. In view of the good comparison of the velocity and temperature profiles with the GABLS1 data, tuning the TKE model is not pursued here and instead forms the subject of further research. Do note, however, that a correct representation of the velocity shear near the wall is very challenging, and that the comparison with empirical relations is an advanced criterion that was not even included in the GABLS1 intercomparison study of Beare *et al.* (2006).

The vertical fluxes of momentum and buoyancy in dimensional form are shown in figures 3.7(a–b) and compared with GABLS1 LES data. As with the velocity and temperature, the fluxes lie almost entirely within the range of data. The non-dimensional values are compared in figures 3.7(c–d) with the experimental observations of Nieuwstadt (1984) and the theoretical model proposed by Nieuwstadt (1985), i.e.,

$$\tau^2/u_*^2 = (1 - z/h)^{3/2}, \tag{3.27}$$

$$-q_z/u_*\theta_* = (1 - z/h), \tag{3.28}$$

with $\tau^2 = \tau_{xz}^2 + \tau_{yz}^2$. Good agreement is found both with the observations and with the theoretical profile. Figures 3.7(c–d) further include the contributions due to resolved and subgrid-scale fluxes, showing that a significant part of the turbulent fluxes is resolved down to $z = 0.2h$.

Finally, the effective eddy viscosity and diffusivity are defined as

$$K_m^{\mathit{eff}} = \tau \left[\left(\frac{\partial \langle \bar{\tilde{u}} \rangle}{\partial z} \right)^2 + \left(\frac{\partial \langle \bar{\tilde{v}} \rangle}{\partial z} \right)^2 \right]^{-0.5} \quad \text{and} \quad K_h^{\mathit{eff}} = -q_z \left[\frac{\partial \langle \bar{\tilde{\theta}} \rangle}{\partial z} \right]^{-1}, \tag{3.29}$$

and non-dimensionalised as

$$\phi_{KM} = \frac{K_m^{\mathit{eff}}}{\Lambda \tau^{1/2}} \quad \text{and} \quad \phi_{KH} = \frac{K_h^{\mathit{eff}}}{\Lambda \tau^{1/2}}. \tag{3.30}$$

According to the local scaling theory (see § 2.3.2), these non-dimensional quantities should only depend on z/Λ and approach a constant value for large z/Λ. As shown in figures 3.7(e–f), comparing the values obtained with SP-Wind with the observations of Nieuwstadt (1984) and the GABLS1 LES data, the results of SP-Wind fall just outside of the range of LES data from GABLS1. In addition, current LES results predict greater diffusion of momentum and heat than observed experimentally, as was also found by the GABLS1 study.

3.6 Summary

The current chapter described the extensions to SP-Wind necessary to model atmospheric boundary layers with thermal stability effects. First, an equation for the potential temperature was added and coupled to the momentum equation, and Coriolis forces were included. Further, the wall stress model was extended with standard correction functions. Two existing SGS models were described and have been implemented in the code. The extended code was verified using a stratified turbulent channel flow. Subsequently, LES of the CNBL and SBL were validated with data from literature. The verification of the code was successful and both validation cases showed very good agreement with literature. Therefore, it is concluded that the extended SP-Wind code is a reliable tool that can be used for simulations of wind-farm–ABL interactions.

Chapter 4

Wind farms in the CNBL: fully developed flow regime

In a fully developed flow regime, the energy extraction in large wind farms is dominated by downward turbulent transport of kinetic energy from the airflow above the farm (Calaf *et al.* 2010). Moreover, wind farms enhance vertical entrainment of air into the farm and increase the boundary-layer growth above the farm. The capping inversion has exactly the opposite effect, i.e., it slows down the turbulent entrainment process and prevents further deepening of the boundary layer (see § 2.3.1). Hence, it is to be expected that the inversion layer has an influence on the amount of energy that can be transported towards the turbines in a fully developed wind-farm boundary layer.

The aim of the current chapter is to assess the performance of large wind farms in the presence of capping inversions in a fully developed flow regime. To this extent, six LES simulations of the CNBL with wind farms are performed, in which the inversion layer height and strength are varied systematically. The study is restricted to offshore conditions where low inversion base heights commonly occur. For example, Brost *et al.* (1982) reported inversion heights as low as 400 m for the marine stratocumulus experiment, and similar heights were observed in several other measurement campaigns (Nicholls 1985; Grant 1986; Tjernström & Smedman 1993). Such low inversion layers will have stronger effects on wind-farm performance than higher land-based inversions.

The structure of this chapter is as follows. In section 4.1, some additional numerical aspects are discussed and the various LES cases are described. Next, the structure and general characteristics of wind-farm boundary layers under

conventionally neutral conditions are discussed in section 4.2. The influence of the capping-inversion parameters on the boundary layer and the wind-farm performance is explored in section 4.3. Subsequently, the observed differences are analysed by means of a closed analytical model, which is developed in section 4.4. Conclusions are summarised in section 4.5. The work discussed in this chapter is an excerpt from Allaerts, D. & Meyers, J. (2015) Large eddy simulation of a large wind-turbine array in a conventionally neutral atmospheric boundary layer, *Phys. Fluids* **27**, 065108, with the permission of AIP Publishing.

4.1 Numerical aspects

The SP-Wind solver is used to perform LES of conventionally neutral boundary layers with wind turbines. In the horizontal directions, periodic boundary conditions are applied so that the asymptotic limit of an "infinite" wind-turbine array is simulated. Further, the stability-dependent Smagorinsky model is used to model the subgrid-scale effects (see § 3.3.2). The simulations are driven by a constant pressure gradient related to the geostrophic wind speed by equation (2.6). The direction of the pressure gradient is regulated by a wind-angle controller, which is introduced in § 4.1.1. The case set-up is described in § 4.1.2, and special attention is paid to the initialisation of velocity and temperature profiles as discussed in § 4.1.3.

4.1.1 Wind-angle controller

The addition of Coriolis forces in the momentum equation causes the wind direction in the boundary layer to change with height (see figure 2.4). As a result, the effective wind direction at hub height is not known a priori, i.e., it depends on the turbulent dissipation and the wind-farm power production. In order to ensure the same geometrical pattern of wind turbines in all simulations, the wind speed at hub height should always be directed in the same way relative to the farm. This is achieved by regulating the direction of the driving pressure gradient through a wind-angle controller. The idea of such a controller was first proposed by Goit & Meyers (2013) and was later adapted by Sescu & Meneveau (2014). Similar to the approach of Sescu & Meneveau (2014), pseudo forces induced by a rotation of the reference frame are added to the momentum equation. The rotation speed is chosen equal to the rotation of the wind velocity at hub height, thereby cancelling out any change in the mean horizontal wind direction:

$$\omega = \frac{\phi^n(z_h) - \phi^{n-1}(z_h)}{\Delta t}, \quad \tan\phi(z_h) = \frac{\langle v(z_h)\rangle}{\langle u(z_h)\rangle} \tag{4.1}$$

Table 4.1: Case set-up for the fully developed, conventionally neutral wind-farm simulations.

	$h_{0(init)}$ [m]	$\Delta\theta_{(init)}$ [K]	$L_x \times L_y \times L_z$ [km×km×km]	$N_x \times N_y \times N_z$
REF	500	2.5	$6 \times 3 \times 1$	$160 \times 320 \times 256$
S00	500	0	$6 \times 3 \times 1.75$	$160 \times 320 \times 448$
S10	500	10	$6 \times 3 \times 1$	$160 \times 320 \times 256$
H02	200	2.5	$6 \times 3 \times 1$	$160 \times 320 \times 256$
H10	1000	2.5	$6 \times 3 \times 1.75$	$160 \times 320 \times 448$
H15	1500	2.5	$6 \times 3 \times 2.5$	$160 \times 320 \times 640$

with $\phi^n(z_h)$ the mean wind direction at hub height z_h at time step n. A first-order time filter with time constant σ is applied to average out rapid turbulent fluctuations. Further, a term proportional to the misalignment of the wind velocity vector is added to prevent steady state errors. The effective rotation speed of the reference frame is then given by

$$\omega_e = \bar{\omega} + \beta(\phi_h - \phi_{h,ref}), \tag{4.2}$$

The tuning parameters of the wind-angle controller are set to $\sigma = 3.33$ min and $\beta = 2\ \mathrm{h}^{-1}$. As the controller induces pseudo forces, this could be interpreted as a change to the Coriolis parameter f_c. However, the effective rotation speed is at least two orders of magnitude smaller than the Coriolis parameter at all times, so the influence of this rotation on the shear-stress profiles and the atmospheric boundary-layer height is negligible.

4.1.2 Case set-up

The influence of the capping inversion on large wind farms is investigated based on a suite of LES simulations with different inversion properties. Table 4.1 gives an overview of the parameters that vary amongst the different simulations.

For typical offshore values of friction velocity $u_* = 0.28$ m/s and capping-inversion strength $\Delta\theta = 2.5$ K (see Brost *et al.* 1982), and using equation (2.8), the equilibrium height is estimated to be about 450 m. Therefore, an inversion base height of 500 m and strength of 2.5 K is chosen for the baseline case REF. The other cases explore the effect of inversion strength and height, covering a range of 0 K to 10 K, and 200 m to 1500 m, respectively (see table 4.1). Note that, e.g., a height of 1500 m would be quite uncommon for offshore boundary

layers, but is included for sake of evaluating the parameters over a wide range. Cases S00 and H02 are chosen such that the initial inversion base height is below the equilibrium height, so that also non-equilibrium CNBLs are studied. The domain size amounts to 6 km and 3 km in streamwise and spanwise directions, and the height of the domain is set to 1 km in most cases. Cases S00, H10 and H15 are simulated in a higher domain in order to cope with large initial heights or strong boundary-layer growth.

As already mentioned in § 2.3.2, several studies revealed that simulations of stratified turbulence require resolution of the buoyancy scale $L_b = 2\pi u_{rms}/N$ to capture the stratified turbulent energy cascade (Lindborg 2006; Brethouwer *et al.* 2007; Waite 2011). Simulation of the strongly stable inversion layer is therefore a challenging numerical task that requires very fine vertical grid sizes. Khani & Waite (2014) found a critical grid spacing of $\Delta < 0.17L_b$ for LES with a standard Smagorinsky model. In the current chapter, grid sizes are varied amongst the LES simulations to guarantee a grid resolution of 37.5 m $\times$ 9.375 m $\times$ 3.9 m in all simulations. With a minimum buoyancy scale in all simulations above 30 m, the vertical grid resolution is sufficient to model the inversion layer with reasonable accuracy.

Atmospheric conditions are chosen to represent a conventionally neutral atmospheric boundary layer over sea. The drag due to ocean waves is simply modelled by a surface roughness length z_0, which is set to a representative value of 2×10^{-4} m (Sullivan *et al.* 2008). Similar values can be found in literature, e.g., Hess (2004) used values between 8×10^{-5} and 3×10^{-4} m to represent the sea surface. The potential temperature of the neutral boundary layer θ_m is 15 °C and the free atmosphere stratification is 1 K/km for all cases. The reference temperature θ_0 is taken to be equal to θ_m. Further, the atmosphere is assumed to be barotropic with a geostrophic wind speed $G = 10$ m/s. The surface Rossby number $Ro = G/z_0 f_c$ is equal to 5×10^8, corresponding to a latitude of $\phi = 43.43°$.

The wind farm under consideration consists of 48 turbines, characterised by a hub height $z_h = 100$ m and a diameter $D = 100$ m. The turbine grid comprises eight rows (at a distance $s_x D$) containing six turbines (at a distance $s_y D$), with $s_x = 7.5$ and $s_y = 5$. All simulations use $C'_T = 4/3$ (similar to Calaf *et al.* (2010)) and a time constant of 5 s for the time-filtered disk velocity.

4.1.3 Initial velocity and temperature profiles

In the absence of subsidence and heat radiation, the potential-temperature distribution in a CNBL is critically dependent on the heating history (Tennekes 1973). Consequently, the choice of initial condition for the potential temperature

has a direct impact on the outcome of a simulation. The typical linear potential-temperature profile used in most LES studies does not allow any control over the inversion height nor strength. Instead, the potential-temperature profile is initialised using equation (2.7), with an initial inversion thickness $\Delta h_{(\mathrm{init})} = 100$ m and the initial inversion height and strength as given in table 4.1.

Next to the potential-temperature profile, also the velocity needs to be carefully initialised. Below the capping inversion, the velocity profile is initialised with a similarity profile for neutral boundary layers (Zilitinkevich 1989) such that the transition time towards a conventionally neutral velocity profile is minimal, i.e.,

$$u_{\downarrow}(z) = \frac{u_*}{\kappa}\left[\ln\frac{z}{z_0} + f_u(\zeta)\right], \tag{4.3}$$

$$v_{\downarrow}(z) = -\frac{u_*}{\kappa} f_v(\zeta)\,\mathrm{sign} f, \tag{4.4}$$

where $f_u = 1.57\zeta - 2.68\zeta^2$ and $f_v = 13.2\zeta - 8.70\zeta^2$ are functions of the non-dimensional height $\zeta = z/h_0$. In the free atmosphere, the horizontal momentum equations describe an undamped harmonic oscillator (Schröter *et al.* 2013). Therefore, the velocity profiles $u_{\uparrow}$, and $v_{\uparrow}$ above the capping inversion are initialised with the prescribed geostrophic wind velocity, so that large undamped inertial oscillations are avoided. The free-atmosphere profile is merged with the neutral boundary-layer profile well below the region of the inversion layer using a tanh function:

$$u = u_{\downarrow}(z)\frac{1-\tanh[(\zeta-0.5)2h_0/\delta]}{2} + G\cos\alpha\frac{1+\tanh[(\zeta-0.5)2h_0/\delta]}{2}, \tag{4.5}$$

and similar for v. Thus, both layers are smoothly merged around $z = h_0/2$, in a merging region with width $\delta = 100$ m.

In order to trigger turbulence in the simulations, random divergence-free perturbations are added to the velocity profile. These perturbations have an amplitude of $0.1G$, and are added below 100 m only. In this way, the initial "non-physical" random noise is not directly interacting with the inversion layer. In order to study the development of a wind-farm boundary layer starting from realistic initial atmospheric conditions, the simulations first aim at reaching a stationary or quasi-stationary state under conventionally neutral conditions. According to Zilitinkevich *et al.* (2007*b*), equilibration is typically reached after 16 to 24 model hours. Thus, the initial condition is progressed in time for 20 hours before the wind farm is inserted. During this time, the initial random noise evolves into turbulence, and fills up the boundary layer under the capping inversion. After these initial 20 hours, the wind turbines are switched on (see further discussion next section).

4.2 General characteristics of the CNBL with wind turbines

In this section, the characteristics of the CNBL with an immersed wind farm will be discussed based on the LES results of the baseline case. First, in § 4.2.1, the growth of the CNBL in time is discussed. Subsequently, velocity profiles and the geostrophic angle are discussed in § 4.2.2, and stress profiles are presented in § 4.2.3.

4.2.1 Boundary-layer growth

First of all, the time-varying behaviour of the CNBL height both during the twenty-hour initialisation and the subsequent wind-farm simulation is discussed. In literature, several methods are proposed to estimate the height of the boundary layer; three of them are assessed here. A first estimate is based on the height where the turbulent shear stress vanishes, following Kosović & Curry (2000). They use the height where the turbulent stress equals 5 % of the wall stress (u_*^2), and linearly extrapolate this height to obtain the height for which the stress vanishes. The height h_M is calculated based on this procedure, but in the presence of wind farms, 5 % of the sum of wall stress and surface-averaged wind-turbine thrust force is used (u_{*hi}^2, with u_{*hi} the friction velocity above the wind farm – see eq. 4.6 for further details). Johnstone & Coleman (2012) suggest an alternative estimate h_G for the boundary-layer height, defined as the height where the mean horizontal velocity lines up with the geostrophic wind for the first time. A third estimate for the boundary-layer height originates from the zero- and first-order jump models (see also fig. 2.5) used for entrainment parametrisation in convective boundary layers (Lilly 1968; Tennekes 1973; Deardorff 1979; VanZanten *et al.* 1999). In these simplified models, the vertical heat flux is assumed to attain its minimum at the inversion base. As discussed further below, the heat flux in the CNBL shows similar behaviour, so the height h_T where the vertical heat flux attains its minimum serves as a third estimate for the boundary-layer height.

Figure 4.1 compares the three estimates of the boundary-layer height h_M, h_G and h_T with the base h_0, centre h_1 and top h_2 of the inversion layer as a function of time. The inversion characteristics h_0, h_1, and h_2 at every time step are determined through a best-fit analysis of the instantaneous vertical potential-temperature profile with the smooth test function in equation (2.7).

As discussed in § 4.1.3, simulations are started from random noise, and run without wind farm for 20 hours before the turbines are switched on. In figure 4.1,

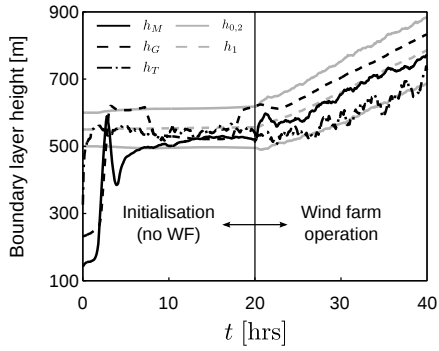

Figure 4.1: Time evolution of boundary-layer height estimators h_M, h_G and h_T and of the vertical structure of the capping inversion, including height of the base h_0, centre h_1 and top of the layer h_2, for the baseline simulation REF.

this development phase is clearly visible. In particular, it is observed that all measures for boundary-layer height start at an artificially low value, related to the fact that random noise is only added in the first 100 m of the domain. Subsequently, the boundary-layer estimates h_M and h_T indicate that the turbulent shear stress and the turbulent heat flux grow rapidly towards the inversion layer. After approximately 2.5 hours, the different measures for the boundary-layer height reach the inversion layer. During the remaining time, the boundary layer slowly evolves towards an equilibrium state. Near the end of the initialisation period, the boundary-layer growth attains a small constant value (less than 0.14 mm/s) indicative of quasi-stationary behaviour. Moreover, it was observed that the relative difference between the hourly averaged velocity and shear-stress profiles is less than one, and three percent, respectively (not shown here). It is thus reasonable to assume that the flow has reached quasi-stationary conditions, and the development of the wind-turbine array boundary layer can be studied starting from this boundary-layer state.

When the wind turbines are switched on, an additional transient occurs. After approximately 10 hours of wind-farm operation, the boundary layer stabilises again into a regime of small, but constant growth. The effective growth rate in the last 10 hours of the simulation is small (about 3 mm/s). Therefore, to discuss and compare mean flow profiles, time statistics are collected over the last 10 hours.

Examining the estimators in more detail during wind-farm operation in figure 4.1 shows that h_M corresponds reasonably well with the centre of the inversion layer h_1, whereas h_G generally lies between h_1 and h_2. The estimation based

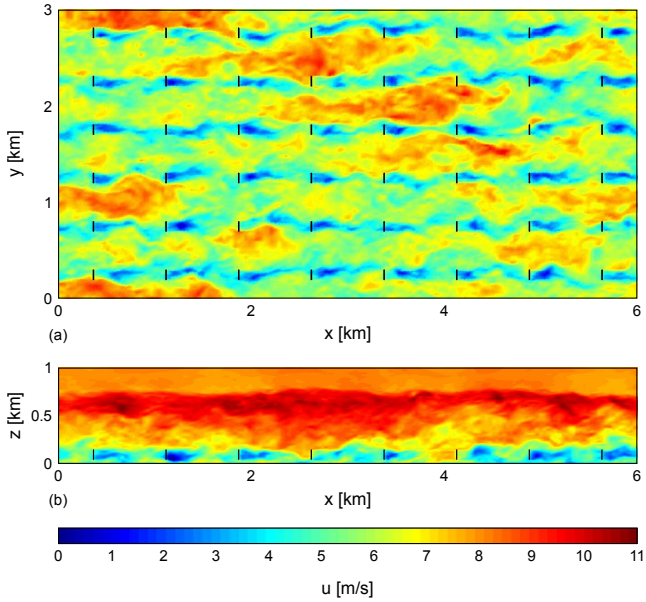

Figure 4.2: Instantaneous contours of streamwise velocity from LES for baseline case REF; (a) An x–y plane at $z = 100$ m through the wind-turbine centres (The location of the wind-turbine disks are shown with vertical black lines). (b) An x–z plane cutting through the middle of a column of wind turbines.

on the turbulent heat flux h_T shows good agreement with the inversion base height. Following these observations, the top of the CNBL with wind turbines is estimated with h_1 in the remainder of this study.

Finally, a sample of instantaneous velocity profiles after 35 hours of simulation is shown in figure 4.2, in which the black lines indicate the locations of the wind-turbine disks. In figure 4.2(a), the x–y plane is taken at $z = 100$ m and cuts through the wind-turbine centres, clearly showing the velocity deficit in the wakes behind the turbines. Further, elongated high-speed streaks are visible along the mean-flow direction. Figure 4.2(b) shows an x–z cut through the middle of a column of wind turbines. Here, strong ejection and sweep motions are observed up to approximately 750 m. At higher altitudes, no turbulent fluctuations occur: this is caused by the presence of the capping inversion, which confines turbulent gusts to the boundary layer.

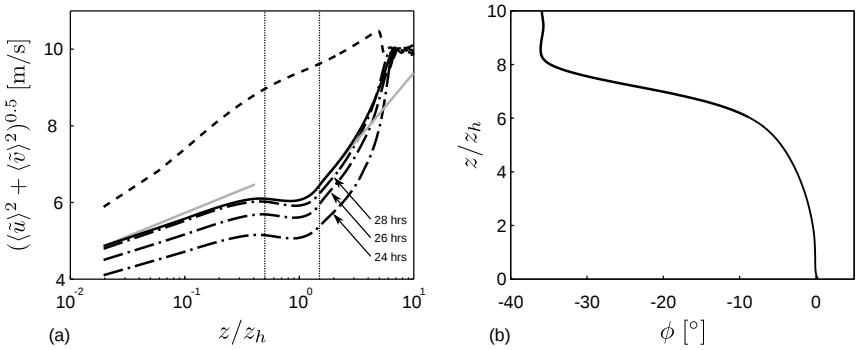

Figure 4.3: Vertical profiles of mean velocity magnitude and direction, averaged over horizontal planes, for the baseline case. (a) Profiles of mean velocity magnitude after the start-up phase of 20 hours (dashed line), at intermediate times (dash–dotted lines) and averaged over the last 10 hours of wind-farm operation (solid line). Vertical dotted lines mark the bottom and top of the turbine region, and reference lines for the log-layers are shown in grey. (b) Mean wind direction, averaged over the last 10 hours of wind-farm operation.

4.2.2 Mean velocity profiles and geostrophic angle

Profiles of mean velocity magnitude at different simulation times are presented in figure 4.3(a). In literature, it has been shown that the velocity profile in fully developed wind-farm boundary layers (with wind turbines situated within the inner layer) is expected to show a double log layer (Frandsen 1992; Calaf *et al.* 2010). In figure 4.3(a), it is clear that, at the start of the wind-farm operation, the velocity profiles quickly transform from the simple log layer in the absence of wind turbines (see the dashed line in figure 4.3(a)) into a double log layer. Below the turbine region, a clear logarithmic region with surface roughness length $z_{0lo} = 2\times10^{-4}$ m and characteristic friction velocity $u_{*lo} = (\tau_w)^{1/2}$ equal to 0.21 m/s can be observed. Above the farm, a second log layer characterised by a friction velocity u_{*hi} is found. Due to the low inversion layer, this second log layer only extends up to about 500 m. Higher up, outer-layer effects start to influence the velocity profile.

The friction velocity u_{*hi} corresponds to the total friction of the surface and the wind turbines (Frandsen 1992; Calaf *et al.* 2010). In the presence of Coriolis forces, it corresponds to

$$u_{*hi}^2 = \|\boldsymbol{\tau}_w + \boldsymbol{f}_t\| \approx \|\boldsymbol{\tau}_w\| + \|\boldsymbol{f}_t\|\,, \tag{4.6}$$

with $\boldsymbol{\tau}_w$ the wall stress and $\boldsymbol{f}_t = \boldsymbol{F}_t/(s_x s_y D^2)$ the area-averaged thrust force

of the wind farm, which is by definition directed along the x-axis. Although $\boldsymbol{\tau}_w$ and $\boldsymbol{f}_t$ need not be perfectly aligned in the presence of Coriolis forces, the angle between these forces turns out to be a few degrees only, so that the vectorial sum may be approximated by the sum of force magnitudes. Using equation (4.6), the friction velocity u_{*hi} for the baseline case is found to be 0.62 m/s. Finally, matching the velocity profile above the turbine region with a log law based on u_{*hi} yields $z_{0hi} = 2.26$ m.

The vertical profile of mean flow direction is shown in figure 4.3(b). Due to the wind-angle controller, the wind speed at hub height is directed along the x-axis. The geostrophic angle α is defined as the change in wind direction between the geostrophic wind vector in the free atmosphere and the x-axis, which corresponds to the direction of the wind flow at hub height. The CNBL with wind turbines and a low capping inversion appears to be characterised by a large geostrophic angle. As seen in figure 4.3(b), the geostrophic angle for the baseline case is about $-36°$. By comparison, Johnstone & Coleman (2012) report a geostrophic angle of $-32.8°$ for a turbulent Ekman boundary layer without capping inversion, but with a more densely spaced wind farm ($s_x = s_y = 5D$) and a disk-based thrust coefficient equal to the Betz limit, i.e., $C_T' = 2$. It is further observed that more than 75 % of the change in wind direction occurs inside the thin inversion layer. The occurrence of such a directional jump at the inversion layer was also reported by Brost *et al.* (1982) for small inversion heights in marine stratocumulus layers.

4.2.3 Stress and heat-flux profiles

Consider next the shear stress profiles in the CNBL. The components of the total shear stress are defined as the sum of the Reynolds, dispersive, and mean SGS stress components (Calaf *et al.* 2010, 2011):

$$\tau_{xz}(z) = -\langle\overline{u'w'}\rangle(z) - \langle\bar{u}''\bar{w}''\rangle(z) - \langle\tau_{xz}^{sgs}\rangle(z), \tag{4.7}$$

$$\tau_{yz}(z) = -\langle\overline{v'w'}\rangle(z) - \langle\bar{v}''\bar{w}''\rangle(z) - \langle\tau_{yz}^{sgs}\rangle(z), \tag{4.8}$$

using a bar for time averaging, and brackets for horizontal averaging. Further, $u_i' = u_i - \bar{u}_i$ and $u_i'' = u_i - \langle\bar{u}_i\rangle$. The dispersive stress components $\langle\bar{u}''\bar{w}''\rangle$ and $\langle\bar{v}''\bar{w}''\rangle$ arise due to correlations among the spatially non-homogeneous mean horizontal and mean vertical velocities (Raupach *et al.* 1991).

The different components of the various shear stresses are shown in figure 4.4(a). It is observed that the momentum transport in the CNBL with wind turbines is mainly provided by the Reynolds stresses. The streamwise dispersive stresses are only important inside the turbine region, and only about 11 % of the

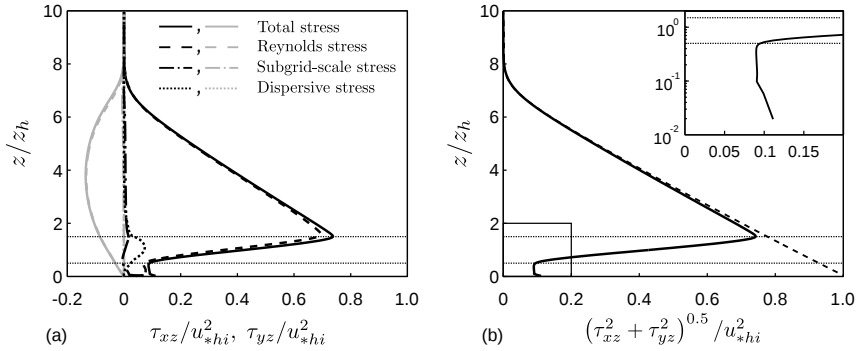

Figure 4.4: Vertical profiles of shear stresses, averaged over horizontal planes and over the last 10 hours of wind-farm operation, for the baseline case. (a) Streamwise (black lines) and spanwise (grey lines) shear stress components, including total shear stresses, Reynolds stresses, subgrid-scale stresses and dispersive stresses. (b) Total shear stress magnitude. The expected stress profile using right-hand side of eqs. (4.9) and (4.10) is shown with a dashed line. In the top right corner, the lowest 20 % of the domain is magnified and plotted in semi-logarithmic scale. The horizontal dotted lines mark the bottom and top of the turbine region.

Reynolds stresses. The spanwise dispersive stresses are completely negligible. Furthermore, the mean subgrid-scale stresses are only significant close to the ground in the x-direction. In the y-direction, mean subgrid-scale stresses remain small throughout the boundary layer, as at the ground the total spanwise shear stress is nearly zero. Finally, above the inversion layer, all shear stress components are zero. In this region, only Coriolis forces and pressure gradient contribute to the force balance.

The magnitude of the total shear stress is shown in figure 4.4(b). In the atmospheric boundary-layer community, the concept of a constant stress layer is widely used, in which it is assumed that the stress varies less than 10 % in the inner layer of the ABL ($z/h \ll 1$). Below the turbine region, a constant stress layer can indeed be observed, in which $\|\boldsymbol{\tau}\| \approx u_{*lo}^2$ within 20 % accuracy (see top right corner in figure 4.4(b)), as, e.g., also observed in Calaf *et al.* (2010). Above the turbine region, the assumption of a constant stress layer no longer holds as the turbines reach up to about 20 % of the shallow boundary-layer height. Here, the expected shear-stress profile follows from integrating the time

and horizontally averaged momentum equations, i.e.,

$$\tau^e_{xz}(z) = \int_z^H f_c\left(\langle\bar{u}_2\rangle(z') - G\sin\alpha\right)\mathrm{d}z', \tag{4.9}$$

$$\tau^e_{yz}(z) = \int_z^H f_c\left(-\langle\bar{u}_1\rangle(z') + G\cos\alpha\right)\mathrm{d}z'. \tag{4.10}$$

In figure 4.4(b), the magnitude of the total shear stress is close to linear near the top of the wind-turbine region and reaches a maximum value of about $0.75u^2_{*hi}$. Note that the friction velocity of the second log layer is defined as the sum of the wall stress and the area-averaged thrust force (see equation (4.6)), and that it can be found by extrapolating the expected shear stress to the ground, i.e., $u^2_{*hi} \approx \tau(z)/(1 - z/h)$. The linear behaviour extends up to about 500 m, i.e. up to the same height as the second log layer in figure 4.3(a).

Based on this observation, an equivalent pressure-driven boundary layer can be defined that approximates the CNBL in its lower part. The height of this equivalent boundary layer h_{eq} is found by linearly extrapolating the lower part of the CNBL shear stresses. This yields a height of 686 m, which is somewhere halfway between the bottom and centre of the inversion layer. The corresponding pressure gradient is equal to $\rho_0 u^2_{*hi}/h_{\mathrm{eq}}$ and is about 6 % lower than the streamwise CNBL pressure gradient $\partial p_\infty/\partial x$ for the baseline case (remember that in the CNBL the Coriolis forces are added in the force balance).

Finally, the potential-temperature and heat-flux profiles are shown in figure 4.5. From the horizontally averaged profiles at various simulation times in figure 4.5(a), it is clear that the mean potential temperature hardly changes during initial start-up phase of 20 hours. After switching on the wind turbines, the potential temperature evolves with a nearly constant speed, and an increase in both the BL height as well as the mixed-layer temperature is observed. Throughout the whole simulation, however, the shape of the profile remains very similar. Note that this enables the use of the fit with the curve of Rampanelli & Zardi (2004) (i.e., eq. (2.7)) for the estimation of capping-inversion strength and height.

The total vertical heat flux q_z and its components are defined similar to the total shear stresses:

$$q_z(z) = \langle\overline{w'\theta'}\rangle(z) + \langle\bar{w}''\bar{\theta}''\rangle(z) + \langle q_z^{sgs}\rangle(z), \tag{4.11}$$

In figure 4.5(b), the total heat flux attains a minimum at the base of the inversion layer. Below the inversion, the heat flux is approximately linear and the boundary layer warms up uniformly with height. Above the inversion, warm air is cooled down due to the entrainment process. In the free atmosphere,

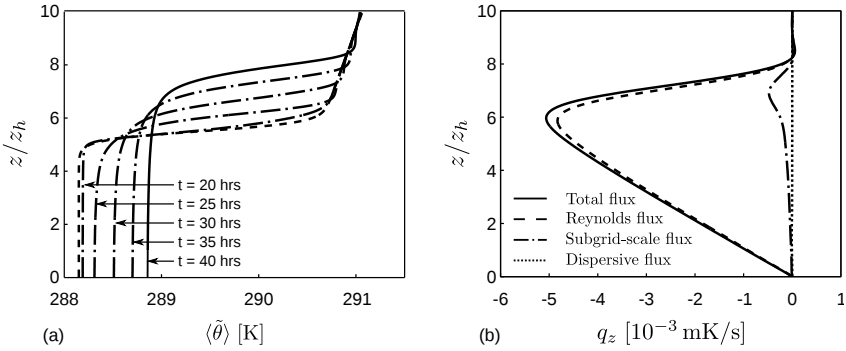

Figure 4.5: Vertical profiles of potential temperature and heat flux, averaged over horizontal planes, for the baseline case. (a) Profiles of mean potential temperature, including the initial potential-temperature condition (dashed line), several profiles at intermediate times (dash–dotted lines) and the potential-temperature profile after 20 hours of wind-farm operation (solid line). (b) Heat fluxes, averaged over the last 10 hours of wind-farm operation, including total heat flux, turbulent heat flux, subgrid-scale heat flux and dispersive heat flux.

the heat flux is zero and the potential temperature stays equal to its initial value. The dispersive heat flux is very small throughout the domain, indicating that the mean vertical velocity and the mean potential temperature are rather uncorrelated. The subgrid-scale fluxes are small everywhere except in the inversion layer, where they attain values up to 10 % of the maximum total heat flux (in absolute value). In this highly stable region, turbulent length scales are reduced and a substantial part of the heat transport is not resolved by the LES grid but modelled through the subgrid-scale model.

4.3 CNBL and wind-farm behaviour under varying inversion layers

In this section, the results of the different LES cases are compared, and the impact of the various inversion-layer characteristics on the CNBL behaviour is assessed.

Figure 4.6 shows the evolution of the boundary-layer height and the geostrophic angle for the different LES cases. In figure 4.6(a), all simulations with an initial inversion layer above the equilibrium height (REF, S10, H10 and H15) show almost no growth during the first 20 hours (i.e., in the absence of wind

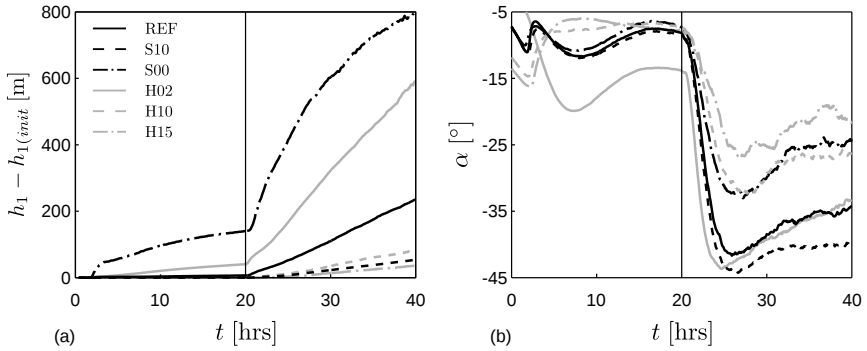

Figure 4.6: (a) Boundary-layer growth $h_1 - h_{1(\text{init})}$ and (b) geostrophic angle α as a function of time for the cases REF, S10, S00, H02, H10 and H15.

turbines). In contrast, simulations S00 and H02 are not in equilibrium and attain a constant growth rate.

Once the wind farm is switched on, the turbines induce additional friction, thereby increasing the equilibrium height of the CNBL. As a result, the boundary layer starts growing in all simulations. Cases REF, S10, H10 and H15 show a modest, nearly constant boundary-layer growth rate during the whole wind-farm operation, and the lowest growth rates correspond to the cases with high or strong inversion layers. The increase in boundary-layer height over the 20 hours of wind-farm operation ranges between 30 and 230 m (1.5 to 11.5 m per hour). On the other hand, cases S00 and H02 show large growth, as they are farther away from the equilibrium height. Although case S00 started without an inversion layer, it is observed that, near the end of the simulation, a weak inversion layer (about 0.7 K) is formed, causing a slow down of the boundary-layer growth. However, at this time, the boundary layer has grown by more than 700 m.

In figure 4.6(b), the evolution of the geostrophic angle is shown. Here the trends are somewhat different. The geostrophic angle increases with increasing inversion strength, but decreases with increasing inversion heights. For all cases, the geostrophic angle increases significantly in magnitude during the first five hours of wind-farm operation, followed by a slow decrease afterwards.

Figure 4.7(a) displays the wind-farm power output, non-dimensionalised with the geostrophic wind speed, for the various LES cases in function of time. In all simulations, the power profile starts with a sharp peak followed by a drop in power output, with a minimum after about 2.5 hours of operation. Near the end of the simulation, the power output partly recovers from the initial drop

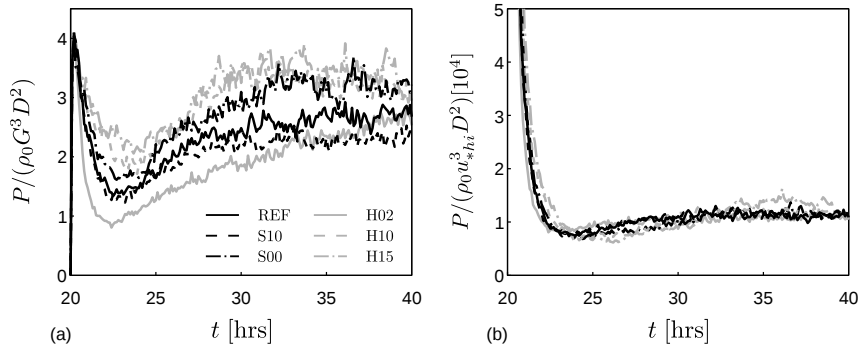

Figure 4.7: Total wind-farm power extraction as a function of time, scaled with (a) the geostrophic wind and (b) the friction velocity, for the cases REF, S10, S00, H02, H10 and H15.

and attains a quasi-steady output level. In this regime, a clear difference in power performance can be observed among the different cases. With respect to the baseline case, it is observed that the power output is (13 ± 0.2) % lower in case S10 (strong inversion) and (20 ± 0.3) % higher in case S00 (very weak inversion). Comparing the baseline case with cases H10 and H15 shows a monotonic increase in power of (25 ± 0.3) % and (31 ± 0.4) % with inversion-layer height. In figure 4.7(b), the ratio of wind-farm power output and u_{*hi}^3 is compared for the different cases. After the initial transient, the wind-farm power output appears to scale roughly with u_{*hi}^3. (The uncertainty on the power averages mentioned above corresponds to the standard deviation on the 10-hour average. It was obtained from the root-mean-square of the power, and the square-root of the number of statistically independent samples in the 10-hour averaging period. The latter was estimated using an integral time scale of 100 seconds, leading to approximately 360 independent samples.)

The dominating factors that explain this power difference are now investigated. To this end, the total kinetic-energy budget of the CNBL is discussed. The total kinetic-energy equation (per unit mass) is derived by first multiplying the momentum equation (3.2) with u_i and subsequently averaging the equation over horizontal planes:

$$\frac{\partial \langle E_k \rangle}{\partial t} + \frac{\partial}{\partial x_j}\left(\langle u_j \rangle \langle E_k \rangle + \langle u_i \rangle \langle u_i' u_j' \rangle + \frac{1}{2}\langle u_j' u_i' u_i' \rangle + \langle u_j' p^\star \rangle + \langle u_i \tau_{ij}^{sgs} \rangle \right)$$

$$= \frac{g}{\theta_0}\langle u_3(\theta - \theta_0) \rangle + \langle \tau_{ij}^{sgs} S_{ij} \rangle + \langle u_i f_i \rangle + \langle u_i \rangle \left(-\frac{1}{\rho_0}\frac{\partial p_\infty}{\partial x_i} \right), \qquad (4.12)$$

where $\langle E_k \rangle$ is defined as $\langle u_i u_i \rangle / 2$, and where here $u_i' = u_i - \langle u_i \rangle$. Equation (4.12) is now integrated over the boundary-layer height $h(t)$, where the Leibniz's rule for differentiation under the integral sign is used for the time-dependent term, i.e.,

$$\frac{\mathrm{d}}{\mathrm{d}t}\int_0^h \langle E_k \rangle \, \mathrm{d}z = \underbrace{\int_0^h \frac{g}{\theta_0}\langle u_3(\theta - \theta_0)\rangle \, \mathrm{d}z}_{\mathscr{P}_\theta} + \underbrace{\int_0^h \langle \tau_{ij}^{sgs} S_{ij} \rangle \, \mathrm{d}z}_{\mathscr{E}} + \underbrace{\int_0^h \langle u_i f_i \rangle \, \mathrm{d}z}_{\mathscr{P}_F}$$

$$+ \underbrace{\int_0^h \langle u_i \rangle \left(-\frac{1}{\rho_0}\frac{\partial p_\infty}{\partial x_i} \right) \mathrm{d}z}_{\mathscr{P}_\infty} + \langle E_k \rangle \Big|_h \frac{\mathrm{d}h}{\mathrm{d}t}, \tag{4.13}$$

The term on the left-hand side indicates the change in time of the total energy in the boundary layer. The terms on the right-hand side include production of potential energy $\mathscr{P}_\theta$, dissipation $\mathscr{E}$, wind-farm power extraction $\mathscr{P}_F$ and driving-power term $\mathscr{P}_\infty$. The last term on the right-hand side arises due to the time dependence of $h(t)$ and corresponds to the amount of energy that is entrained from the free atmosphere due to the growth of the boundary layer. No transport terms arise in equation (4.13) due to the choice of integration limits.

Figure 4.8(a) shows the energy sources and sinks of total kinetic energy for the baseline case. In the CNBL, the entrainment of kinetic energy is very small but positive, and the production from potential energy is negligible. Further, turbulent dissipation appears to be of the same magnitude as the wind-farm power output throughout the whole simulation. The evolution of the wind-farm power output, the driving-pressure term and the time-dependent term can be divided into three periods, starting at simulation hour 20, 22.5 and 30, respectively. The first period, i.e., the first two and a half hours of wind-farm operation, starts with a large peak in wind-farm power output and turbulent dissipation. In this period, the time-dependent term attains a large negative value, indicating that the flow is slowed down by the wind farm. Near the end of the first period, the wind-farm power output decreases and the driving-power term increases, both of which reduce the global deceleration of the flow. The second period starts when the wind-farm power output reaches a local minimum. In this period, the energy content of the boundary layer increases again and the wind-farm power recovers slightly. In the last part of the simulation ($t > 30$ hours), the time derivative of the mean kinetic energy reaches a steady, slightly positive level, and is almost exactly equal to the energy entrainment. Wind-farm power output, turbulent dissipation and driving power increase very slowly.

The same trends are observed in figure 4.8(b), showing the energy-budget terms for case S10, characterised by a higher inversion strength. As the boundary-

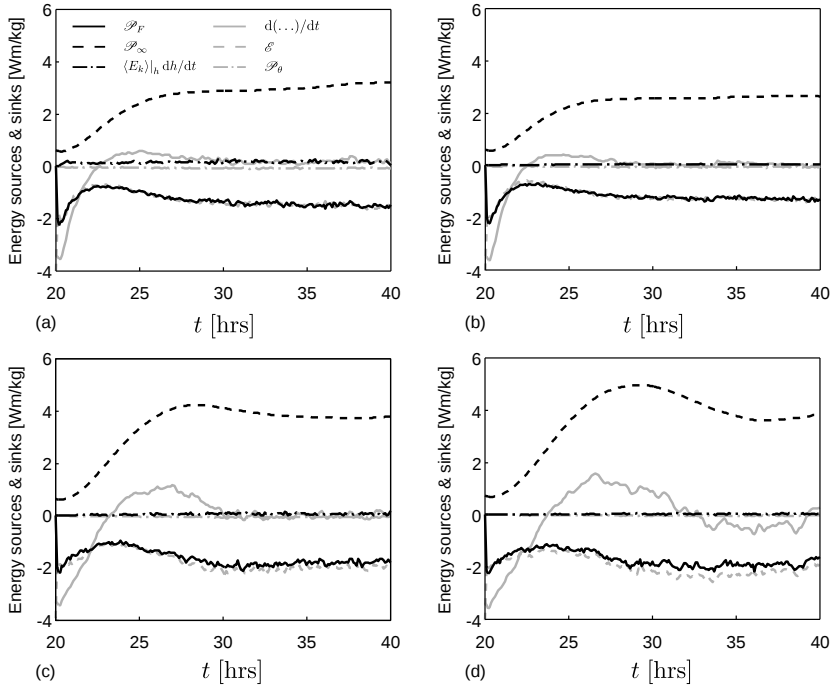

Figure 4.8: Energy sources and sinks in the mean kinetic-energy budget as a function of time for cases (a) REF, (b) S10, (c) H10 and (d) H15, including wind-farm power extraction $\mathscr{P}_F$, driving power $\mathscr{P}_\infty$, energy entrainment, time-dependent term, dissipation term $\mathscr{E}$ and production of potential energy $\mathscr{P}_\theta$.

layer growth of this case is lower than the baseline case (see figure 4.6(a)), the energy entrainment is also lower. Similarly, figures 4.8(c–d) show lower energy-entrainment rates for the cases H10 and H15. These cases have higher initial inversion layers compared to the baseline case, also leading to slower boundary-layer growth. Overall, the kinetic-energy entrainment is very low in all cases, so this is not explaining the difference in wind-farm power output.

4.4 A simple model for wind-farm power equilibrium in quasi-steady conditions

In the current section, the focus lies on the power balance in wind farms, and a simple model is derived that explains the main mechanics for quasi-steady

conditions, i.e., conditions where the temporal variation in total boundary-layer energy and vertical entrainment are very small or cancel out. In particular, the dependence of $\mathscr{P}_F/G^3$, $\mathscr{P}_\infty/G^3$, and $\mathscr{E}/G^3$ on parameters such as Rossby number, boundary-layer height, etc. is of interest. As seen in the previous section, quasi-steady conditions are obtained after 15 to 20 hours of wind-farm model time. Under these conditions, the power balance is simply governed by $\mathscr{P}_\infty = \mathscr{P}_F + \mathscr{E}$, since all other terms can be neglected (see fig. 4.8 and eq. 4.13).

In figure 4.7(b), it is observed that the wind-farm power extraction scales with u_{*hi}^3 in quasi-steady regime. This can be explained as follows. First of all, the total farm power per farm surface area is given by $\mathscr{P}_F = c'_{ft}\langle\bar{u}^T\rangle_d^3/2$, with $c'_{ft} = \pi C'_T/(4s_x s_y)$. Similarly, the total farm thrust per surface area $\|\boldsymbol{f}_t\| = c'_{ft}\langle\bar{u}^T\rangle_d^2/2$. Combining these two equations with eq. (4.6) yields

$$\frac{\mathscr{P}_F}{u_{*hi}^3} = (2/c'_{ft})^{1/2}\left(1+\frac{2u_{*lo}^2}{c'_{ft}\langle\bar{u}^T\rangle_d^2}\right)^{-3/2} = (2/c'_{ft})^{1/2}\left(1-\frac{u_{*lo}^2}{u_{*hi}^2}\right)^{3/2}. \quad (4.14)$$

Thus, $u_{*lo}^2 \ll u_{*hi}^2$ implies $\mathscr{P}_F/u_{*hi}^3 \approx (2/c'_{ft})^{1/2}$, independent of outer-layer parameters such as Rossby number or boundary-layer height, and independent of turbine arrangement pattern. Moreover, in the inner layer, it is logical to assume that $2u_{*lo}^2/(c'_{ft}\langle\bar{u}^T\rangle_d^2)$ is not influenced by outer-layer scales. In the LES data, it is found that $2u_{*lo}^2/(c'_{ft}\langle\bar{u}^T\rangle_d^2)$ is nearly constant over the various cases and equals 0.135. Thus, it is found that this value is not influenced by outer-layer scales even when the wind turbines are located well above the inner layer. To further confirm this for another arrangement pattern, three additional simulations are performed with a staggered wind farm, using the same turbine density and c'_{ft} as for the aligned case, and further equivalent to cases REF, S10, and H10. For these cases, $2u_{*lo}^2/(c'_{ft}\langle\bar{u}^T\rangle_d^2) = 0.124$ is found, which is very close to the aligned case. The difference in $\mathscr{P}_F/u_{*hi}^3$ between the staggered and aligned wind-farm layout is less then 3 %, which follows directly from eq. (4.14). Hints of this near independence in fully developed conditions are also observed in field experiments, e.g., in the well documented Horns Rev farm typical efficiency loss is roughly (40 ± 5) % in the last rows of the farm, independent of wind direction (and thus turbine arrangement pattern) (Barthelmie *et al.* 2007*b*, 2009). Finally, given above scaling for $\mathscr{P}_F$, it follows that

$$\frac{\mathscr{P}_F}{G^3} = \frac{\mathscr{P}_F}{u_{*hi}^3}C_g^3 \approx (2/c'_{ft})^{1/2}C_g^3, \quad (4.15)$$

with $C_g = u_{*hi}/G$ the geostrophic drag (see further below). Note that the approximation in eq. (4.15) is not valid for $c'_{ft} \to 0$, as in that case $u_{*lo}^2 \to u_{*hi}^2$.

The driving power $\mathscr{P}_\infty$ in the boundary layer can also be further elaborated. Similar to Zilitinkevich (1989), it can be reformulated using the horizontally

averaged and integrated momentum equations for u_1 and u_2, eq. (3.2) (assuming steady state):

$$-\int_0^\infty f_c G \sin\alpha + \int_0^\infty f_c \langle u_2 \rangle \, \mathrm{d}z = -\tau_{w1} - \int_0^\infty \langle \boldsymbol{f} \cdot \boldsymbol{e}_1 \rangle \, \mathrm{d}z, \tag{4.16}$$

$$\int_0^\infty f_c G \cos\alpha \; - \int_0^\infty f_c \langle u_1 \rangle \, \mathrm{d}z = -\tau_{w2}. \tag{4.17}$$

Using equations (4.6), (4.16) and (4.17), the driving-power term $\mathscr{P}_\infty$ can be written as

$$\mathscr{P}_\infty = \int_0^\infty f_c G \left(\langle u_2 \rangle \cos\alpha - \langle u_1 \rangle \sin\alpha \right) \, \mathrm{d}z \tag{4.18}$$

$$= G\cos\alpha \left(-\tau_{w1} - \int_0^\infty \langle \boldsymbol{f}_t \cdot \boldsymbol{e}_1 \rangle \, \mathrm{d}z \right) - G \sin\alpha \; \tau_{w_2} \tag{4.19}$$

$$= G\cos(\alpha - \alpha_*) \; u_{*hi}^2, \tag{4.20}$$

where α_* is the angle between $-(\boldsymbol{\tau}_w + \boldsymbol{f}_t)$ and the x-coordinate. This angle remains small for all cases, i.e., ranging between $-4°$ and $4°$. Hence, neglecting α_*, the ratio of the driving-power term and u_{*hi}^3 is given by

$$\frac{\mathscr{P}_\infty}{u_{*hi}^3} \approx \frac{G\cos\alpha}{u_{*hi}} = \frac{1}{\kappa} \ln\left(\frac{C_g Ro_h}{\bar{z}_{0hi}} \right) - F_1(C_g, Ro_h, \bar{h}), \tag{4.21}$$

with $Ro_h = G/f_c z_h$ the Rossby number based on the turbine hub height (Meyers & Meneveau 2012), $\bar{z}_{0hi} = z_{0hi}/z_h$ the non-dimensional surface roughness, and $\bar{h} = h/z_h$ the non-dimensional boundary-layer height (for which the measure h_1/z_h is used). The second equality in equation (4.21) follows from the classical resistance law for the matched layer (Tennekes & Lumley 1972), where F_1 is usually considered constant. However, as postulated by Csanady (1974), amongst others (Nieuwstadt 1983; Zilitinkevich & Esau 2002; Hess 2004), F_1 is a function of outer-layer parameters. Explicit expressions for $F_1(C_g, Ro_h, \bar{h})$ can be derived by solving the Ekman-layer equations and using, e.g., constant (Csanady 1974), quadratic, or cubic (Nieuwstadt 1983) eddy-viscosity profiles in the outer layer of the ABL to express the shear stresses (see appendix B for details). Further, the wind-farm induced surface roughness z_{0hi} is used in the resistance law, as suggested by Meyers & Meneveau (2012). This surface roughness can be computed from the LES velocity profiles, or may be estimated using an effective surface roughness model (Frandsen 1992; Frandsen *et al.* 2006; Calaf *et al.* 2010). Finally, normalised with respect to the geostrophic wind, the driving-power term is given by

$$\frac{\mathscr{P}_\infty}{G^3} = \left[\frac{1}{\kappa} \ln\left(\frac{C_g Ro_h}{\bar{z}_{0hi}} \right) - F_1(C_g, Ro_h, \bar{h}) \right] C_g^3. \tag{4.22}$$

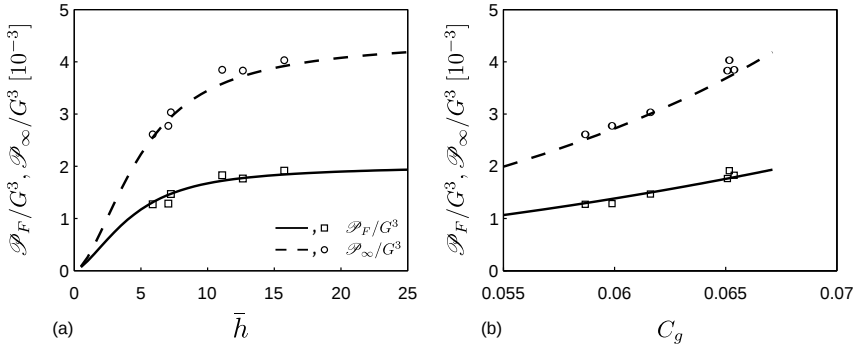

Figure 4.9: Wind-farm power extraction $\mathscr{P}_F/G^3$ and driving power $\mathscr{P}_\infty/G^3$ as a function of (a) dimensionless BL height $\bar{h}$ and (b) geostrophic drag C_g, obtained from the presented power model (plotted using lines) governed by eqs. (4.15), (4.22) and (4.23), using a cubic eddy-viscosity profile (Nieuwstadt 1983) with $\kappa = 0.43$. LES results averaged over the last ten simulation hours are represented with symbols.

An expression for C_g follows from $G \sin\alpha / u_{*hi} = -F_2(C_g, Ro_h, \bar{h})$ (see appendix B for details) in combination with eq. (4.22), yielding

$$\frac{1}{C_g^2} = [F_2(C_g, Ro_h, \bar{h})]^2 + \left[\frac{1}{\kappa} \ln\left(\frac{C_g Ro_h}{\bar{z}_{0hi}}\right) - F_1(C_g, Ro_h, \bar{h})\right]^2 . \qquad (4.23)$$

Thus, in summary eqs. (4.15), (4.22) and (4.23), together with expressions for F_1 and F_2, form a closed analytical model that allows to express $\mathscr{P}_F/G^3$, and $\mathscr{P}_\infty/G^3$.

Figure 4.9 shows the wind-farm power extraction $\mathscr{P}_F/G^3$ and the driving power $\mathscr{P}_\infty/G^3$ as a function of the dimensionless boundary-layer height $\bar{h}$ and the geostrophic drag C_g. Data from the LES cases has been averaged over the last 10 simulation hours and are shown with symbols. For the analytical model, a cubic eddy-viscosity profile is used (Nieuwstadt 1983) (see appendix B), and the model is fitted to LES data using the von Kármán constant as fitting parameter, yielding $\kappa = 0.43$. Further, $\mathscr{P}_F/u_{*hi}^3$ and the wind-farm induced surface roughness $\bar{z}_{0hi}$ were estimated from LES data to be 6.4 and 0.0223, respectively. The analytical model matches good with the LES results. It is observed that the wind-farm power extraction $\mathscr{P}_F/G^3$ and the driving power $\mathscr{P}_\infty/G^3$ are monotonous increasing functions of the boundary-layer height. The driving power $\mathscr{P}_\infty/G^3$ increases faster since $\cos\alpha$ increases faster than C_g. From this figure, it is concluded that the difference in wind-farm power extraction between the LES cases REF, H02, H10 and H15 is directly caused by

the difference in initial inversion-layer height, whereas the difference between the cases REF, S10 and S00 is only indirectly caused by the varying inversion strength through its effect on the entrainment rate of the boundary layer.

4.5 Summary

This chapter aimed at determining the behaviour of an infinite wind-turbine array located in a conventionally neutral atmospheric boundary layer. Such a CNBL is often capped by a strong temperature inversion layer, which limits vertical entrainment of kinetic energy in the boundary layer, and thus potentially reduces the energy available for power extraction by the wind turbines.

A suite of large-eddy simulations was used to study the performance of a wind farm under capping inversions with varying strengths and heights, and the limit of an infinite wind-turbine array was used, allowing for periodic boundary conditions in the simulations, similar to the approach followed by Calaf *et al.* (2010) for a pressure-driven boundary layer. In order to obtain a CNBL with the required capping-inversion structure, special attention was paid to the initial conditions of the different simulations. In addition, a wind-angle controller was implemented to ensure that the wind at the hub height of the turbines was directed along the x-axis. In this way, the wind-farm geometrical pattern was independent of the geostrophic angle and identical for all simulations.

LES results of the CNBL with wind turbines revealed some essential differences between the current approach and the frequently used neutral pressure-driven boundary layers. For instance, the double log layer in the mean velocity profile does not reach up to the top of the domain in the CNBL, and the expected shear stress deviates from the well-known linear profile near the inversion. Further, it was observed that the direction of the flow changes with height, and a sharp change in wind direction was observed inside the inversion layer.

Comparison of the various LES cases showed that the strength and the height of the capping inversion have a strong influence on the boundary-layer flow. For example, the growth rate of the wind-farm boundary layer was shown to decrease with increasing inversion strength or height. Moreover, in the presence of a capping inversion, only modest boundary-layer growth rates were observed. In contrast, the boundary-layer growth in absence of an inversion was about three times the growth rate of the baseline case. The geostrophic angle also decreased for increasing inversion height.

For the simulations in this chapter, it was observed that the power extraction by the wind farm depends on the height and strength of the inversion layer.

Increasing the strength of the inversion layer from 2.5 to 10 K resulted in a (13 ± 0.2) % decrease in wind-farm power output. On the other hand, starting the simulation without an inversion layer resulted in a (20 ± 0.3) % increase compared to the 2.5 K baseline case. The height of the inversion base had an even bigger influence on the power output, resulting in an increase of up to (31 ± 0.4) %. A detailed analysis of the mean kinetic-energy balance illustrated that the variation in power extraction between these different cases mainly originates from the work done by the driving pressure gradient related to the boundary-layer height and the geostrophic angle, while entrainment of kinetic energy from the free atmosphere did not play a significant role. Furthermore, it was found that the variation in power extraction for different inversion strengths is energetically not related to different amounts of energy entrained, but explained by a difference in boundary-layer growth, leading to higher boundary layers for lower inversion strengths.

Based on the observation that the wind-farm power extraction scales with the friction velocity cubed, a simple analytical model was developed that allows to obtain wind-farm power output and driving power for the fully developed regime as function of Rossby number, and boundary-layer height. From this model, it was shown that the wind-farm power extraction and the work done by the driving pressure gradient are monotonous increasing functions of boundary-layer height and geostrophic drag, but driving power increases faster due to the effect of the geostrophic angle.

Finally, it was shown that the definition of a steady state in a wind-farm–CNBL regime may only be possible after several hours of simulation. Even then, the boundary layer slowly evolves, and a true equilibrium state can only emerge after very long simulation times, with a capping inversion that has risen above the asymptotic equilibrium height of the CNBL. In practice, the CNBL may not exist that long in real atmospheric conditions, in which the absence of positive or negative heat fluxes at the ground surface is often limited in time.

Chapter 5

Boundary-layer development in wind farms under conventionally neutral conditions

This chapter investigates the streamwise development of boundary-layer flow through large wind farms under conventionally neutral conditions. Of particular interest is the development of an internal boundary layer at the wind farm entrance, and its downstream interaction with the overlying inversion layer. Furthermore, the activation and related feedback effect of gravity waves occurring in the free atmosphere above the CNBL are studied. It is shown that both effects play an important role in the overall energy extraction of the wind farm, and strongly depend on the height of the CNBL.

In order to simulate developing wind-farm behaviour, the periodic boundary conditions inherent to pseudo-spectral LES codes need to be circumvented. This is accomplished by applying the *concurrent-precursor* method developed by Stevens *et al.* (2014*b*). The method has been implemented in the SP-Wind solver by Munters *et al.* (2016), and it is extended here for non-neutral simulations. Moreover, the dimensions of the numerical domain and the boundary conditions at the top are chosen carefully in order to prevent spurious reflection of gravity waves.

The effect of inflow conditions on boundary-layer development and wind-farm performance is analysed based on three LES simulations with inflow boundary-layer heights of about 300 m, 500 m and 1000 m, respectively. These inflow conditions are realised in two phases, starting from a specific choice of inversion-layer characteristics representative of the offshore conventionally neutral boundary layer.

The structure of this chapter is further as follows. In section 5.1, the boundary conditions are described, and an overview of the wind-farm parameters and the case set-up is provided. Subsequently, the initialisation procedure of the boundary-layer flow is elaborated in section 5.2, and general trends of developing wind-farm boundary layers are discussed in section 5.3. In section 5.4, the sensitivity of the boundary-layer flow and the wind-farm performance to the inflow conditions is analysed. Conclusions are summarised in section 5.5. The material in this chapter is adapted from Allaerts, D. & Meyers, J. (2016) Boundary layer development and gravity waves in conventionally neutral wind farms, *J. Fluid Mech.*, revision submitted.

5.1 Numerical aspects

As in the previous chapter, the SP-Wind code equipped with the stability-dependent Smagorinsky model is used to perform LES of conventionally neutral boundary layers with wind turbines. The specification of boundary conditions is discussed in § 5.1.1. Further, the wind farm under consideration is described in § 5.1.2, and an overview of the various LES cases is given in § 5.1.3.

5.1.1 Boundary conditions

At the top of the domain, non-reflecting boundary conditions are needed so that gravity waves can travel outwards without generating spurious reflections. As it is very difficult to determine appropriate radiation conditions for the highly non-linear Navier–Stokes equations, wave reflections are alleviated with a simple wave-absorbing layer. In particular, Rayleigh damping is used (Klemp & Lilly 1978; Durran & Klemp 1983), for which the erroneous backward reflection was shown to be less scale-dependent than for viscous damping (Israeli & Orszag 1981). A cosine profile is chosen for the damping coefficient so that it increases smoothly throughout the damping layer. Boundary conditions still need to be imposed at the top of the domain, for which simple rigid-lid conditions are used, i.e., zero stress and vertical velocity, and a fixed potential temperature. Further, the classic wall model discussed in section 3.2 is applied at the bottom of the

domain. No stability corrections are needed as the surface heat flux is equal to zero.

In lateral directions, the pseudo-spectral discretisation implies periodic boundary conditions. In order to prevent turbine wake effects from being recycled back to the inlet, an artificial *fringe region* is added to the domain in streamwise direction, in which the flow variables are forced to an unperturbed inflow profile (Spalart & Watmuff 1993; Lundbladh *et al.* 1999; Nordström *et al.* 1999). Within the fringe region, the masking function of Nordström *et al.* (1999) is used for both the velocity and potential-temperature forcing, and the smoothing parameters Δ_s and Δ_e are set to $0.06L_x$. To obtain a fully developed inflow profile with consistent turbulent structures and non-Gaussian statistics, the *concurrent-precursor* method is applied (Stevens *et al.* 2014*b*; Munters *et al.* 2016). This method obtains inflow conditions from a precursor simulation that runs on an independent domain simultaneously with the main domain.

Although extending the fringe region method to non-neutral simulations is straightforward, this method is not widely used for atmospheric flows. Only Inoue *et al.* (2014) have used this technique to model the transition of stratocumulus to shallow cumulus clouds. Nevertheless, the fringe region method, besides providing a desired inflow profile, also absorbs gravity waves leaving through either side of the domain (mathematically, the fringe region is just a Rayleigh damping layer with a time-varying input velocity). In this way, it prevents the formation of non-physical standing wave patterns. Inoue *et al.* (2014) report that this method is less affected by artificially reflected waves than an inflow–outflow method (Mayor *et al.* 2002).

5.1.2 Wind-farm set-up

In the current chapter, a very large generic wind farm is considered, consisting of 180 wind turbines with hub height $z_h = 100$ m and diameter $D = 100$ m. The disk-based thrust coefficient $C_T' = 4/3$ (similar to Calaf *et al.* (2010)), and a time constant of 5 s is used for the time-filtered disk velocity. The wind farm contains 20 rows of turbines so that spatially developing features of various length scales can be investigated. The streamwise spacing is set to $s_x D = 7.5D$, which yields a wind-farm length of 15 km. In the spanwise direction, 9 turbine columns with spanwise spacing $s_y D = 5.33D$ are simulated, giving a width of 4.8 km. Note that, as no fringe region is applied in the spanwise direction and as the wind farm spans the full width of the simulation domain, the current set-up simulates the asymptotic limit of an "infinitely" wide wind farm. This will result in slightly increased wind-farm flow blockage and gravity-wave excitation compared to "fully finite" wind farms, where the wind can also flow around

Table 5.1: Case set-up for the developing conventionally neutral wind-farm simulations.

	h [m]	$\Delta\theta$ [K]	domain	$L_x \times L_y \times L_z$ [km]	$N_x \times N_y \times N_z$
S1	1000	1.0	precursor	$9.6 \times 4.8 \times 25.0$	$320 \times 320 \times 700$
			main	$38.4 \times 4.8 \times 25.0$	$1280 \times 320 \times 700$
S2	500	2.0	precursor	$9.6 \times 4.8 \times 25.0$	$320 \times 320 \times 620$
			main	$38.4 \times 4.8 \times 25.0$	$1280 \times 320 \times 620$
S4	250	4.0	precursor	$9.6 \times 4.8 \times 25.0$	$320 \times 320 \times 620$
			main	$38.4 \times 4.8 \times 25.0$	$1280 \times 320 \times 620$

the farm in spanwise direction and waves can expand in three instead of two dimensions. The results of this chapter therefore reflect the flow behaviour in the middle turbine columns in a very wide wind farm. The large number of turbine columns is chosen to allow fairly large turbulent structures as well as sufficient averaging in the spanwise direction.

The local wind direction may vary throughout the wind farm due to the combination of flow deceleration and Coriolis effects. Therefore, a simple yaw controller is implemented to keep the rotor disks perpendicular to the incident wind flow. The incident flow angle is measured $1D$ upstream of the turbine disk so as to ignore the flow deflection in the near vicinity of the turbine. Further, as the effective spanwise width is infinite, incident flow angles can be averaged per turbine row. Additional averaging of the flow angle by means of a first-order time filter is performed. A relatively large time constant of 15 min is taken as the dynamics of the yaw angle are not studied here.

5.1.3 Case set-up

A suite of LES simulations is performed in order to study the behaviour of developing wind farms under conventionally neutral inflow conditions. More specifically, the height of the undisturbed CNBL upstream of the wind farm is varied amongst the different cases, which is achieved by careful selection of initial conditions. Table 5.1 provides an overview of the numerical set-up of the various LES cases. The parameters specifying the inversion layer are discussed in § 5.2.1.

Atmospheric conditions are set to represent a typical offshore CNBL, with a constant geostrophic wind speed of $G = 12$ m/s and a surface roughness length

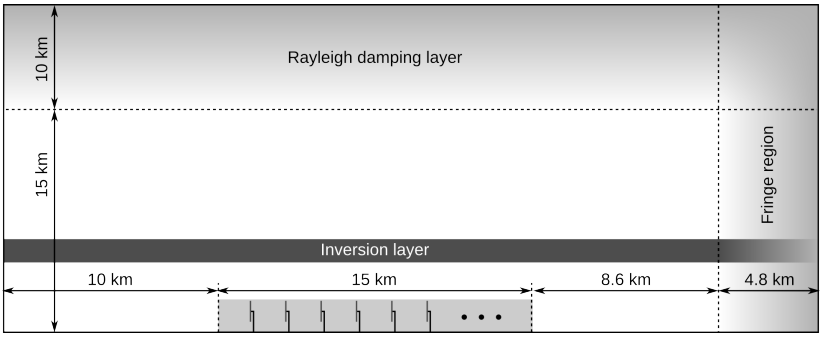

Figure 5.1: Sketch of the numerical domain, showing the relative positions of the wind farm, the fringe region and Rayleigh damping layer. The vertical scale is exaggerated as the inversion layer occurs at 1 km or less.

$z_0 = 2 \times 10^{-4}$ m (Sullivan *et al.* 2008). The free atmosphere lapse rate γ equals 1 K/km and the temperature of the mixed layer is $\theta_m = 15°$ C, which is also taken as the reference temperature θ_0. Finally, the Coriolis parameter f_c is set to 10^{-4} s^{-1}, corresponding to a latitude of $\phi = 43.43°$.

The dimensions of the numerical domain, the depth and damping coefficients of the Rayleigh damping layer and fringe region, and the location of the wind farm all influence the gravity wave solution in the LES output. In order to obtain a physically correct representation of gravity waves, these parameters should be chosen collectively to avoid unwanted wave reflections. Unfortunately, very little guidelines are available in literature to determine these parameters, and the only way to find an adequate set of parameters appears to be by trial and error. As this approach is not feasible with full-scale LES simulations, a reasonable set-up was determined based on a simplified two-dimensional flow solver. The details of this approach are discussed in appendix C, and the results are described below.

In the streamwise direction, sufficient spacing between the wind farm and the fringe region is needed to avoid too large distortions of the wind-farm generated gravity wave field. Inoue *et al.* (2014) found that the influence of the fringe region is limited to about 10 km upstream. For the wind-farm length under consideration, good results were found with 10 km upstream and 8.6 km downstream distance between the fringe region and the wind farm (see figure 5.1). A fringe region of $L^{fr} = 4.8$ km with a damping coefficient λ^{fr}_{max} equal to 0.03 s^{-1} was found sufficient to damp out horizontally propagating gravity waves. Hence, the total domain size in streamwise direction of the main simulation sums up to $L_x = 38.4$ km. The precursor domain simulates a simple

atmospheric boundary layer without wind turbines. Accordingly, the streamwise size of the domain can be reduced to save computational costs, so $L_x = 9.6$ km in the precursor simulation.

Klemp & Lilly (1978) found that the depth of the damping layer at the top of the domain should be on the order of one vertical wavelength. Under the hydrostatic assumption, the vertical wavelength of gravity waves is given by $\lambda_z = 2\pi U/N$, which is approximately 12.8 km under the given atmospheric conditions. The depth of the damping layer is therefore set to $L^{ra} = 10$ km, which corresponds to $0.78\lambda_z$. Further, Durran & Klemp (1983) found that "the numerical solution is not strongly sensitive to the strength of the damping in the wave-absorbing layer, but it can be very sensitive to changes in the height at which the absorbing layer begins, i.e., the effective height of the upper boundary." Good results were found when at least one vertical wavelength fitted into the domain. Therefore, the Rayleigh damping layer starts at a height of 15 km, resulting in a total domain height of 25 km (see figure 5.1). The Rayleigh damping coefficient λ^{ra}_{max} is set to 0.0001 s^{-1}.

Using SP-Wind, Calaf *et al.* (2010) and Meyers & Meneveau (2013) performed sensitivity studies for wind farms with turbine spacing similar to the one considered here (i.e., $s_x \times s_y = 7.85 \times 5.24$), and they found only small influences of the horizontal resolution when 25 m $\leq \Delta x \leq$ 50 m and 10 m $\leq \Delta y \leq$ 25 m. Accordingly, the grid resolution is set to 30 m and 15 m in streamwise and spanwise directions, respectively. In the vertical direction, the finite difference scheme requires a finer resolution to accurately resolve turbulent structures. In particular, the inversion layer forms the most stringent region as its strong stability results in fine-scale turbulent motions. These structures should still be resolved in order for LES to provide a good estimate of the turbulent entrainment rate. Taylor & Sarkar (2008*a*) found that the scale of turbulent eddies responsible for entrainment into the boundary layer can be estimated by the Ellison scale, defined as

$$L_E = \frac{\sqrt{\langle \theta'^2 \rangle}}{\partial \langle \theta \rangle / \partial z}. \tag{5.1}$$

From figure 5.2, showing the time-averaged Ellison scale for the different simulations, it is found that a vertical resolution of 5 m is sufficient for all simulations to capture the Ellison scale in the inversion layer. Starting at a height of 1 km, the grid is stretched in the vertical direction with a grid stretching factor $f_s = 1.0603$ and a maximum resolution of 40 m (starting at 1.5 km with $f_s = 1.0966$ for case S1). The damping layer is made up of 50 grid points, with the grid size stretching from 40 m to 300 m and $f_s = 1.0689$. In total, the simulations use approximately 320 million grid cells (360 for case S1), for the combination of main and precursor domain.

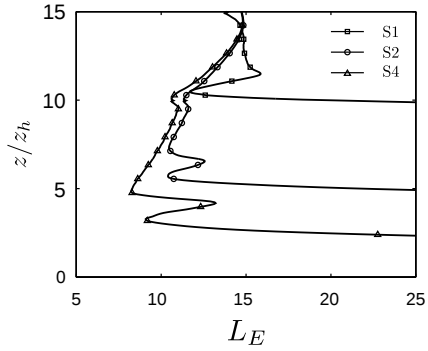

Figure 5.2: Ellison scale, averaged over the last five hours of the spin-up phase, for cases S1, S2 and S4.

5.2 Boundary-layer initialisation

The wind-farm boundary layer needs to be initialised properly before any flow statistics can be collected over time. This is achieved in two phases, namely the spin-up phase (§ 5.2.1) and the wind-farm start-up phase (§ 5.2.2). After these two initialisation phases, flow statistics are collected over a period of two hours.

5.2.1 CNBL spin-up phase

In the first phase, an equilibrium CNBL is simulated in the precursor domain. To this end, the properties of the inversion layer are determined with the empirical formulation of Csanady (1974) (see eq. (2.8)). Using typical values of 0.26–0.28 m/s for the friction velocity over sea, the set of inversion heights and strengths mentioned in table 5.1 is obtained. Initial velocity and potential-temperature profiles are then obtained with the procedure explained in § 4.1.3, and random divergence-free perturbations are added in the velocity field to trigger turbulence. The perturbations have an amplitude of $0.1G$ and are added below 100 m only, so that the initial "non-physical" random noise does not interact directly with the inversion layer.

This initial condition is progressed in time until a steady-state, fully developed turbulent CNBL is obtained. As already mentioned in § 4.1.3, equilibration times of the CNBL are reported in literature to be between 16 and 24 model hours (see, e.g., Zilitinkevich *et al.* 2007*b*; Pedersen *et al.* 2014). The duration of the spin-up phase is therefore set to 20 h, similar to the CNBL initialisation in the previous chapter. As the fully periodic precursor domain contains no

Table 5.2: Steady state parameters of the various spin-up cases, including the boundary-layer height h, the boundary-layer growth $\partial h/\partial t$, the hub-height velocity M_{hub}, the friction velocity u_*, the geostrophic wind angle α and the turbulent intensity at hub height TI.

	h [m]	$\partial h/\partial t$ [mm/s]	M_{hub} [m/s]	u_* [m/s]	α [°]	TI [%]
S1	997	0.11	10.96	0.310	-7.72	4.18
S2	520	0.25	11.20	0.315	-11.03	3.90
S4	296	0.50	11.13	0.306	-17.50	3.85

wind turbines, there are no mechanisms to trigger large-scale gravity waves in this phase. Therefore, only the lower 5 km of the domain are simulated, with a damping layer between 1 and 5 km (1.5 for case S1). Furthermore, the wind-angle controller of § 4.1.1 is used during this phase to vary the geostrophic wind angle α, such that the flow direction at hub height is aligned with the x-direction. The control parameters are again set to $\beta = 2\ \mathrm{h}^{-1}$ and $\sigma = 3.33$ min.

Some steady state parameters are given in table 5.2 for the various spin-up cases. The height of the inversion layer changes slightly during the spin-up phase, but the total increase remains below 50 m in all cases. Near the end of the first phase, the boundary-layer growth attains a small constant value (less than 0.5 mm/s), indicating that the boundary layer has reached a quasi-steady state. Note that Pedersen *et al.* (2014) found larger growth rates for the CNBL, i.e., 1 to 2.1 mm/s (see also table 3.3), but this is for a surface roughness length of $z_0 = 0.01$ m and without an initial inversion layer. The hub-height velocity M_{hub} and the friction velocity u_* are found to be nearly constant for the different cases, and the geostrophic angle α increases with decreasing boundary-layer height. The turbulent intensity is defined as $TI = (\langle\overline{u_i'u_i'}\rangle/3)^{1/2}/M_{hub}$ and is about 4 % at hub height in every case. For comparison, Bergström (2009) measured turbulent intensities at Lillgrund in the range 1 to 18 % with a mean of 6 % (measured at 65 m), and Barthelmie *et al.* (2009) reported low turbulent intensities (< 8 %) for the Horns Rev I wind farm.

Figure 5.3 shows vertical profiles of various flow variables for the different spin-up cases, averaged over the horizontal directions and over the last five hours of the first phase. In figure 5.3(a), showing the horizontal velocity magnitude, all cases develop a supergeostrophic jet near the boundary-layer top with a maximum wind speed of approximately $1.05\,G$, similar to Pedersen *et al.* (2014). Further, the vertical profiles of stress and wind direction (see figure 5.3(b) and (c)) follow the expected trends, i.e., linear (or close to) in the boundary layer and zero or constant above. Finally, the potential-temperature profile in figure

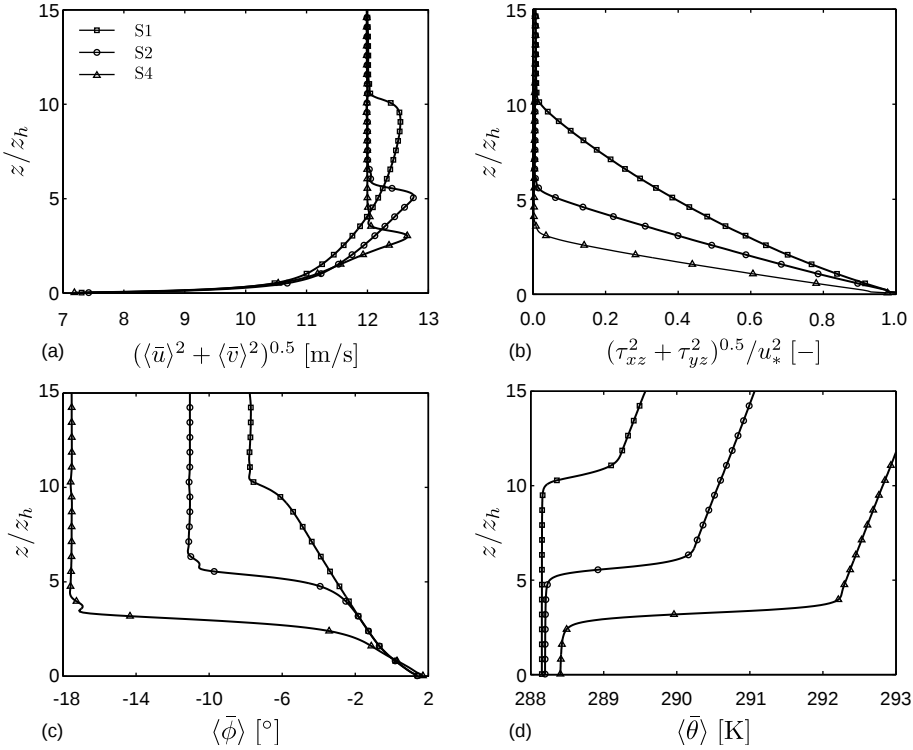

Figure 5.3: Vertical profiles, averaged over the horizontal directions and over the last five hours of the spin-up phase, of (a) horizontal velocity magnitude, (b) total shear stress magnitude, (c) horizontal wind direction and (d) potential temperature for cases S1, S2 and S4.

5.3(d) shows that the general shape of the inversion layer is preserved, and the temperature in the boundary layer increases only very little. Overall, these results demonstrate that the first initialisation phase yields a steady-state, fully turbulent CNBL, which can be used to produce accurate inflow conditions for the developing wind farm.

5.2.2 Wind-farm start-up phase

In the second phase, both precursor and main domain are simulated. The precursor simulation now starts from the velocity and potential-temperature fields developed in the spin-up phase, and produces realistic inflow fields for the

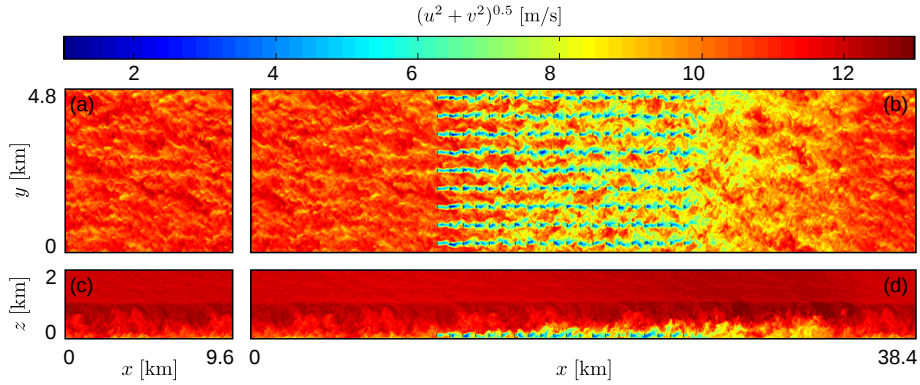

Figure 5.4: Instantaneous contours of horizontal velocity, obtained at the end of the second initialisation phase, for case S1; (a,b) An x–y plane at turbine hub height $z_h = 100$ m; (c,d) An x–z plane through the middle of a turbine column (only the lower 2 km of the numerical domain are shown). The left pane shows the precursor domain (a,c) and the right pane shows the main domain (b,d), where turbine disk locations are indicated with vertical black lines.

main domain. This phase is advanced for one hour, corresponding to about two and a half wind-farm flow-through times, during which the farm goes through its start-up phase, the yaw controller converges to a steady yaw angle and the flow generally adapts to the presence of the wind turbines. By the end of this phase, any transitional effects of the wind-farm start-up have died out, and the wind-farm boundary layer has reached a statistically stationary state.

Instantaneous contours of the horizontal velocity in the precursor and main domain, obtained at the end of this initialisation phase, are shown in figure 5.4 for case S1. On the left, figures 5.4(a) and 5.4(c) show an x–y plane (at $z_h = 100$ m) and an x–z plane of the precursor domain (only the lower 2 km of the numerical domain are shown). In the top view, typical elongated streaks in streamwise direction are observed. The side view, on the other hand, shows that turbulent structures are only present up to the capping inversion, which is located here at about 1 km. The flow above the capping inversion is non-turbulent and shear free. Similar cross sections of the main domain are shown in figures 5.4(b) and 5.4(d), where turbine disk locations are indicated with vertical black lines. The x–y plane through the centre of the rotor disks shows the meandering of the turbine wakes, which appears to intensify downstream. Especially from the fifth turbine row onward, significant meandering is visible, which is in agreement with the findings of Churchfield *et al.* (2012*b*). Further, a gradually increasing velocity deficit appears throughout the farm. In the side

view, the vertical extent of the turbine wakes increases downstream, and the height of the capping inversion appears to increase as well. Behind the farm, the velocity in the boundary layer is lower but more turbulent than upstream, indicating the existence of a long wind-farm wake. In conclusion, figure 5.4 shows that the flow in both the precursor and main domain is fully turbulent and contains the proper turbulent structures, so flow statistics may be collected starting from this state onward.

5.3 General behaviour of a developing wind farm in the CNBL

First, the general behaviour of large developing wind farms under conventionally neutral conditions is described using the LES results from case S1, averaged over two simulation hours. For this case, the inversion layer is located relatively far away from the turbine region, so direct interactions between inner- and outer-layer dynamics are less likely to occur. This allows a first study of the wind-farm flow without having to cope with complex interactions between wind turbines and the inversion layer. The flow behaviour in the boundary layer is first examined in § 5.3.1. After that, the wind-farm performance is analysed quantitatively in § 5.3.2 by looking at the energy budget terms. Finally, atmospheric gravity waves and the corresponding structures in velocity, pressure and potential-temperature fields are discussed in § 5.3.3.

5.3.1 Boundary-layer flow behaviour

Contours of the time-averaged horizontal velocity magnitude $(\bar{u}^2 + \bar{v}^2)^{0.5}$ are shown in figure 5.5 for case S1. The planes are taken at the same locations as in figure 5.4, i.e., an x–y plane through the wind-turbine centres and an x–z plane through the middle of a column of turbines. The individual turbine wakes are clearly visible, and strong velocity deficits behind the first and second turbine rows are observed. Further downstream, wake recovery increases and the velocity deficit immediately behind the turbines is smaller. Figure 5.5(a) further shows that high-speed channels exist between turbine columns in the beginning of the farm. However, these channels gradually decelerate as turbine wake expansion fills up the spanwise spacing between the turbines.

In figure 5.5(b), an increasing velocity deficit above the wind turbine region is observed due to the wake expansion in the vertical direction. This expansion is quantified by the height of the internal boundary layer (IBL), i.e., the height up to which the flow has been modified by the increased drag of the wind turbines.

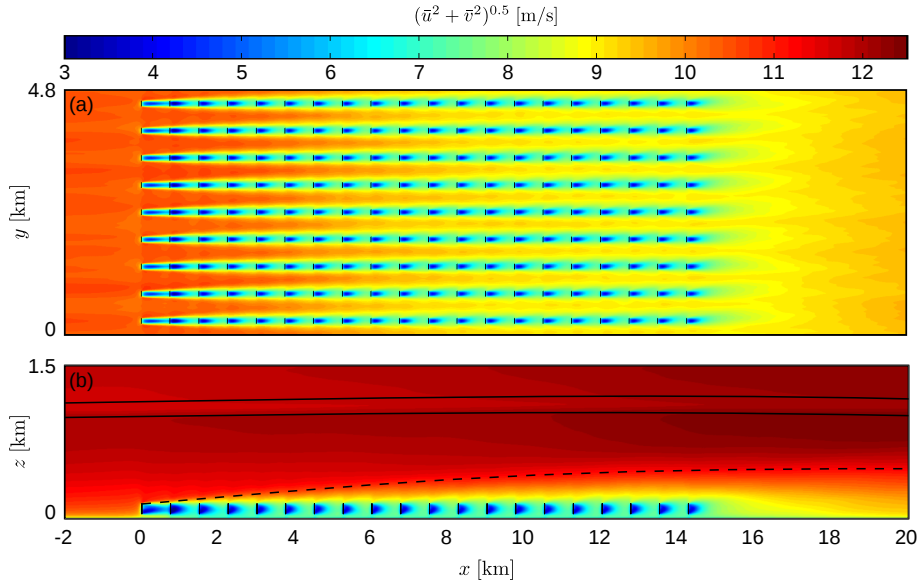

Figure 5.5: Contours of time-averaged horizontal velocity magnitude $(\bar{u}^2+\bar{v}^2)^{0.5}$, for case S1; (a) An x–y plane at turbine hub height $z_h = 100$ m; (b) An x–z plane through the middle of a turbine column (only the lower 1.5 km of the numerical domain are shown), showing the evolution of the inversion layer base and top (solid lines) as well as the growth of an internal boundary layer (dashed line). In (a) and (b), the location of the wind-turbine disks are indicated with vertical black lines.

Similar to Wu & Porté-Agel (2013), the IBL height is calculated as the height where the ratio of the time-averaged velocity and the inflow velocity at the same height, taken in a plane two kilometres upstream, reaches a threshold of 97 %. This height is shown as a dashed line in figure 5.5(b), together with the base and top of the inversion layer (solid lines). The internal boundary layer grows with increasing downstream distance, and it does not interact with the inversion layer located far above.

Figure 5.6(a) shows the increase in turbulent kinetic energy Δk with respect to the inflow in an x–z plane through the middle of a turbine column. The change in turbulent kinetic energy (TKE) starts in the turbine wakes in the lower part of the boundary layer and then spreads upwards with increasing downstream distance. The region of increased turbulence corresponds remarkably well with the internal boundary layer (marked by the dashed line), which certifies the estimate of the IBL height based on the velocity contours. Further, it is also

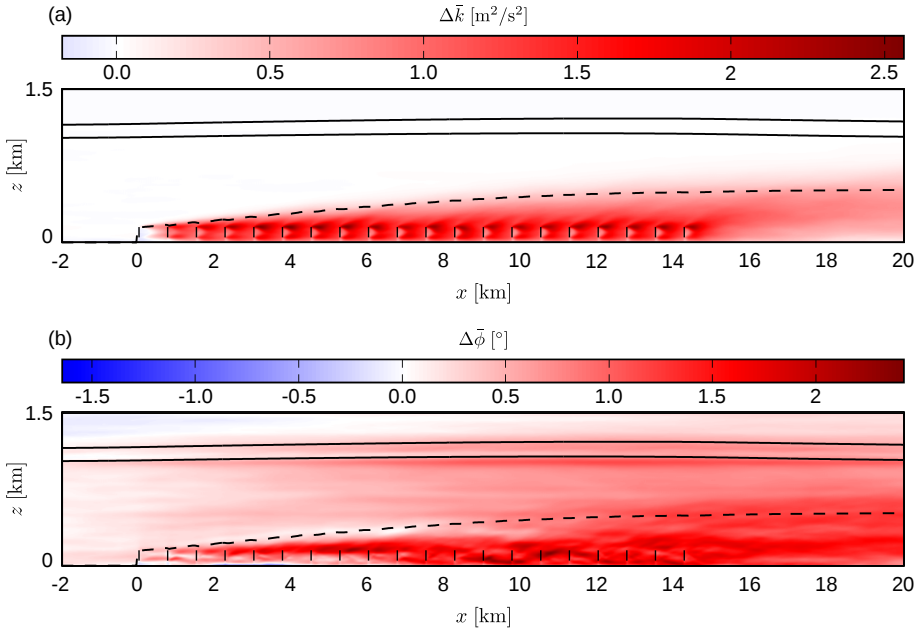

Figure 5.6: Contours of (a) turbulent kinetic energy increase $\Delta\bar{k}$ and (b) wind veer $\Delta\bar{\phi}$ with respect to the inflow, taken in an x–z plane through the middle of a turbine column (only the lower 1.5 km of the numerical domain are shown) and averaged over the last two simulation hours, for case S1. The evolution of the inversion layer base and top (solid lines) as well as the growth of an internal boundary layer (dashed line) are shown. Wind-turbine disk locations are indicated with vertical black lines, and only part of the numerical domain is shown.

clear that the flow behind the wind farm is significantly more turbulent than the flow upstream, indicating the existence of a wind-farm wake.

The streamwise mass transport inside the IBL is reduced due to the lower wind speed compared to upstream conditions. The continuity constraint requires this blockage effect to be compensated by either flow acceleration or boundary layer thickening. Whereas the neutral pressure-driven approach only allows for flow acceleration above the IBL because of the fixed boundary-layer height, a combination of both aspects is observed in figure 5.5(b). In fact, as can be seen in the figure, the inversion layer is pushed slightly upward, while at the same time, the flow also slightly accelerates below the inversion layer. It is further found that the centre of the inversion layer coincides almost exactly with a

streamline (not shown). This finding indicates that the lifting of the inversion layer is only due to the flow divergence and the accompanying displacement of streamlines, and that it is not related to enhanced turbulent mixing. This idea is supported by figure 5.6(a) showing no increased turbulence in or close to the inversion layer due its location far above the IBL.

The flow deceleration induces a second effect related to the Coriolis force and the horizontal force balance. As the Coriolis force scales linearly with the wind velocity, a slow down of the flow will reduce this force and cause the wind velocity to turn towards the direction of the pressure gradient. In figure 5.6(b), showing the difference in wind direction with respect to the inflow direction, this deceleration-induced flow rotation is clearly visible. Moreover, comparison with the TKE increase in figure 5.6(a) shows that the change in the wind direction occurs more uniformly across the boundary layer. Hence, the observation of Taylor (1969) that the wind direction and turbulent stress adapt very different to a surface roughness transition also holds for wind-farm boundary layers. In the current case, the maximal directional change is about 2° near the end of the farm. Dörenkämper *et al.* (2015) also observed a slight deviation to the left for a wind farm under stable atmospheric conditions, and attributed this deflection to the decrease in Coriolis force. Other studies reported wind-farm wakes turning away from the pressure gradient towards the geostrophic wind direction (Van der Laan *et al.* 2015; Volker *et al.* 2015), and they attributed this effect to turbulent transport of momentum from above. For the current simulations, however, it is found that enhanced turbulent mixing remains limited to the IBL and that the decrease in Coriolis forces dominates the turbulent transport of spanwise momentum, resulting in a wake deflection towards the pressure gradient.

5.3.2 Energy budget analysis

The gradual flow deceleration and turbine wake expansion will have an impact on the energy household in both the wind farm and the boundary layer. In order to understand the different processes that deliver energy to the turbines, the kinetic energy budget is analysed. The time-averaged kinetic energy equation (per unit mass) can be derived by multiplying equation (3.2) with u_i and

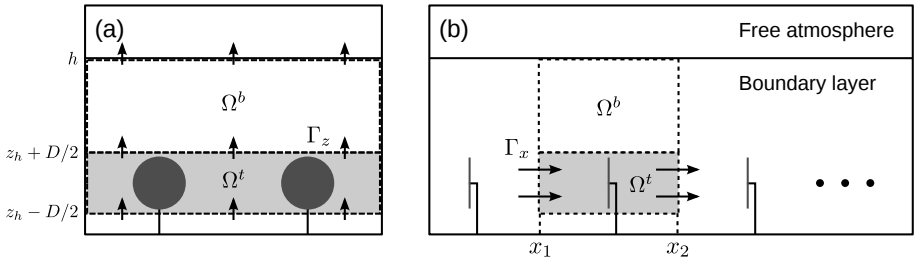

Figure 5.7: (a) Front view and (b) side view of the computational domain, illustrating the control volumes in the turbine region (Ω^t, grey encircled area) and in the layer above (Ω^b, white encircled area) over which the kinetic energy equation is integrated.

subsequently averaging the equation in time, resulting in

$$\frac{\partial}{\partial x_j}\left[\bar{u}_j\overline{E}_k + \bar{u}_i\overline{u_i'u_j'} + \frac{1}{2}\overline{u_i'u_i'u_j'} + \overline{u_i\tau_{ij}^{sgs}}\right] =$$

$$-\overline{\frac{u_i}{\rho}\frac{\partial p^\star}{\partial x_i}} + \frac{g}{\theta_0}\overline{u_3(\theta-\theta_0)} + \overline{\tau_{ij}^{sgs}S_{ij}} + \overline{u_i f_i} - \frac{\bar{u}_i}{\rho}\frac{\partial p_\infty}{\partial x_i}, \quad (5.2)$$

with $\overline{E}_k = (\bar{u}_i\bar{u}_i + \overline{u_i'u_i'})/2$ and $u_i' = u_i - \bar{u}_i$. The variation of the energy budget terms with streamwise distance is now of interest, i.e., how do the various terms change when going through the farm. In order to average out local oscillations around the turbines, equation (5.2) is integrated for every turbine row over a control volume. In fact, two different control volumes Ω^t and Ω^b are used to interpret the results, as indicated in figure 5.7. The kinetic energy budget for any control volume Ω can be written as

$$-\int_\Omega \underbrace{\frac{\partial \bar{u}_j\overline{E}_m}{\partial x_j}}_{\mathscr{D}}\,\mathrm{d}\Omega - \left[\int_\Gamma \left(\underbrace{\bar{u}_i\overline{u_i'u_1'} + \frac{1}{2}\overline{u_i'u_i'u_1'} + \overline{u_1'p'}/\rho + \overline{u_i\tau_{i1}^{sgs}}}_{\mathscr{F}_x}\right)\mathrm{d}\Gamma_x\right]_{x_1}^{x_2}$$

$$-\left[\int_\Gamma \left(\underbrace{\bar{u}_i\overline{u_i'u_3'} + \frac{1}{2}\overline{u_i'u_i'u_3'} + \overline{u_3'p'}/\rho + \overline{u_i\tau_{i3}^{sgs}}}_{\mathscr{F}_z}\right)\mathrm{d}\Gamma_z\right]_{z_l}^{z_u} - \int_\Omega \underbrace{\frac{\bar{u}_i}{\rho}\frac{\partial p_\infty}{\partial x_i}}_{\mathscr{P}_\infty}\,\mathrm{d}\Omega$$

$$+\int_\Omega \underbrace{\frac{g}{\theta_0}\overline{u_3(\theta-\theta_0)}}_{\mathscr{P}_\theta}\,\mathrm{d}\Omega + \int_\Omega \underbrace{\overline{\tau_{ij}^{sgs}S_{ij}}}_{\mathscr{E}}\,\mathrm{d}\Omega + \int_\Omega \underbrace{\overline{u_i f_i}}_{\mathscr{P}_F}\,\mathrm{d}\Omega = 0, \quad (5.3)$$

where p' is the turbulent fluctuation in $p^\star$ and (x_1, x_2, z_l, z_u) correspond to the boundaries of the control volume. The integrals need to be computed either over the entire control volume ($\mathrm{d}\Omega$), or over the y-z faces ($\mathrm{d}\Gamma_x$) or x–y faces ($\mathrm{d}\Gamma_z$) of the control volume. There is no transport through the x–z faces as all control volumes span the full domain width (remember that the domain is periodic in spanwise direction). Further, the total mechanical energy per unit mass is defined as the sum of kinetic energy and pressure, i.e., $\overline{E}_m = \overline{E}_k + \bar{p}^\star/\rho$. Note that the mean background pressure p_∞ is not included in the mechanical energy as its gradient represents constant meso-scale forcing.

Equation (5.3) expresses the balance between all energy sources (positive terms) and sinks (negative terms) in a control volume. The term $\mathscr{D}$ is the divergence of mechanical energy flux and combines the effects of mean-flow energy fluxes and pressure gradients. The terms $\mathscr{F}_x$ and $\mathscr{F}_z$ correspond to the net energy influx due to turbulent transport through the faces of the control volume in streamwise and vertical direction, respectively. These terms are positive (i.e., they act as a source of energy) when turbulence transports more energy in than out of the control volume. The fourth term ($\mathscr{P}_\infty$) is related to the mean background pressure, and the fifth term ($\mathscr{P}_\theta$) represents the conversion between kinetic and potential energy. The last two terms in equation (5.3) are energy sinks due to turbulent dissipation $\mathscr{E}$ and wind-turbine power extraction $\mathscr{P}_F$.

The kinetic energy balance in the turbine region is investigated first by considering control volumes Ω^t extending from $0.5 s_x D$ upstream of the turbine to $0.5 s_x D$ downstream in the streamwise direction. The turbine region is taken between $z_l = z_h - D/2$ and $z_u = z_h + D/2$ in the vertical direction, so the control volumes have dimensions $s_x D \times L_y \times D$ and are centred around the rotor disk (see figure 5.7).

For this configuration, figure 5.8(a) shows the streamwise variation of mechanical energy flux divergence $\mathscr{D}^t$, vertical energy transport related to turbulence $\mathscr{F}_z^t$, energy dissipation $\mathscr{E}^t$ and wind-turbine power extraction $\mathscr{P}_F$, scaled with the mean power output of the first turbine row (the subscript t indicates integration over Ω^t). The other terms ($\mathscr{F}_x^t, \mathscr{P}_\infty^t, \mathscr{P}_\theta^t$) in equation (5.3) are small compared to these dominant terms and are not shown. First, a large drop in power extraction is observed between the first and second turbine row, which is typical for aligned wind farms and reported in several studies (see, e.g., Barthelmie *et al.* 2009; Newman *et al.* 2013; Wu & Porté-Agel 2013; Stevens *et al.* 2014*b*). For the current case, the observed power drop of 63.5 % is more severe than the typical 40 % often documented in literature. This larger power deficit is attributed to the lower level of turbulent intensity in the current simulations. Following the sudden drop, the power increases slightly in the next couple of rows, after which it remains constant throughout the rest of the farm. Overall, the variation in power output from the third turbine row onward is less than

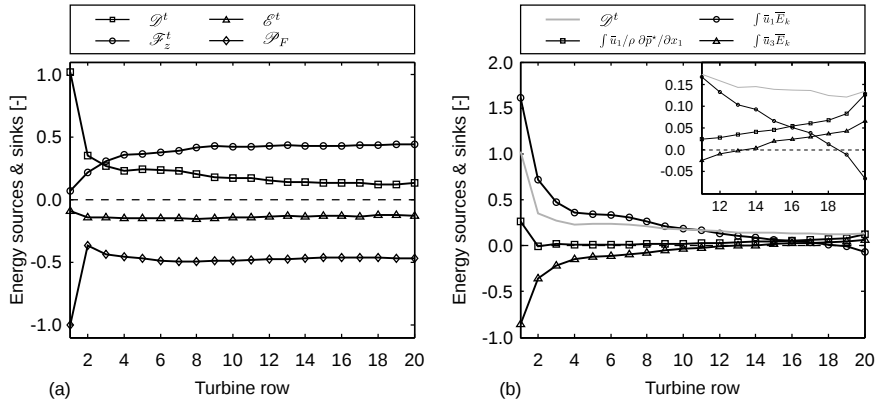

Figure 5.8: Streamwise variation of energy sources and sinks in the turbine region for case S1, normalised by the mean power extraction of the first turbine row. (a) Dominant energy sources and sinks in eq. (5.3), including mechanical energy flux divergence $\mathscr{D}^t$, vertical energy transport related to turbulence $\mathscr{F}_z^t$, energy dissipation $\mathscr{E}^t$ and wind-turbine power extraction $\mathscr{P}_F$; (b) Decomposition of the mechanical energy flux divergence $\mathscr{D}^t$ into energy related to streamwise pressure gradient and mean-flow kinetic energy transport in streamwise and vertical direction (see eq. (5.4)). In the top right corner, the components in the second part of the wind farm are magnified.

6 % of the power output of the first turbine. Further, the energy dissipation in the turbine region only varies about 3 % throughout the farm (w.r.t. the power output of the first turbine), except for the first turbine row where the dissipation is lower.

The energy extraction and dissipation are balanced by two different processes. The divergence of mechanical energy flux acts as a first source of energy. As observed in figure 5.8(a), this term is dominant in the first row but then quickly decreases throughout the farm. More insight can be gained by decomposing this energy source into four terms:

$$\mathscr{D} = \int_\Omega \left(\frac{\bar{u}_1}{\rho} \frac{\partial \bar{p}^\star}{\partial x_1} + \frac{\bar{u}_3}{\rho} \frac{\partial \bar{p}^\star}{\partial x_3} \right) \mathrm{d}\Omega + \left[\int_\Gamma \bar{u}_1 \overline{E}_k \, \mathrm{d}\Gamma_x \right]_{x_1}^{x_2} + \left[\int_\Gamma \bar{u}_3 \overline{E}_k \, \mathrm{d}\Gamma_z \right]_{z_l}^{z_u} . \quad (5.4)$$

The first two terms refer to the energy delivered or consumed by pressure gradients (excluding the mean background pressure), whereas the last two terms indicate the kinetic energy transported by the mean flow through the boundaries of the control volume. Figure 5.8(b) shows the mechanical energy divergence and the various components, except for the energy related to the vertical pressure

gradient which is negligible. From this figure, it is clear that, for every turbine row, there is more kinetic energy entering the control volume than leaving it through the y-z faces, thereby releasing a large amount of energy. However, a considerable amount of this energy leaves the control volume again through the upper or lower face. This is a logical consequence of the vertical mass flux out of the turbine region due to the flow deceleration and the continuity constraint. In other words, these results indicate that, although the flow deceleration releases a lot of energy, not all of this energy is available for power extraction by the wind turbines. Inevitably, part of the kinetic energy leaves the turbine region with the vertical mass flux. Furthermore, it is surprising to see that neither of these components nor the total mechanical energy divergence becomes zero in the farm, though the streamwise variations are expected to be negligible in a fully developed flow regime. This finding therefore suggests that, with respect to the mean flow, a fully developed regime is nowhere achieved. Figure 5.8(b) also contains a detailed view of the second half of the wind farm, showing some interesting developments near the end of the farm. First, both streamwise and vertical energy transport change sign in the last few rows, indicating that the wind is flowing downwards and accelerating. Second, there is a streamwise pressure gradient that is delivering energy, although its contribution remains relatively small. As discussed below, this pressure gradient is related to the effect of gravity waves.

The second source of energy that balances energy extraction and dissipation is related to vertical turbulent fluxes transporting kinetic energy from above the wind farm into the turbine region (see figure 5.8(a)). For fully developed wind farms, this energy transport provides almost all the kinetic energy extracted by the turbines (Calaf *et al.* 2010). For the developing case considered here, vertical turbulent energy transport is small at first but becomes the dominant source of energy starting from the third turbine row. From the eighth turbine row onward, this term varies less than 3 % of the power output of the first turbine. This means that, with respect to turbulent stresses and contrary to mean-flow behaviour, the turbulence can be considered fully developed after eight turbine rows.

In summary, figure 5.8 shows that the energy extracted by the turbines is provided by mean-flow deceleration in the turbine region and vertical turbulent energy transport from above the farm. However, the question then arises as to which processes are balancing the vertical energy transport in the boundary layer. In chapter 4, it was shown that the work by the background pressure gradient is the main source of energy in a fully developed wind farm, but it is unclear whether this conclusion also holds for developing wind farms. To answer this question, the energy budget analysis is repeated for control volumes Ω^b extending from $z_l = z_h + D/2$ up to the height of the boundary layer $z_u = h$

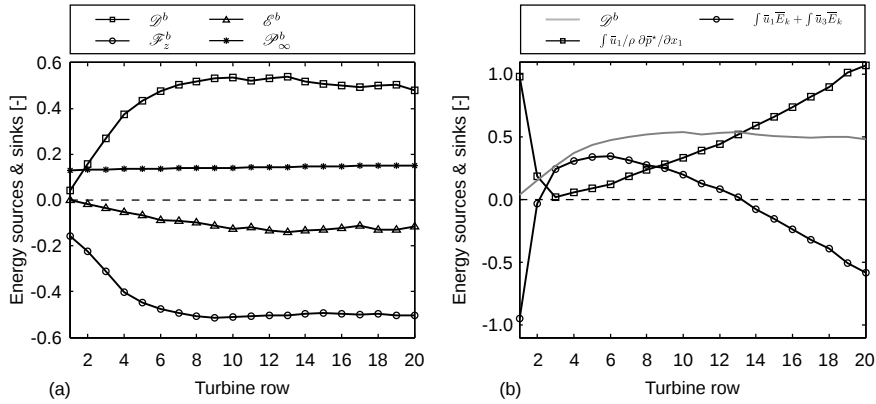

Figure 5.9: Streamwise variation of energy sources and sinks in the layer above the wind farm for case S1, normalised by the mean power extraction of the first turbine row. (a) Dominant energy sources and sinks in eq. (5.3), including mechanical energy flux divergence $\mathscr{D}^b$, vertical energy transport related to turbulence $\mathscr{F}_z^b$, energy dissipation $\mathscr{E}^b$ and work by the mean background pressure $\mathscr{P}_\infty^b$; (b) Decomposition of the mechanical energy flux divergence $\mathscr{D}^b$ into energy related to streamwise pressure gradient and divergence of the mean-flow kinetic energy flux (i.e., the sum of the last two terms in eq. (5.4)).

(the streamwise and spanwise dimensions are unchanged, see figure 5.7), and the results are presented in figure 5.9.

The energy balance in the region above the wind farm is governed by mechanical energy divergence $\mathscr{D}^b$, vertical turbulent transport $\mathscr{F}_z^b$, energy dissipation $\mathscr{E}$ and work by the mean background pressure $\mathscr{P}_\infty^b$ (potential energy conversion and streamwise turbulent transport are again small and therefore not shown). Contrary to the results of the previous chapter, figure 5.9(a) shows that the vertical turbulent transport is mainly balanced by the mechanical energy flux divergence $\mathscr{D}^b$, and the work by the mean background pressure is only about $0.3\mathscr{D}^b$ except above the first few rows. As before, the dominant energy source can be further investigated by decomposing it according to equation (5.4), as shown in figure 5.9(b). The energy related to the vertical pressure gradient is again negligible, and the last two terms are combined to give the divergence of the mean-flow kinetic energy flux. This mean-flow divergence indicates whether the total kinetic energy of the layer above the farm is increasing or decreasing when advancing in streamwise direction. Negative values thereby correspond to a kinetic energy increase and are mainly related to flow acceleration, whereas positive values are caused by the IBL growth and the accompanying velocity

deficit inside it. It appears that the flow acceleration is dominant at the beginning and end of the farm, but the IBL growth dominates in the middle and causes the total kinetic energy to decrease. Finally, it is observed that a considerable amount of energy is delivered by a streamwise pressure gradient. This pressure gradient is caused by gravity waves, further discussed in the next section.

5.3.3 Wind-farm induced gravity waves

The displacement of the streamlines above the IBL, observed in figure 5.5(b), excites gravity waves in the inversion layer and the stably stratified free atmosphere. The evidence of these waves is found in figure 5.10, showing contours of streamwise and vertical velocity, pressure and potential temperature, averaged in time and in spanwise direction, for case S1. Note that the mean inflow profile has been subtracted from the time-averaged solution fields of streamwise velocity and potential temperature. The wind-farm induced atmospheric gravity waves create a slanted pattern of alternating positive and negative perturbations in the solution field of every variable. The size and inclination of these structures is the same for every variable, but the exact location of minima and maxima differs according to the polarisation equations (Nappo 2002). For instance, the streamwise velocity and the pressure are anti-correlated, whereas the potential temperature perturbations have a 90° phase difference with the other variables (e.g., $\langle\bar{\theta}\rangle - \theta_{ref} = 0$ when $\langle\bar{p}^\star\rangle$ reaches an extremum, and vice versa). It is further observed that the group velocity of these waves forms an angle of about 20° with the horizontal.

In the vertical velocity field, the wave pattern appears less orderly than in the other wave fields. These distortions are caused by partial wave reflection from the top of the domain, which are most obvious in the vertical velocity field. In order to verify the efficiency of the upper boundary condition, the method provided by Taylor & Sarkar (2007) is used. Based on the intrinsic property that the sign of the vertical group velocity is opposite to the sign of the vertical phase velocity, the wave field can be decomposed into upward and downward propagating waves. As the only source of gravity waves is located near the bottom of the domain, downward propagating waves must be due to reflection from the top. For case S1, the vertical kinetic energy ($0.5w^2$) associated with downward propagating waves is about 7.8 % of the energy associated with upward propagating waves, which is similar in order of magnitude to Taylor & Sarkar (2007). For other cases discussed in the current work (S2 and S4), the reflected energy is 6.2 % and 4.8 %, respectively.

The mechanism triggering the gravity wave solution can also be appreciated

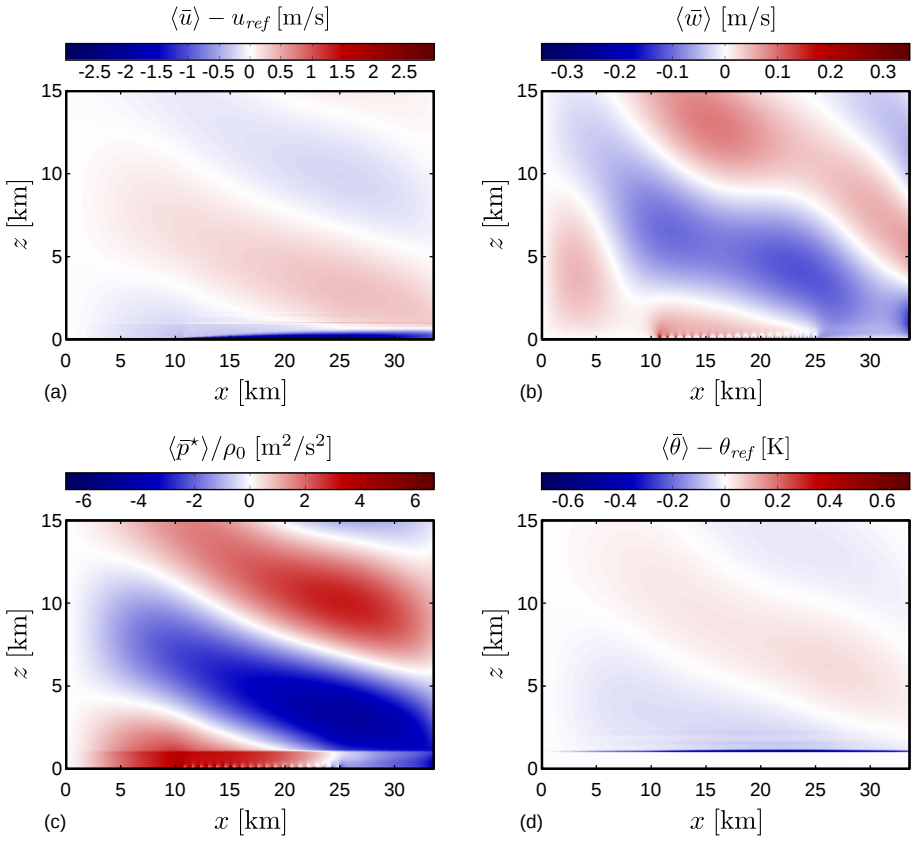

Figure 5.10: Contours of (a) streamwise velocity, (b) vertical velocity, (c) pressure and (d) potential temperature, averaged in time and in spanwise direction, for case S1. The mean inflow profile has been subtracted from the time-averaged solution fields of streamwise velocity and potential temperature to obtain perturbation quantities.

from figure 5.10. As the wind turbines extract energy from the flow, a momentum deficit accumulates in the wind farm, indicated by the negative velocity perturbation inside the wind farm in figure 5.10(a). As mentioned before, the continuity constraint results in an upward flow deflection, which appears as a positive vertical velocity above the farm in figure 5.10(b)). This vertical velocity pushes the inversion layer upwards and results in a thickening of the boundary layer. The upward displacement of the inversion layer appears as a negative perturbation in the potential-temperature field (see figure 5.10(d)), as cold air is brought up from below. Finally, similar to stratified flow over topography, the combination of temperature stratification and boundary-layer displacement results in the formation of gravity waves.

Besides the obvious vertically propagating gravity waves in the free atmosphere, a strong vertical pressure gradient is also observed near the inversion layer in figure 5.10(c). The difference in pressure above and below the inversion is caused by the simple fact that a cold temperature anomaly induces a high pressure anomaly below (Smith 2010). As the boundary-layer height increases, the column of cold, heavy air grows taller and result in a higher pressure. The pressure inside the boundary layer is thus the sum of two components related to the vertically propagating waves and to the inversion strength. Figure 5.10(c) shows that the gravity waves induce a favourable pressure gradient inside the wind farm, similar to the findings of Smith (2010) based on linear gravity wave theory. The amplitude of the induced pressure gradient is of the same order of magnitude as the background pressure gradient in streamwise direction, which is on the order of 10^{-4} m/s^2.

5.4 Developing wind farms under various inflow conditions

In the current section, the effects of varying inflow heights on wind-farm boundary layers is investigated. As before, the focus lies first on the flow behaviour inside and above the wind farm (§ 5.4.1). Subsequently, wind-farm power extraction and energy budget terms of the different cases will be discussed in § 5.4.2.

5.4.1 Flow modification under low inversion layers

Figure 5.11 shows contours of time-averaged horizontal velocity in an x–z plane through the middle of a turbine column for the various cases. Inside the farm, the velocity fields look very similar apart from the small differences in velocity

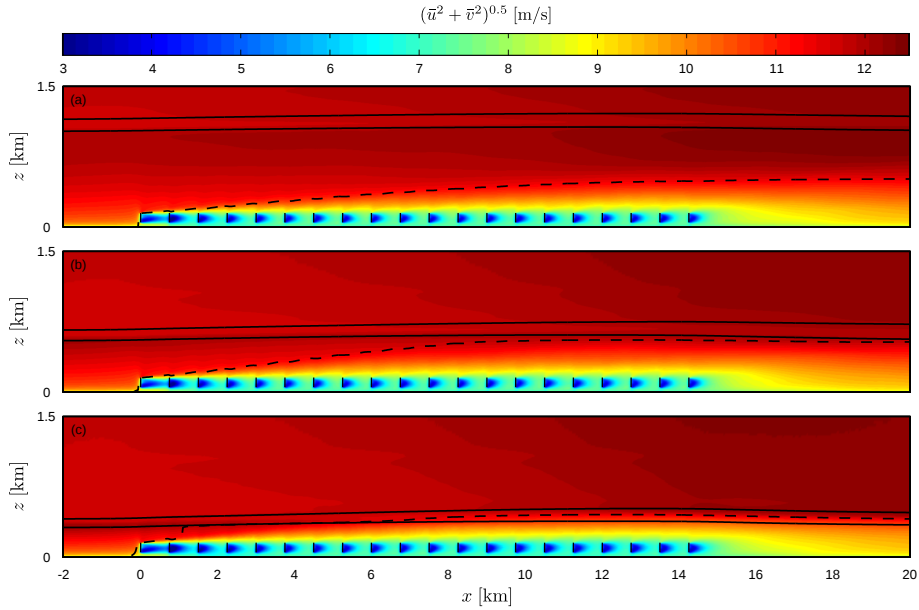

Figure 5.11: Contours of time-averaged horizontal velocity $M = (\bar{u}^2 + \bar{v}^2)^{0.5}$ in an x–z through the middle of a turbine column, for cases (a) S1, (b) S2 and (c) S4. The evolution of the inversion layer base and top (solid lines) as well as the growth of the IBL height (dashed line) are included. The location of the wind-turbine disks are indicated with vertical black lines.

deficit in the turbine wakes. However, the shape of the internal boundary layer indicates that there are important differences in the boundary-layer flow between the three cases. In the previous section, it was found that the IBL does not interact with the inversion layer in the baseline case. Lowering the inflow height results in a collision between the IBL and the inversion at some point in the farm, and the IBL growth is limited further downstream. This event occurs around the twelfth turbine row for case S2, whereas in case S4 the IBL and the inversion coincide almost immediately. In fact, it is difficult to define the exact height of the IBL for the latter case, as the wind farm causes a strong reduction in wind speed upstream of the farm.

Figure 5.11 further shows that, in contrast to case S1, the wind-farm blockage effect does not result in flow acceleration between the IBL and the inversion in case S2 and S4. Instead, the entire reduction in streamwise mass transport is compensated by the displacement of the boundary layer top, as shown in figure 5.12(a). For the wind farm under consideration, lowering the inversion from

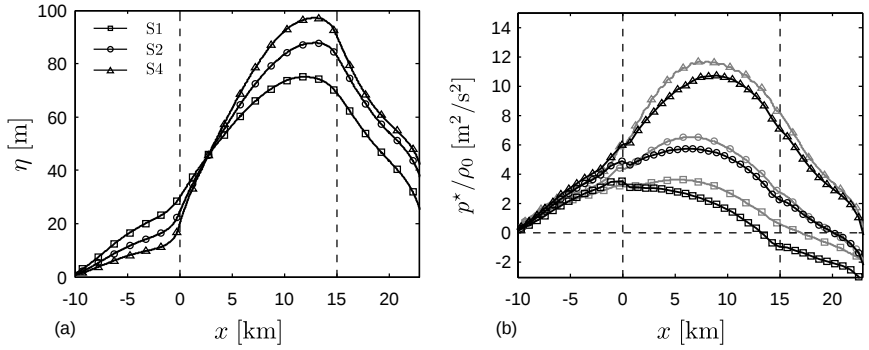

Figure 5.12: Streamwise variation of (a) boundary-layer top displacement and (b) mean pressure perturbation for cases S1, S2 and S4. The vertical dashed lines indicate the start and end of the wind farm. In (b), the pressure prediction based on linear theory is included (gray linestyles).

1000 m to 300 m raises the maximum displacement from 75 m to 97 m. This corresponds to a relative thickening of the boundary layer of 33 % in case S4. Further, it is observed that the ascent of the boundary-layer top already starts upstream of the wind farm. On the other hand, the maximum displacement of the boundary-layer top and the onset of its descend always occur before the end of the farm.

Figure 5.12(b) shows the mean pressure perturbation in the boundary layer averaged over a control volume with dimensions $s_x D \times L_y \times h$ with h the height of the boundary layer. As the pressure perturbations are directly related to the boundary-layer displacement, the pressure also increases for decreasing inflow heights. The general shape of the perturbation is similar in all cases: the pressure increases upstream of the farm, reaches a maximum somewhere inside the farm and then decreases. For case S1, the maximum pressure occurs at the beginning of the farm, creating a favourable pressure gradient throughout the farm. However, the location of the maximum moves downstream with decreasing inflow heights, which induces counteracting pressure gradients in the first part of the farm. According to linear theory (Smith 2010), the Fourier transformation of the pressure at the top of the boundary layer is given by $\hat{p}/\rho_0 = (iN^2/m + g')\,\hat{\eta}$, where the first term is the perturbation caused by vertically propagating gravity waves, and $g' = g\Delta\theta/\theta_0$ is a reduced gravity accounting for the inversion strength. Using the LES data for the boundary-layer displacement η, predictions of the pressure perturbation are obtained from linear theory and also included in figure 5.12(b). The agreement with the actual pressure is remarkably good, both in terms of perturbation magnitude and

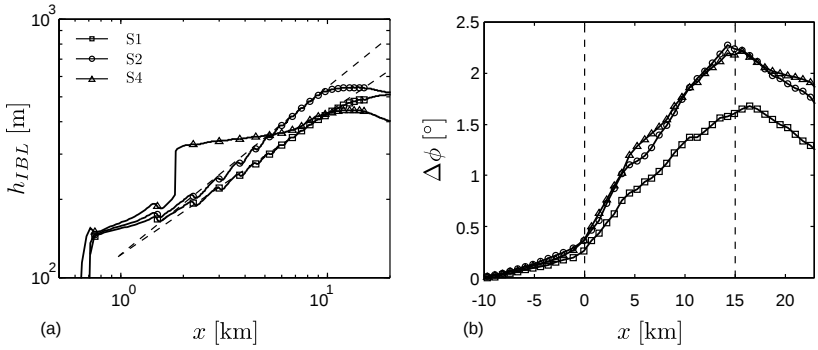

Figure 5.13: (a) Internal boundary layer height, shown in a double logarithmic scale, and (b) difference in wind direction at hub height with respect to the inflow wind direction, averaged over the full spanwise direction and over a streamwise distance $s_x D$ centred around each turbine row, for cases S1, S2 and S4. The dashed lines in (a) correspond to slopes of 0.55 and 0.65. The vertical dashed lines in (b) indicate the start and end of the wind farm.

shape. Linear theory overestimates pressure perturbations from the LES, and the location of the maximum is predicted too far downstream for case S1.

The IBL height of the different cases are compared in figure 5.13 in a double logarithmic scale. For cases S1 and S2, the height evolution follows a slope of 0.55 and 0.65, respectively. These findings indicate that the 0.8 law of Elliott (1958) overpredicts the IBL growth in wind farms, which was also concluded by Blom & Wartena (1969) and Walmsley (1989) for surface roughness transitions. In case S2, the growth rate is limited near the end of the farm when the IBL collides with the inversion layer. In case S4, the IBL behaves totally different as the growth is limited by the inversion layer already after two turbines rows.

Figure 5.13(b) shows the difference in wind direction at hub height with respect to the inflow wind direction, averaged over the full spanwise direction and over a streamwise distance $s_x D$ centred around each turbine row. The mean wind deviation at hub height increases almost linearly through the farm and reaches a maximum of about 1.5° for case S1. The maximum wind deviation increases to 2.3° when lowering the inversion from 1000 m to 500 m, but stays the same when the inflow height is further reduced.

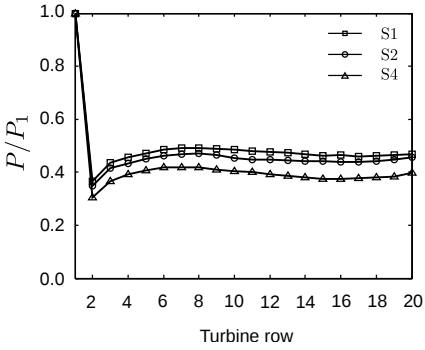

Figure 5.14: Mean power extraction per turbine row, normalised by the first row, for cases S1, S2 and S4.

5.4.2 Wind-farm power extraction

The wind-farm performance in the various cases is presented in figure 5.14, showing the mean turbine power extraction per row. The results have been normalised by the mean power (per unit density) of a first row turbine, which was found to be 2.80, 2.79 and 2.73 [$\times 10^6$ m^5/s^3] in cases S1, S2 and S4, respectively. The general trend in the power extraction per turbine row is very similar among the various cases, but the power deficits are slightly larger for decreasing inflow boundary-layer heights. For example, the turbine power output in case S4 is 6 to 9 percentage points (pp) lower than the power output in the same row in case S1. Note that these differences are much smaller than those observed in the fully developed case in chapter 4.

The variation of the power deficit with varying inflow height can be further clarified by investigating the dominant energy sources in the turbine region, i.e., the turbulent transport of kinetic energy from above and the mechanical energy divergence, as shown in figure 5.15(a). For all cases, mechanical energy divergence is large in the beginning of the farm, and vertical turbulent energy transport becomes dominant after a couple of turbine rows. Decreasing the inflow height reduces turbulent energy transport with about 12 pp between S1 and S4, whereas the maximum difference in mechanical energy divergence is only 5 pp for these cases. Hence, the difference in wind-farm performance is mainly due to the difference in turbulent energy transport. Note also that the mechanical energy divergence stays significant throughout the farm in all cases, i.e., about 30 to 35 % of the turbulent flux.

The small differences in mechanical energy divergence are further explained in

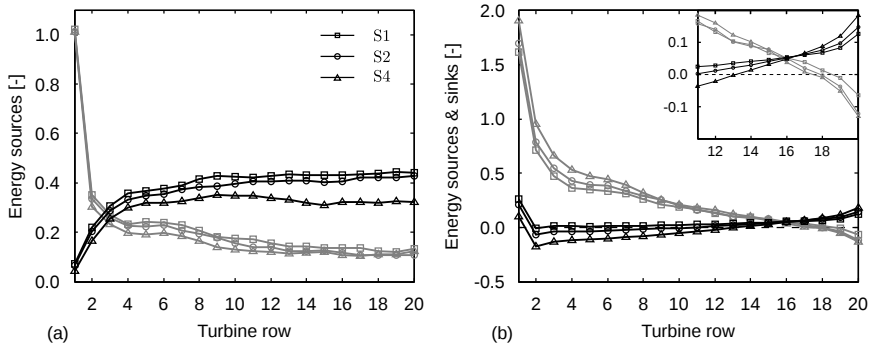

Figure 5.15: Streamwise variation of energy sources and sinks in the turbine region for cases S1, S2 and S4, normalised by the mean power extraction of the first turbine row. (a) Dominant energy sources of eq. (5.3), including mechanical energy flux divergence $\mathscr{D}^t$ (gray linestyles) and vertical energy transport related to turbulence $\mathscr{T}_z^t$ (black linestyles); (b) Energy related to streamwise pressure gradient (black linestyles) and mean flow kinetic energy transport in streamwise direction (gray linestyles) (see eq. (5.4)). In the top right corner, the components in the second part of the wind farm are magnified.

figure 5.15(b), showing terms one and three in equation (5.4) for the various cases. In accordance with the pressure profiles in figure 5.12(b), the cases with a lower inflow height experience an energy sink in the first part of the farm due to the counteracting pressure gradient. Further downstream, the induced pressure gradients become favourable and act as a source, as can be seen in the detailed plot in the top right corner. Interestingly, the streamwise mean-flow deceleration increases with decreasing inflow boundary-layer heights due to counteracting pressure gradient and partially due to the higher vertical mass flux (not shown here). This term becomes negative near the end of the farm in all cases, indicating that the wind is flowing downwards and accelerating.

Similar to the analysis in § 5.3.2, the processes that balance vertical turbulent energy transport can be investigated by looking at the energy budget in the region above the wind farm. The dominant energy terms in this region are shown in figure 5.16(a). The work by the mean background pressure is highest when the inflow height is high, but remains small in all cases compared to the mechanical energy divergence. The latter rises sharply in the first few rows and then decreases slowly towards the end of the farm. The initial rise collapses for all cases, whereas the subsequent decrease is strongest for the lowest case.

The decomposition of the mechanical energy divergence into work by streamwise

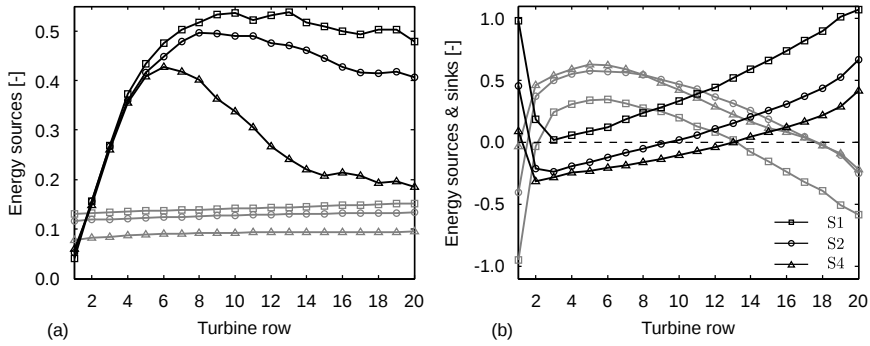

Figure 5.16: Streamwise variation of energy sources and sinks in the layer above the wind farm for cases S1, S2 and S4, normalised by the mean power extraction of the first turbine row. (a) Dominant energy sources of eq. (5.3), including mechanical energy flux divergence $\mathscr{D}^b$ (black linestyles) and work by the mean background pressure $\mathscr{P}^b_\infty$ (gray linestyles); (b) Energy related to streamwise pressure gradient (black linestyles) and divergence of the mean-flow kinetic energy flux (gray linestyles) (see eq. (5.4)).

pressure gradients and divergence of mean-flow kinetic energy flux is shown in figure 5.16(b). Despite the relatively small changes in the mechanical energy divergence, large variations are observed in both contributing terms. Furthermore, the behaviour of both terms is almost reversed, i.e., an increase in work by pressure gradients is mostly accompanied by a decrease in mean-flow divergence and vice versa. This complex interplay can be better understood in terms of the energy flux. Therefore, figure 5.17 presents the total flux of mechanical energy through the boundary layer and the contributions of kinetic energy and pressure (excluding the mean background pressure). The results are normalised by the flux at the entrance of the farm, and figure 5.17(b) shows the relative change in both contributions with respect to the inflow. In figure 5.17(a), the energy flux is nearly constant upstream of the farm which indicates that the boundary layer is in a quasi-equilibrium state. Inside the farm, the total mechanical energy flux decreases monotonically throughout the wind farm as energy is being extracted by wind turbines and dissipated by turbulence. It is observed that the relative reduction in energy flux increases for decreasing boundary-layer heights, i.e., a reduction of 11 %, 22 % and 31 % in cases S1, S2 and S4, respectively. Downstream of the farm, the energy flux is considerably lower than upstream, and the flux remains constant or increases slightly.

Figure 5.17(b) shows that the mechanical energy in the boundary layer is not always available in the form of kinetic energy, as part of the energy is contained

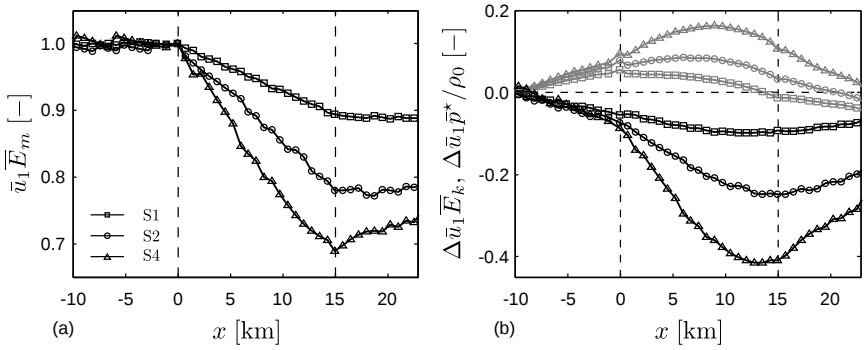

Figure 5.17: (a) Total mechanical energy flux in the boundary layer and (b) contributions of kinetic energy (black linestyles) and pressure (gray linestyles), for cases S1, S2 and S4. All results are normalised by the total mechanical energy flux at the entrance of the farm, and in (b) the relative change with respect to the inflow ($x = -10$) is shown.

in the pressure field that is induced by the gravity waves. Moreover, significant conversion between kinetic energy and pressure occurs throughout the boundary layer, even when the total mechanical energy flux remains constant. Upstream of the farm, the kinetic energy flux decreases and causes the pressure to rise. At some point in the farm, the pressure starts to decrease, thereby releasing its energy to the boundary layer. The effect of the pressure gradient is thus to redistribute energy throughout wind farm. This effect is largest for the lowest CNBL case where, at the pressure peak, more than 16 % of the total mechanical energy flux is comprised of pressure contributions, all of which is gathered upstream and in the beginning of the farm and released again in the last rows and in the wind-farm wake.

5.5 Summary

The current chapter set out to analyse how boundary-layer flow adapts to the presence of a large wind farm under conventionally neutral conditions. Streamwise flow development was obtained by breaking the solver's periodicity with the concurrent-precursor method, and special care was taken to avoid wave reflection at the domain boundaries. Further, the boundary-layer flow and the wind farm were initialised in several steps in order to represent a realistic, offshore wind farm operating in steady state conditions. A set of simulations was performed with varying inflow boundary-layer heights, allowing to study

the impact of the boundary-layer depth and the overlying inversion layer on the flow behaviour.

Boundary-layer flow was found to adapt gradually to the increased drag of the wind turbines in the form of an internal boundary layer. The observed growth rates were lower than Elliott's 0.8 power law, and interaction with the capping inversion occurred downstream for the two lowest CNBL cases. The wind farm also caused an upward displacement of the inversion layer, which was related to the blockage effect and flow divergence, not to enhanced turbulent mixing. This displacement in turn excited gravity waves in the inversion and in the free atmosphere, which imposed pressure perturbations on the boundary layer.

A detailed analysis of the kinetic energy equation showed that the energy extracted by the turbines is provided by two different processes, i.e., the deceleration of mean flow and the transport of energy from above the farm by turbulent fluxes. With respect to the turbulent stresses, the flow in the wind farm reached a fully developed regime after about eight turbine rows. However, streamwise variations in the mean-flow behaviour were observed up till the last turbine row, which suggests that the mean flow did not reach a fully developed regime. Further, it was found that the vertical turbulent energy transport was balanced by mechanical energy divergence in the layer above the wind farm, and that, contrary to the fully developed case, the background pressure gradient was only of minor importance.

The wind-farm efficiency was found to be sensitive to the undisturbed boundary-layer height, showing increasing power deficits for decreasing inflow heights. For the wind farm under consideration, lowering the inflow height from 1000 m to 300 m increased the power deficits in downstream turbine rows with 6 to 9 percentage points. The observed differences were caused by a decrease in turbulent energy transport, while variations in the mechanical energy divergence in the turbine region were small. Further analysis showed that nearly all energy available at turbine level comes from upstream mechanical energy in the boundary layer. This mechanical energy, however, was not always present in the form of kinetic energy as some part was stored in the pressure field induced by gravity waves. Gravity waves thereby tend to redistribute the kinetic energy throughout the farm, and this effect was largest for low boundary-layer heights.

In the current chapter, the case of a finite-length wind farm but with an infinite width was considered. In real wind farms, the blockage effect due to turbine drag will be lower as the wind can flow around the wind farm in the spanwise direction. Therefore, the boundary-layer displacement and excitation of gravity waves found in the current chapter may be overestimated compared to operational wind farms of finite width. Furthermore, the free atmosphere was assumed to be in steady-state, barotropic conditions with a fixed stratification of 1 K/km.

Allowing for baroclinity or varying the free-atmosphere stratification will affect gravity wave properties considerably. As the pressure gradients induced by gravity waves were found to play an important role in the energy budget of the boundary layer, further research is required to determine the effect of gravity waves in fully finite wind farms and subject to various atmospheric conditions. Next to this, equilibrium CNBLs over sea can be even lower than the cases considered in the current chapter, so that turbines may penetrate the inversion layer. This case also forms an interesting topic for further research.

Chapter 6

Wind farms in stable atmospheric boundary layers

The present chapter studies wind-farm boundary-layer flow under stably stratified conditions. The stable atmospheric boundary layer (§ 2.3.2) is characterised by lower turbulent intensity and higher velocity shear than the conventionally neutral ABL considered thus far. Therefore, less efficient turbine-wake recovery and increased wind-farm power deficits are expected. Moreover, the reduced vertical mixing of momentum in the SBL compared to the CNBL gives rise to larger geostrophic wind angles, so that the relative wind-farm layout in the mean wind direction gradually changes in time as the stable boundary layer develops.

Simulations of an equilibrium, conventionally neutral boundary layer developing into a stable boundary layer due to surface cooling are performed. This situation represents the evening transition of an onshore ABL into the nocturnal boundary layer. Two cases with surface cooling rates of 0.25 K/h and 0.75 K/h are simulated to investigate the performance of a large wind farm, in which the turbines are arranged in an aligned pattern with respect to the initial flow direction. As in chapter 5, the concurrent-precursor method is applied to allow the study of entrance effects and boundary-layer development in the wind farm.

This chapter is further organised as follows. The numerical set-up of the wind farm and the computational domain is summarised in section 6.1. Next, section 6.2 describes the initialisation and transition of the boundary-layer flow in the precursor simulation. The results of the wind-farm simulations are discussed in section 6.3, and conclusions are given in section 6.4.

Table 6.1: Case set-up for the wind-farm–SBL simulations.

Main domain size	$L_x \times L_y \times L_z = 28.8 \text{ km} \times 4.8 \text{ km} \times 25 \text{ km}$
Precursor domain size	$L_x \times L_y \times L_z = 9.6 \text{ km} \times 4.8 \text{ km} \times 25 \text{ km}$
Main domain grid	$N_x \times N_y \times N_z = 2304 \times 384 \times 700$
Precursor domain grid	$N_x \times N_y \times N_z = 768 \times 384 \times 700$
Vertical grid resolution	$\begin{cases} \Delta z = 5 \text{ m}, & 0 < z < 1.5 \text{ km} \\ \Delta z = 5 - 40 \text{ m}, & 1.5 < z < 15 \text{ km} \\ \Delta z = 40 - 300 \text{ m}, & 15 < z < 25 \text{ km} \end{cases}$
Horizontal grid resolution	$\Delta x \times \Delta y = 12.5 \text{ m} \times 12.5 \text{ m}$
Turbine arrangement	14 rows × 9 columns
Turbine dimensions	$D = 100 \text{ m}$ and $z_h = 100 \text{ m}$
Turbine spacing	$s_x = 7.5D$ and $s_y = 5.33D$

6.1 Numerical set-up

The SP-Wind solver is used to simulate a large, onshore wind farm subject to varying surface cooling rates. Wind-farm entrance effect and boundary-layer development are again included in the simulations by using the concurrent-precursor method. Based on the conclusions of the SBL validation study in § 3.5.3, the TKE model (see § 3.3.1) is used as subgrid-scale model and the horizontal grid resolution is refined to 12.5 m × 12.5 m. The current section describes the set-up of the wind farm and the numerical domain, whereas the atmospheric conditions and the initialisation procedure are discussed in the next section.

Table 6.1 summarises the set-up of the wind farm and the numerical domain. The wind farm considered here is slightly smaller than that of the previous chapter as the finer grid resolution significantly increases the computational cost. The wind farm now consists of 126 turbines with diameter $D = 100$ m and hub height $z_h = 100$ m, arranged in an aligned pattern of 14 rows by 9 columns with respect to the mean flow direction under conventionally neutral conditions. Using the same turbine spacing as before, i.e., $s_x = 7.5$ and $s_y = 5.33$, the wind farm covers an area of roughly 10 km × 4.8 km. Furthermore, the disk-based thrust coefficient C_T' is again set to 4/3, the time-filtered disk velocity is based on a time constant of 5 s, and the yaw controller of § 5.1.2 is applied with an averaging time of 10 min.

Atmospheric turbulence is generated in a precursor domain with the same

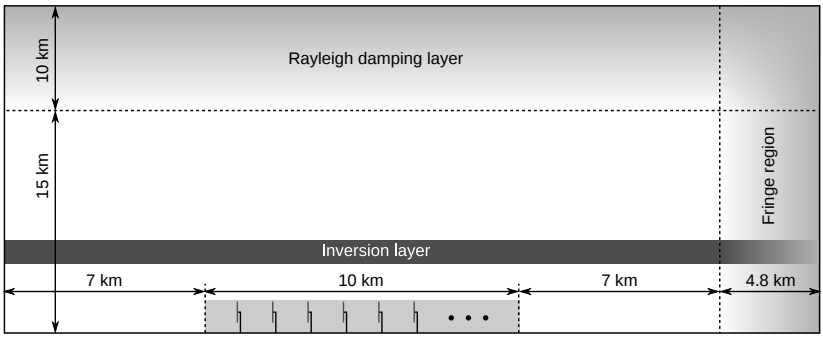

Figure 6.1: Sketch of the numerical domain, showing the relative positions of the wind farm, the fringe region and Rayleigh damping layer. The vertical scale is exaggerated as the inversion layer occurs at 1 km.

horizontal domain size as that used in the previous chapter, i.e., $L_x \times L_y = 9.6\text{ km} \times 4.8\text{ km}$. The size of the main domain is reduced to $L_x = 28.8$ km, so it is now only three instead of four times the length of the precursor domain. The vertical domain size and vertical grid resolution are equal to that of case S1 in the previous chapter, i.e., a vertical grid resolution of 5 m up to 1.5 km, above which the grid is stretched in two steps: a resolution of 5–40 m up to $z = 15$ km ($f_s = 1.0966$) and a resolution of 40–300 m above 15 km ($f_s = 1.0689$). The spatial layout of the numerical domain is very similar to that used before and is shown in figure 6.1. The wind farm is placed in the middle of the domain and is separated from the fringe region by 7 km in both upstream and downstream direction. The fringe region and Rayleigh damping layer are identical to the ones used in the previous chapter, i.e., widths of 4.8 km and 10 km, respectively, and damping coefficients equal to 0.03 s^{-1} and 0.0001 s^{-1}, respectively.

6.2 Precursor simulation: CNBL to SBL transition

In the precursor domain, the evening transition from a daytime CNBL to a surface-cooled SBL at night is simulated in order to provide inflow conditions for the wind farm in the main domain. First, an equilibrium CNBL is simulated, the set-up and result of which are discussed in § 6.2.1. Subsequently, surface cooling is activated and the CNBL evolves into an SBL, which is described is section 6.2.2.

6.2.1 An equilibrium onshore CNBL

The spin-up of the equilibrium CNBL is very similar to the procedure used in the previous chapter. However, the surface roughness length z_0 is now set to 0.1 m to represent flow over land. As in the previous chapter, barotropic conditions with a geostrophic wind speed of $G = 12$ m/s are considered, and the Coriolis parameter $f_c = 10^{-4}$ s^{-1}. Further, the height of the inversion layer is chosen to be 1000 m, the free atmosphere lapse rate γ equals 1 K/km and the temperatures θ_0 and θ_m are taken to be 288.15 K.

The strength of the inversion layer should be high enough to limit turbulent entrainment and to keep the CNBL in equilibrium. An estimate can be obtained with the empirical formulation of Csanady (1974) (i.e., eq. (2.8)). All parameters in this formula are known except for the friction velocity u_*, which can be obtained from the CNBL model developed in section 4.4 and appendix B. Solving equation (4.23) for the geostrophic drag $C_g = u_*/G$ with the given surface roughness, boundary-layer height and Rossby number yields a friction velocity of 0.53 m/s. Equation (2.8) then finds $\Delta\theta > 4.06$ K, so the inversion strength is set to 5 K.

Initial velocity and potential-temperature profiles are obtained with the procedure explained in § 4.1.3, and random divergence-free perturbations with an amplitude of $0.1G$ are added in the velocity field below 100 m to trigger turbulence. As in the previous chapter, only the lower 5 km of the numerical domain are simulated as no large-scale gravity waves occur during the first spin-up, and Rayleigh damping is applied between 2 and 5 km. Furthermore, the wind-angle controller discussed in § 4.1.1 is activated during this step to align the flow direction at hub height with the x-direction. The CNBL is allowed to develop for 15 hours in the precursor domain until a quasi-steady, fully turbulent state is reached.

Some steady state parameters of the equilibrium state are given in table 6.2. The *offshore* values are obtained from case S1 of the previous chapter and are given here for reference. The height of the inversion centre is almost unchanged and the boundary-layer growth is very small, demonstrating that the CNBL is in equilibrium and that an adequate inversion strength was chosen. The higher surface roughness of land compared to sea leads to lower wind velocity and higher turbulent intensities at hub height. The friction velocity has also increased, and matches very well with the estimate based on equation (4.23). Further, the lower wind speeds near the surface cause the wind to turn more towards the direction of the pressure gradient, which leads to a larger geostrophic angle compared to the offshore case.

After the initial 15 hours, the simulation is advanced for an additional 20 min

Table 6.2: Steady state parameters of the onshore equilibrium CNBL, including the height of the inversion layer centre h_1, the boundary-layer growth $\partial h_1/\partial t$, the hub-height velocity M_{hub}, the friction velocity u_*, the geostrophic wind angle α and the turbulent intensity at hub height TI. The offshore values are given for reference and are obtained from case S1 of the previous chapter (see table 5.2)

	h_1 [m]	$\partial h_1/\partial t$ [mm/s]	M_{hub} [m/s]	u_* [m/s]	α [°]	TI [%]
onshore	**1061**	**0.30**	**9.54**	**0.515**	**-17.35**	**8.35**
offshore	1058	0.13	10.96	0.310	-7.72	4.18

during which both main and precursor domain are simulated. During this period, which corresponds to about one wind-farm flow-through time, the wind farm goes through its start-up phase, the yaw controller converges to a steady state and the flow in the main domain adapts to the presence of the wind turbines. When all transitional effects of the wind-farm start-up have died out, the wind-angle controller in the precursor domain is turned off and simulations of the evening transition can start. This time is defined as $t = 0$.

6.2.2 A growing nocturnal SBL

Surface cooling is applied in both the precursor and main domain starting from $t = 0$, simulating the development of a nocturnal boundary layer. Two different cases are considered, i.e., Q25 and Q75, in which the surface temperature is reduced at a constant rate of 0.25 K/h and 0.75 K/h, respectively. The smallest cooling rate corresponds to that applied in the GABLS1 benchmark case, and the transient behaviour is therefore expected to last for about 6 to 8 hours, after which the boundary-layer flow presumably reaches a quasi-steady state. However, only the transition during the first 4 hours is simulated here due to the very long computation times. Furthermore, a reference case Q00 is included, in which the simulation of a wind farm under conventionally neutral conditions is continued. The boundary layer is in equilibrium in this case, and statistics are collected over a period of 1 hour.

The time evolution of some characteristic parameters of the surface layer (i.e., the layer where the fluxes vary less than 10 % with height (Stull 1988, p. 10)) are shown in figure 6.2 for cases Q25 and Q75, including the friction velocity, the surface heat flux, the difference in wind direction between the flow at hub height and in the free atmosphere, and the stability parameter z_{10}/L.

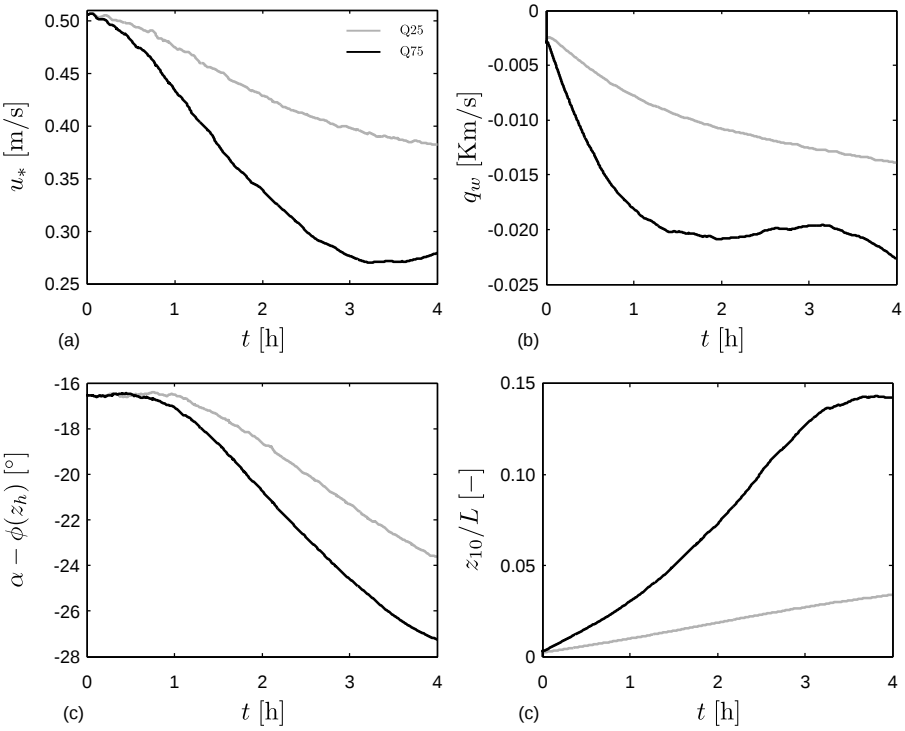

Figure 6.2: Time evolution of surface layer characteristics, including (a) friction velocity, (b) surface heat flux, (c) difference in wind direction between hub height and free atmosphere, and (d) stability parameter z_{10}/L (using $z_{10} = 10$ m), for cases Q25 and Q75.

As stable stratification tends to destroy turbulent kinetic energy, the vertical momentum flux and hence the friction velocity decrease in time, as can be seen in figure 6.2(a). The strongest decline thereby corresponds to the highest surface cooling rate in case Q75. However, the decrease in friction velocity ceases after about three hours for this case, after which it remains nearly constant. In figure 6.2(b), the magnitude of the surface heat flux increases in time and is highest for case Q75. After about two hours, the increase in heat flux levels off in case Q75. It is further observed that both the friction velocity and the surface heat flux react immediately to the reduced surface temperature. By contrast, a substantial change in wind direction only occurs after about 30 and 60 minutes in cases Q75 and Q25, respectively (see figure 6.2(c)). As expected, the wind near the surface turns towards the pressure gradient and the geostrophic angle increases. After the initial transient, a nearly constant rate of 2.1°/h and 3.7°/h

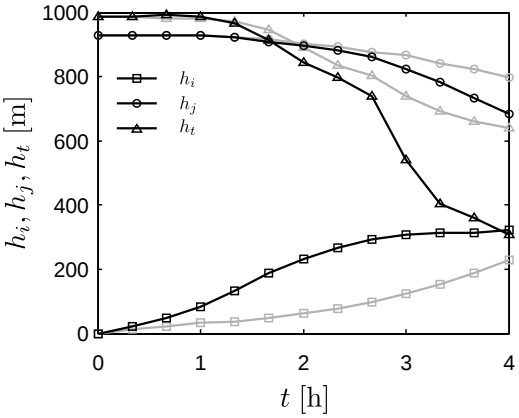

Figure 6.3: Time evolution of characteristic height scales, including the height of the turbulent layer h_t, the height of the surface inversion layer h_i and the height of the low-level jet h_j, for cases Q25 (gray linestyles) and Q75 (black linestyles).

are found in cases Q25 and Q75, respectively, and the total increase after 4 hours of simulation is 7.1° and 10.7°.

The stability of the surface layer is often quantified with the parameter z/L, with L the Obukhov length based on the surface fluxes and z located in the surface layer (typically in the lowest 10 m (Mahrt 1999)). Figure 6.2(d) displays the stability parameter evaluated at a height of $z_{10} = 10$ m, for further comparison with experimental results. The figure shows that the stability of the surface layer increases in time, and the strongest stability always corresponds to the highest surface cooling rate. After about three hours, the surface layer stability in case Q75 attains a nearly constant value of 0.14. In § 2.3.2, it was mentioned that the transition from weakly stable to strongly stable regime occurs for some threshold value of z/L, and that the downward heat flux reaches its maximum at this point. Based on experimental data collected at $z = 9$ m, Malhi (1995) found a maximal heat flux for $z/L \approx 0.2$. Furthermore, Mahrt *et al.* (1998) reported values of $z/L \approx 0.02$ and 0.06 measured at heights of 3 m and 10 m, respectively, and concluded that the exact value of z/L signalling the transition is probably not universal. Keeping these threshold values in mind, it is likely that the surface layer stability of case Q75 approaches the strongly stable regime near the end of the simulation, and this could explain the non-monotonic behaviour observed in both the friction velocity and surface heat flux.

Three important height scales characterise the transition towards a stable

boundary layer: the height of the turbulent layer h_t, the height of the surface inversion layer h_i and the height of the low-level jet h_j (André & Mahrt 1982). First, the height of the turbulent layer represent the level above which all turbulence has decayed. Following Kosović & Curry (2000), an estimate is obtained by linearly extrapolating the height where the turbulent shear stress equals 5 % of the wall stress u_*^2. Second, the height of the surface inversion layer indicates the height up to which the temperature is affected by the surface cooling. André & Mahrt (1982) define this height as the level where the temperature gradient is lower than a given value. Here, the free atmosphere stratification is used as threshold, i.e., $\gamma = 1$ K/km. The third measure is simply calculated as the height where the horizontal wind speed attains it maximum value.

The temporal evolution of these characteristic heights is depicted in figure 6.3. As the SBL develops in time, the height of the turbulent layer decreases while the height of the surface inversion increases. This was also reported by, e.g., André & Mahrt (1982); Smedman (1991); Kumar *et al.* (2006). In case Q75, the turbulent layer and surface inversion are found to be equally high after 4 hours of simulation. Due to the weaker cooling in case Q25, the surface inversion is not as deep and turbulence decays slower, so the turbulent layer is still deeper than the surface inversion after 4 hours. Note, however, that the height of the surface inversion is very sensitive to the threshold value applied in its definition.

The height of the low-level jet is shown to decrease in time, which agrees with the finding of Kumar *et al.* (2006). Furthermore, stronger cooling results in a lower LLJ. An explanation is found in the study of Shapiro & Fedorovich (2010), which showed that LLJs have greater wind speeds and occur at lower heights for larger reductions in ambient turbulence levels. Hence, the lower values of h_j in case Q75 are caused by the stronger reduction of turbulence in this case.

The boundary-layer structure is further illustrated in figure 6.4. Vertical profiles of cases Q25 and Q75, averaged over the horizontal directions, are shown for various points in time and are compared with the time-averaged profiles of the CNBL (case Q00). In all figures, it is observed that the largest changes correspond to case Q75 with the strongest surface cooling. Figure 6.4(a) shows that the horizontal velocity decreases near the surface, which is in agreement with the reduced friction velocity observed in figure 6.2(a). Above the wind turbine region, the formation of a low-level jet is visible. Near the end of the current simulations, the LLJ is characterised by a broad maximum in both cases. This finding is in agreement with the study of Kumar *et al.* (2006), who reported a broad LLJ during the early transition phase and a narrow LLJ after about 7 hours of surface cooling. The changes in velocity magnitude are accompanied by local turning of the wind direction, i.e., near the surface the wind turns towards the pressure gradient (the wind angle increases), whereas in

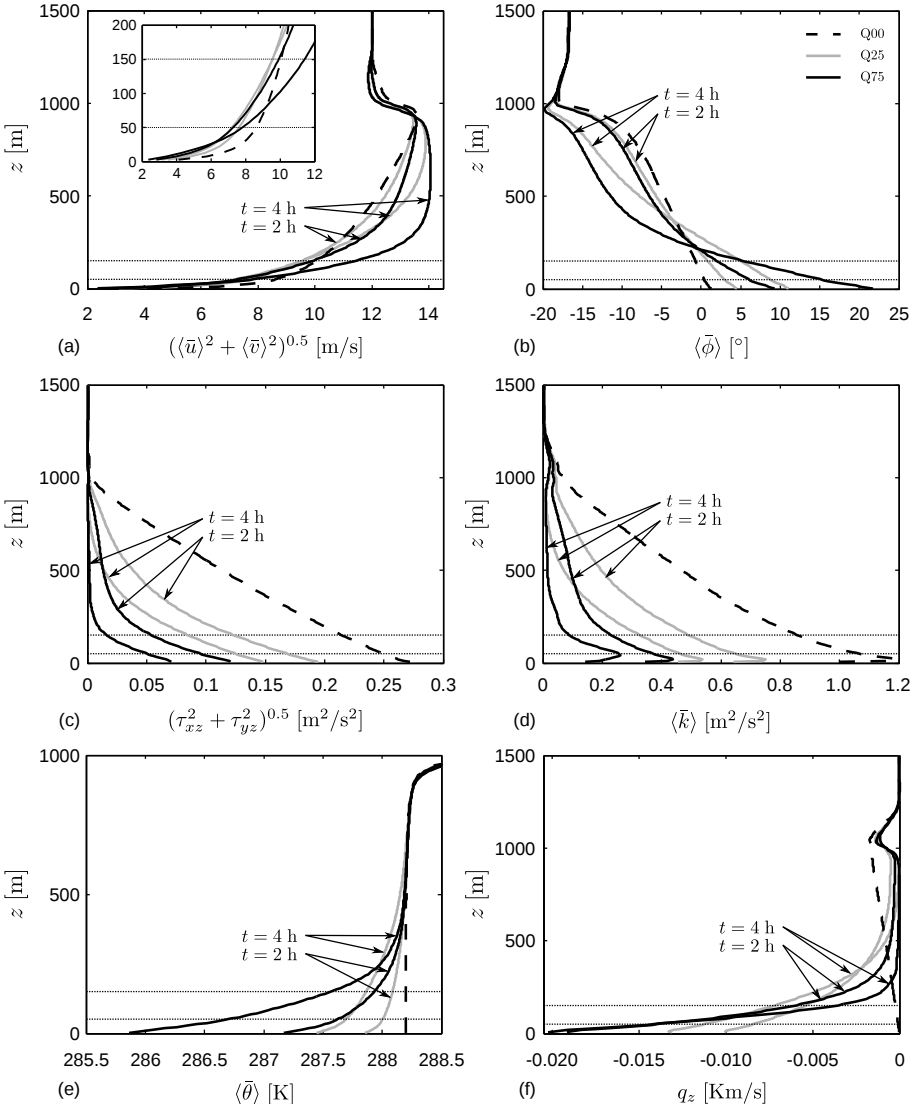

Figure 6.4: Vertical profiles in the precursor simulation, averaged over the horizontal directions, of (a) horizontal velocity magnitude, (b) horizontal wind direction, (c) total shear stress magnitude, (d) turbulent kinetic energy, (e) potential temperature and (f) total heat flux. Results are shown for cases Q00, Q25 and Q75 at various times t. First-order statistics (a,b,e) are obtained from instantaneous LES data, while second-order statistics (c,d,f) have been averaged between $t - 20$ min and t. The horizontal dotted lines illustrate the location of the turbine region (note that no wind turbines are simulated in the precursor domain). The insert in (a) shows a detailed view of the velocity in the lower 200 m.

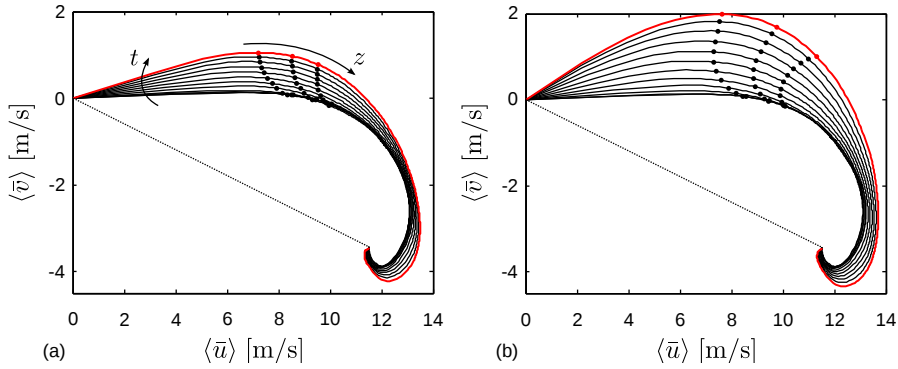

Figure 6.5: Wind hodographs, averaged per 20 min, for case (a) Q25 and (b) Q75. The wind hodographs at $t = 4$ h are shown in red, and the dotted lines correspond to the geostrophic wind velocity. The three dots on every curve mark the location of the bottom, centre and top of the turbine region.

the outer layer the ageostrophic wind speed decreases (the wind angle becomes more negative) (see figure 6.4(b)). As discussed further below, these changes in velocity magnitude and direction are caused by inertial oscillations.

Figures 6.4(c–d) show the total shear stress and turbulent kinetic energy. Throughout the boundary layer, turbulence decays much faster for the stronger cooling rate. Near the end of the simulation, both cases clearly show a residual layer above the turbulent layer, starting at a height h_t of about 640 m and 300 m in case Q25 and Q75, respectively. However, some turbulent kinetic energy is still present at the top of the boundary layer, even after 4 hours of surface cooling. This turbulence might be related to shear instability at the top of the low-level jet (Taylor & Sarkar 2008*b*).

The potential temperature and heat flux are shown in figures 6.4(e–f). The magnitude of the heat flux is maximal at the surface and decreases with height in the lowest part of the boundary layer. Higher up, the heat flux becomes zero in the residual layer, i.e., above 640 m and 300 m in case Q25 and Q75 in the profiles obtained after 4 hours.

The sudden decrease of turbulence triggers an inertial oscillation in the horizontal wind speed, which affects both the velocity magnitude and velocity direction, as observed in figures 6.4(a–b). In order to visualise the directional effects, inertial oscillations are often analysed in wind hodographs, in which the horizontal velocity vector at different heights is represented in a polar diagram. Figure 6.5 shows the wind hodographs for cases Q25 and Q75 at various times. The

location of the bottom, centre and top of the turbine region is indicated by three dots on every curve, illustrating the temporal evolution of the velocity vector at these heights. First of all, it is observed that, for a fixed height, the tip of the velocity vector follows a circular path in clockwise direction (note that the Northern Hemisphere is considered), which is in accordance with theory of inertial oscillation (see, e.g., van de Wiel *et al.* 2010). This rotation explains the observed changes in wind direction towards the pressure gradient near the surface.

The velocity magnitude at a given height is found in the hodographs as the distance from that point to the origin. Hence, figure 6.5 shows that the wind speed at hub height decreases in both cases in the beginning of the simulation. In case Q75, the velocity at hub height starts to increase again after about 2.5 hours.

6.3 Wind-farm simulation

In this section, the results of the wind-farm simulations are analysed. First, the wind-farm power output during the transition is discussed in § 6.3.1. Afterwards, § 6.3.2 describes the boundary-layer flow in and above the wind farm, and the effect of gravity waves is analysed in § 6.3.3.

6.3.1 Wind-farm energy extraction

The evolution of the wind-farm power during the boundary-layer transition is represented in figure 6.6 for cases Q25 and Q75. In figure 6.6(a), the total wind-farm power is normalised by the mean power under conventionally neutral conditions (i.e., the mean power in case Q00). Figure 6.6(b) shows the wind-farm efficiency, which is defined as the total wind-farm power divided by $N_t \times P_1$, where N_t is the number of turbines in the farm and P_1 is the mean power output of a first-row turbine.

Next to high frequency components related to turbulence, both the wind-farm power output and efficiency are slowly varying in time, and a clear steady state is not achieved within the first 4 hours after the onset of surface cooling. Several different aspects influence the power performance, and, based on the dominant effects, three regimes are identified. In the first regime, the total power decreases while the efficiency remains nearly constant. This regime is dominated by the decreasing velocity at hub height. The behaviour of both cases is very similar

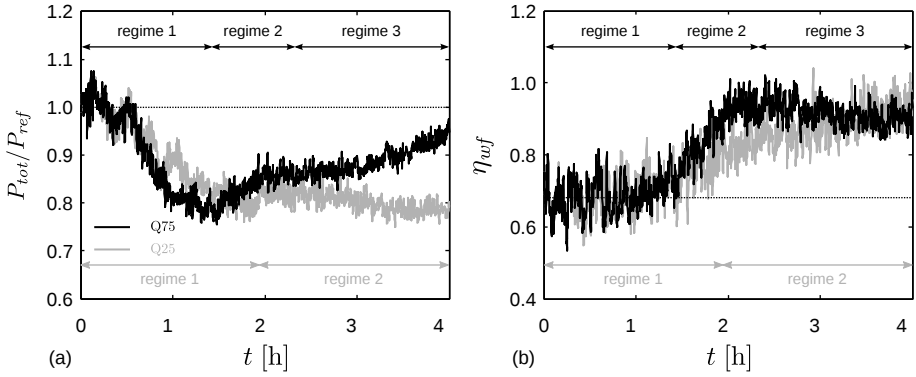

Figure 6.6: (a) Total wind-farm power, normalised by the mean power under conventionally neutral conditions, and (b) wind-farm efficiency as a function of time, for cases Q25 and Q75. The dotted lines correspond to the power output under conventionally neutral conditions.

in this regime, and the power decreases more rapidly in case Q75 due to the stronger reduction in hub height velocity.

In the second regime, the wind-farm efficiency starts to increase. This is caused by the changing wind direction at hub height, i.e., the effective wind-farm layout in the mean flow direction is evolving from an aligned pattern towards a staggered pattern (see also § 6.3.2). In case Q75, the second regime starts after roughly 1.5 hours when the wind has turned almost 2° (see figure 6.2(c)). For the current wind-turbine spacing ($s_x D = 750$ m), this angle correspond to a spanwise deflection of $D/4$. The increase in wind-farm efficiency compensates for the decreasing wind speed, and causes the power to increase in case Q75. In case Q25, on the other hand, regime two only starts after about 2 hours, which is in agreement with the slower rotation rate observed in figure 6.2(c). The increasing efficiency is not able to compensate for the decreasing hub height velocity in this case, and the power output continues to decline.

It should be stressed, however, that the impact of the changing wind direction on the wind-farm efficiency is highly dependent on the wind-farm layout, i.e., the observed increase in efficiency is related to the initial aligned turbine pattern and does not hold in general. For example, a wind farm whose turbines form a staggered pattern relative to the daytime wind direction would experience a decreasing efficiency as the effective layout evolves towards a less efficient, aligned pattern.

In case Q75, a third regime arises due to the development of a low-level jet.

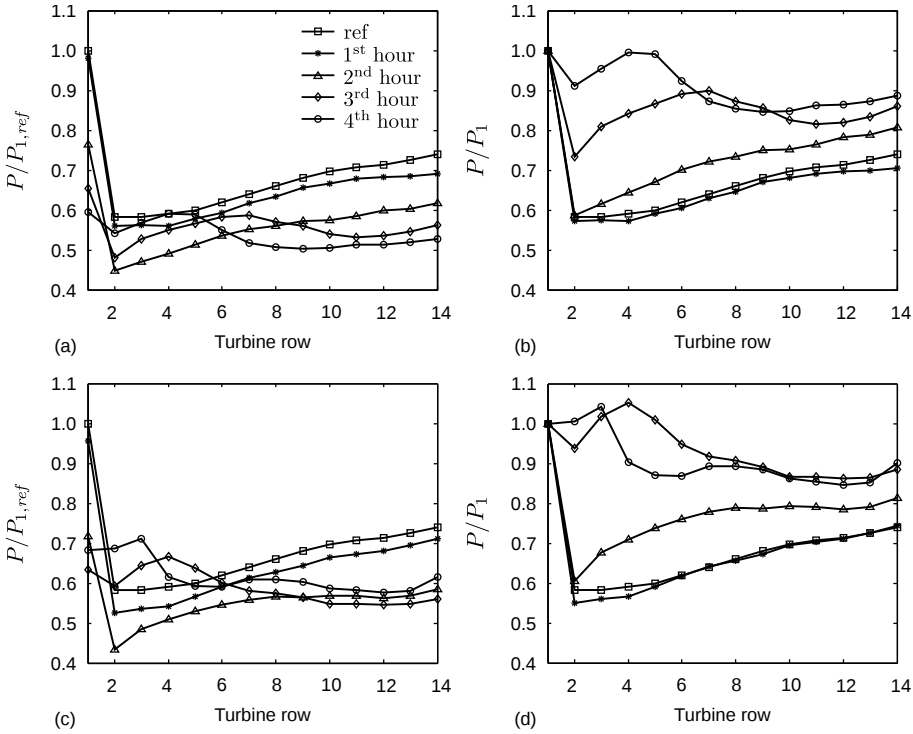

Figure 6.7: Turbine power output, averaged per row and over consecutive time windows of 1 h, for case Q25 (a,b) and Q75 (c,d). The results have been normalised by the mean power output of a first row turbine in the conventionally neutral case (a,c) and in the same time window (b,d).

As observed in figure 6.5(b), the hub height velocity starts to increase after about 2.5 hours, causing the power output to rise even further. The wind-farm efficiency levels off and slowly decreases in this regime. This could be related to the wind-farm layout approaching less efficient geometrical patterns (e.g., Stevens *et al.* (2014*a*) showed that a perfectly staggered pattern does not yield the highest power output), or due to decaying turbulence deteriorating the wake recovery rate. In case Q25, the hub height velocity does not increase during the first 4 hours, and therefore regime three does not occur. Near the end of the simulation, the wind-farm efficiency of both cases is almost the same, and the difference in power output is only due to the difference in hub height velocity.

The turbine power output, averaged per row and over consecutive time windows of 1 h, is shown in figure 6.7 for cases Q25 (a,b) and Q75 (c,d). The figures

on the left are normalised by the mean power of a first row turbine in the conventionally neutral case, whereas the figures on the right are normalised by the output of a first-row turbine obtained from the same time window. In case Q25, the first and second time window fall within the first regime, in which the reduced wind speed causes the power of the first turbine row to decrease monotonically in time (see fig. 6.7(a)). The power output of the downstream turbine rows also decreases in these two windows because less energy is being transported downwards due to the reduced turbulent intensity. In windows three and four, the first row output continues to decrease, but the power output of rows 2 to 6 increases as the effective wind-farm layout is changing. Figure 6.7(b) shows that the power deficits decrease and approach typical staggered behaviour. Note again that the decrease in power deficit is caused by the particular choice of initial wind-farm layout, and that other layouts will result in different behaviour.

The evolution of the power output in case Q75 is very similar, with the notable difference that the profiles change more rapidly in time. Furthermore, the power of the first turbine row is observed to increase in the last time window, corresponding to the increasing hub height velocity in regime three. Figure 6.7(d) shows that the power deficits in case Q75 have decreased considerably due to the changing wind direction, and in the third and fourth time window some turbine rows produce even more power than the first row. This could be related to in-field blockage effects which are sometimes observed in staggered wind farms (McTavish *et al.* 2015).

6.3.2 Boundary-layer flow

A sample of the instantaneous horizontal velocity field in both precursor and main domain is shown in figure 6.8 for two different times. First, figures 6.8(a–d) illustrate the statistically steady state of the wind farm in the CNBL at $t = 0$. Figures 6.8(a,b) and (c,d) show an x–y plane at hub height and an x–z plane through the centre of the turbine disks, respectively. These figures are compared with figure 5.4, showing the same plot for an offshore CNBL with similar boundary-layer height and geostrophic wind speed. As before, elongated velocity streaks are observed in the x–y plane, and the turbulent structures in the x–z plane are limited by the overlying inversion layer. However, compared to figure 5.4, considerably more turbulent fluctuations occur throughout the boundary layer, leading to better wake recovery and lower velocity deficits. Furthermore, the wake behind the wind farm is less obvious than in the offshore case.

Second, figure 6.8(e–h) shows instantaneous contours of horizontal velocity in the same planes but now for case Q75 at $t = 4$ h. The turbulent structures in

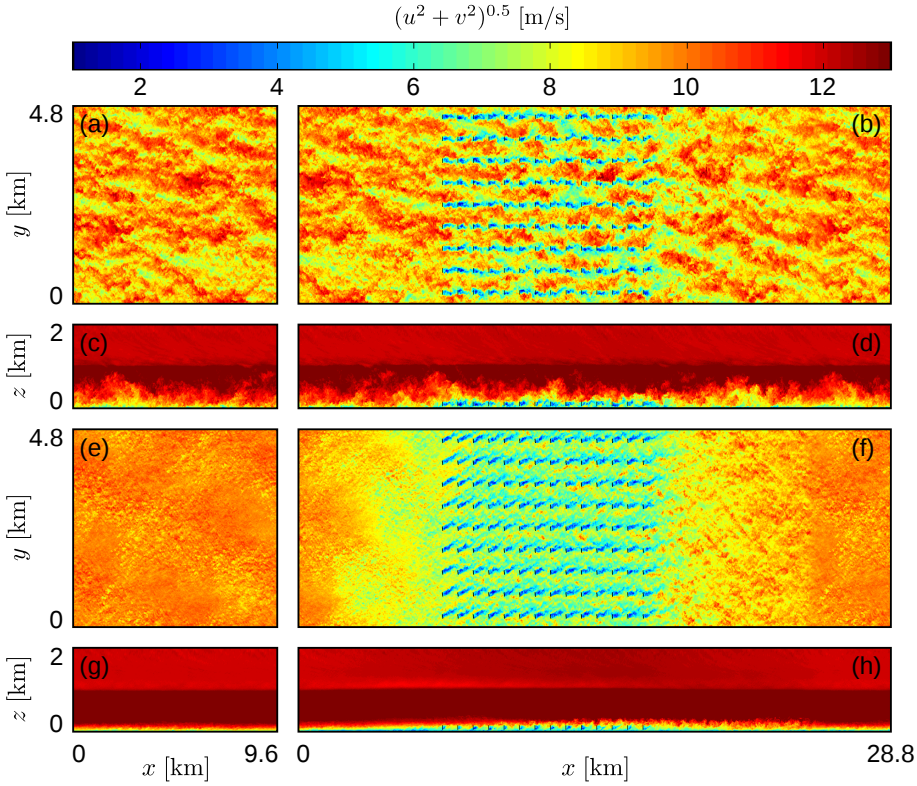

Figure 6.8: Instantaneous contours of horizontal velocity at $t = 0$ (a–d), and at $t = 4$ h for case Q75 (e–h); (a,b,e,f) An x–y plane at turbine hub height $z_h = 100$ m; (c,d,g,h) An x–z plane through the middle of a turbine column (only the lower 2 km of the numerical domain are shown). The left pane shows the precursor domain (a,c,e,g) and the right pane shows the main domain (b,d,f,h), where turbine disk locations are indicated with black lines.

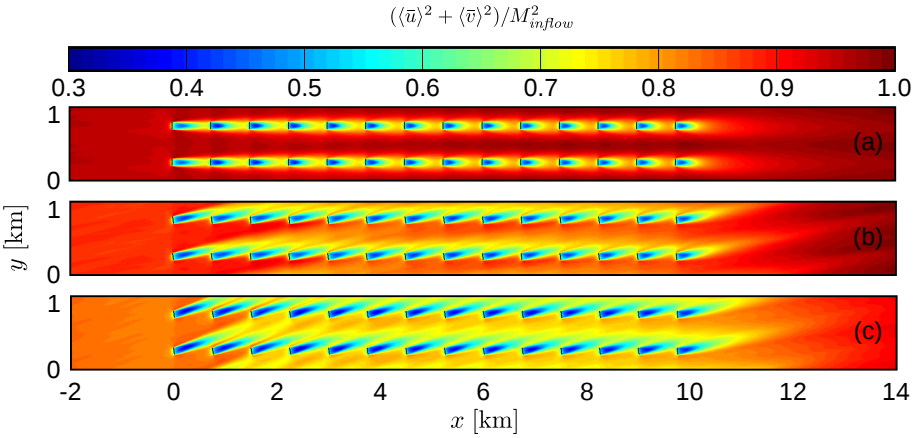

Figure 6.9: Horizontal wind speed, normalised by the inflow velocity, in an x–y plane at hub height, averaged over the last 20 min of the simulation and per turbine column, for cases (a) Q00, (b) Q25 and (c) Q75. Results are only shown from 2 km upstream to 4 km downstream of the wind farm.

the stably stratified case are clearly smaller than in the conventionally neutral case, and the typical elongated velocity streaks have disappeared. In the x–z planes, the vertical extent of the turbulent structures is severely reduced as well. It is further observed that the mean flow decreases significantly upstream of the wind farm in the stable case, which is related to a strong pressure gradient in that region caused by gravity waves (see further below). Regarding the wind-turbine wakes, wake meandering appears to be less intense under stable stratification, at least in the beginning of the farm. España *et al.* (2011) pointed out that wake meandering is generated by turbulent length scales larger than the wake width, so the reduced meandering could be explained by the absence of large-scale structures under stable conditions.

The mean flow structure is discussed hereafter in figures 6.9–6.11. The results of cases Q25 and Q75 have been averaged over the last 20 min of the simulation. Further, the mean flow structure is periodic in the spanwise direction with a length $s_y D$ (i.e., per turbine column), which allows to take an average over all the turbine columns as well. The figures depict a horizontal x–y plane at turbine hub height $z_h = 100$ m, in which the mean flow around two turbine columns is shown, allowing a good visualisation of both the wake structure and the channel between the turbine columns.

The horizontal wind speed is shown in figure 6.9, normalised by the inflow velocity. It is clear that the effective farm layout changes in the stable cases

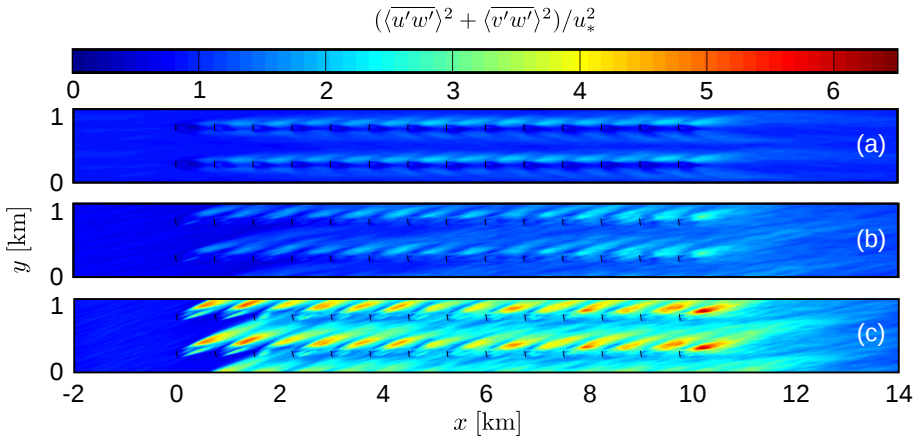

Figure 6.10: Resolved shear stress, normalised by the square of the friction velocity in the precursor simulation, in an x–y plane at hub height, averaged over the last 20 min of the simulation and per turbine column, for cases (a) Q00, (b) Q25 and (c) Q75. Results are only shown from 2 km upstream to 4 km downstream of the wind farm.

as the turbine wakes align with the incoming flow direction. In case Q25, this causes turbine rows 2 to 5 to operate in partial wake flow which increases the wind-farm efficiency. The wind direction has changed even more in case Q75, and there the first three rows operate in almost unperturbed wind flow. Furthermore, it is observed both within and downstream of the wind farm that wake recovery is less efficient under stable conditions, causing velocity deficits to extend over longer distances. Finally, it is found, with respect to the first turbine row, that the turbine wakes (and also the yaw angle of the wind turbines) rotate towards the right throughout the farm, i.e., about 1.4° and 4.9° in cases Q25 and Q75, respectively. This effect is related to gravity wave effects, which are further discussed in § 6.3.3.

Figure 6.10 depicts the resolved shear stress, normalised by the square of the friction velocity in the precursor simulation. In all simulations, an elevated shear stress level is observed in the wake of the wind turbines. Furthermore, the relative increase of the shear stress is highest in the strongest cooling case. Similar trends are observed in the heat flux, which is shown in figure 6.11 (values are normalised by the surface heat flux obtained from the precursor simulation). The heat flux in the neutral case is negligible, so only cases Q25 and Q75 are shown. Strong increase in vertical heat flux is observed in the wake regions, with the largest effects corresponding to case Q75.

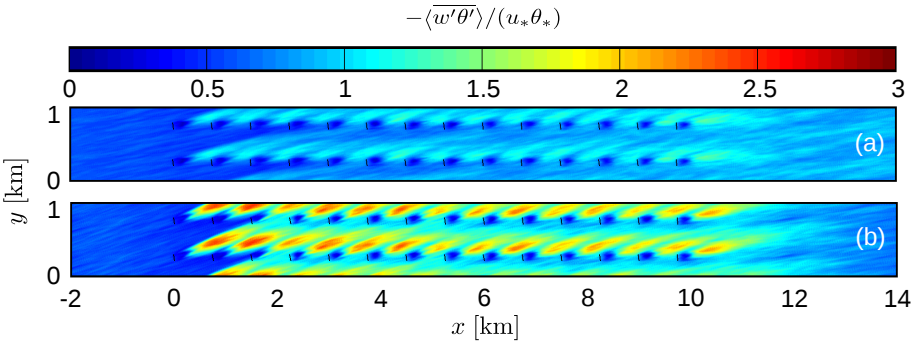

Figure 6.11: Resolved heat flux normalised by the surface heat flux in the precursor simulation, in an x–y plane at hub height, averaged over the last 20 min of the simulation and per turbine column, for cases (a) Q25 and (b) Q75. Results are only shown from 2 km upstream to 4 km downstream of the wind farm.

6.3.3 Gravity wave effects

In the current simulations, large-scale gravity waves inducing pressure gradients in the boundary layer are again observed. As before, these waves are triggered by the displacement of the inversion layer due to the flow blockage in the wind farm. Figure 6.12 shows the inversion displacement and the induced pressure perturbation. The maximum displacement under conventionally neutral conditions is found to be 37 m, which is about half of the displacement found in offshore conditions with the same boundary-layer height (see fig. 5.12(a)). Under stable conditions, the maximum displacement rises to 60 m and 70 m in cases Q25 and Q75, respectively. The induced pressure follows the same trend, i.e., the highest perturbations are found in case Q75.

A question that remains is why increased stability enhances boundary-layer displacement. In the traditional view of wind-farm–ABL interactions, without feedback of gravity waves through induced pressure gradients, it is expected that the highest displacement corresponds to the case with the largest flow blockage, i.e., the largest relative reduction in wind speed caused by the total thrust force of the wind turbines and the surface. The relative slow down of the flow is related to the wind-farm efficiency, which was found to be almost equal for cases Q25 and Q75 near the end of the simulation (see fig. 6.6(b)). Hence, the observed differences in boundary-layer displacement between case Q25 and Q75 are not explained by the relative flow blockage (without gravity-wave feedback).

A possible explanation for the current trends may be the *choking effect* mentioned

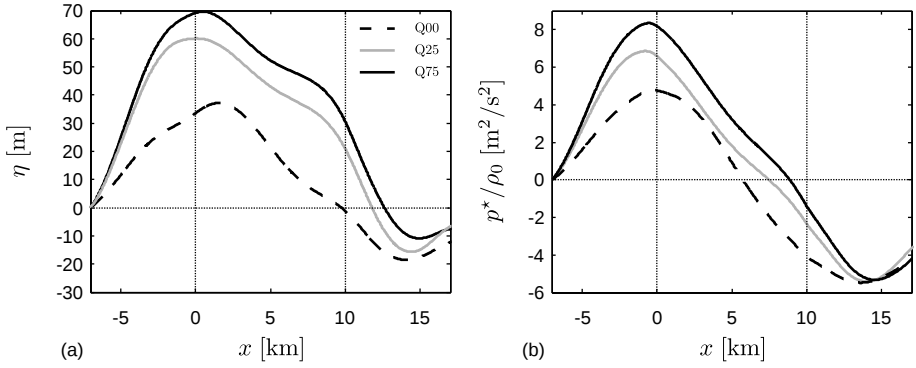

Figure 6.12: Streamwise variation of (a) boundary-layer top displacement and (b) pressure perturbation, averaged over the last 20 min of the simulation, for cases Q00, Q25 and Q75. The vertical dotted lines indicate the start and end of the wind farm.

by Smith (2010). This effect is best illustrated by means of a parallel with incompressible open channel flows bounded by a free surface (see, e.g., White 2011). Such a flow type has several fundamental analogies with atmospheric flow capped by an inversion layer (Durran 1990). For one-dimensional free surface flow near an obstacle, it is easily shown that the ratio of the non-linear advection term to the pressure gradient arising from changes in the fluid depth is given by $-Fr^2$ (Durran 1990), where the Froude number is defined as $Fr = U/\sqrt{gh}$. The minus sign indicates that a decelerating fluid is always accompanied by an unfavourable pressure gradient, and vice versa. For $Fr > 1$ (supercritical flow), the magnitude of the advection term is larger than that of the induced pressure, and the flow will decelerate and thicken when encountering an obstacle. In case $Fr < 1$ (subcritical flow), the flow accelerates and thins as the induced favourable pressure dominates the force balance. In the absence of friction, a singularity occurs at $Fr = 1$ as the induced pressure exactly matches the advection term, i.e., an imposed force cannot be balanced by an acceleration or deceleration of the flow as the sum of the advection and pressure gradient forces is always equal to zero. In this situation, the flow *chokes* and the upstream height or mass flow adapts to cope with the obstacle.

In the atmosphere, a similar type of behaviour is found, but complicated by the influence of vertically propagating gravity waves in the free atmosphere. However, when the induced pressure perturbations of these waves are small (i.e., for low free atmosphere stratification), the frictionless case becomes singular for $Fr \to 1$ (with Fr based on the reduced gravity $g' = g\Delta\theta/\theta_0$). Smith (2010) introduced a simple analytical two-layer model which clearly shows that the

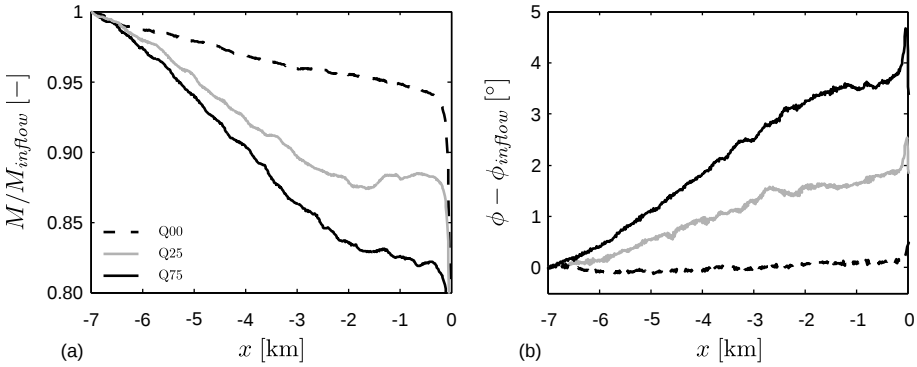

Figure 6.13: Upstream influence of gravity waves on (a) hub height wind speed (normalised by the inflow velocity) and (b) wind direction, averaged over the last 20 min of the simulation, for cases Q00, Q25 and Q75.

displacement goes to infinity at the singularity, and that energy dissipation due to friction or vertical wave propagation resolves the singularity. Smith reported strong boundary-layer displacement and very large pressure perturbations causing a severe restriction of the wind speed for Fr slightly larger than unity. In the current simulations, the Froude number is 0.92 and the flow is subcritical. In accordance with the open channel flow similarity, figure 6.12 shows that the boundary-layer displacement and pressure decrease in the wind-farm region. As the Froude number is close to unity, the decreasing turbulence levels with stable stratification may explain the observed increase in pressure and displacement in case Q25 and Q75. However, many other effects influence the flow behaviour, and further investigation of this phenomenon is necessary.

The influence of the induced pressure gradients on the upstream flow characteristics is illustrated in figure 6.13, showing the wind speed (normalised by the inflow velocity) and the change in wind direction at hub height. It is found that gravity waves cause a severe reduction in wind speed in front of the farm, which in turn causes the wind to turn towards the pressure gradient. In line with the trends observed in figure 6.12, the upstream influence of gravity waves increases with increasing stability. With respect to the inflow velocity, a reduction of 5.7 %, 11.6 % and 18 % is observed in cases Q00, Q25 and Q75, respectively. Moreover, the decrease in velocity causes an additional rotation of the wind velocity of 1.8° and 3.6° in cases Q25 and Q75, respectively.

The energetic consequences of these gravity waves are demonstrated in figure 6.14, which follows the analysis of figure 5.17, i.e., showing the total flux of mechanical energy in the boundary layer and the contributions of kinetic

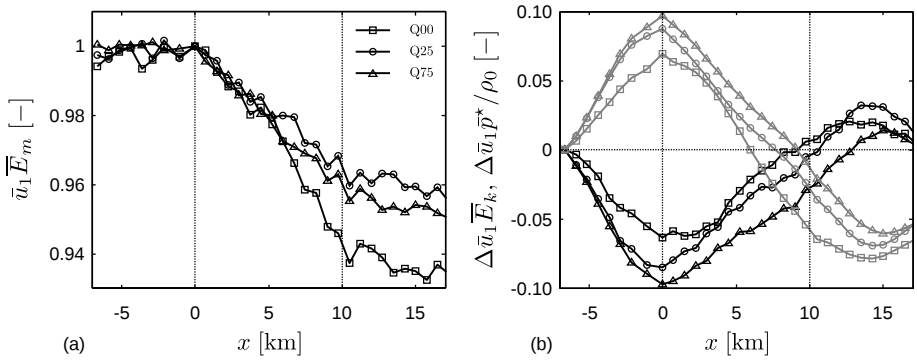

Figure 6.14: (a) Total mechanical energy flux in the boundary layer and (b) contributions of kinetic energy (black linestyles) and pressure (gray linestyles), for cases Q00, Q25 and Q75. All results are normalised by the total mechanical energy flux at the entrance of the farm, and in (b) the relative change with respect to the inflow ($x = -7$) is shown.

energy and pressure (excluding the mean background pressure). Similar to the results of wind-farm simulations in offshore CNBLs, the total flux of mechanical energy is roughly constant upstream and downstream of the farm and decreases almost linearly inside the farm. In case Q00, the wind farm reduces the energy flux with almost 5 %, compared to the 11 % found in case S1 (note that the fetch of the wind farm in case S1 is 5 km longer than that considered here). Similar behaviour is found in stable conditions, but the reduction of energy flux is slightly lower. The dependence on surface cooling rate is thereby small.

As before, it is found that the mechanical energy is not always available in the form of kinetic energy because part of the energy is stored in the pressure field (see figure 6.14(b)). The relative amount of energy associated with the pressure perturbations increases a little with increasing stable stability, i.e., at the pressure peak, about 7 %, 9 % and 10 % of the mechanical energy flux is due to pressure contributions in case Q00, Q25 and Q75, respectively. Note that part of this energy is located in the residual layer above the stable boundary layer. This layer is decoupled from the wind-turbine region due to the fact that the turbulent fluxes become equal to zero. It is therefore difficult to determine how much energy contained in the pressure field is potentially available for the wind farm. To further determine this, the energy tube approach by Meyers & Meneveau (2013) could prove a useful analysis tool. This is a subject of further research.

6.4 Summary

The current chapter analysed wind-farm power output and boundary-layer flow during the evening transition of an onshore, equilibrium CNBL into a nocturnal stable boundary layer. Two simulations with different cooling rates were performed, and a third simulation with neutral boundary conditions was included for reference. Although quasi-steady conditions were expected to occur after 6 to 8 hours of surface cooling, the large computational cost only allowed to simulate 4 hours of boundary-layer transition.

As in the previous chapter, wind farms of finite streamwise length were simulated, and wake effects were prevented from being recycled back to the inlet by applying the concurrent-precursor method. In view of the restricted turbulent length scales under stably stratified conditions, the subgrid-scale motions were modelled by the TKE model, and horizontal grid resolutions were reduced with respect to the wind-farm studies performed earlier. The starting point of the three simulations was a wind farm operating in a fully developed, equilibrium, onshore CNBL, which was obtained through a careful initialisation and spin-up procedure similar to the previous chapter.

In a first step, the results of the precursor simulation without wind turbines were analysed. Applying a constant surface cooling caused the growth of a stable boundary layer, in which the turbulence decayed and the wind speed near the ground decreased and turned towards the pressure gradient. The case with higher surface cooling resulted in stronger stability, and both the surface fluxes and the boundary-layer structure evolved more rapidly in time compared to the weakly cooled case. Above the surface inversion, a low-level jet with a broad maximum developed during the first 4 hours due to the decreasing shear stress. Increasing the surface cooling resulted in LLJs at lower heights with larger wind speed maxima. Furthermore, the height of the LLJ decreased in time, causing the wind speed at hub height to first decrease and then increase.

The various processes affecting the wind speed and wind direction at hub height were reflected in the wind-farm energy extraction, in which three distinct regimes were identified. During the first regime at the beginning of the transition, the energy extraction decreased due to the decreasing wind velocity at hub height, and the power output was lowest in the strongly stable case. Subsequently, the changing wind direction started to affect the effective layout of the wind farm in a second regime. The particular choice to start from an aligned pattern resulted in a wind-farm efficiency increase. In the third regime, the low-level jet started to play a role and increased the power output of the strongly stable case. The weakly stable case evolved more slowly, and the LLJ did not affect the power output during the first 4 hours of transition.

Atmospheric gravity waves were again excited by flow displacement due to wind-farm blockage effects. Boundary-layer displacement and induced pressure gradients were thereby found to increase with increasing stability, which may have been caused by the decrease in turbulence levels combined with a Froude number close to unity. The energetic consequences of gravity waves were found to be rather small, and the main effect of the waves was the significant modification of the wind speed and wind direction upstream of the farm, which had a direct impact on the overall energy extraction in the farm.

Chapter 7

Summary, conclusions and outlook

The current dissertation improved the understanding of wind-farm–ABL interactions, with a main focus on the influence of atmospheric stability and outer-layer dynamics on wind-farm energy extraction. New insights were thereby gained based on numerical simulations of large wind farms in the ABL. Two particular boundary-layer types were investigated: the conventionally neutral and the stable atmospheric boundary layer. Furthermore, both the transition and fully developed regime of wind-farm boundary layers were considered. Numerical simulations were based on the large-eddy simulation technique and were performed with the SP-Wind code developed at KU Leuven.

The results of this dissertation are summarised in section 7.1, and main conclusions are drawn in section 7.2. Suggestions for future research are provided in section 7.3.

7.1 Summary of results

For the purpose of the present thesis, the SP-Wind code was extended to account for thermal stability effects and Coriolis forces, and the code was verified and validated with data from literature. Further, new initialisation procedures were derived to maintain control over the inversion-layer height, and a wind-angle controller was developed to set a fixed wind-farm layout independent of the effective geostrophic wind angle. Finally, a novel approach based on simplified

2D potential-flow simulations was introduced to find an optimal configuration of wave damping layers.

In a first study, the fully develop flow regime in wind farms under conventionally neutral conditions was investigated. It was found that energy extraction in very large wind farms is controlled by the amount of work done by the large-scale pressure gradient, which depends on boundary-layer height and geostrophic wind angle. Moreover, entrainment of kinetic energy from the free atmosphere does not play a significant role in the overall energy balance. In a set of LES simulations, varying the inversion characteristics led to differences in energy extraction on the order of 13 % (for increasing the strength from 2.5 K to 10 K), and 31 % (for increasing the height from 500 m to 1500 m). With respect to varying inversion strengths, it was found that the differences in energy extraction are energetically not related to different amounts of energy entrained, but are explained by a difference in boundary-layer growth, leading to higher boundary layers for lower inversion strengths.

The adaptation of an equilibrium offshore CNBL to the presence of a large wind farm with a fetch of 15 km formed the subject of a second study. The height of the inflow boundary layer was varied in several LES cases, and was shown to have a significant impact on the wind-farm flow development. First of all, above the farm, an internal boundary layer develops that interacts downstream with the capping inversion for the two lowest CNBL cases. Secondly, the upward displacement of the boundary layer by flow deceleration in the wind farm excites gravity waves in the inversion layer and the free atmosphere above. For the lower CNBL cases, these waves induce significant pressure gradients in the farm (both favourable and unfavourable depending on location and case). A detailed energy budget analysis in the turbine region showed that energy extracted by the wind turbines is coming from both flow deceleration and vertical turbulent entrainment. Though turbulent transport dominates near the end of the farm, flow deceleration remains significant, i.e., up till 35 % of the turbulent flux for the lowest CNBL case. In fact, while the turbulent fluxes are fully developed after eight turbine rows, the mean flow does not reach a stationary regime. A further energy budget analysis over the rest of the CNBL revealed that all energy available at turbine level comes from upstream kinetic energy in the boundary layer, while the work done by the large-scale pressure gradient, i.e., the dominant energy source in the previous wind-farm study, is only of minor importance in the current case. In the lower CNBL cases, the pressure field induced by gravity waves plays an important role in redistributing the kinetic energy throughout the farm. Similar to the fully developed regime, entrainment at the capping inversion was very small in all cases.

The third study of the dissertation dealt with wind farms under stably stratified conditions. To this end, the evening transition from an equilibrium, onshore

CNBL into the nocturnal stable boundary layer was simulated. It was observed that several processes influence the wind-farm power output. Immediately after the onset of surface cooling, the wind speed decreases in the wind-turbine region and results in reduced power output. The lower wind speed also causes a change in wind direction, which starts to influence the wind-farm efficiency after 1 to 2 hours by changing the effective layout of the turbines. Meanwhile, a low-level jet with a broad maximum develops above the wind farm and descends over time. In the moderately stable case, increased hub height velocities were observed after about 2.5 hours, which increased the power output. Gravity waves were again observed, and their amplitude increased with stability. The main effect of the waves is the significant modification of the wind speed and wind direction upstream of the farm due to the induced pressure gradients.

In summary, the current dissertation demonstrated the importance of the boundary-layer structure for large wind farms. Overlying inversion layers actively control the height of the boundary layer, which is directly related to the energy content of the ABL. Moreover, Coriolis forces affect the wind-energy extraction indirectly by causing wake deflection and modifying the effective wind-farm layout. In addition to these outer-layer effects, it was found that atmospheric gravity waves on the inversion layer and in the free atmosphere strongly influence the wind-farm flow behaviour by inducing pressure gradients in the boundary layer. These pressure gradients lead to considerable changes in wind speed and direction upstream of the wind farm and modify the wind-farm energy balance.

7.2 Main conclusions

Based on the physical insights gained in the current dissertation, a number of general conclusions and recommendations can be made regarding the modelling of wind-farm boundary-layer flow.

First, it is concluded that the pressure-driven boundary-layer (PBL) approach, which is currently the standard method in large-eddy simulations of wind farms subject to atmospheric turbulence, neglects important physical aspects for wind-farm performance. This is especially true for shallow boundary layers, tall wind turbines and large wind farms, in which case outer-layer dynamics directly affect the wind turbines. But also in more general situations, the rigid-lid condition of the PBL approach prohibits the flow to react in a natural way to the presence of a wind farm, i.e., by establishing a new equilibrium height governed by the stability of the overlying inversion layer and the turbulent mixing in the outer layer. As the height of the boundary layer is directly related to the available

energy, the PBL approach cannot correctly represent the energy balance in the ABL.

A second conclusion concerns the asymptotic limit of fully developed flow in wind farms. This regime is often assumed in numerical simulations as it allows to use simple periodic boundary conditions and avoids the need to specify turbulent inflow conditions. The simulations performed in this thesis, however, indicate that in wind farms with a finite fetch the flow is never truly fully developed, i.e., despite the fast response of turbulence to the wind turbines, the mean flow continues to change throughout the wind farm. Moreover, it has been shown that the dominant energy source in a finite wind farm differs from that in an infinite wind farm. It is therefore concluded that the fully developed flow regime does not exist in real wind farms, and that simulations of wind-farm–ABL interactions should always include streamwise flow development.

Finally, the concept of wind-farm induced gravity waves is demonstrated in this thesis. These waves enable a coupling mechanism between the wind farm as a whole and boundary-layer meteorology on a regional scale. An important consequence of this mechanism is that wind farms may influence upstream wind conditions. This is currently not taken into account in wind-farm simulations nor in experiments, in which the inflow conditions are specified at an arbitrary location close the first turbine row. The results of the current dissertation, however, indicate that numerical modellers should carefully consider how far upstream inflow conditions need to be specified. Also for the design and operation of wind farms, this means that there can be a considerable difference between the "unperturbed" wind speed obtained from prior measurement campaigns or wind-atlas data and the actual wind conditions during commercial operation.

7.3 Suggestions for future research

Various ABL aspects encountered in this thesis revealed the need for further investigations and opened up several new research questions. In the current section, the limitation of this dissertation are discussed, and suggestions for future research are made.

First of all, it is acknowledged that unstable conditions, which are ubiquitous in the ABL, are not covered in this thesis. Despite the fact that convective boundary layers have been treated in numerous LES studies and that the research on this topic is gradually reaching its maturity, the interaction of the CBL with large wind farms has not received much attention. It is true that wind-farm power deficits are likely to be small due to the vigorous turbulent mixing

driven by positive buoyancy, but it would be at least worthwhile to confirm this prognosis with numerical simulations. Furthermore, the present dissertation showed that, under conventionally neutral or stable conditions, the energy extraction in large wind farms is mainly coming from kinetic energy upstream of the farm, and not from the background pressure like in the fully developed regime. The wind farm thereby reduces the total energy flux through the boundary layer, but the observed decrease is only a fraction of the total energy flux. In unstable conditions, the strong vertical mixing could result in larger reductions of energy flux, and a fully developed boundary-layer regime might be attained in this situation. Therefore, further research into the interaction between wind farms and the convective boundary layer and the energy household are of interest.

Second, it is stressed that side effects in the spanwise direction due to the finite width of wind farms have not been considered in the current thesis. The studies in the asymptotic limit of "infinite" width are thereby representative of the wind turbines in the middle of a wind farm whose width exceeds the height of the boundary layer by an order of magnitude. In real wind farms, part of the wind will flow around the wind farm in the spanwise direction. The blockage effect due to the turbine drag will therefore be lower compared to the idealised infinite-width case, resulting in lower boundary-layer displacement and gravity wave excitation. As the pressure gradients induced by gravity waves were found to play an important role in the energy budget of the boundary layer, it is believed that further research into gravity wave effects in fully finite wind farms is also necessary.

It is also important to confirm the existence of wind-farm induced gravity waves with observations in operational wind farms. New measurement campaigns should therefore investigate the influence of large wind farms on the wind speed and wind direction upstream of the farm. Moreover, very large wind farms may lead to local cloud formation behind the farm due to trapped lee waves. Such clouds often indicate the presence of topographic gravity waves, and it would be interesting to see if these clouds also occur due to wind-farm generated waves. Further, the results of the present thesis revealed that the traditional classification of ABL regimes, which is solely based on the surface heat flux, does not capture all the aspects that influence wind-farm performance. Therefore, it would be beneficial for measurement campaigns to adopt a more extensive classification of ABL regimes including the height of the boundary layer and the free atmosphere stratification. State-of-the-art developments in LiDAR technology may open up these perspectives.

The Rayleigh damping layer applied at the top of the computational domain provided a simple approach to allow gravity waves to leave the domain, but the non-reflecting boundary condition can definitely be refined with more advanced

techniques. Wave damping layers have the downside that they have to be rather thick to ensure adequate absorption over a large wave number spectrum. Improved performance could be obtained by combining damping layers with the approximate radiation condition of Klemp & Durran (1983). Alternatively, the perfectly matched layer technique could be employed (see, e.g., Hu *et al.* 2008). In a broader context, it would be interesting to investigate meso–micro-scale coupling of LES simulations, which could provide more accurate boundary conditions for gravity waves. However, a remaining challenge in this research field is the spin-up of atmospheric turbulence (Wu 2017).

The large-scale forcing was always assumed to be barotropic in the present thesis. However, baroclinic conditions, in which the background pressure gradients are a function of height, are very common in the atmosphere. This situation arises due to horizontal temperature gradients and can be induced by synoptic scales, land–sea temperature differences, frontal systems or sloping terrain (see, e.g., Stull 1988, p. 522). With respect to large wind farms, baroclinity can play an important role for two reasons. First, baroclinity can result in the formation of low-level jets during both day and night. The maximum of such a jet is always subgeostrophic, whereas a LLJ due to inertial oscillations can yield supergeostrophic wind speeds. Nevertheless, related high wind speeds may have a significant positive impact on wind-farm power output. Second, the variation of wind speed with height under baroclinic conditions can have an influence on the vertical propagation of gravity waves. In particular, the changing wind speed will modify the intrinsic wave frequency, which can yield a different propagation direction and can even result in partial wave reflection. These effects may alter the induced pressure perturbations and hence change the flow behaviour in the vicinity of large wind farms.

Numerical simulations of wind-farm–ABL interactions are computationally very costly, and, as experienced in the current dissertation, often only a limited amount of case studies can be performed. These simulations are therefore useful to gain insight into the complex physical phenomena, but they are unsuited for design and operation applications, such as wind-farm layout optimisation or real-time wind-farm control. For these purposes, the wind-energy community heavily relies on fast engineering models to compute the wind-turbine wakes, such as the Jensen model (Jensen 1983; Katic *et al.* 1986) or the eddy-viscosity model proposed by Ainslie (1988). More recently, several new wake models have been formulated (see, e.g., Larsen *et al.* 2007; Niayifar & Porté-Agel 2015; Stevens *et al.* 2015*a*). In general, these models represent the wind-turbine wakes with an expansion coefficient based on the ambient turbulent intensity, and thermal stability effects are accounted for by increasing or decreasing the turbulence levels. However, the current dissertation demonstrated that outer-layer dynamics have a significant impact on the direction and magnitude of

the wakes, and these aspects should be included in future engineering models. Furthermore, it was shown that the excitation of gravity waves modifies the upstream wind conditions considerably, which poses a clear need to develop low-order models that can predict the feedback effect of wind-farm induced gravity waves. The coupling of such models with existing engineering models of wind farms would not only improve the accuracy of wind-flow predictions, but also allow to explore the parameter space that governs gravity wave phenomena, which may provide valuable insight into their feedback effect on wind-farm performance.

Appendix A

Monin–Obukhov similarity theory

This appendix describes the classic similarity theory for the ABL surface layer. The theory was originally formulated by Monin & Obukhov (1954) and has since been validated and extended by various studies. A historical overview and a summary of the present status of the Monin–Obukhov theory is given by Foken (2006). An important application of similarity theory is that it can be used to predict mean profiles of wind speed and potential temperature. In particular, it is frequently used in large-eddy simulations of ABL flows for modelling of wall effects. The classic similarity relationships are briefly discussed in § A.1, after which the application to wall modelling and implementation details are given in § A.2.

A.1 Similarity relationships

In similarity theory, the non-dimensional gradients of velocity ϕ_m and temperature ϕ_h (defined in equations (3.21) and (3.22)) are expressed as a function of $\zeta = z/L$, with L the Obukhov length (see eq. (2.13)). Many different formulations have been proposed (see, e.g., Holtslag *et al.* 2014 for a discussion), and here the classical Businger–Dyer flux-profile relationships (Businger *et al.*

1971) are used, i.e.,

$$z/L > 0 \quad \text{(stable):} \qquad \phi_m = 1 + \beta_m \zeta \qquad \text{and} \quad \phi_h = 1 + \beta_h \zeta \tag{A.1a}$$

$$z/L < 0 \quad \text{(unstable):} \quad \phi_m = (1 - \gamma_m \zeta)^{-\frac{1}{4}} \quad \text{and} \quad \phi_h = (1 - \gamma_h \zeta)^{-\frac{1}{2}} \tag{A.1b}$$

In literature, various values for the parameters $\beta_m, \beta_h, \gamma_m, \gamma_h$ can be found (Businger *et al.* 1971; Högström 1988; Foken 2006). For stable conditions, the recommendations of the GABLS1 intercomparison study (Beare *et al.* 2006) are adopted, i.e., $\beta_m = 4.8$ and $\beta_h = 7.8$. For unstable conditions, $\gamma_m = 19.3$ and $\gamma_h = 11.6$ are used. Relations (A.1) can be integrated to yield an expression for the vertical profiles of wind speed and potential temperature in the atmospheric surface layer (Stull 1988, p. 385):

$$M(z) = \frac{u_*}{\kappa} \left[\ln\left(\frac{z}{z_0}\right) - \Psi_m\left(\frac{z}{L}\right) + \Psi_m\left(\frac{z_0}{L}\right) \right], \tag{A.2}$$

$$\theta(z) = \theta_s + \frac{\theta_*}{\kappa} \left[\ln\left(\frac{z}{z_0}\right) - \Psi_h\left(\frac{z}{L}\right) + \Psi_h\left(\frac{z_0}{L}\right) \right], \tag{A.3}$$

where the stability corrections functions Ψ_m and Ψ_h have the general form

$$\Psi(\zeta) = \int_0^\zeta \frac{1 - \phi(x)}{x} \mathrm{d}x. \tag{A.4}$$

Integrating equation (A.4) using the Businger–Dyer relationships for stable conditions (A.1a) yields the correction functions

$$\Psi_m = -\beta_m \zeta, \tag{A.5}$$

$$\Psi_h = -\beta_h \zeta, \tag{A.6}$$

and for unstable conditions (A.1b) (Paulson 1970)

$$\Psi_m = \ln\left[\left(\frac{1 + \phi_m^{-2}}{2}\right) \left(\frac{1 + \phi_m^{-1}}{2}\right)^2 \right] - 2 \arctan \phi_m^{-1} + \frac{\pi}{2}, \tag{A.7}$$

$$\Psi_h = \ln\left[\left(\frac{1 + \phi_h^{-1}}{2}\right)^2 \right]. \tag{A.8}$$

Finally, note that the last terms in equations (A.2) and (A.3) are usually neglected since $\Psi_{m,h}(z/L) \gg \Psi_{m,h}(z_0/L)$.

A.2 Application to wall modelling

In LES, Monin–Obukhov theory is often used to estimate the friction velocity u_* and the temperature scale θ_* based on the velocity and potential temperature in the first grid point with wall-normal coordinate z_1. Rewriting equations (A.2) and (A.3) gives

$$u_* = \frac{\kappa M_1}{\ln(z_1/z_0) - \Psi_m(\zeta_1)}, \tag{A.9}$$

$$\theta_* = \frac{\kappa\,(\theta_1 - \theta_s)}{\ln(z_1/z_0) - \Psi_h(\zeta_1)}. \tag{A.10}$$

The stability parameter ζ_1 is given by

$$\zeta_1 = \frac{z_1}{L} = \frac{\kappa g z_1 \theta_*}{u_*^2 \theta_0}. \tag{A.11}$$

Equations (A.9) and (A.10) are implicit equations for u_* and θ_* through the dependence on the stability parameter ζ_1. The solution method therefore depends on the form of the stability correction functions Ψ_m and Ψ_h and the type of boundary conditions.

A.2.1 Stable conditions

For stable conditions, the form of the stability correction functions (i.e., equations (A.5) and (A.6)) is rather simple. Therefore, the implicit set of equations (A.9)–(A.11) can be solved analytically.

Surface temperature given

Extracting θ_* from equation (A.11) and equating it with equation (A.10) yields the following expression:

$$\theta_* = \frac{\zeta_1 u_*^2 \theta_0}{\kappa g z_1} = \frac{\kappa\,(\theta_1 - \theta_s)}{\ln(z_1/z_0) - \Psi_h(\zeta_1)}. \tag{A.12}$$

Inserting equations (A.5), (A.6) and (A.9) gives

$$\left(\frac{\kappa M_1}{\ln(z_1/z_0) + \beta_m \zeta_1}\right)^2 \frac{\zeta_1 \theta_0}{\kappa g z_1} = \frac{\kappa\,(\theta_1 - \theta_s)}{\ln(z_1/z_0) + \beta_h \zeta_1}, \tag{A.13}$$

which can be written as

$$\zeta_1 \frac{1 + a_1\zeta_1}{(1 + a_2\zeta_1)^2} = a_3 \tag{A.14}$$

with

$$a_1 = \frac{\beta_h}{\ln(z_1/z_0)}, \tag{A.15}$$

$$a_2 = \frac{\beta_m}{\ln(z_1/z_0)}, \tag{A.16}$$

$$a_3 = \frac{gz_1}{M_1^2\theta_0}(\theta_1 - \theta_s)\ln(z_1/z_0). \tag{A.17}$$

With some algebra, this equation in ζ_1 can be written as

$$\left(a_1 - a_2^2 a_3\right)\zeta_1^2 + (1 - 2a_2a_3)\,\zeta_1 - a_3 = 0, \tag{A.18}$$

with solution

$$\zeta_1 = \frac{2a_2a_3 - 1 \pm \sqrt{1 + 4a_3\,(a_1 - a_2)}}{2\,(a_1 - a_2^2a_3)}. \tag{A.19}$$

The solution should be positive under stable conditions. Therefore, in conditions that are not too stably stratified (i.e., $a_1 - a_2^2 a_3 > 0$, which is normally satisfied when $\theta_1 - \theta_s < 20K$), the plus sign should be chosen.

Surface heat flux given

In this case, q_w is a constant and the temperature scale is given by $\theta_* = -q_w/u_*$. Inserting in equations (A.5) and (A.9) in equation (A.11) yields:

$$\zeta_1 = b_1\left[1 + b_2\zeta_1\right]^3, \tag{A.20}$$

with

$$b_1 = -\frac{gz_1q_w}{\kappa^2 M_1^3\theta_0}\left[\ln(z_1/z_0)\right]^3, \tag{A.21}$$

$$b_2 = \frac{\beta_m}{\ln(z_1/z_0)}. \tag{A.22}$$

This is a cubic function and can be written as

$$a\zeta_1^3 + b\zeta_1^2 + c\zeta_1 + d = 0, \tag{A.23}$$

with

$$a = b_1 b_2^3, \tag{A.24}$$

$$b = 3b_1 b_2^2, \tag{A.25}$$

$$c = 3b_1 b_2 - 1, \tag{A.26}$$

$$d = b_1. \tag{A.27}$$

In literature, there are several methods to solve cubic equations, and here a trigonometric method is used. First, the cubic is reduced to a depressed cubic by substituting $\zeta_1 = t - b/3a = t - 1/b_2$ in equation (A.23) and dividing the result by a, which yields

$$t^3 + pt + q = 0, \tag{A.28}$$

where

$$p = \frac{3ac - b^2}{3a^2} = -\frac{1}{b_1 b_2^3}, \tag{A.29}$$

$$q = \frac{2b^3 - 9abc + 27a^2 d}{27a^3} = \frac{1}{b_1 b_2^4}. \tag{A.30}$$

The roots of equation (A.28), due to the French mathematician François Viète (1540–1603), are given by

$$t_k = 2\sqrt{-\frac{p}{3}} \cos\left[\frac{1}{3} \arccos\left(\frac{3q}{2p}\sqrt{-\frac{3}{p}}\right) - \frac{2\pi k}{3}\right] \quad \text{for} \quad k = 0, 1, 2. \tag{A.31}$$

The three roots are real when the argument of the arc-cosine lies between -1 and 1, which is equivalent to

$$4p^3 + 27q^2 \leq 0 \quad \Leftrightarrow \quad b_1 b_2 \leq \frac{4}{27}. \tag{A.32}$$

Taylor (1971) showed that equation (A.20) always has exactly one negative root (he actually showed it for the cubic equation in u_*, but these equations are equivalent). Therefore, equation (A.20) has two positive real roots if condition (A.32) holds. The fact that a given surface heat flux results in two possible solutions is called the *dual* nature of sensible heat flux under stable conditions (see § 2.3.2 for a discussion on the physical mechanism behind this duality). Condition (A.32) can be rewritten using the definitions of b_1 and b_2:

$$q_w \geq -\frac{4}{27} \frac{\kappa^2 \theta_0}{g z_1 \beta_m} \frac{M_1^3}{\left[\ln(z_1/z_0)\right]^2} \equiv q_{w,min}. \tag{A.33}$$

This important result has been discussed by Taylor (1971) and afterwards by Basu *et al.* (2008). Equation (A.33) states that no solution exists if the surface

heat flux exceeds the minimal heat flux $q_{w,min}$. In other words, there is a physical limit on the amount of heat that the turbulent flow can transport towards the surface (cf. § 2.3.2). When higher heat fluxes are applied, the flow will become intermittent and the Monin–Obukhov theory no longer applies.

When equation (A.28) has three real roots, it can be shown that $t_0 \geq t_1 \geq t_2$. Hence, t_2 must be negative according to Taylor (1971), which is not a valid solution. The stable solution is then given by the weakest stable case corresponding to t_1:

$$\zeta_1 = 2\sqrt{\frac{1}{3b_1b_2^3}}\cos\left[\frac{1}{3}\arccos\left(-\frac{3}{2b_2}\sqrt{3b_1b_2^3}\right) - \frac{2\pi}{3}\right] - \frac{1}{b_2}. \tag{A.34}$$

A.2.2 Unstable conditions

Under unstable conditions, the boundary conditions can not be expressed explicitly. Instead, an iterative scheme is needed to compute the correct surface stress and heat flux. The following scheme is used

1. Start with initial guess for friction velocity:

$$u_*^0 = \frac{\kappa M_1}{\ln(z_1/z_0)}. \tag{A.35}$$

2. If the surface temperature is specified, an initial guess for the temperature scale is obtained with

$$\theta_*^0 = \frac{\kappa\,(\theta_1 - \theta_s)}{\ln(z_1/z_0)}. \tag{A.36}$$

3. Compute ζ_1 using equation (A.11).

4. Compute Ψ_m using equation (A.7). If the surface temperature is specified, also compute Ψ_h with equation (A.8).

5. Compute a new friction velocity u_*^{n+1} using equation (A.9). If the surface temperature is specified, also compute a new temperature scale θ_*^{n+1} with equation (A.10).

6. Repeat steps 3–5 until the solution for ζ_1 has converged.

This scheme corresponds to a basic substitution method, but it can easily be replaced by more advanced iterative schemes such as, e.g., the Newton–Raphson method. In the current implementation, the convergence criterion is based on

the relative change in friction velocity, with a tolerance of 10^{-10}. As the initial guess appears to be relatively close to the final value, the suggested scheme was found to converge within only a few iterations. Therefore, the maximum iteration count is set to 10 iterations. Note, however, that this scheme is not used in the current thesis as no unstable conditions are considered.

Appendix B

Resistance law coefficients for the CNBL

In this appendix, explicit expressions are derived for the resistance law coefficients $F_1(C_g, Ro_h, \bar{h})$ and $F_2(C_g, Ro_h, \bar{h})$ used in equations (4.22) and (4.23). These coefficients depend on the geostrophic drag $C_g = u_{*hi}/G$, the Rossby number $Ro_h = G/f_c z_h$ and the dimensionless boundary-layer height $\bar{h} = h/z_h$.

By matching the law of the wall with the velocity-defect law in the surface layer, it can be shown that $F_1(C_g, Ro_h, \bar{h})$ and $F_2(C_g, Ro_h, \bar{h})$ are given by (see, e.g., Tennekes & Lumley 1972, p. 169)

$$F_1(C_g, Ro_h, \bar{h}) = \frac{u - U_g}{u_*} - \frac{1}{\kappa} \ln\left(\frac{\zeta \bar{h}}{C_g Ro_h}\right), \tag{B.1}$$

$$F_2(C_g, Ro_h, \bar{h}) = -\frac{V_g}{u_*}, \tag{B.2}$$

using $V \approx 0$ in the surface layer. Further, $U_g = G\cos\alpha$, $V_g = G\sin\alpha$ and $\zeta = z/h$. For wind farms in fully developed boundary layers, the friction velocity u_{*hi} characterising the log layer above the turbine region should be used in equations (B.1) and (B.2) (see § 4.2.2).

The velocity defect can be found by solving the so-called Ekman-layer equations, which hold for a stationary, horizontally homogeneous atmospheric boundary

layer (Tennekes & Lumley 1972, p. 167):

$$-f_c\,(v - V_g) = \frac{\partial \tau_{xz}}{\partial z}, \tag{B.3}$$

$$f_c\,(u - U_g) = \frac{\partial \tau_{yz}}{\partial z}, \tag{B.4}$$

where use has been made of the geostrophic balance (2.6). These equations can be closed using gradient transfer theory: $(\tau_{xz}, \tau_{yz}) = K(\partial u/\partial z, \partial v/\partial z)$, with K the eddy viscosity. Non-dimensionalising equations (B.3) and (B.4) and writing them in complex notation yields a second-order complex differential equation for the velocity defect vector $w_d = (u - U_g)/u_* + i\,(v - V_g)/u_*$:

$$\frac{\mathrm{d}^2 w_d}{\mathrm{d}\zeta^2} - i\frac{\bar{h}}{C_g Ro_h}\frac{w_d}{\bar{K}} = 0, \tag{B.5}$$

with $\bar{K}(\zeta) = K/u_* h$ a non-dimensional eddy viscosity.

In literature, closed-form solutions to equation (B.5) are found for some specific eddy viscosity profiles. Csanady (1974) found a solution assuming a constant eddy viscosity:

$$w_d = (i-1)\left(\frac{C_g Ro_h}{2\bar{K}\bar{h}}\right)^{1/2}\frac{\cosh\left[\gamma(\zeta-1)\right]}{\sinh\left(\gamma\right)} \tag{B.6}$$

with $\gamma = (i+1)\left(2\bar{K}C_g Ro_h/\bar{h}\right)^{-1/2}$. Inserting (B.6) in equations (B.1) and (B.2) yields

$$F_1(C_g, Ro_h, \bar{h}) = -\frac{1}{\kappa}\ln\left(\frac{\zeta_s \bar{h}}{C_g Ro_h}\right) + \Re\left\{w_d(\zeta_s)\right\}, \tag{B.7}$$

$$F_2(C_g, Ro_h, \bar{h}) = \Im\left\{w_d(0)\right\}, \tag{B.8}$$

where $\zeta_s = h_s/h$, with h_s the top of the surface layer (i.e., the location where inner and outer profile are matched).

Nieuwstadt (1983) provided solutions to equation (B.5) for a quadratic profile, i.e., $\bar{K}_I = \kappa\zeta(1-\zeta)$, and a cubic profile, i.e., $\bar{K}_{II} = \kappa\zeta(1-\zeta)^2$:

$$w_{d,I} = -\frac{1}{\kappa}\frac{\pi}{\cos\pi\beta}\,{}_2F_1\left(\tfrac{1}{2}+\beta, \tfrac{1}{2}-\beta; 1; 1-\zeta\right), \tag{B.9}$$

$$w_{d,II} = \frac{1}{\kappa} i \frac{\alpha^2\Gamma^2(\alpha)}{C\Gamma(2\alpha)}(1-\zeta)^{\alpha-1}\,{}_2F_1\left(\alpha+1, \alpha-1; 2\alpha; 1-\zeta\right), \tag{B.10}$$

where

$$\beta = \frac{1}{2}\sqrt{1-4iC}, \quad \alpha = \frac{1}{2} + \frac{1}{2}\sqrt{1+4iC} \quad \text{and} \quad C = \frac{\bar{h}}{\kappa C_g Ro_h}. \tag{B.11}$$

In these expressions, $\Gamma(x)$ is the gamma function and ${}_2F_1(a,b;c;x)$ is the hypergeometric function. Nieuwstadt also derives an expression for $F_1(C_g, Ro_h, \bar{h})$ and $F_2(C_g, Ro_h, \bar{h})$ by taking the limit of equations (B.9) and (B.10) for $z \to 0$ and matching it to a surface-layer profile. This gives for the quadratic profile

$$F_1(C_g, Ro_h, \bar{h}) = -\frac{1}{\kappa}\ln\left(\frac{\bar{h}}{C_g Ro_h}\right) + \frac{1}{\kappa}\Re\left\{\psi\left(\tfrac{1}{2}-\beta\right) + \psi\left(\tfrac{1}{2}+\beta\right) - 2\psi(1)\right\}, \tag{B.12}$$

$$F_2(C_g, Ro_h, \bar{h}) = \frac{1}{\kappa}\Im\left\{\psi\left(\tfrac{1}{2}-\beta\right) + \psi\left(\tfrac{1}{2}+\beta\right) - 2\psi(1)\right\}, \tag{B.13}$$

and for the cubic profile

$$F_1(C_g, Ro_h, \bar{h}) = -\frac{1}{\kappa}\ln\left(\frac{\bar{h}}{C_g Ro_h}\right) + \frac{1}{\kappa}\Re\left\{\psi\left(\alpha+1\right) + \psi\left(\alpha-1\right) - 2\psi(1)\right\}, \tag{B.14}$$

$$F_2(C_g, Ro_h, \bar{h}) = \frac{1}{\kappa}\Im\left\{\psi\left(\alpha+1\right) + \psi\left(\alpha-1\right) - 2\psi(1)\right\}, \tag{B.15}$$

with $\psi(x)$ the psi function or digamma function.

Appendix C

Tuning boundary conditions for gravity waves

Atmospheric boundary layers developing over large wind farms experience an upward displacement of the capping inversion and the free atmosphere due to flow blockage by the farm, which in turn excites gravity waves. Numerical simulation of large wind farms therefore requires adequate boundary conditions that allow gravity waves to leave the computational domain without spurious reflections. As discussed in § 5.1.1, wave reflection is prevented by a Rayleigh damping layer at the top of the domain, and by the fringe region in the streamwise direction.

This appendix describes how the parameters defining the Rayleigh damping layer and the fringe region are determined. Section C.1 first illustrates the importance of adequate boundary conditions. Subsequently, section C.2 introduces a fast, two-dimensional potential-flow approach that is used for tuning of the damping regions, and discusses the configuration of boundary conditions applied in the LES simulations.

C.1 Problem statement

The importance of gravity wave damping at the domain boundaries is best illustrated by showing what happens when inadequate boundary conditions are used. In a first attempt to simulate a developing boundary layer over a large wind farm, Rayleigh damping was only applied in the precursor domain, and the

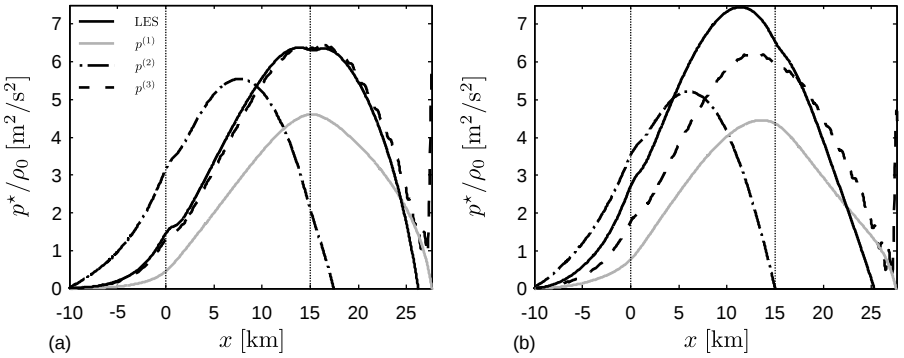

Figure C.1: Mean pressure perturbation in (a) an LES case without Rayleigh damping and (b) an LES case with inadequate Rayleigh damping, as computed by LES and by linear theory, assuming only inversion displacement ($p^{(1)}$), a combination of inversion displacement and upward wave propagation ($p^{(2)}$), and a combination of inversion displacement, upward and downward wave propagation ($p^{(3)}$). The vertical dotted lines indicate the start and end of the wind farm.

main domain used simple rigid-lid conditions at a height of 5 km. Furthermore, the fringe region was only 800 m wide with a very strong damping coefficient $\lambda^{fr}_{max} = 0.4$ s^{-1}. Other set-up parameters corresponded to case S1 defined in § 5.1.3.

Figure C.1(a) shows the mean pressure perturbation for this LES simulation. The LES result, shown as a solid black line, is compared with three estimates obtained with linear theory of gravity waves. A first estimate is calculated with the assumption that the pressure perturbation is only induced by the inversion displacement, which yields $p^{(1)} = g'\eta$ (shown by a solid gray line) (Smith 2010), with $g' = g\Delta\theta/\theta_0$ a reduced gravity accounting for the inversion strength and η the inversion displacement obtained from the LES result. The other two estimates include vertically propagating gravity waves, so that $p^{(2,3)} = g'\eta + p_{top}$ where p_{top} is the pressure perturbation just above the inversion layer. This pressure is found by solving equation (2.16) in the free atmosphere and using the solution for w_1 in equations (2.15c) and (2.15d) to obtain p_1. Assuming that only upward propagating waves occur can be translated into boundary conditions for equation (2.16) and results in a second estimate $p^{(2)}$, represented by the dash–dotted line in figure C.1(a). The third estimate $p^{(3)}$, shown by a dashed line, is obtained by solving equation (2.16) with a rigid-lid condition at a height of 5 km, as is actually simulated by the LES.

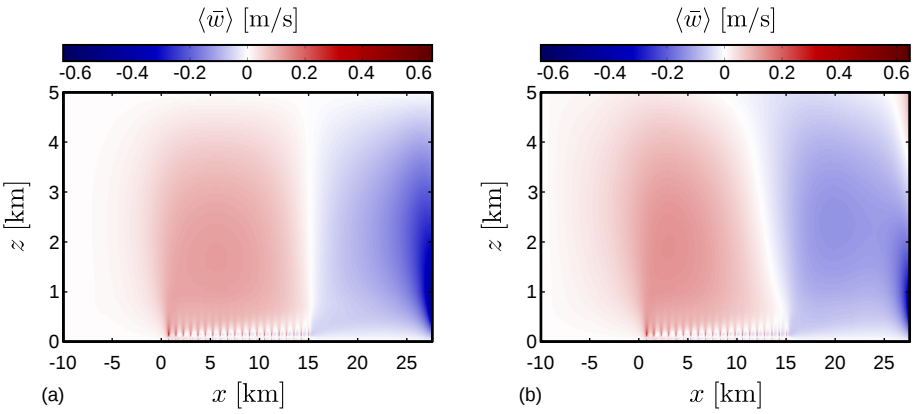

Figure C.2: Contours of time-averaged vertical velocity for (a) an LES case without Rayleigh damping and (b) an LES case with inadequate Rayleigh damping.

The pressure obtained with LES agrees very well with $p^{(3)}$, which contains upward propagating waves excited by the inversion displacement as well as downward propagating waves that have been reflected at the top of the domain. Obviously, this reflection is a numerical issue, and the pressure in the wind-farm simulation should preferably follow $p^{(2)}$. The magnitude of the pressure perturbation obtained by LES is not very different from $p^{(2)}$, but the location of its maximum is predicted too far downstream by the LES. Therefore, simply applying a rigid-lid condition in LES results in gravity wave reflection and non-physical pressure distributions.

Figure C.1(b) shows a similar comparison, but now for an LES simulation with a Rayleigh damping layer of 2 km starting at a height of 5 km. The damping coefficient is set to 0.0166 s^{-1}. The location of the maximum induced pressure now lies somewhere between the linear theory estimates $p^{(2)}$ and $p^{(3)}$. The Rayleigh damping layer thus seems to improve the LES result a little, but the choice of parameters is certainly not optimal.

The issue of gravity wave reflection is further illustrated in figure C.2, showing the time-averaged vertical velocity field. When no damping is applied at the top, a horizontal, standing wave pattern is observed. In the case with damping, some inclination is observed, which points to vertically propagating waves. The method of Taylor & Sarkar (2007) can be used to compute the fraction of downward propagating waves from the vertical velocity field (see also § 5.3.3). In figure C.2(a), the vertical kinetic energy associated with downward propagating waves is 68.5 % of the energy associated with upward propagating waves. This

fraction is reduced to 48.2 % when a damping layer is added (figure C.2(b)). These values are still very high (e.g., Taylor & Sarkar (2007) only have about 6 % reflection) and indicate that too much wave reflection occurs, even when a Rayleigh damping layer is added.

In summary, adding a Rayleigh damping layer near the top of the LES domain can reduce wave reflection, but the choice used here does not give satisfying results and tuning of the parameters is necessary. Furthermore, it is unclear how the fringe region influences the results, and this region probably needs to be tuned as well. To date, very little guidelines are available in literature on the set-up of efficient Rayleigh damping layers. Currently, the only way to find a good configuration appears to be by systematically varying all relevant parameters. However, this approach is too costly and too time consuming to apply in full-scale, three-dimensional LES (e.g., computing two physical hours takes about 9 days on 640 cores). Instead, the parameter space is explored with a simplified flow solver, which is discussed in the next section.

C.2 Two-dimensional potential-flow simulations

The length scales associated with wind-farm induced gravity waves are typically one or two orders of magnitude larger than the largest turbulent length scales in the ABL. Furthermore, the gravity waves only occur in the free atmosphere where the flow behaves as a simple potential flow without viscous or turbulent forces. In addition, the gravity waves considered in this thesis are two-dimensional as the wind farms triggering these waves are of "infinite" width. Gravity waves can therefore be simulated in a two-dimensional domain with a coarse grid resolution, for which the computation times will be much faster than for a three-dimensional, fine resolution LES. These cheap simulations allow efficient testing of boundary conditions for gravity waves.

The simplified, two-dimensional simulations are performed with SP-Wind so that the numerical schemes and the implementation of the boundary conditions are the same as in the full-scale LES simulations. In order to obtain a potential flow, a uniform inflow is applied in the fringe region, i.e., no precursor simulation is used. Furthermore, no pressure gradient or wall stress is applied, and to make sure that the flow is non-turbulent, no initial perturbations are added. A capping inversion is included in the simulations at a height of 1 km, and the vertical structure is defined with a zeroth-order model (see § 2.3.1 and figure 2.5). In the y-direction, a couple of grid points are used so that the 3D parallellisation and communication patterns of SP-Wind do not need to be

adapted. This does not change the outcome of the simulation as only the mean mode in this direction will be non-zero.

The effect of the wind farm is modelled with a continuous forcing function $f(x,z) = \lambda f_x(x) f_z(z)/f_{scale}$, the shape of which is defined by

$$f_x(x) = \begin{cases} \cos\left(\pi \dfrac{x - (x_0 - \frac{L}{2} + \delta_1)}{4\delta_1}\right), & x_0 - \frac{L}{2} - \delta_1 < x < x_0 - \frac{L}{2} + \delta_1 \\ 1, & x_0 - \frac{L}{2} + \delta_1 < x < x_0 + \frac{L}{2} - \delta_1 \\ \cos\left(\pi \dfrac{x - (x_0 + \frac{L}{2} - \delta_1)}{4\delta_1}\right), & x_0 + \frac{L}{2} - \delta_1 < x < x_0 + \frac{L}{2} + \delta_1 \\ 0, & \text{otherwise} \end{cases} \tag{C.1}$$

$$f_z(z) = \begin{cases} 1, & 0 < z < H - \delta_2 \\ \cos\left(\pi \dfrac{z - (H - \delta_2)}{4\delta_2}\right), & H - \delta_2 < z < H + \delta_2 \\ 0, & \text{otherwise} \end{cases} \tag{C.2}$$

and

$$f_{scale} = \left(L + 2\frac{4-\pi}{\pi}\delta_1\right)\left(H + \frac{4-\pi}{\pi}\delta_2\right). \tag{C.3}$$

The functions f_x, f_z and f_{scale} are chosen so that the integrated force over the entire region is equal to λ, which is set here to $0.01G^2/D$. The parameters L and H determine the size of the forcing region and are set to 15 km and 600 m, respectively. Note that the force is not confined to the traditional turbine region but instead smeared out over the boundary-layer height, similar to the approach of Smith (2010). Moreover, a smooth profile is chosen to avoid non-linear wave interactions triggered by abrupt changes in the forcing function. The smoothness is thereby controlled by δ_1 and δ_2, which are set to 2 km and 400 m, respectively. Finally, x_0 corresponds to the centre of the forcing region.

Table C.1 summarises the configuration of the numerical domain and the boundary conditions in three potential-flow simulations and one full-scale LES (i.e., case S1 from chapter 5). Case PF1 uses a very large computational domain of 400 km × 40 km and is used as a reference case to assess the performance of boundary conditions in other simulations with smaller domains. Due to the large width of the damping layers in case PF1, the actual value of the damping coefficient is less important. Simulating two physical hours for this case requires approximately 12 computation hours on 64 cores (with Ivy Bridge architecture). The pressure and streamwise pressure gradient below the capping inversion for this case are compared with the prediction from linear theory in figure C.3. Both the shape and the magnitude of the numerical results agree very well

Table C.1: Case set-up for finding adequate boundary conditions for simulations with gravity waves. Cases PF1, PF2 and PF3 are two-dimensional potential flow simulations, while LES represents a full-scale, three-dimensional, turbulent simulation.

	$L_x \times L_z$ [km]	$\Delta x \times \Delta z$ [m]	L^{fr} [km]	λ^{fr}_{max} [s^{-1}]	L^{ra} [km]	λ^{ra}_{max} [s^{-1}]
PF1	400×40	250×25	30	0.033	15	0.016
PF2	40×25	$250 \times 25/300$	5	0.03	10	0.0001
PF3	40×25	$40 \times 5/300$	5	0.03	10	0.0001
LES	38.4×25	$30 \times 5/300$	4.8	0.03	10	0.0001

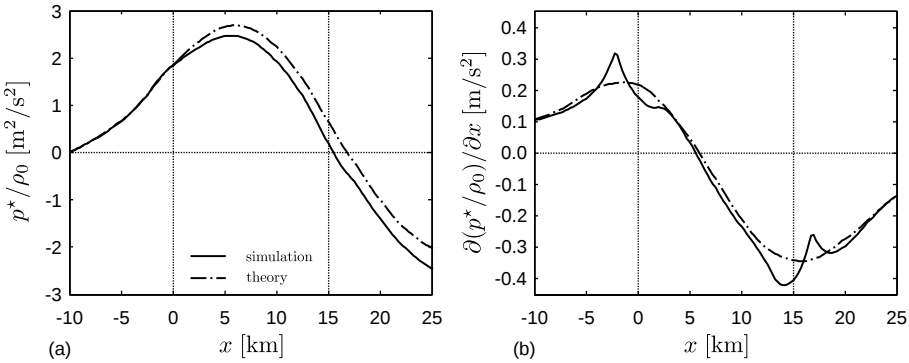

Figure C.3: (a) Pressure and (b) streamwise pressure gradient below the capping inversion for case PF1, comparing results from the numerical simulation with linear theory. The vertical dotted lines indicate the start and end of the wind farm, and only part of the numerical domain is shown.

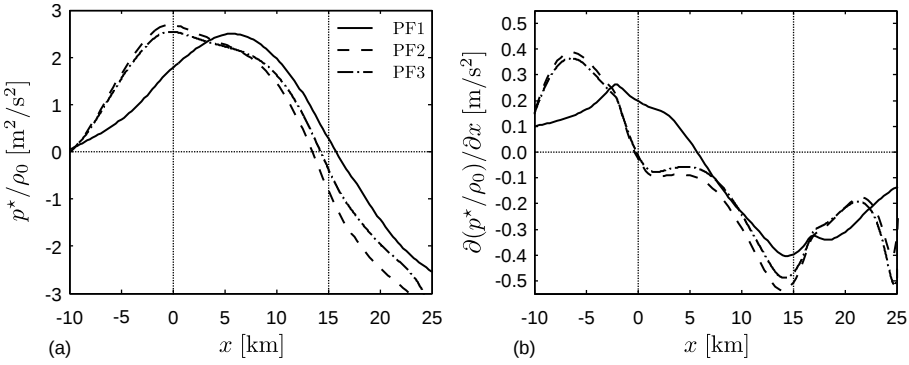

Figure C.4: (a) Pressure and (b) streamwise pressure gradient below the capping inversion for cases PF1, PF2 and PF3. The vertical dotted lines indicate the start and end of the wind farm, and only part of the numerical domain is shown.

with linear theory. Some small oscillations are observed at the start and end of the wind farm, which are attributed to non-linear wave interactions. Further, decomposing the vertical velocity field using the method of Taylor & Sarkar (2007) reveals that the energy associated with downward propagating waves is less than 5 % of the energy associated with upward propagating waves.

It is now attempted to obtain the same pressure profile using a numerical domain with reduced streamwise length ($L_x = 40$ km) and smaller fringe region ($L^{fr} = 5$ km) by varying all the relevant parameters. This configuration only requires about half an hour of computation time on 16 cores to calculate two physical hours (compared to the 9 days and 640 cores of a full-scale LES), thereby allowing a thorough parameter sweep. Table C.2 summarises the various series of potential-flow simulations and gives an indication of the explored parameters space. The first column indicates the amount of simulations with a given set-up, and the numbers between brackets represent the explored parameter range. In total, 189 simulations were performed.

From this large set of simulations, case PF2 has been selected and is discussed here. This simulation is performed on a grid with uniform resolution in the vertical direction up to 15 km, above which the grid is stretched with $f_s = 1.0954$. Further, it uses a Rayleigh damping layer of $L^{ra} = 10$ km starting at a height of 15 km and a fringe region of $L^{fr} = 5$ km. Note that the fringe region is considerably wider than the 800 m used in the previous section, and that it is also 2.5 to 4 times as wide as what is typically used in literature for wind farms in neutral, pressure-driven boundary layers (Stevens *et al.* 2014*b*; Munters *et al.* 2016). Reasonable agreement is found between the pressure profiles of

Table C.2: Various series of potential-flow simulations used to find optimal boundary conditions for gravity waves, indicating the explored parameter space.

# sim.	configuration z-grid	λ^{fr}_{max} [s^{-1}]	L^{ra} [km]	λ^{ra}_{max} [s^{-1}]
15	Uniform ($L_z = 10$ km, $\Delta z = 50$ m)	[0.001 – 0.3]	5	0.3
30	Uniform ($L_z = [10, 15, 20]$ km, $\Delta z = 50$ m)	0.033	5	[0 – 0.15]
16	Uniform ($L_z = 20$ km, $\Delta z = 50$ m)	0.033	[0 – 15]	0.005
40	Uniform ($L_z = 5$ km, $\Delta z = 50$ m) with stretched region above ($L_z = [3, 7.6, 12.6, 17.6]$ km, $\Delta z = 50 - 500$ m, $f_s = 1.0966$)	0.033	[3,7.6,12.6,17.6]	[0 – 0.15]
14	Uniform ($L_z = 20$ km, $\Delta z = 25$ m)	[0.001 – 0.3]	5	0.01
10	Uniform ($L_z = 20$ km, $\Delta z = 25$ m)	0.03	5	[0 – 0.15]
10	Uniform ($L_z = 15$ km, $\Delta z = 25$ m) with stretched region above ($L_z = 5$ km, $\Delta z = 25 - 300$ m, $f_s = 1.0954$)	0.03	5	[0 – 0.15]
10	Uniform ($L_z = 15$ km, $\Delta z = 25$ m) with stretched region above ($L_z = 10$ km, $\Delta z = 25 - 300$ m, $f_s = 1.0954$)	0.03	10	[0 – 0.15]
10	Uniform ($L_z = 15$ km, $\Delta z = 25$ m) with stretched region above ($L_z = 5$ km, $\Delta z = 25 - 300$ m, $f_s = 1.0234$)	0.03	5	[0 – 0.15]
10	Uniform ($L_z = 15$ km, $\Delta z = 25$ m) with stretched region above ($L_z = 10$ km, $\Delta z = 25 - 300$ m, $f_s = 1.0234$)	0.03	10	[0 – 0.15]
14	Uniform ($L_z = 15$ km, $\Delta z = 25$ m) with stretched region above ($L_z = 10$ km, $\Delta z = 25 - 300$ m, $f_s = 1.0954$)	[0.001 – 0.3]	10	0.0001

case PF2 and the reference case, as shown in figure C.4. It is observed that the pressure gradient is overestimated in the beginning of the simulation in case PF2. Moreover, the maximum pressure is located more upstream than in the reference case. Despite these differences, the overall shape and magnitude of the pressure are very similar. Figure C.4 further shows the results of case PF3, which is still a two-dimensional potential flow simulation but approaches the x–z grid resolution of a realistic LES simulation. The grid refinement does not seem to modify the pressure profile significantly, which suggests that this configuration should also work in full-scale LES simulations.

Figure C.5 shows the results of a full-scale LES with the optimal configuration compared to the reference case PF1. The pressure and vertical velocity fields of both simulations have been scaled by the maximum perturbation. The wind-farm forcing is not the same in both cases, so only a qualitative comparison can be made here. The vertical velocity field of the full-scale LES is very similar to the reference case, and the agreement between the pressure fields is even better. In particular, the size and the inclination of the wave structures is well represented in the full-scale LES, especially when comparing this figure with figure C.2(a) where spurious wave reflection resulted in purely vertical structures. As before, a quantitative assessment can be obtained by estimating the energy associated with downward wave propagation, which is about 7.8 % of the upward propagation wave energy. It is therefore concluded that the current configuration of boundary conditions allows a representation of wind-farm induced gravity waves in full-scale LES simulations that is sufficiently accurate for the purpose of the present dissertation.

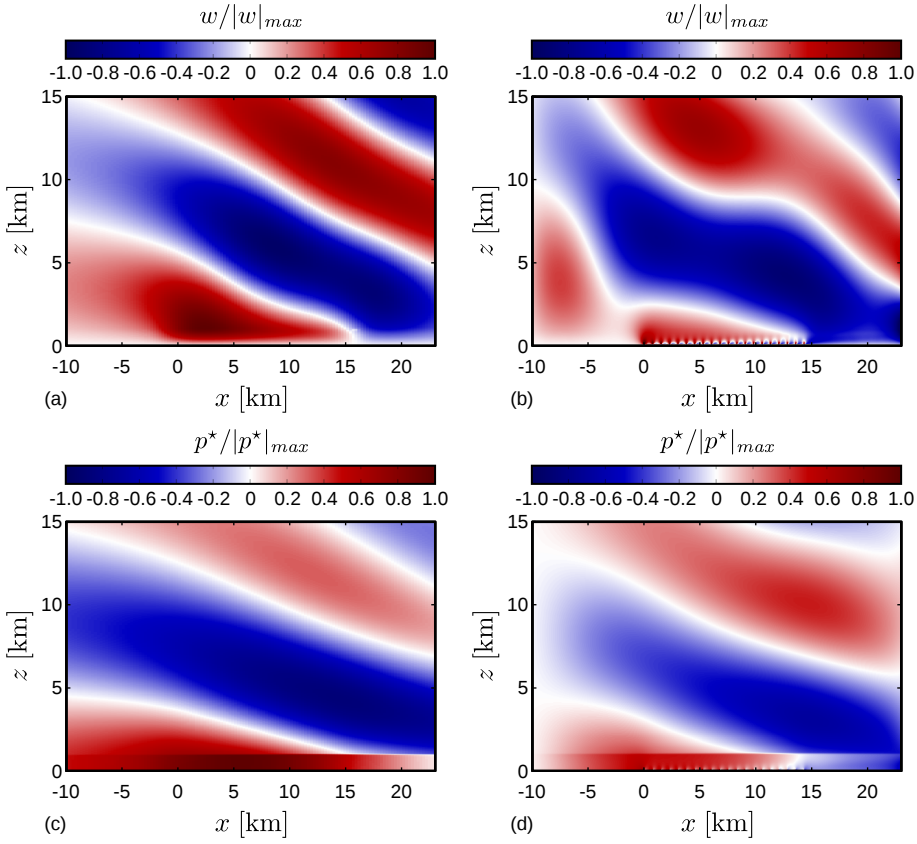

Figure C.5: Contours of (a–b) vertical velocity and (c–d) pressure for case PF1 (a,c) and a full-scale LES (b,d). Results have been scaled by the maximum perturbation to allow a qualitative comparison of the gravity wave structures.

References

Abkar, M. & Porté-Agel, F. 2013 The effect of free-atmosphere stratification on boundary-layer flow and power output from very large wind farms. *Energies* **6** (5), 2338–2361.

Abkar, M. & Porté-Agel, F. 2014 Mean and turbulent kinetic energy budgets inside and above very large wind farms under conventionally-neutral conditions. *Renewable Energy* **70** (0), 142–152.

Abkar, M. & Porté-Agel, F. 2015 Influence of atmospheric stability on wind-turbine wakes: A large-eddy simulation study. *Phys. Fluids* **27** (3).

Abkar, M., Sharifi, A. & Porté-Agel, F. 2016 Wake flow in a wind farm during a diurnal cycle. *J. Turbul.* **17** (4), 420–441.

Ainslie, J. F. 1988 Calculating the flowfield in the wake of wind turbines. *J. Wind Eng. Ind. Aerodyn.* **27** (1), 213–224.

Allaerts, D. & Meyers, J. 2015 Large eddy simulation of a large wind-turbine array in a conventionally neutral atmospheric boundary layer. *Phys. Fluids* **27**, 065108.

Allaerts, D. & Meyers, J. 2016 Boundary layer development and gravity waves in conventionally neutral wind farms. *J. Fluid Mech.* revision submitted.

Ammara, I., Leclerc, C. & Masson, C. 2002 A viscous three-dimensional differential/actuator-disk method for the aerodynamic analysis of wind farms. *J. Solar Energ. Eng.* **124** (4), 345–356.

André, J. C. & Mahrt, L. 1982 The nocturnal surface inversion and influence of clear-air radiative cooling. *J. Atmos. Sci.* **39** (4), 864–878.

Andren, A. 1995 The structure of stably stratified atmospheric boundary layers: A large-eddy simulation study. *Q. J. R. Meteorol. Soc.* **121** (525), 961–985.

Andren, A., Brown, A. R., Mason, P. J., Graf, J., Schumann, U., Moeng, C.-H. & Nieuwstadt, F. T. M. 1994 Large-eddy simulation of a neutrally stratified boundary layer: A comparison of four computer codes. *Q. J. R. Meteorol. Soc.* **120** (520), 1457–1484.

Andren, A. & Moeng, C.-H. 1993 Single-point closures in a neutrally stratified boundary layer. *J. Atmos. Sci.* **50** (20), 3366–3379.

Antonopoulos-Domis, M. 1981 Large-eddy simulation of a passive scalar in isotropic turbulence. *J. Fluid Mech.* **104**, 55–79.

Archer, C. L., Mirzaeisefat, S. & Lee, S. 2013 Quantifying the sensitivity of wind farm performance to array layout options using large-eddy simulation. *Geophys. Res. Lett.* **40** (18), 4963–4970.

Armenio, V. & Sarkar, S. 2002 An investigation of stably stratified turbulent channel flow using large-eddy simulation. *J. Fluid Mech.* **459**, 1–42.

Arya, S. P. S. 1975 Comments on "Similarity theory for the planetary boundary layer of time-dependent height". *J. Atmos. Sci.* **32** (4), 839–840.

Arya, S. P. S. 1978 Comparative effects of stability, baroclinity and the scale-height ratio on drag laws for the atmospheric boundary layer. *J. Atmos. Sci.* **35** (1), 40–46.

Baidya Roy, S. 2011 Simulating impacts of wind farms on local hydrometeorology. *J. Wind Eng. Ind. Aerodyn.* **99** (4), 491–498.

Baidya Roy, S., Pacala, S. W. & Walko, R. L. 2004 Can large wind farms affect local meteorology? *J. Geophys. Res.* **109**, D19101.

Baidya Roy, S. & Traiteur, J. J. 2010 Impacts of wind farms on surface air temperatures. *Proc. Natl. Acad. Sci. USA* **107** (42), 17899–17904.

Bannon, P. R. 1996 On the anelastic approximation for a compressible atmosphere. *J. Atmos. Sci.* **53** (23), 3618–3628.

Barthelmie, R. J., Frandsen, S. T., Nielsen, M. N., Pryor, S. C., Rethore, P.-E. & Jørgensen, H. E. 2007*a* Modelling and measurements of power losses and turbulence intensity in wind turbine wakes at Middelgrunden offshore wind farm. *Wind Energy* **10** (6), 517–528.

Barthelmie, R. J., Hansen, K., Frandsen, S. T., Rathmann, O., Schepers, J. G., Schlez, W., Phillips, J., Rados, K., Zervos, A., Politis, E. S. & Chaviaropoulos, P. K. 2009 Modelling and measuring flow and wind turbine wakes in large wind farms offshore. *Wind Energy* **12** (5), 431–444.

Barthelmie, R. J. & Jensen, L. E. 2010 Evaluation of wind farm efficiency and wind turbine wakes at the Nysted offshore wind farm. *Wind Energy* **13** (6), 573–586.

Barthelmie, R. J., Pryor, S. C., Frandsen, S. T., Hansen, K. S., Schepers, J. G., Rados, K., Schlez, W., Neubert, A., Jensen, L. E. & Neckelmann, S. 2010 Quantifying the impact of wind turbine wakes on power output at offshore wind farms. *J. Atmos. Oceanic Technol.* **27** (8), 1302–1317.

Barthelmie, R. J., Rathmann, O., Frandsen, S. T., Hansen, K. S., Politis, E., Prospathopoulos, J., Rados, K., Cabezón, D., Schlez, W., Phillips, J., Neubert, A., Schepers, J. G. & van der Pijl, S. P. 2007*b* Modelling and measurements of wakes in large wind farms. *J. Phys.: Conf. Ser.* **75** (1), 012049.

Basu, S., Holtslag, A. A. M. & Bosveld, F. C. 2012 GABLS3-LES intercomparison study. In *Proc. ECMWF Workshop on Diurnal Cycles and the Stable Boundary Layer*, pp. 75–82. Reading, England, ECMWF/WCRP.

Basu, S., Holtslag, A. A. M., Van De Wiel, B. J. H., Moene, A. F. & Steeneveld, G.-J. 2008 An inconvenient "truth" about using sensible heat flux as a surface boundary condition in models under stably stratified regimes. *Acta Geophysica* **56** (1), 88–99.

Basu, S. & Porté-Agel, F. 2006 Large-eddy simulation of stably stratified atmospheric boundary layer turbulence: A scale-dependent dynamic modeling approach. *J. Atmos. Sci.* **63** (8), 2074–2091.

Bazile, E., Le Moigne, P. & Couvreux, F. 2016 GABLS4: a model intercomparison study in extremely stable conditions. In *Geophysical Research Abstract*, *18* EGU2016-13005. EGU General Assembly 2016.

Beare, R. J., Macvean, M. K., Holtslag, A. A. M., Cuxart, J., Esau, I., Golaz, J.-C., Jimenez, M. A., Khairoutdinov, M., Kosović, B., Lewellen, D., Lund, T. S., Lundquist, J. K., Mccabe, A., Moene, A. F., Noh, Y., Raasch, S. & Sullivan, P. P. 2006 An intercomparison of large-eddy simulations of the stable boundary layer. *Boundary-Layer Meteorol.* **118** (2), 247–272.

Belcher, S. E., Jerram, N. & Hunt, J. C. R. 2003 Adjustment of a turbulent boundary layer to a canopy of roughness elements. *J. Fluid Mech.* **488**, 369–398.

Beljaars, A. C. M. & Holtslag, A. A. M. 1991 Flux parameterization over land surfaces for atmospheric models. *J. Appl. Meteor.* **30** (3), 327–341.

Bergström, H. 2009 Meteorological conditions at Lillgrund. *Tech. Rep.*. Vattenfall Vindkraft AB, 6_2 LG Pilot Report.

Betts, A. K. 1973 Non-precipitating cumulus convection and its parametrization. *Q. J. R. Meteorol. Soc.* **99**, 178–196.

Betts, A. K. 1974 Reply to comment on the paper "Non-precipitating cumulus convection and its parametrization.". *Q. J. R. Meteorol. Soc.* **100**, 469–471.

Blackadar, A. K. 1957 Boundary layer wind maxima and their significance for the growth of nocturnal inversions. *Bull. Amer. Meteor. Soc.* **38**, 283–290.

Blom, J. & Wartena, L. 1969 The influence of changes in surface roughness on the development of the turbulent boundary layer in the lowest layer of the atmosphere. *J. Atmos. Sci.* **26**, 255–265.

Bou-Zeid, E., Meneveau, C. & Parlange, M. 2005 A scale-dependent Lagrangian dynamic model for large eddy simulation of complex turbulent flows. *Phys. Fluids* **17** (2), 025105.

Bou-Zeid, E., Meneveau, C. & Parlange, M. B. 2004 Large-eddy simulation of neutral atmospheric boundary layer flow over heterogeneous surfaces: Blending height and effective surface roughness. *Water Resour. Res.* **40** (2), 1–18.

Brethouwer, G., Billant, P., Lindborg, E. & Chomza, J.-M. 2007 Scaling analysis and simulation of strongly stratified turbulent flows. *J. Fluid Mech.* **585**, 343–368.

Brost, R. A., Lenschow, D. H. & Wyngaard, J. C. 1982 Marine stratocumulus layers. Part I: Mean conditions. *J. Atmos. Sci.* **39** (4), 800–817.

Brown, A. R., Derbyshire, S. H. & Mason, P. J. 1994 Large-eddy simulation of stable atmospheric boundary layers with a revised stochastic subgrid model. *Q. J. R. Meteorol. Soc.* **120** (520), 1485–1512.

Burton, T., Sharpe, D., Jenkins, N. & Bossanyi, E. 2001 *Wind Energy Handbook*. Wiley, New York.

Businger, J. A. & Charnock, H. 1983 Boundary layer structure in relation to larger-scale flow: Some remarks on the JASIN observations. *Philos. Trans. R. Soc. London. Series A, Mathematical and Physical Sciences* **308** (1503), 445–449.

Businger, J. A., Wyngaard, J. C., Izumi, Y. & Bradley, E. F. 1971 Flux-profile relationships in the atmospheric surface layer. *J. Atmos. Sci.* **28** (2), 181–189.

Cal, R. B., Lebron, J., Castillo, L., Kang, H. S. & Meneveau, C. 2010 Experimental study of the horizontally averaged flow structure in a model wind-turbine array boundary layer. *J. Renewable Sustainable Energy* **2**, 013106.

Calaf, M., Meneveau, C. & Meyers, J. 2010 Large eddy simulation study of fully developed wind-turbine array boundary layers. *Phys. Fluids* **22**, 015110.

Calaf, M., Parlange, M. B. & Meneveau, C. 2011 Large eddy simulation study of scalar transport in fully developed wind-turbine array boundary layers. *Phys. Fluids* **23** (12), 126603.

Canuto, C., Hussaini, M. Y., Quarteroni, A. & Zang, T. A. 1988 *Spectral Methods in Fluid Dynamics*. Springer-Verlag, Berlin.

Chamorro, L. P. & Porté-Agel, F. 2010 Effects of thermal stability and incoming boundary-layer flow characteristics on wind-turbine wakes: A wind-tunnel study. *Boundary-Layer Meteorol.* **136** (3), 515–533.

Chamorro, L. P. & Porté-Agel, F. 2011 Turbulent flow inside and above a wind farm: A wind-tunnel study. *Energies* **4** (11), 1916.

Christiansen, M. B. & Hasager, C. B. 2005 Wake effects of large offshore wind farms identified from satellite SAR. *Remote Sens. Environ.* **98**, 251–268.

Churchfield, M. J., Lee, S., Michalakes, J. & Moriarty, P. J. 2012*a* A numerical study of the effects of atmospheric and wake turbulence on wind turbine dynamics. *J. Turbul.* **13** (14), 1–32.

Churchfield, M. J., Lee, S., Moriarty, P. J., Martinez, L. A., Leonardi, S., Vijayakumar, G. & Brasseur, J.G. 2012*b* A large-eddy simulation of wind-plant aerodynamics. In *Proceedings of 50th AIAA Aerospace Sciences Meeting including the New Horizons Forum and Aerospace Exposition*.

Coleman, G. N. 1999 Similarity statistics from a direct numerical simulation of the neutrally stratified planetary boundary layer. *J. Atmos. Sci.* **56** (6), 891–900.

Coleman, G. N., Ferziger, J. H. & Spalart, P. R. 1990 A numerical study of the turbulent Ekman layer. *J. Fluid Mech.* **213**, 313–348.

Crespo, A., Frandsen, S., Gómez-Elvira, R. & Larsen, S. 1999*a* Modelization of a large wind farm, considering the modification of the atmospheric boundary layer. In *1999 European Wind Energy Conference:*

Wind Energy for the Next Millennium (ed. E. L. Petersen, P. Hjuler Jensen, K. Rave, P. Helm & H. Ehmann), pp. 1109–1112. James & James Science Publishers.

Crespo, A., Hernández, J. & Frandsen, S. 1999*b* Survey of modelling methods for wind turbine wakes and wind farms. *Wind Energy* **2** (1), 1–24.

Csanady, G. T. 1974 Equilibrium theory of the planetary boundary layer with an inversion lid. *Boundary-Layer Meteorol.* **6** (1-2), 63–79.

Dahlberg, J.-A., Norling, J., Loman, G. & Thor, S.-E. 2009 Assessment of the lillgrund wind farm: Power performance and wake effects. *Tech. Rep.*. Vattenfall Vindkraft AB, 6_1 LG Pilot Report.

de Bruin, H. A. R. 1994 Analytic solutions of the equations governing the temperature fluctuation method. *Boundary-Layer Meteorol.* **68** (4), 427–432.

Deardorff, J. W. 1979 Prediction of convective mixed-layer entrainment for realistic capping inversion structure. *J. Atmos. Sci.* **36** (3), 424–436.

Deardorff, J. W. 1980 Stratocumulus-capped mixed layers derived from a three-dimensional model. *Boundary-Layer Meteorol.* **18** (4), 495–527.

Delport, S., Baelmans, M. & Meyers, J. 2009 Constrained optimization of turbulent mixing-layer evolution. *J. Turbul.* **10** (18), 1–26.

Deusebio, E., Brethouwer, G., Schlatter, P. & Lindborg, E. 2014 A numerical study of the unstratified and stratified Ekman layer. *J. Fluid Mech.* **755**, 672–704.

Dörenkämper, M., Witha, B., Steinfeld, G., Heinemann, D. & Kühn, M. 2015 The impact of stable atmospheric boundary layers on wind-turbine wakes within offshore wind farms. *J. Wind Eng. Ind. Aerodyn.* **144**, 146–153, selected papers from the 6th International Symposium on Computational Wind Engineering CWE 2014.

Durran, D. R. 1989 Improving the anelastic approximation. *J. Atmos. Sci.* **46** (11), 1453–1461.

Durran, D. R. 1990 Mountain waves and downslope winds. In *Atmospheric Processes over Complex Terrain* (ed. W. Blumen), *Meteorological Monographs*, vol. 23, pp. 59–81. American Meteorological Society.

Durran, D. R. & Klemp, J. B. 1983 A compressible model for the simulation of moist mountain waves. *Mon. Weather Rev.* **111** (12), 2341–2361.

Dutton, J. A. & Fichtl, G. H. 1969 Approximate equations of motion for gases and liquids. *J. Atmos. Sci.* **26** (2), 241–254.

Ekman, V. W. 1905 On the influence of the Earth's rotation on ocean currents. *Arkiv. Math. Astron. Fyjik.* **2**, 1–53.

Elliott, W. P. 1958 The growth of the atmospheric internal boundary layer. *Trans. Am. Geophys. Union* **39** (6), 1048–1054.

Esau, I. N. 2004*a* Parameterization of a surface drag coefficient in conventionally neutral planetary boundary layer. *Ann. Geophys.* **22** (10), 3353–3362.

Esau, I. N. 2004*b* Simulation of Ekman boundary layers by large eddy model with dynamic mixed subfilter closure. *Environ. Fluid Mech.* **4** (3), 273–303.

España, G., Aubrun, S., Loyer, S. & Devinant, P. 2011 Spatial study of the wake meandering using modelled wind turbines in a wind tunnel. *Wind Energy* **14** (7), 923–937.

EWEA 2016*a* The European offshore wind industry – key trends and statistics 2015. The European Wind Energy Association.

EWEA 2016*b* Wind in power: 2015 European statistics. The European Wind Energy Association.

Fernando, H. J. S. & Weil, J. C. 2010 Whither the stable boundary layer? *Bull. Amer. Meteor. Soc.* **91** (11), 1475–1484.

Fiedler, B. H. & Bukovsky, M. S. 2011 The effect of a giant wind farm on precipitation in a regional climate model. *Environ. Res. Lett.* **6** (4), 045101.

Fitch, A. C. 2015 Climate impacts of large-scale wind farms as parameterized in a global climate model. *J. Climate* **28** (15), 6160–6180.

Fitch, A. C., Lundquist, J. K. & Olson, J. B. 2013 Mesoscale influences of wind farms throughout a diurnal cycle. *Mon. Wea. Rev.* **141** (7), 2173–2198.

Fitch, A. C., Olson, J. B., Lundquist, J. K., Dudhia, J., Gupta, A. K., Michalakes, J. & Barstad, I. 2012 Local and mesoscale impacts of wind farms as parameterized in a mesoscale NWP model. *Mon. Wea. Rev.* **140** (9), 3017–3038.

Foken, T. 2006 50 years of the Monin–Obukhov similarity theory. *Boundary-Layer Meteorol.* **119** (3), 431–447.

Frandsen, S. 1992 On the wind speed reduction in the center of large clusters of wind turbines. *J. Wind Eng. Ind. Aerodyn.* **39** (1-3), 251–265.

Frandsen, S., Barthelmie, R., Pryor, S., Rathmann, O., Larsen, S., Højstrup, J. & Thøgersen, M. 2006 Analytical modelling of wind speed deficit in large offshore wind farms. *Wind Energy* **9** (1-2), 39–53.

García-Villalba, M. & del Álamo, J. C. 2011 Turbulence modification by stable stratification in channel flow. *Phys. Fluids* **23**, 045104.

Garg, R. P., Ferziger, J. H., Monismith, S. G. & Koseff, J. R. 2000 Stably stratified turbulent channel flows. I. Stratification regimes and turbulence suppression mechanism. *Phys. Fluids* **12** (10), 2569–2594.

Garratt, J. R. 1987 The stably stratified internal boundary layer for steady and diurnally varying offshore flow. *Boundary-Layer Meteorol.* **38** (4), 369–394.

Garratt, J. R. 1990 The internal boundary layer – a review. *Boundary-Layer Meteorol.* **50** (1-4), 171–203.

Garratt, J. R. 1992 *The atmospheric boundary layer*. Cambridge University Press.

Garratt, J. R. & Ryan, B. F. 1989 The structure of the stably stratified internal boundary layer in offshore flow over the sea. *Boundary-Layer Meteorol.* **47**, 17–40.

Gill, A. E. 1982 *Atmosphere-Ocean Dynamics*, *International Geophysics Series*, vol. 30. Academic Press.

Goit, J. P. & Meyers, J. 2013 Effect of Ekman layer on windfarm roughness and displacement height. In *Proceedings of Direct and large-eddy simulation IX, Dresden, Germany*, pp. 423–434. Springer International Publishing.

Goit, J. P. & Meyers, J. 2015 Optimal control of energy extraction in wind-farm boundary layers. *J. Fluid Mech.* **768**, 5–50.

Goit, J. P., Munters, W. & Meyers, J. 2016 Optimal coordinated control of power extraction in LES of a wind farm with entrance effects. *Energies* **9** (1), 29.

Grant, A. L. M. 1986 Observations of boundary layer structure made during the 1981 KONTUR experiment. *Q. J. R. Meteorol. Soc.* **112** (473), 825–841.

GWEC 2015 Global wind report: Annual market update. Global Wind Energy Council.

Hancock, P. E. & Pascheke, F. 2014 Wind-tunnel simulation of the wake of a large wind turbine in a stable boundary layer: Part 2, the wake flow. *Boundary-Layer Meteorol.* **151** (1), 23–37.

Hansen, K. S., Barthelmie, R., Jensen, L. E. & Sommer, A. 2012 The impact of turbulence intensity and atmospheric stability on power deficits due to wind turbine wakes at Horns rev wind farm. *Wind Energy* **15** (1), 183–196.

Hess, G. D. 2004 The neutral, barotropic planetary boundary layer, capped by a low-level inversion. *Boundary-Layer Meteorol.* **110** (3), 319–355.

Hess, G. D. & Garratt, J. R. 2002*a* Evaluating models of the neutral, barotropic planetary boundary layer using integral measures: Part I. overview. *Boundary-Layer Meteorol.* **104** (3), 333–358.

Hess, G. D. & Garratt, J. R. 2002*b* Evaluating models of the neutral, barotropic planetary boundary layer using integral measures: Part II. modelling observed conditions. *Boundary-Layer Meteorol.* **104** (3), 359–369.

Högström, U. 1988 Non-dimensional wind and temperature profiles in the atmospheric surface layer: A re-evaluation. *Boundary-Layer Meteorol.* **42** (1-2), 55–78.

Holton, J. R. 2004 *An Introduction to Dynamic Meteorology*, 4th edn., *International Geophysics Series*, vol. 88. Elsevier Academic Press.

Holtslag, A. A. M. 2006 GEWEX Atmospheric Boundary-Layer Study (GABLS) on stable boundary layers. *Boundary-Layer Meteorol.* **118**, 243–246.

Holtslag, A. A. M. & Nieuwstadt, F. T. M. 1986 Scaling the atmospheric boundary layer. *Boundary-Layer Meteorol.* **36** (1), 201–209.

Holtslag, A. A. M., Svensson, G., Baas, P., Basu, S., Beare, B., Beljaars, A. C. M., Bosveld, F. C., Cuxart, J., Lindvall, J., Steeneveld, G. J., Tjernström, M. & van de Wiel, B. J. H. 2013 Stable atmospheric boundary layers and diurnal cycles: Challenges for weather and climate models. *Bull. Amer. Meteor. Soc.* **94** (11), 1691–1706.

Holtslag, A. A. M., Svensson, G., Basu, S., Beare, B., Bosveld, F. C. & Cuxart, J. 2012 Overview of the GEWEX Atmospheric Boundary Layer Study (GABLS). In *Proc. ECMWF Workshop on Diurnal Cycles and the Stable Boundary Layer*, pp. 11–23. Reading, England, ECMWF/WCRP.

Holtslag, M. C., Bierbooms, W. A. A. M. & van Bussel, G. J. W. 2014 Estimating atmospheric stability from observations and correcting wind shear models accordingly. *Journal of Physics: Conference Series* **555** (1), 012052.

Hu, F. Q., Li, X. D. & Lin, D. K. 2008 Absorbing boundary conditions for nonlinear Euler and Navier–Stokes equations based on the perfectly matched layer technique. *J. Comput. Phys.* **227** (9), 4398–4424.

Hunt, J. C. R., Orr, A., Rottman, J. W. & Capon, R. 2004 Coriolis effects in mesoscale flows with sharp changes in surface conditions. *Q. J. R. Meteorol. Soc.* **130** (603), 2703–2731.

IEA 2013 Technology roadmap: Wind energy. International Energy Agency.

Inoue, M., Matheou, G. & Teixeira, J. 2014 LES of a spatially developing atmospheric boundary layer: Application of a fringe method for the stratocumulus to shallow cumulus cloud transition. *Mon. Wea. Rev.* **142** (9), 3418–3424.

Israeli, M. & Orszag, S. A. 1981 Approximation of radiation boundary conditions. *J. Comput. Phys.* **41** (1), 115–135.

Iungo, G. V. & Porté-Agel, F. 2014 Volumetric lidar scanning of wind turbine wakes under convective and neutral atmospheric stability regimes. *J. Atmos. Oceanic Technol.* **31** (10), 2035–2048.

Ivanell, S. 2009 Numerical computations of wind turbine wakes. PhD thesis, Dept. of Mechanics, Royal Institute of Technology, Stockholm, Sweden.

Jensen, N. O. 1978 Change of surface roughness and the planetary boundary layer. *Q. J. R. Meteorol. Soc.* **104** (440), 351–356.

Jensen, N. O. 1983 A note on wind generator interaction. Technical Report Risø-M-2411, Risø National Laboratory, Roskilde, Denmark.

Jimenez, A., Crespo, A., Migoya, E. & Garcia, J. 2007 Advances in large-eddy simulation of a wind turbine wake. *J. Phys.: Conf. Ser.* **75** (1), 012041.

Jimenez, A., Crespo, A., Migoya, E. & Garcia, J. 2008 Large-eddy simulation of spectral coherence in a wind turbine wake. *Environ. Res. Lett.* **3** (1), 015004.

Johnstone, R. & Coleman, G. N. 2012 The turbulent Ekman boundary layer over an infinite wind-turbine array. *J. Wind Eng. Ind. Aerodyn.* **100** (1), 46–57.

Katic, I., Højstrup, J. & Jensen, N. O. 1986 A simple model for cluster efficiency. In *European Wind Energy Association Conference and Exhibition*, pp. 407–410.

Keck, R.-E., de Maré, M., Churchfield, M. J., Lee, S., Larsen, G. & Aagaard Madsen, H. 2014 On atmospheric stability in the dynamic wake meandering model. *Wind Energy* **17** (11), 1689–1710.

Khani, S. & Waite, M. L. 2014 Buoyancy scale effects in large-eddy simulations of stratified turbulence. *J. Fluid Mech.* **754**, 75–97.

Kim, J. & Moin, P. 1987 Transport of passive scalars in a turbulent channel flow. In *Proceedings of Turbulent Shear Flows 6* (ed. J.-C. André), pp. 85–96. Springer Berlin Heidelberg.

Kim, S.-W., Park, S.-U. & Moeng, C.-H. 2003 Entrainment processes in the convective boundary layer with varying wind shear. *Boundary-Layer Meteorol.* **108** (2), 221–245.

Klein, R. 2010 Scale-dependent models for atmospheric flows. *Annu. Rev. Fluid Mech.* **42** (1), 249–274.

Klemp, J. B. & Durran, D. R. 1983 An upper boundary condition permitting internal gravity wave radiation in numerical mesoscale models. *Mon. Wea. Rev.* **111** (3), 430–444.

Klemp, J. B. & Lilly, D. K. 1978 Numerical simulation of hydrostatic mountain waves. *J. Atmos. Sci.* **35** (1), 78–107.

Kosović, B. 1997 Subgrid-scale modelling for the large-eddy simulation of high-Reynolds-number boundary layers. *J. Fluid Mech.* **336**, 151–182.

Kosović, B. & Curry, J. A. 2000 A large eddy simulation study of a quasi-steady, stably stratified atmospheric boundary layer. *J. Atmos. Sci.* **57** (8), 1052–1068.

Kraus, E. B. 1968 What we do not know about the sea surface wind stress. *Bull. Am. Meteorol. Soc.* **49**, 247–253.

Kumar, V., Kleissl, J., Meneveau, C. & Parlange, M. B. 2006 Large-eddy simulation of a diurnal cycle of the atmospheric boundary layer: Atmospheric stability and scaling issues. *Water Resour. Res.* **42** (6), 1–18.

Kumar, V., Svensson, G., Holtslag, A. A. M., Meneveau, C. & Parlange, M. B. 2010 Impact of surface flux formulations and geostrophic forcing on large-eddy simulations of diurnal atmospheric boundary layer flow. *J. Appl. Meteor. Climatol.* **49** (7), 1496–1516.

Lange, B., Larsen, S., Højstrup, J. & Barthelmie, R. 2004 The influence of thermal effects on the wind speed profile of the coastal marine boundary layer. *Boundary-Layer Meteorol.* **112** (3), 587–617.

Larsen, G. C., Aagaard Madsen, H., Bingöl, F., Mann, J., Ott, S., Sørensen, J. N., Okulov, V., Troldborg, N., Nielsen, M., Thomsen, K., Larsen, T. J. & Mikkelsen, R. 2007 Dynamic wake meandering modeling. Technical Report Risø-R-1607(EN), Risø National Laboratory, Roskilde, Denmark.

Leweke, T., Quaranta, H. U., Bolnot, H., Blanco-Rodríguez, F. J. & Le Dizès, S. 2014 Long- and short-wave instabilities in helical vortices. *J. Phys.: Conf. Ser.* **524** (1), 012154.

Lilly, D. K. 1967 The representation of small scale turbulence in numerical simulation experiments. In *Proc. IBM Scientific Computing Symp. on environmental sciences* (ed. H. H. Goldstine), pp. 195–210. Yorktown Heights, NY, USA.

Lilly, D. K. 1968 Models of cloud-topped mixed layers under a strong inversion. *Q. J. R. Meteorol. Soc.* **94** (401), 292–309.

Lilly, D. K. 1996 A comparison of incompressible, anelastic and Boussinesq dynamics. *Atmos. Res.* **40** (2-4), 143 – 151.

Lin, C.-L., McWilliams, J. C., Moeng, C.-H. & Sullivan, P. P. 1996 Coherent structures and dynamics in a neutrally stratified planetary boundary layer flow. *Phys. Fluids* **8** (10), 2626–2639.

Lindborg, E. 2006 The energy cascade in a strongly stratified fluid. *J. Fluid Mech.* **550**, 207–242.

Lipps, F. B. & Hemler, R. S. 1982 A scale analysis of deep moist convection and some related numerical calculations. *J. Atmos. Sci.* **39** (10), 2192–2210.

Lu, H. & Porté-Agel, F. 2010 A modulated gradient model for large-eddy simulation: Application to a neutral atmospheric boundary layer. *Phys. Fluids* **22**, 015109.

Lu, H. & Porté-Agel, F. 2011 Large-eddy simulation of a very large wind farm in a stable atmospheric boundary layer. *Phys. Fluids* **23** (6), 065101.

Lu, H. & Porté-Agel, F. 2013 A modulated gradient model for scalar transport in large-eddy simulation of the atmospheric boundary layer. *Phys. Fluids* **25**, 015110.

Lu, H. & Porté-Agel, F. 2014 On the development of a dynamic nonlinear closure for large-eddy simulation of the atmospheric boundary layer. *Boundary-Layer Meteorol.* **151** (3), 429–451.

Lu, H. & Porté-Agel, F. 2015 On the impact of wind farms on a convective atmospheric boundary layer. *Boundary-Layer Meteorol.* **157** (1), 81–96.

Lumley, J. L. 1964 The spectrum of nearly inertial turbulence in a stably stratified fluid. *J. Atmos. Sci.* **21** (1), 99–102.

Lundbladh, A., Berlin, S., Skote, M., Hildings, C., Choi, J., Kim, J. & Henningson, D. S. 1999 An efficient spectral method for a simulation of incompressible flow over a flat plate. TRITA-MEK 1999:11. KTH Stockholm, Sweden.

Lynch, A. H. & Cassano, J. J. 2006 *Applied Atmospheric Dynamics*. John Wiley & Sons, Ltd.

Magnusson, M. & Smedman, A.-S. 1994 Influence of atmospheric stability on wind turbine wakes. *Wind Eng.* **18** (3), 139–152.

Magnusson, M. & Smedman, A.-S. 1999 Air flow behind wind turbines. *J. Wind Eng. Ind. Aerodyn.* **80** (1–2), 169–189.

Mahrt, L. 1998 Stratified atmospheric boundary layers and breakdown of models. *Theor. Comp. Fluid Dyn.* **11** (3), 263–279.

Mahrt, L. 1999 Stratified atmospheric boundary layers. *Boundary-Layer Meteorol.* **90** (3), 375–396.

Mahrt, L. 2014 Stably stratified atmospheric boundary layers. *Annu. Rev. Fluid Mech.* **46** (1), 23–45.

Mahrt, L., Sun, J., Blumen, W., Delany, T. & Oncley, S. 1998 Nocturnal boundary-layer regimes. *Boundary-Layer Meteorol.* **88** (2), 255–278.

Malhi, Y. S. 1995 The significance of the dual solutions for heat fluxes measured by the temperature fluctuation method in stable conditions. *Boundary-Layer Meteorol.* **74** (4), 389–396.

Mann, J. 1994 The spatial structure of neutral atmospheric surface-layer turbulence. *J. Fluid Mech.* **273**, 141–168.

Mason, P. J. 1989 Large-eddy simulation of the convective atmospheric boundary layer. *J. Atmos. Sci.* **46** (11), 1492–1516.

Mason, P. J. & Derbyshire, S. H. 1990 Large-eddy simulation of the stably-stratified atmospheric boundary layer. *Boundary-Layer Meteorol.* **53** (1-2), 117–162.

Mason, P. J. & Thomson, D. J. 1987 Large-eddy simulations of the neutral-static-stability planetary boundary layer. *Q. J. R. Meteorol. Soc.* **113** (476), 413–443.

Mason, P. J. & Thomson, D. J. 1992 Stochastic backscatter in large-eddy simulations of boundary layers. *J. Fluid Mech.* **242**, 51–78.

Mayor, S. D., Spalart, P. R. & Tripoli, G. J. 2002 Application of a perturbation recycling method in the large-eddy simulation of a mesoscale convective internal boundary layer. *J. Atmos. Sci.* **59** (15), 2385–2395.

McTavish, S., Rodrigue, S., Feszty, D. & Nitzsche, F. 2015 An investigation of in-field blockage effects in closely spaced lateral wind farm configurations. *Wind Energy* **18** (11), 1989–2011.

McWilliams, J. C., Gallacher, P. C., Moeng, C.-H. & Wyngaard, J. C. 1993 Modeling the oceanic planetary boundary layer. In *Large-Eddy Simulations of Complex Engineering and Geophysical Flows* (ed. B. Galperin & S. A. Orszag), pp. 441–454. Cambridge University Press.

Mehta, D., van Zuijlen, A. H., Koren, B., Holierhoek, J. G. & Bijl, H. 2014 Large eddy simulation of wind farm aerodynamics: A review. *J. Wind Eng. Ind. Aerodyn.* **133**, 1–17.

Melas, D. 1989 The temperature structure in a stably stratified internal boundary layer over a cold sea. *Boundary-Layer Meteorol.* **48** (4), 361–375.

Meneveau, C. 2012 The top-down model of wind farm boundary layers and its applications. *J. Turbul.* **13** (7), 1–12.

Meneveau, C. & Katz, J. 2000 Scale-invariance and turbulence models for large-eddy simulation. *Annu. Rev. Fluid Mech.* **32** (1), 1–32.

Meneveau, C., Lund, T. S. & Cabot, W. H. 1996 A Lagrangian dynamic subgrid-scale model of turbulence. *J. Fluid Mech.* **319**, 353–385.

Meyers, J. 2011 Error-landscape assessment of large-eddy simulations: a review of the methodology. *J. Sci. Comput.* **49** (1), 65–77.

Meyers, J. & Meneveau, C. 2010 Large eddy simulations of large wind-turbine arrays in the atmospheric boundary layer. *AIAA Paper No. 2010-827* pp. 1–10.

Meyers, J. & Meneveau, C. 2012 Optimal turbine spacing in fully developed wind farm boundary layers. *Wind Energy* **15** (2), 305–317.

Meyers, J. & Meneveau, C. 2013 Flow visualization using momentum and energy transport tubes and applications to turbulent flow in wind farms. *J. Fluid Mech.* **715**, 335–358.

Meyers, J. & Sagaut, P. 2007 Evaluation of Smagorinsky variants in large-eddy simulations of wall-resolved plane channel flows. *Phys. Fluids* **19** (9), 095105.

Moeng, C.-H. 1984 A large-eddy-simulation model for the study of planetary boundary-layer turbulence. *J. Atmos. Sci.* **41** (13), 2052–2062.

Moeng, C.-H. & Sullivan, P. P. 1994 A comparison of shear- and buoyancy-driven planetary boundary layer flows. *J. Atmos. Sci.* **51** (7), 999–1022.

Moeng, C.-H. & Wyngaard, J. C. 1988 Spectral analysis of large-eddy simulations of the convective boundary layer. *J. Atmos. Sci.* **45** (23), 3573–3587.

Momen, M. & Bou-Zeid, E. 2016 Large-eddy simulations and damped-oscillator models of the unsteady Ekman boundary layer. *J. Atmos. Sci.* **73** (1), 25–40.

Monin, A. S. & Obukhov, A. M. 1954 Basic laws of turbulent mixing in the atmosphere near the ground. *TR. Akad. Nauk., SSSR Geophiz. Inst.* **24** (151), 1963–1987.

Munters, W., Meneveau, C. & Meyers, J. 2016 Turbulent inflow precursor method with time-varying direction for large-eddy simulations and applications to wind farms. *Boundary-Layer Meteorol.* **159** (2), 305–328.

Nappo, C. J. 2002 *An Introduction to Atmospheric Gravity Waves*, *International Geophysics Series*, vol. 85. Academic Press.

Newman, J., Lebron, J., Meneveau, C. & Castillo, L. 2013 Streamwise development of the wind turbine boundary layer over a model wind turbine array. *Phys. Fluids* **25** (8), 085108.

Niayifar, A. & Porté-Agel, F. 2015 A new analytical model for wind farm power prediction. *J. Phys.: Conf. Ser.* **625** (1), 012039.

Nicholls, S. 1985 Aircraft observations of the Ekman layer during the joint air-sea interaction experiment. *Q. J. R. Meteorol. Soc.* **111** (468), 391–426.

Nieuwstadt, F. T. M. 1983 On the solution of the stationary, baroclinic Ekman-layer equations with a finite boundary-layer height. *Boundary-Layer Meteorol.* **26** (4), 377–390.

Nieuwstadt, F. T. M. 1984 The turbulent structure of the stable, nocturnal boundary layer. *J. Atmos. Sci.* **41** (14), 2202–2216.

Nieuwstadt, F. T. M. 1985 A model for the stationary, stable boundary layer. In *Turbulence and Diffusion in Stable Environments* (ed. J. C. R. Hunt), pp. 149–179. Oxford University Press.

Nieuwstadt, F. T. M., Mason, P. J., Moeng, C.-H. & Schumann, U. 1993 Large-eddy simulation of the convective boundary layer: A comparison of four computer codes. In *Turbulent Shear Flows 8* (ed. Durst H. et al.), pp. 343–367. Springer-Verlag, Berlin.

Nilsson, K., Ivanell, S., Hansen, K. S., Mikkelsen, R., Sørensen, J. N., Breton, S.-P. & Henningson, D. 2015 Large-eddy simulations of the Lillgrund wind farm. *Wind Energy* **18** (3), 449–467.

Nordström, J., Nordin, N. & Henningson, D. S. 1999 The fringe region technique and the Fourier method used in the direct numerical simulation of spatially evolving viscous flows. *SIAM J. Sc. Comput.* **20** (4), 1365–1393.

Nygaard, N. G. 2014 Wakes in very large wind farms and the effect of neighbouring wind farms. *J. Phys.: Conf. Ser.* **524** (1), 012162.

Ogura, Y. & Phillips, N. A. 1962 Scale analysis of deep and shallow convection in the atmosphere. *J. Atmos. Sci.* **19** (2), 173–179.

Orr, A., Hunt, J. C. R., Capon, R., Sommeria, J., Cresswell, D. & Owinoh, Ant. 2005 Coriolis effects on wind jets and cloudiness along coasts. *Weather* **60** (10), 291–299.

Ozmidov, R. V. 1965 On the turbulent exchange in a stably stratified ocean. *Bull. Acad. Sci. U.S.S.R. Atmos. Ocean. Phys.* **1**, 493–497.

Paulson, C. A. 1970 The mathematical representation of wind speed and temperature profiles in the unstable atmospheric surface layer. *J. Appl. Meteor.* **9** (6), 857–861.

Pedersen, J. G., Gryning, S.-E. & Kelly, M. 2014 On the structure and adjustment of inversion-capped neutral atmospheric boundary-layer flows: Large-eddy simulation study. *Boundary-Layer Meteorol.* **153** (1), 43–62.

Phillips, O. M. 1977 Entrainment. In *Modelling and Prediction of the Upper Layers of the Ocean* (ed. E. B. Kraus). Pergamon Press, Oxford.

Pollard, R. T., Rhines, P. B. & Thompson, R. O. R. Y. 1972 The deepening of the wind-mixed layer. *Geophys. Dyn.* **4** (1), 381–404.

Porté-Agel, F., Meneveau, C. & Parlange, M. B. 2000 A scale-dependent dynamic model for large-eddy simulation: application to a neutral atmospheric boundary layer. *J. Fluid Mech.* **415**, 261–284.

Porté-Agel, F., Wu, Y.-T. & Chen, C.-H. 2013 A numerical study of the effects of wind direction on turbine wakes and power losses in a large wind farm. *Energies* **6** (10), 5297–5313.

Porté-Agel, F., Wu, Y.-T., Lu, H. & Conzemius, R. J. 2011 Large-eddy simulation of atmospheric boundary layer flow through wind turbines and wind farms. *J. Wind Eng. Ind. Aerodyn.* **99** (4), 154 – 168.

Queney, P. 1948 The problem of the airflow over mountains: a summary of theoretical studies. *Bull. Amer. Meteor. Soc.* **29**, 16–26.

Rajewski, D. A., Takle, E. S., Lundquist, J. K., Oncley, S., Prueger, J. H., Horst, T. W., Rhodes, M. E., Pfeiffer, R., Hatfield, J. L., Spoth, K. K. & Doorenbos, R. K. 2013 Crop wind energy experiment (CWEX): Observations of surface-layer, boundary layer, and mesoscale interactions with a wind farm. *Bull. Amer. Meteor. Soc.* **94** (5), 655–672.

Rampanelli, G. & Zardi, D. 2004 A method to determine the capping inversion of the convective boundary layer. *J. Appl. Meteor.* **43** (6), 925–933.

Raupach, M. R., Antonia, R. A. & Rajagopalan, S. 1991 Rough-wall turbulent boundary layers. *Appl. Mech. Rev.* **44** (1), 1–25.

Ren21 2016 Global status report. Renewable Energy Policy Network for the 21st Century, Paris, France.

Riley, J. J. & Lelong, M.-P. 2000 Fluid motions in the presence of strong stable stratification. *Annu. Rev. Fluid Mech.* **32** (1), 613–657.

Saiki, E. M., Moeng, C.-H. & Sullivan, P. P. 2000 Large-eddy simulation of the stably stratified planetary boundary layer. *Boundary-Layer Meteorol.* **95** (1), 1–30.

Sanderse, B., van der Pijl, S. P. & Koren, B. 2011 Review of computational fluid dynamics for wind turbine wake aerodynamics. *Wind Energy* **14** (7), 799–819.

Schlichting, H. 1979 *Boundary-Layer Theory*, 7th edn. McGraw-Hill, Hamburg, translated by J. Kestin.

Schröter, J. S., Moene, A. F. & Holtslag, A. A. M. 2013 Convective boundary layer wind dynamics and inertial oscillations: the influence of surface stress. *Q. J. R. Meteorol. Soc.* **139** (676), 1694–1711.

Sescu, A. & Meneveau, C. 2014 A control algorithm for statistically stationary large-eddy simulations of thermally stratified boundary layers. *Q. J. R. Meteorol. Soc.* **140** (683), 2017–2022.

Shapiro, A. & Fedorovich, E. 2010 Analytical description of a nocturnal low-level jet. *Q. J. R. Meteorol. Soc.* **136** (650), 1255–1262.

Shingai, K. & Kawamura, H. 2004 A study of turbulence structure and large-scale motion in the Ekman layer through direct numerical simulations. *J. Turbul.* **5** (13), 1–18.

Smagorinsky, J. 1963 General circulation experiments with the primitive equations. *Mon. Weather Rev.* **91** (3), 99–164.

Smedman, A.-S. 1991 Some turbulence characteristics in stable atmospheric boundary layer flow. *J. Atmos. Sci.* **48** (6), 856–868.

Smedman, A.-S., Bergström, H. & Grisogono, B. 1997 Evolution of stable internal boundary layers over a cold sea. *J. Geophys. Res.* **102** (C1), 1091–1099.

Smith, R. B. 1980 Linear theory of stratified hydrostatic flow past an isolated mountain. *Tellus* **32** (4), 348–364.

Smith, R. B. 2010 Gravity wave effects on wind farm efficiency. *Wind Energy* **13** (5), 449–458.

Smolarkiewicz, P. K. & Margolin, L. G. 1997 On forward-in-time differencing for fluids: an Eulerian/semi-Lagrangian non-hydrostatic model for stratified flows. *Atmos.-Ocean* **35** (1), 127–152.

Sorbjan, Z. 1996 Effects caused by varying the strength of the capping inversion based on a large eddy simulation model of the shear-free convective boundary layer. *J. Atmos. Sci.* **53** (14), 2015–2024.

Sørensen, J. N. 2011 Aerodynamic aspects of wind energy conversion. *Annu. Rev. Fluid Mech.* **43** (1), 427–448.

Spalart, P. R. & Watmuff, J. H. 1993 Experimental and numerical study of a turbulent boundary layer with pressure gradients. *J. Fluid Mech.* **249**, 337–371.

Spiegel, E. A. & Veronis, G. 1960 On the Boussinesq approximation for a compressible fluid. *Astrophys. J.* **131**, 442–447.

Steeneveld, G. J., van de Wiel, B. J. H. & Holtslag, A. A. M. 2007 Comments on deriving the equilibrium height of the stable boundary layer. *Q. J. R. Meteorol. Soc.* **133** (622), 261–264.

Stevens, B., Moeng, C.-H. & Sullivan, P. P. 2000 Entrainment and subgrid lengthscales in large-eddy simulations of atmospheric boundary-layer flows. In *IUTAM Symposium on Developments in Geophysical Turbulence* (ed. R. M. Kerr & Y. Kimura), *Fluid Mechanics and Its Applications*, vol. 58, pp. 253–269. Springer Netherlands.

Stevens, R. J. A. M., Gayme, D. F. & Meneveau, C. 2014*a* Large eddy simulation studies of the effects of alignment and wind farm length. *J. Renewable Sustainable Energy* **6** (2), 023105.

Stevens, R. J. A. M., Gayme, D. F. & Meneveau, C. 2015*a* Coupled wake boundary layer model of wind-farms. *J. Renewable Sustainable Energy* **7**, 023115.

Stevens, R. J. A. M., Gayme, D. F. & Meneveau, C. 2015*b* Effects of turbine spacing on the power output of extended wind-farms. *Wind Energy* **19**, 359–370.

Stevens, R. J. A. M., Graham, J. & Meneveau, C. 2014*b* A concurrent precursor inflow method for large eddy simulations and applications to finite length wind farms. *Renewable Energy* **68**, 46–50.

Stoll, R. & Porté-Agel, F. 2008 Large-eddy simulation of the stable atmospheric boundary layer using dynamic models with different averaging schemes. *Boundary-Layer Meteorol.* **126** (1), 1–28.

Stull, R. B. 1988 *An Introduction to Boundary Layer Meteorology*. Springer.

Sullivan, P. P., Edson, J. B., Hristov, T. & McWilliams, J. C. 2008 Large-eddy simulations and observations of atmospheric marine boundary layers above nonequilibrium surface waves. *J. Atmos. Sci.* **65** (4), 1225–1245.

Sullivan, P. P., McWilliams, J. C. & Moeng, C.-H. 1994 A subgrid-scale model for large-eddy simulation of planetary boundary-layer flows. *Boundary-Layer Meteorol.* **71** (3), 247–276.

Sullivan, P. P., Weil, J. C., Patton, E. G., Jonker, H. J. J. & Mironov, D. V. 2016 Turbulent winds and temperature fronts in large-eddy simulations of the stable atmospheric boundary layer. *J. Atmos. Sci.* **73** (4), 1815–1840.

Taylor, J. R. & Sarkar, S. 2007 Internal gravity waves generated by a turbulent bottom Ekman layer. *J. Fluid Mech.* **590**, 331–354.

Taylor, J. R. & Sarkar, S. 2008*a* Direct and large eddy simulations of a bottom Ekman layer under an external stratification. *Int. J. Heat Fluid Flow*

29 (3), 721–732, the Fifth International Symposium on Turbulence and Shear Flow Phenomena (TSFP5).

Taylor, J. R. & Sarkar, S. 2008*b* Stratification effects in a bottom Ekman layer. *J. Phys. Oceanogr.* **38** (11), 2535–2555.

Taylor, P. A. 1969 The planetary boundary layer above a change in surface roughness. *J. Atmos. Sci.* **26** (3), 432–440.

Taylor, P. A. 1971 A note on the log-linear velocity profile in stable conditions. *Q. J. R. Meteorol. Soc.* **97** (413), 326–329.

Teixeira, M. A. C. 2014 The physics of orographic gravity wave drag. *Front. Phys.* **2** (43), 1–24.

Tennekes, H. 1973 A model for the dynamics of the inversion above a convective boundary layer. *J. Atmos. Sci.* **30** (4), 558–567.

Tennekes, H. & Lumley, J. L. 1972 *A First Course in Turbulence*. MIT Press.

Thompson, R. O. R. Y. 1973 Stratified Ekman boundary layer models. *Geophys. Dyn.* **5** (1), 201–210.

Thomsen, K. & Sørensen, P. 1999 Fatigue loads for wind turbines operating in wakes. *J. Wind Eng. Ind. Aerodyn.* **80** (1–2), 121–136.

Tjernström, M. & Smedman, A.-S. 1993 The vertical turbulence structure of the coastal marine atmospheric boundary layer. *J. Geophys. R.: Oceans* **98** (C3), 4809–4826.

van de Wiel, B. J. H., Moene, A. F., Steeneveld, G. J., Baas, P., Bosveld, F. C. & Holtslag, A. A. M. 2010 A conceptual view on inertial oscillations and nocturnal low-level jets. *J. Atmos. Sci.* **67** (8), 2679–2689.

van de Wiel, B. J. H., Moene, A. F., Steeneveld, G. J., Hartogensis, O. K. & Holtslag, A. A. M. 2007 Predicting the collapse of turbulence in stably stratified boundary layers. *Flow Turb. Comb.* **79** (3), 251–274.

Van der Laan, M. P., Hansen, K. S., Sørensen, N. N. & Réthoré, P.-E. 2015 Predicting wind farm wake interaction with rans: an investigation of the coriolis force. *J. Phys.: Conf. Ser.* **625** (1), 012026.

Vanderwende, B. J. & Lundquist, J. K. 2012 The modification of wind turbine performance by statistically distinct atmospheric regimes. *Environ. Res. Lett.* **7** (3), 034035.

VanZanten, M. C., Duynkerke, P. G. & Cuijpers, J. W. M. 1999 Entrainment parameterization in convective boundary layers. *J. Atmos. Sci.* **56** (6), 813–828.

VerHulst, C. & Meneveau, C. 2014 Large eddy simulation study of the kinetic energy entrainment by energetic turbulent flow structures in large wind farms. *Phys. Fluids* **26** (2), 025113.

Vermeer, L. J., Sørensen, J. N. & Crespo, A. 2003 Wind turbine wake aerodynamics. *Prog. Aerosp. Sci.* **39** (6–7), 467–510.

Verstappen, R.W.C.P. & Veldman, A.E.P. 2003 Symmetry-preserving discretization of turbulent flow. *J. Comput. Phys.* **187** (1), 343–368.

Volker, P. J. H., Badger, J., Hahmann, A. N. & Ott, S. 2015 The explicit wake parametrisation v1.0: a wind farm parametrisation in the mesoscale model WRF. *Geosci. Model Dev.* **8** (11), 3715–3731.

Waite, M. L. 2011 Stratified turbulence at the buoyancy scale. *Phys. Fluids* **23** (6), 066602.

Waite, M. L. & Bartello, P. 2004 Stratified turbulence dominated by vortical motion. *J. Fluid Mech.* **517**, 281–308.

Walmsley, J. L. 1989 Internal boundary-layer height formulae – a comparison with atmospheric data. *Boundary-Layer Meteorol.* **47**, 251–262.

Weatherly, G. L. & Martin, P. J. 1978 On the structure and dynamics of the oceanic bottom boundary layer. *J. Phys. Oceanogr.* **8** (4), 557–570.

Wharton, S. & Lundquist, J. K. 2012*a* Assessing atmospheric stability and its impacts on rotor-disk wind characteristics at an onshore wind farm. *Wind Energy* **15** (4), 525–546.

Wharton, S. & Lundquist, J. K. 2012*b* Atmospheric stability affects wind turbine power collection. *Environ. Res. Lett.* **7** (1), 014005.

White, F. M. 2011 *Fluid mechanics*, 7th edn. McGraw Hill.

Witha, B., Steinfeld, G., Dörenkämper, M. & Heinemann, D. 2014 Large-eddy simulation of multiple wakes in offshore wind farms. *J. Phys.: Conf. Ser.* **555** (1), 012108.

Wright, S. D., Elliott, L., Ingham, D. B. & Hewson, M. J. C. 1998 The adaptation of the atmospheric boundary layer to a change in surface roughness. *Boundary-Layer Meteorol.* **89** (2), 175–195.

Wu, X. 2017 Inflow turbulence generation methods. *Annu. Rev. Fluid Mech.* **49** (1).

Wu, Y.-T. & Porté-Agel, F. 2011 Large-eddy simulation of wind-turbine wakes: Evaluation of turbine parametrisations. *Boundary-Layer Meteorol.* **138** (3), 345–366.

Wu, Y.-T. & Porté-Agel, F. 2013 Simulation of turbulent flow inside and above wind farms: Model validation and layout effects. *Boundary-Layer Meteorol.* **146** (2), 181–205.

Wu, Y.-T. & Porté-Agel, F. 2015 Modeling turbine wakes and power losses within a wind farm using LES: An application to the Horns Rev offshore wind farm. *Renewable Energy* **75** (0), 945–955.

Wyngaard, J. C. 1973 On surface-layer turbulence. In *Workshop on Micrometeorology* (ed. D. A. Haugen), pp. 109–149. Amer. Meteorol. Soc.

Wyngaard, J. C. 2010 *Turbulence in the Atmosphere*. Cambridge University Press.

Yang, D., Meneveau, C. & Shen, L. 2014*a* Effect of downwind swells on offshore wind energy harvesting – a large-eddy simulation study. *Renewable Energy* **70**, 11–23, Special issue on aerodynamics of offshore wind energy systems and wakes.

Yang, D., Meneveau, C. & Shen, L. 2014*b* Large-eddy simulation of offshore wind farm. *Phys. Fluids* **26**, 025101.

Yang, X., Kang, S. & Sotiropoulos, F. 2012 Computational study and modeling of turbine spacing effects in infinite aligned wind farms. *Phys. Fluids* **24**, 115107.

Zhang, W., Markfort, C. D. & Porté-Agel, F. 2013*a* Experimental study of the impact of large-scale wind farms on land–atmosphere exchanges. *Environ. Res. Lett.* **8** (1), 015002.

Zhang, W., Markfort, C. D. & Porté-Agel, F. 2013*b* Wind-turbine wakes in a convective boundary layer: A wind-tunnel study. *Boundary-Layer Meteorol.* **146** (2), 161–179.

Zhou, B. & Chow, F. K. 2012 Turbulence modeling for the stable atmospheric boundary layer and implications for wind energy. *Flow Turb. Comb.* **88** (1), 255–277.

Zhou, L., Tian, Y., Baidya Roy, S., Thorncroft, C., Bosart, L. F. & Hu, Y. 2012 Impacts of wind farms on land surface temperature. *Nature Climate Change* **2**, 539–543.

Zilitinkevich, S. S. 1989 Velocity profiles, the resistance law and the dissipation rate of mean flow kinetic energy in a neutrally and stably stratified planetary boundary layer. *Boundary-Layer Meteorol.* **46** (4), 367–387.

Zilitinkevich, S. S. 2002 Third-order transport due to internal waves and non-local turbulence in the stably stratified surface layer. *Q. J. R. Meteorol. Soc.* **128** (581), 913–925.

Zilitinkevich, S. S. & Calanca, P. 2000 An extended similarity theory for the stably stratified atmospheric surface layer. *Q. J. R. Meteorol. Soc.* **126** (566), 1913–1923.

Zilitinkevich, S. S., Elperin, T., Kleeorin, N. & Rogachevskii, I. 2007*a* Energy- and flux-budget (EFB) turbulence closure model for stably stratified flows. Part I: Steady-state, homogeneous regimes. *Boundary-Layer Meteorol.* **125** (2), 167–191.

Zilitinkevich, S. S., Elperin, T., Kleeorin, N., Rogachevskii, I. & Esau, I. 2013 A hierarchy of energy- and flux-budget (EFB) turbulence closure models for stably-stratified geophysical flows. *Boundary-Layer Meteorol.* **146** (3), 341–373.

Zilitinkevich, S. S. & Esau, I. N. 2002 On integral measures of the neutral barotropic planetary boundary layer. *Boundary-Layer Meteorol.* **104** (3), 371–379.

Zilitinkevich, S. S. & Esau, I. N. 2003 The effect of baroclinicity on the equilibrium depth of neutral and stable planetary boundary layers. *Q. J. R. Meteorol. Soc.* **129** (595), 3339–3356.

Zilitinkevich, S. S. & Esau, I. N. 2005 Resistance and heat-transfer laws for stable and neutral planetary boundary layers: Old theory advanced and re-evaluated. *Q. J. R. Meteorol. Soc.* **131** (609), 1863–1892.

Zilitinkevich, S. S., Esau, I. N. & Baklanov, A. 2007*b* Further comments on the equilibrium height of neutral and stable planetary boundary layers. *Q. J. R. Meteorol. Soc.* **133** (622), 265–271.

Curriculum vitae

Dries Allaerts was born in Leuven (Belgium) in 1989. He obtained his bachelor's degree in Mechanical Engineering at KU Leuven in 2010, and graduated at the same university with magna cum laude as Master of Science in Engineering: Energy in 2012. His master's thesis was part of nuclear fusion research and concerned *Drifts and currents in the PSI-2 Linear Plasma Device*, supervised by Prof. dr. ir. M. Baelmans.

In October 2012, he started as a PhD researcher in the Turbulent Flow Simulation and Optimization Group at the Mechanical Engineering Department, KU Leuven, under the supervision of Prof. dr. ir. J. Meyers. His main research interests are in computational fluid dynamics, dynamics of large wind farms and atmospheric boundary layers (ABLs). He is particularly interested in wind-farm–ABL interactions and the effects of rotation and thermal stratification. His PhD is part of the Active Wind Farms project funded by the European Research Council (FP7-Ideas, grant no. 306471).

List of publications

International peer reviewed journal articles

Allaerts, D. & Meyers, J. 2015 Large eddy simulation of a large wind-turbine array in a conventionally neutral atmospheric boundary layer. *Phys. Fluids* **27**, 065108.

Allaerts, D. & Meyers, J. 2016 Boundary layer development and gravity waves in conventionally neutral wind farms. *J. Fluid Mech.*, revision submitted.

Chatterjee, F., Allaerts, D., Blahak, U., Meyers, J. & van Lipzig, N. 2016 Evaluation of a wind farm parametrization in a regional climate model using large eddy simulations. *Q. J. R. Meteorol. Soc.*, accepted for publication.

Papers at international scientific conferences and symposia

Allaerts, D. & Meyers, J. 2016 Effect of inversion-layer height and Coriolis forces on developing wind-farm boundary layers. *AIAA Paper No. 2016-1989*. American Institute of Aeronautics and Astronautics. 34th Wind Energy Symposium, AIAA Science and Technology Forum and Exposition. San Diego, CA, USA, 4-8 January 2016.

Allaerts, D. & Meyers, J. 2015 Simulation of large wind farms in the conventionally neutral atmospheric boundary layer using LES. In *Proceedings of the 10th International ERCOFTAC Workshop on Direct and Large-Eddy Simulation, Limassol, Cyprus*, in press.

Allaerts, D. & Meyers, J. 2014 Wind farm performance in conventionally neutral atmospheric boundary layers with varying inversion strengths. *Journal of*

Physics: Conference Series **524**, 012114. IOP Publishing. The Science of Making Torque from Wind, Lyngby, 18-20 June 2014.

Abstracts presented at international scientific conferences and symposia

Allaerts, D. & Meyers, J. 2016 Internal boundary layer growth over large wind farms under conventionally neutral conditions. Abstract No. 2B.4, American Meteorological Society. 22nd Symposium on Boundary Layers and Turbulence, Salt Lake City, Utah, USA, 20-24 June 2016.

Allaerts, D. & Meyers, J. 2015 Outer layer effects in wind-farm boundary layers: Coriolis forces and boundary layer height. *Bulletin of the American Physical Society* **60**, L12.00011. Annual Meeting of the APS Division of Fluid Dynamics, Boston, MA, USA, 22-24 November 2015.

Allaerts, D. & Meyers, J. 2015 Importance of boundary layer height and Coriolis forces for energy extraction in large wind farms. *International Colloquium on Large Wind Power-Plants: Interaction, Control and Integration. Book of Abstracts*. Windfarms 2015, Leuven, 8-10 July 2015.

Allaerts, D. & Meyers, J. 2014 Modeling large wind farms in conventionally neutral atmospheric boundary layers under varying initial conditions. European Geoscience Union: General Assembly, Vienna, 27 April - 02 May 2014.

FACULTY OF ENGINEERING SCIENCE
DEPARTMENT OF MECHANICAL ENGINEERING
DIVISION OF APPLIED MECHANICS AND ENERGY CONVERSION
TURBULENT FLOW SIMULATION & OPTIMIZATION GROUP
Celestijnenlaan 300 box 2421
B-3001 Leuven, Belgium
dries.allaerts@kuleuven.be
http://www.mech.kuleuven.be/en/tme/research/tfso